Rational design and modelling of f-block molecular nanomagnets

TESIS DOCTORAL

Instituto de Ciencia Molecular (ICMol)
Universitat de València

. . .

Memoria presentada por **José Jaime Baldoví Jachán** para aspirar al grado de Doctor en Nanociencia y Nanotecnología (programa ref. 3045)

. . .

Dirigida por:

Prof. Eugenio Coronado Miralles
Dr. Juan Modesto Clemente Juan
Dr. Alejandro Gaita Ariño

D. **EUGENIO CORONADO MIRALLES**, Profesor Catedrático del Departamento de Química Inorgánica de la Universitat de València, D. **JUAN MODESTO CLEMENTE JUAN**, Profesor Titular del Departamento de Química Inorgánica de la Universitat de València y D. **ALEJANDRO GAITA ARIÑO**, doctor por la misma universidad.

CERTIFICAN: Que la presente memoria, titulada: **"Rational design and modelling of f-block molecular nanomagnets"**, corresponde a la Tesis Doctoral de JOSÉ JAIME BALDOVÍ JACHÁN y ha sido desarrollada bajo su dirección en el Instituto de Ciencia Molecular, autorizando mediante este escrito la presentación de la misma para optar al grado de Doctor.

En Paterna, a 8 de enero de 2016.

Dr. Eugenio Coronado Miralles Dr. Juan M. Clemente Juan

Dr. Alejandro Gaita Ariño José Jaime Baldoví Jachán

The pursuit of truth and beauty
is a sphere of activity in which
we are permitted to remain children
all our lives

Albert Einstein

A mis padres

A María

Agradecimientos

Como toda obra humana, el desarrollo de esta tesis doctoral sería inimaginable sin contar con el conjunto de conocimientos y valores que otros seres humanos han ido acumulando desde los albores de la humanidad, proporcionándonos así la luz necesaria para progresar en la conquista de las fronteras del conocimiento. La ciencia, en su continua búsqueda de la comprensión del universo a través de la observación, la razón y la experimentación, abraza la experiencia, inteligencia e imaginación de un gran número de profesionales que interactúan y se benefician entre sí. Por lo tanto, no podría empezar la redacción de este proyecto de otra manera que mostrando mi más sincero agradecimiento a todas esas personas que me han guiado y acompañado en esta ardua tarea durante los últimos años.

Mis primeras palabras están dedicadas a Eugenio, a quien le agradezco toda la confianza depositada en mí, sus brillantes ideas y por ser tan eficaz a la hora de trazar el rumbo más adecuado. Desde mi llegada al ICMol ha sabido transmitirme su pasión por la investigación y su visión interdisciplinar de la ciencia, ofreciéndome una formación de primer nivel que me permitirá avanzar en el desarrollo de una carrera investigadora. Asimismo, me siento increíblemente agradecido a Modesto, cuyos amplios conocimientos en programación y Hamiltonianos efectivos han sido claves para el desarrollo del marco teórico y computacional de este trabajo. Todo ello siempre acompañado de una sonrisa amable y sincera que me ha permitido adquirir esas nuevas competencias disfrutando del trabajo en equipo.

Un párrafo especial en esta sección de agradecimientos se merece Álex Gaita. Álex ha sido un magnífico director de tesis que ha estado a mi lado en todo momento, guiándome a través de buenas ideas, enseñándome buena ciencia y brindándome su generosa ayuda y amistad –valga decir que es una de las mejores personas que he conocido en mi vida–. Con él he podido construir un ambiente de investigación altamente motivador y productivo que estoy seguro que perdurará más allá de esta tesis.

También quiero dedicar unas palabras de agradecimiento a Salva, con el que he compartido muy buenos momentos de trabajo, 'cardonismo' y amistad, y que siempre ha estado dispuesto a compartir lo mejor de su experiencia en cálculos teóricos y su talento como diseñador gráfico. Posteriormente llegó Luis, 'nuestro' matemático, con el que he compartido el gusto por la historia y que con su trabajo persistente asegura la continuidad de varias de las líneas trazadas en este proyecto.

Por otro lado, estoy enormemente agradecido a todos los colaboradores que desde varios puntos del planeta han interactuado conmigo en el transcurso de esta investigación: Eliseo Ruiz (Barcelona), Manuel Almeida y Laura C. Pereira (Lisboa), Anna Proust (París), Ulrich Kortz (Bremen), Shang-Da Jiang (Stuttgart), Naresh Dalal (Tallahassee), Song Gao (Pekín), Chang Seop Hong (Seúl), etc. También guardo muy gratos recuerdos de discusiones científicas y conversaciones interesantes con Fernando Luis (Zaragoza), Guillem Aromí (Barcelona), Joris van Slageren (Stuttgart) y Stephen Hill (Tallahassee) en diferentes conferencias internacionales. Thank you very much!

Las siguientes líneas van dedicadas a las personas del grupo con las que he tenido la suerte de poder colaborar durante este proyecto. A Guille, por enseñarme a utilizar la Cambridge Structural Database y por ser un excelente investigador. A Helena, por ser una profesional incansable y

compartir tantas gratas sorpresas con las medidas EPR. A Yan, por la síntesis de varios de los sistemas tratados en esta tesis y por estar siempre tan dispuesta con la mejor de sus sonrisas. A Chema y Gloria por las medidas magnéticas. A Andrei Palii, Boris Tsukerblat, Nicolas Suaud, y especialmente a Hans Güdel, por sus buenos consejos durante sus visitas. A Sara y Walter, su interés por el programa y su trabajo experimental con las diferentes familias de quinolinas. A Lorena Rosaleny por sus cálculos de tiempos de decoherencia y compartir el placer de la divulgación.

Esta etapa de mi vida no hubiese sido tan divertida y enriquecedora sin los buenos momentos vividos con Gonzalo, Dani, Toni y Á. Recuenco, con los que he recargado las pilas cada mediodía en el Rincón Exclusivo, compartiendo risas y mucha cultura general. Además de los mencionados, no me quiero olvidar del resto de *football players made in ICMol* y de nuestras pachangas, en las que nos convencimos definitivamente de que el fútbol no era lo nuestro. También merecen una mención especial mis compañeros de viaje: A. Abhervé y Michele (Equipo India), así como Paco y Eva, con los que he disfrutado de momentos inolvidables compartiendo la mayor de mis aficiones. También quiero expresar mi gratitud al resto de miembros del ICMol con los que he compartido inquietudes, buena ciencia y diversión. Además de su profesionalidad, en esta maleta de recuerdos me llevo la sonrisa de Miguel, la amabilidad de Alicia, la determinación de Carlos Martí, el buen humor de Carlos Gómez, la simpatía y eficacia de Marian, Estrella y María Jesús, la alegría de Mauri, Elena Pinilla y Alejandra, la ilusión y comprensión de María M. y Mónica, la pasión por las cosas bien hechas de Efrén y Samuel, las reflexiones de Juampi, el buen trato de Ángel, el carisma de Josep, y un largo etcétera de virtudes de tantos otros miembros, incluyendo las nuevas generaciones de estudiantes de Máster, con los que he compartido el día a día del grupo.

Ya casi terminando, quisiera dedicar unas líneas al magnífico trato recibido durante mi estancia en el Institut de Chimie Moléculaire et des Matériaux d'Orsay. Je tiens à remercier vivement Talal pour me donner l'opportunité de travailler dans son groupe et tous les membres pour m'avoir accueilli si bien. Además doy mil gracias a Mauri, Ramón, Sergio, Irene y Ricardo, por todo lo vivido en la ciudad de la luz.

Por último, pero no menos importante, deseo manifestar mi agradecimiento a mis amigos de toda la vida y familia en general, en especial a mis abuelos, porque siempre habéis estado ahí, así como, a mis compañeras de 'piso sanus' Clara y Mar, por la buena convivencia y amistad, haciendo más agradable el día a día.

A mi hermano Javier, muchas gracias por el diseño de la portada de la tesis, por haber estado siempre a mi lado y por los grandes momentos que hemos compartido en multitud de lugares desde hace 27 años. A mi cuñada Arantxa: te agradezco mucho tus palabras de ánimo en esta recta final y por interesarte constantemente por mi trabajo.

A María, por todo tu apoyo, amor y comprensión incondicional. Por haber llenado mi corazón en estos últimos cinco años y seguir diseñando cada día la más bonita de las historias. Mis palabras de agradecimiento son infinitas. Esta tesis nunca sería la misma sin ti.

A mis padres, José Félix y Mari Carmen, por haber despertado en mí la curiosidad infinita por el mundo que me rodea y haberme dotado de todos los medios necesarios para poder desarrollarme personal y académicamente. Porque siempre me habéis apoyado en todas y cada una de mis decisiones. Aunque no la entendáis, esta tesis está repleta de los valores que me habéis inculcado desde que nací. Muchas gracias.

José Jaime

One never notices what has been done;
one can only see what remains to be done.

Marie Skłodowska-Curie

Table of contents

Abstract

The project developed in this thesis is to provide a suitable framework to further develop an emerging research area in nanoscience that deals with the chemical design of molecular systems exhibiting interesting magnetic phenomena. In particular, it focuses on the setting up, application and benchmarking of a theoretical and computational framework for the inexpensive rationalisation and prediction of new f-element molecular nanomagnets. These systems are amongst the most complex entities in molecular magnetism, exhibiting slow relaxation of the magnetisation and magnetic hysteresis at low temperatures. They have been proposed as promising candidates for the development of high-density magnetic memories, magnetic refrigeration, quantum computing devices and for several applications in molecular spintronics.

The first part of this thesis describes the development of the theoretical framework. The main tool of this project, the computational package SIMPRE, is presented in Chapter 2, providing some practical information about its organisation and usage. Chapter 3 consists in a preliminary attempt to rationalise the conditions that a lanthanoid-based magnetic molecule needs to satisfy to act as a single-ion magnet (SIM) using the original point charge electrostatic model. The inherent drawbacks of the PCEM are overcome in Chapter 4, where two effective electrostatic approaches that include covalent effects, the Radial Effective Charge (REC) and the Lone Pair Effective Charge (LPEC) models, are presented.

The second part deals with the application of these effective electrostatic models to a series of lanthanide homoleptic coordination

compounds. In Chapter 5, a simultaneous systematic study of four isostructural families coordinated by halogen atoms using spectroscopic information permits an estimation of the REC parameters by relating them to chemical concepts such as Pauling electronegativity and the coordination number. This simplifies the task of obtaining an initial set of CFPs for phenomenological fittings. Chapter 6 extends the application of the REC model to systems coordinated by oxygen-donor ligands. These include five octa-coordinated polyoxometalate (POM) complexes with interest in molecular magnetism and quantum computing and a high-symmetry oxydiacetate family, where the capabilities of the model are benchmarked owing to the available photoluminiscence spectra. Furthermore, the model is used to interpret the properties of two layered dysprosium hydroxides and played a key role in the rational design of the first example of metal-organic framework having lanthanide SIMs as nodes. In Chapter 7, the LPEC model is used to model the magnetic and spectroscopic properties of the first SIM reported in the literature, based on phthalocyaninato ligands, where the electron density is not pointing directly to the lanthanoid. Two complexes coordinated to pyrazolyl-based ligands are also analysed in terms of the REC model on that chapter, which completes the trilogy presented in this part of the thesis.

The final part of the work is centred on the current challenges of the developed framework. Chapter 8 discusses the capabilities of both the program and the REC model to deal with the understanding of uranium SIMs, and introduces the use of the CONDON package to complement the limitations of the first. A second challenge –the modelling of magnetic molecular anisotropy– is addressed in Chapter 9 using an organometallic SIM as model system. Subsequently, the REC model is used to investigate the treatment of heteroleptic complexes coordinated by oxygen and

nitrogen atoms. The determination of the chemical structure at different temperatures allows to quantify, for the first time, the influence of the thermal evolution of the molecular structure in the electronic structure and magnetic anisotropy. Finally, Chapter 11 provides a few insights for the rational design of molecular spin qubits based on mononuclear lanthanide and uranium complexes. Through two examples, the chapter also describes the main features that make POM complexes particularly interesting for quantum information purposes.

List of publications

The following **list of publications** are derived totally (first author) or partially (in works that include experimental section) from the present Ph.D. thesis. They will be described in detail throughout this dissertation.

Chapter 2

1.- **Baldoví, J.J.,** Cardona-Serra, S., Clemente-Juan, J.M., Coronado, E., Gaita-Ariño, A. & Palii, A. SIMPRE: a software package to calculate crystal field parameters, energy levels, and magnetic properties on mononuclear lanthanoid complexes based on charge distributions. *J. Comput. Chem.*, **34**, 1961–1967 (2013).

2.- **Baldoví, J.J.,** Clemente-Juan, J.M., Coronado, E., Gaita-Ariño A. & Palii, A. An updated version of the computational package SIMPRE that uses the standard conventions for Stevens crystal field parameters. *J. Comput. Chem.*, **35**, 1930–1934 (2014).

Chapter 3

3.- **Baldoví, J.J.,** Cardona-Serra, S., Clemente-Juan, J.M., Coronado, E., Gaita-Ariño, A. & Palii, A. Rational Design of Single-ion Magnets and Spin Qubits Based on Mononuclear Lanthanoid Complexes. *Inorg. Chem.*, **51**, 12565–12574 (2012).

Chapter 4

4.- **Baldoví, J.J.,** Borrás-Almenar, J.J., Clemente-Juan, J.M., Coronado, E. & Gaita-Ariño, A. Modeling the properties of lanthanoid single-ion

magnets using an effective point-charge approach. *Dalton Trans.*, **41**, 13705–13710 (2012).

Chapter 5

5.- **Baldoví, J.J.,** Coronado, E. & Gaita-Ariño, A. Modeling the magnetic properties of lanthanide complexes: relation of the REC parameters with Pauling electronegativity and coordination number. *Dalton Trans.*, **44**, 12535–12538 (2015).

Chapter 6

6.- **Baldoví, J.J.,** Clemente-Juan, J.M., Coronado, E., Duan, Y., Gaita-Ariño, A. & Giménez-Saiz, C. Construction of a General Library for the Rational Design of Nanomagnets and Spin Qubits Based on Mononuclear f-Block Complexes. The Polyoxometalate Case. *Inorg. Chem.*, **53**, 9976–9980 (2014).

7.- **Baldoví**, **J.J.,** Duan, Y., Bustos, C., Cardona-Serra, S., Clemente-Juan, J.M., Gaita-Ariño, A., Villanneau, R., Giménez-Saiz, C., Proust, A. & Coronado, E. Single Ion Magnets based on Lanthanoid Polyoxomolybdate complexes. A route to processability. *In preparation*.

8.- **Baldoví**, **J.J.,** Rosaleny, L.E., Ramachandran, V., Dalal, N.S., Clemente-Juan, J.M., Yang, P., Kortz, U., Gaita-Ariño, A. & Coronado, E. Molecular spin qubits based on lanthanide ions encapsulated in cubic polyoxopalladates: design criteria to enhance quantum coherence. *Inorg. Chem. Front.*, **2**, 893–897 (2015).

9.- **Baldoví**, **J.J.,** Duan, Y., Morales, R., Gaita-Ariño, A., Ruiz, E. & Coronado, E. Benchmarking the capabilities of *ab initio* and effective electrostatic calculations in single-ion magnets. *Submitted*.

10.- Monteiro, B., Coutinho, J.T., Pereira, C.C.L., Pereira, L.C.J., Marçalo, J., Almeida, M., **Baldoví**, **J.J.,** Coronado, E. & Gaita-Ariño, A. Magnetic Properties of the Layered Lanthanide Hydroxide Series $Y_xDy_{8-x}(OH)_{20}Cl_4{\cdot}6H_2O$: From Single Ion Magnets to 2D and 3D Interaction Effects. *Inorg. Chem.*, **54**, 1949–1957 (2015).

11.- **Baldoví**, **J.J.,** Coronado, E., Gaita-Ariño, A., Gamer, C., Giménez-Marqués, M. & Mínguez Espallargas, G. A SIM-MOF: Three-Dimensional Organisation of Single-Ion Magnets with Anion-Exchange Capabilities. *Chem.-Eur. J.*, **20**, 10695–10702 (2014).

Chapter 7

12.- **Baldoví**, **J.J.,** Clemente-Juan, J.M., Coronado, E. & Gaita-Ariño, A. Two pyrazolylborate dysprosium (III) and neodymium (III) single ion magnets modeled by a Radial Effective Charge approach. *Polyhedron*, **66**, 39–42 (2013).

Chapter 8

13.- **Baldoví**, **J.J.,** Cardona-Serra, S., Clemente-Juan, J.M., Coronado, E. & Gaita-Ariño, A. Modeling the properties of uranium-based single-ion magnets. *Chem. Sci.*, **4**, 938–946 (2013).

14.- Antunes, M.A., Coutinho, J.T., Santos, I.C., Marçalo, J., Pereira, L.C.J., Almeida, M., **Baldoví**, **J.J.,** Coronado, E. & Gaita-Ariño, A. A Mononuclear Uranium (IV) Single-Molecule Magnet with an Azobenzene Radical Ligand. *Chem.-Eur. J.*, **21**, 17817–17826 (2015).

Chapter 9

15.- **Baldoví, J.J.,** Clemente-Juan, J.M., Coronado E. & Gaita-Ariño, A. Molecular Anisotropy Analysis of Single-Ion Magnets Using an Effective Electrostatic Model. *Inorg. Chem.*, **53**, 11323–11327 (2014).

Chapter 10

16.- Qian, K., **Baldoví, J.J.,** Jiang, S.-D., Gaita-Ariño, A., Zhang, Y.-Q., Overgaard, J. Wang, B.-W., Coronado, E. & Gao, S. Does the Thermal Evolution of Molecular Structures Critically Affect Electronic and Magnetic Structure?. *Chem. Sci.*, **6**, 4587–4593 (2015).

Chapter 11

17.- **Baldoví**, **J.J.**, Cardona-Serra, S., Clemente-Juan, J.M., Coronado, E., Gaita-Ariño, A. & Prima-García, H. Coherent manipulation of spin qubits based on polyoxometalates: the case of the single ion magnet $[GdW_{30}P_5O_{110}]^{14-}$. *Chem. Commun.*, **49**, 8922–8924 (2013).

Other contributions

18.- **Baldoví, J.J.,** Cardona-Serra, S., Clemente-Juan, J.M., Coronado, E., Escalera-Moreno, L., Gaita-Ariño, A. & Mínguez Espallargas, G. Quantum Error Correction with magnetic molecules. *Europhys. Lett.*, **110**, 33001 (2015).

19.- [Science Education] Abellán, G., Rosaleny, L.E., Carnicer, J., **Baldoví, J.J.** & Gaita-Ariño, A. La aproximación crítica a las pseudociencias como ejercicio didáctico: homeopatía y diluciones sucesivas. *Anales de Química*, **110**, 211–217 (2014).

20.- Mead, M.I., Popoola, O.A.M., Stewart, G.B., Landshoff, P., Calleja, M., Hayes, M., **Baldovi, J.J.,** McLeod, M.W. Hodgson, T.F., Dicks, J., Lewis, A., Cohen, J., Baron, R., Saffell, J.R. & Jones, R.L. The use of electrochemical sensors for monitoring urban air quality in low-cost, high-density networks. *Atmos. Environ.*, **70**, 186-203 (2013).

21.- Popoola, O.A.M., Mead, M., Stewart, G., Hodgson, T., McLoed, M., **Baldovi, J.**, Landshoff, P., Hayes, M., Calleja, M. & Jones, R. Low-Cost Sensor Units for Measuring Urban Air Quality. *AGU Fall Meeting Abstracts*, **1**, 0054 (2010).

22.- Cardona-Serra, S., Escalera-Moreno, L., **Baldoví, J.J.**, Gaita-Ariño, A., Clemente-Juan, J.M. & Coronado, E. SIMPRE1.2: considering the hyperfine and quadrupolar couplings and the nuclear spin bath decoherence. *Accepted manuscript*.

23.- Lim, K.S., **Baldoví**, **J.J.,** Lee, W.R., Song, J.H., Yoon, S.W., Suh, B.J., Coronado, E., Gaita-Ariño, A. & Hong C.S. Control of the slow relaxation of magnetisation in D_{4d} mononuclear dysprosium complexes via ligand charge. *Submitted*.

24.- Gaita-Ariño, A., Prima-García, H., Cardona-Serra, S., Escalera-Moreno, L., Rosaleny, L.E. & **Baldoví, J.J**. Coherence and organisation in lanthanoid complexes as spin qubits. *Submitted*.

25.- Lim, K.S., Jiang, S.-D., Koo, B.H., Ryu, D.W., Lee, W.R., Koh, E.K., **Baldoví, J.J.,** Gaita-Ariño, A., Coronado, E., Slota, M., Bogani, L. & Hong, C.S. Magnets based on octahedral Dy: a step farther in the understanding of rare-earth magnetism. *In preparation*.

26.- Miralles, S.G., Bedoya-Pinto, A., **Baldoví**, **J.J.,** Cañón-Mancisidor, W., Prado, Y., Gaita-Ariño, A., Mínguez-Espallargas, G., Hueso, L. & Coronado, E. Sublimatable Single Ion Magnets: Deposition on Ferromagnetic Substrates. *In preparation*.

27.- Cañón-Mancisidor, W., Miralles, S.G., Y., Mínguez-Espallargas, G., **Baldoví, J.J.**, Gaita-Ariño, A. & Coronado, E. Sublimatable Materials based on Lanthanide Quinoline Complexes. *In preparation*.

28.- **Baldoví, J.J**., Gaita-Ariño, A., & Coronado, E. Modelling lanthanide coordination complexes: a critical perspective. *In preparation*.

Abbreviations and symbols

ac	alternate current
acac	acetylacetonate
AOM	Angular Overlap Model
bath	bathophenanthroline
BIPMTMS	$C(PPh_2NSiMe_3)_2$
bipy / bpy	2,2'-bipyridine
B_{kq}	crystal field parameters (Wybourne notation)
BPz	(pyrazolyl)borate
C-NOT	controlled NOT gate
ca.	circa (approximately)
CASPT2	Complete Active Space second-order Perturbation Theory
CASSCF	Complete Active Space Self-Consistent Field
CF / CFP(s)	crystal field / crystal field parameter(s)
CI	configuration interaction
CN	coordination number
COT	cyclooctatetraene dianion ($C_8H_8^{2-}$)
Cp*	pentamethylcyclopentadiene anion (C_5Me_5)
CSD	Cambridge Structural Database
D	uniaxial anisotropy parameter
dc	direct current
DFT	Density Functional Theory
D_h	horizontal displacement
d_{in}	internal distance between atoms placed in the same plane
dme	dimethoxyethane

DOTA	1,4,7,10-tetraazacyclododecane-N,N′,N′′,N′′′-tetraacetate
d_{pp}	distance between the upper and lower planes
dppz	dipyridophenazine
dpq	dipyridoquinoxaline
D_r	radial displacement
D_v	vertical displacement
e.g.	exemplī grātiā (for example)
E_{Bkq}	absolute error between phenomenological and theoretical crystal field parameters
ECM	Effective Charge Model
$\mathbf{E_L}$	electronegativity of the ligand
$\mathbf{E_M}$	electronegativity of the metal
emu	electromagnetic units
EPR	electron paramagnetic resonance
ESOs	extended Stevens operators
et al.	et alii (and the others)
E_{Δ}	relative error between experimental and theoretical Stark sublevels
F	scale factor
$f_{X,CN}$	Effective charge – radial displacement factor
$\mathbf{F^k}$	electron repulsion parameters (Slater parameters)
FC	field-cooled
FIR	far infrared
Fortran	Formula Translating System
g_i	charge factor of the Simple Overlap Model
g_J	Landé g-factor
GMR	giant magnetoresistance
$g_{//}$	electron paramagnetic resonance g-factor g-parallel

H	magnetic field
h	2,4-hexanedione
H-NMR	proton nuclear magnetic resonance
H_{CF}	crystal field Hamiltonian
hfac	hexafluoroacetylacetonate
H_3trensal	2,2′,2′′-tris(salicylideneimino)triethylamine
i.e.	id est (that is)
ICMol	Instituto de Ciencia Molecular
Im	imaginary
INS	inelastic neutron scattering
ITO	irreducible tensor operators
J	total angular momentum
L	total orbital angular momentum
LAPACK	Linear Algebra PACKage
LLHs	layered lanthanide hydroxides
LPEC	Lone-Pair Effective Charge
MCD	magnetic circular dichroism
M_J	Angular momentum quantum number associated with J_z
mnt	maleonitriledithiolate
MOF	metal organic framework
MRAM	magnetoresistive random-access memory
M_S	spin quantum number associated with S_z
NDC	naphtalene dicarboxylate
NIR	near-infrared
NIT	nitronyl nitroxide
NIT-pic	nitronyl nitroxide picolinate
NV	nitrogen-vacancy
ODA	oxydiacetate

OKIA	Olivier Kahn International Award
Pc	phthalocyaninato
PCEM	Point-Charge Electrostatic Model
pdmH	pyridine-2,6-dimethanol
Ph	phenyl group ($C_6H_5^-$)
Ph.D.	Philosophiæ doctor **(**Doctor of Philosophy degree)
phen	phenanthroline
phen	phenomenological
pinene-bpy	4,5-pinene bipyridine
p_{kq}	prefactor in the tesseral harmonics
POM	polyoxometalate
qubit	quantum bit
R_0	smallest among the distances metal-ligand in the Simple Overlap Model
RASSCF	Restricted Active Space Self-Consistent Field
RASSI	Restricted Active Space State Interaction
Re	real
REC	Radial Effective Charge
R_{eff}	effective distance
Ref.	reference
$\{R_i, \theta_i, \varphi_i\}$	spherical coordinates
$\langle r^k \rangle$	expectation value of the radius
Rot1, Rot2	experimental single-crystal rotations
R_μ	distance metal-ligand in the Simple Overlap Model
S	total spin angular momentum
SIM	Single-ion magnet
SIMPRE	Single Ion Magnet PREdiction
SMM	Single-molecule magnet

SOM	Simple Overlap Model
S_P	continuous shape measure in SHAPE software
S_Q	goodness of fit
SQUID	Superconducting Quantum Interference Device
STNO	spin-transfer nano-oscillators
SWAP	quantum gate that swaps two quantum bits
tacn	1,4,7-triazacyclononane
^{t}Bu	tert-butyl
terpy	terpyridine
tfpb	4,4,4-trifluoro-1-phenyl-1,3-butandionate
theo	theoretical
THF	tetrahydrofuran
TIP	temperature independent paramagnetism
Tp	trispyrazolylborate
Tp^{Me2}	hydrotris(3,5-dimethylpyrazolyl)
tta	2-thenoyltrifluoroacetone
TTF	tetrathiafulvalene
T_1	spin-lattice relaxation time
T_2	spin-spin relaxation time
U_{eff}	effective barrier
UHV	ultra high vaccum
UV	ultraviolet
V_M	valence of the metal
vs.	versus
$V(r_i)$	electrostatic potential felt by the electron
x, y, z	cartesian coordinates
Y_k^q	spherical harmonics
Z	atomic number

ZEE	Zeeman effect
Z_{eff}, Z_i	effective electrostatic charge
ZFC	zero field-cooled
ZFS	zero-field splitting
$Z_{k0}^{c}, Z_{kq}^{c}, Z_{kq}^{s}$	tesseral harmonics (c, cosine; s, sine)
α, β, γ	Stevens coefficients
Δ	tunnelling splitting
Δz	axial compression
ξ_{5f}	spin-orbit coupling constant
λ_{kq}	ratios of the Stevens to the real valued Wybourne normalised parameters
μ_{eff}	effective magnetic moment
ρ_i, $\rho(R)$	time-independent charge distribution
ρ_j	overlap between a 4f orbital and the valence orbitals of the j^{th} ligand
σ_k	Sternheimer shielding parameters
τ_0	Arrhenius pre-exponential factor
τ_n	decoherence time caused by the nuclear spin bath
τ_R	Rabi decay time
χ	magnetic susceptibility
χ'	in-phase, or real, magnetic susceptibility
χ''	out-of-phase, or imaginary, magnetic susceptibility
ψ	wave function
Ω_R	Rabi frequency

0

Introduction

1 Introduction to f-block molecular nanomagnets

1.1 Magnetic molecular materials

Magnetochemistry is the branch of chemistry concerned with the synthesis and study of substances that exhibit interesting magnetic phenomena.[1] The main subject of this discipline is precisely the relation between the magnetic and the structural and chemical properties of these materials. As magnetochemists focused on molecular systems, magnetochemistry gradually evolved into an interdisciplinary field namely molecular magnetism.[2,3] This field combines the efforts from organic and inorganic chemists, solid-state physicists and theoretical researchers, and aims at the design, synthesis and characterisation of the magnetic properties of molecular-based materials. Both magnetochemistry and molecular magnetism combine experimental measurements with model Hamiltonians in order to rationalise the magnetic behaviour of molecule-based materials.[4] Such procedures are intended to obtain an approximation to their electronic structures, in the case of ions or molecules, or to their band structures, in the case of extended solids.

One of the pioneers who moved magnetochemistry into molecular magnetism was the French scientist Olivier Kahn. He rejuvenated areas like spin crossover and created a new language that combines the languages of chemistry and physics. Such a language has been extensively utilised in theoretical modelling of molecular-based magnets. From the extensive work from his group, one can highlight the development of ferromagnetic Cu^{2+}-VO^{2+} dinuclear complexes, Cu^{2+}-Mn^{2+} bimetallic chains that order ferrimagnetically via supramolecular interactions and room temperature Fe^{2+}-triazole spin crossover chains with hysteresis.[5–8] Apart from that, this excellent scientist was especially committed to the promotion of proficient young researchers. This was recognised by the community through the creation of the Olivier Kahn International Award (OKIA) in 2006.[9] The OKIA award recognises every year a young scientist who has completed his/her Ph.D. within the last decade.

The development of the emerging field of molecular magnetism has been really fast.[10] The current trends in the field are mainly focused on two main classes of materials: molecular nanomagnets and multifunctional magnetic materials.[11] In this section of the thesis we are going to briefly introduce these two main topics. As the developed Ph.D. thesis is framed within molecular nanomagnetism, the subsection 1.1.1 will be appropiately more extense in order to provide a better comprehension of the type of molecules that we will later be analysing throughout this dissertation.

1.1.1 Nanomagnetism

For more than two decades single-molecule magnets (SMMs) have been a hot topic in molecular magnetism due to their rich physical behaviour.[12] By definition, a SMM is a molecule that displays magnetic bistability

generated by an energy barrier to magnetisation reversal. These systems are amongst the most complex magnetic entities, exhibiting slow relaxation of the magnetisation and magnetic hysteresis loops at liquid-helium temperatures. The superparamagnetic blocking gives rise to a magnetic memory effect similar to that encountered in hard magnets, together with quantum phenomena like quantum tunnelling of the magnetisation,[13,14] quantum coherence[15] or quantum interference[16]. Unlike conventional bulk magnets, the magnetic properties have a molecular origin. This means that collective long-range magnetic ordering of magnetic moments is not necessary for bistability and the characteristic molecular magnetic behaviour appears even at high dilutions in a diamagnetic matrix.[17]

The first generation of SMMs was based on polynuclear magnetic complexes with strong magnetic coupling between d-transition metal ions. In these clusters governed by magnetic exchange, a small number of paramagnetic transition metal ions are connected through linkers such as F^-, Cl^-, OH^-, OCH_3^-, $RCOO^-$ or O^{2-}. The first and most renowned example is a molecule formed by twelve manganese nuclei[18] that form a magnetic cluster with general formula $[Mn_{12}O_{12}(O_2CMe)_{16}(H_2O)_4]$ (in short: Mn_{12}).[19,20] The cluster is composed by eight Mn^{3+} ions (S = 2) which in the ground state have their spins oriented in a parallel fashion, and four Mn^{4+} ions (S = 3/2), whose spins are also parallel (Figure 1.1). These two spin moieties have an antiparallel orientation, giving a total giant spin of $S = 10$ for the ground state. The classical projections of S are quantised into 21 permitted states $(2S+1)$ corresponding to S_z from $-S$ to $+S$. The spin reversal can occur either by passing through all those permitted states –thermally assisted– or by quantum tunnelling between quasidegenerate states placed on the opposite sides of the barrier.[13] This tunnelling mechanism for the relaxation of the magnetisation is responsible of the characteristic steps at regular field

intervals registered in 1995 in the hysteresis curve of Mn_{12} (quantum tunnelling of the magnetisation).[21,22] Transitions between spin microstates induced by phonons are limited to $\Delta M_s = \pm 1, \pm 2$.[23–25] The uniaxial anisotropy, characterised by a negative D value, splits the ground state in such a way that the $M_s = \pm 10$ doublet becomes the ground spin state of the molecule. This results in Ising-type magnetic anisotropy. The rest of sublevels are occupying the excited states as the $|M_s|$ component decreases, as illustrated in Figure 1.1 (right).[26–28]

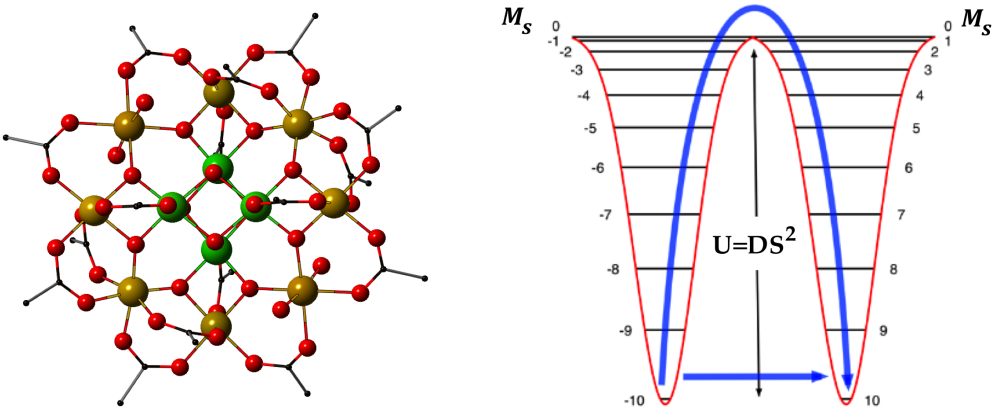

Figure 1.1: (left) Molecular structure, Mn^{3+} (gold) and Mn^{2+} (green); (right) energy level scheme showing the two-wells of $[Mn_{12}O_{12}(O_2CMe)_{16}(H_2O)_4]$.

The research work devoted to the understanding of the magnetic properties of Mn_{12} concluded into two main requirements that served to guide the synthesis of molecules exhibiting SMM behaviour. The first one was to design a cluster with a high total spin S. For a long time, scientists were looking for increasingly larger nuclearities[29–32] in an attempt to increase the spin state of the cluster by coupling many magnetic ions. The second requirement was having a remarkable negative D in the cluster in order to stabilise the highest M_S sublevel.[33] The combination of both

requirements was intended to increase the superparamagnetic barrier.[12] Nevertheless, the success of this approach has been very limited and nowadays Mn_{12} is still among the transition-metal clusters exhibiting the highest effective barriers (ca. 45-50 cm^{-1}). In fact, it has theoretically been shown that for fundamental reasons, achieving a high spin of the ground state in high-nuclearity clusters is in contradiction with achieving a large magnetic anisotropy.[34]

Three years after the discovery of single-magnetic behaviour in Mn_{12}, an octanuclear iron complex $[Fe_8O_2(OH)_{12}(tacn)_6]^{8+}$ (known as Fe_8), where tacn = 1,4,7-triazacyclononane, was also found to exhibit such a behaviour.[35,36] Since then, this system has attracted numerous studies, mainly by the physics community.[37–39] Subsequently, a rising number of lower nuclearity systems were reported to exhibit slow relaxation of the magnetisation, as for example, the tetranuclear complex $[Mn_4(O_2CMe)_2(pdmH)_6](ClO_4)_2$.[40,41] Other examples included a polyoxometalate acting as a template to encapsulate a transition metal cluster, including iron(II) ions,[42] or even further mixed-valence manganese species.[43] In both cases the barriers obtained were close to 10 cm^{-1}. More recently, polynuclear clusters formed by lanthanoid ions have also been synthesised and characterised.[44–47] These complexes do present effective barriers of approximately 100 cm^{-1} and show hysteresis up to 8 K in the best case. In this context, Dy_3 triangles were also rationalised to understand the cooperative blocking phenomena and their slow magnetic relaxation.[47–49]

An important breakthrough in molecular magnetism was the discovery of a new approach for the design of SMMs.[50] This new way of thinking, proposed by Ishikawa and his co-workers,[51] consisted in the development of minimalistic nanomagnets based on coordination complexes with a central lanthanide ion as the source of magnetic

anisotropy. This type of compounds are known as mononuclear SMMs or single-ion magnets (SIMs).[52] In contrast to the first generation of SMMs, whose properties rely on the ability of exchange interactions to stabilise anisotropic high spin states, the magnetic properties of SIMs depend primarily on the single ion anisotropy resulting from the combination of spin-orbit coupling and ligand field.[53] Hence, these two variables play a key role in the creation of a thermal barrier which slows down the magnetisation reversal.[54] The first examples of SIMs were the Tb^{3+} and Dy^{3+} derivatives of the family of bis(phthalocyaninato) lanthanoid complexes with 'double-decker' structure, in short $LnPc_2$ (Figure 1.2(a)). In this family, the magnetic center is surrounded by eight nitrogen atoms in a pseudo-axial crystal field of D_{4d} symmetry (Figure 1.2(c)). The square antiprismatic D_{4d} CF induced by the two moieties of phthalocyaninato ligands around the rare earth splits its ground magnetic state, characterised by the total angular momentum, J, in $\pm M_J$ sublevels. In some cases this leads to a sublevel scheme in which the levels with the higher $|M_J|$ values are stabilised with respect to the levels with the lower $|M_J|$ values. According to Ishikawa's description,[55] the ground magnetic doublet of the Tb derivative corresponds to that with the maximum M_J value (= ±6) and is separated from the first excited level (M_J = ±5) by more than 300 cm^{-1}. Phthalocyaninato-lanthanoid complexes have been extensively studied and a large amount of analogues were fabricated with the goal of increasing the blocking temperature.[56] A particular successful example derived from this family keeps the thermal barrier record for a single-ion magnet (652 cm^{-1}) up to the time of this writing.[57]

Recognising that the coordination environment around the magnetic cation plays a key role to obtain SMM behaviour,[58] the concept of SIMs could be extended to different ligands other than phthalocyaninato ligands

in 2008, when researchers from our group reported the second family of SIMs (Figure 1.2(b)).[59] Thus, slow relaxation of the magnetisation could be achieved in a family of polyoxometalates encapsulating lanthanoid ions with a sandwich-type structure similar to that of $LnPc_2$. This Lindqvist-type family has the general formula $Na_9[Ln(W_5O_{18})_2]$ (in short, LnW_{10}), displaying a square-antiprismatic D_{4d} symmetry.[60] The most promising candidate for this series was the Er derivative (U_{eff} = 38.5 cm^{-1}, close to that observed in Mn_{12}, $U_{eff} \approx 50$ cm^{-1}), whereas in the preceding family such behaviour was more remarkable in $[TbPc_2]^-$.

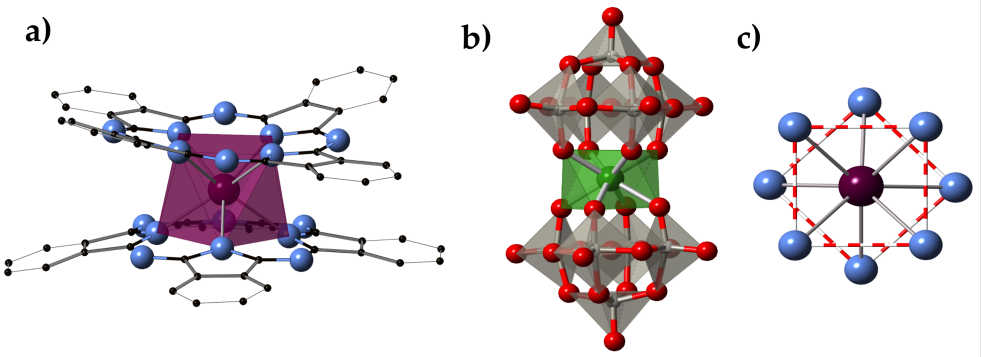

Figure 1.2: Representation of the two first families of SIMs: (a) phthalocyaninato-based SIMs $[LnPc_2]^-$; (b) polyoxometalate-based SIMs of general formula $[Ln(W_5O_{18})_2]^{9-}$; (c) view of the square antiprismatic coordination sphere around the lanthanide ion in $[LnPc_2]^-$. Hydrogens are omitted for clarity.

The reason for this difference was assumed to lie on the different distortion of the square antiprismatic site, which is compressed in the second family, in contrast with the axially elongated $[LnPc_2]^-$ (Figure 1.2). The interplanar distance of the ErW_{10} compound (d_{pp} = 2.47 Å), which was calculated as the distance between the upper and lower planes containing the four oxygen atoms, is considerably smaller than the one of $TbPc_2$ (d_{pp} = 2.76 Å). As we will discuss throughout this dissertation, these differences in

the coordination environment (oblate vs. prolate) have severe consequences in the energy level structures.[61] The magnetic relaxation process was observed to happen faster in the LnW_{10} analogues in comparison with the phthalocyaninato-based series, which was attributed to the fact that the Stark sublevels are more compressed at lower energies.[58]

The experimental studies of the first series of POM-based SIMs were extended to the Keggin-type series $K_{13}[Ln(\beta_2\text{-}SiW_{11}O_{39})_2]$ (in short, LnW_{22}).[62] This permitted the analysis of the effects produced by a more distorted antiprismatic environment over the spin relaxation processes. A few years later, a third family of mononuclear lanthanide SMMs based on polyoxometalates was also synthesised and characterised by our group.[63] The molecule, which is based on the well-known Preyssler anion, is formulated as $K_{12}[LnP_5W_{30}O_{110}] \cdot nH_2O$ (in short, LnW_{30}) and presents an unusual C_5 axial symmetry (see Figure 1.3).[64] The 5-fold geometry gives rise to large off-diagonal anisotropy parameters. The spin dynamics, mainly at low temperatures, is dominated by fast tunnelling processes and strongly affected by hyperfine interactions.[65]

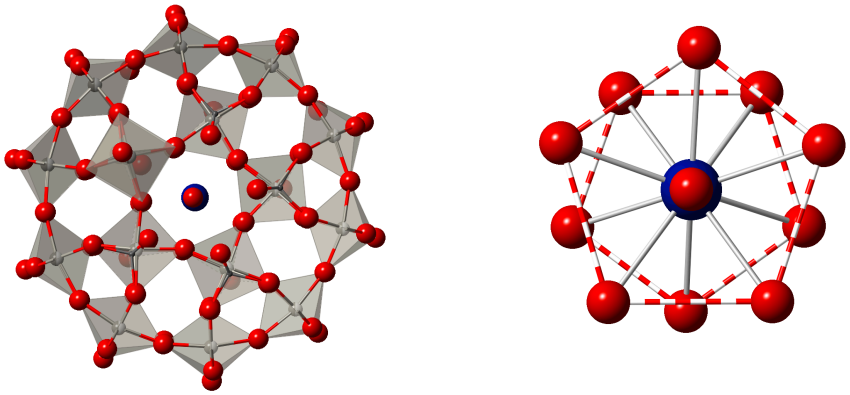

Figure 1.3: (left) Molecular structure of the $[LnP_5W_{30}O_{110}]^{12-}$ anion; (right) schematic view showing the 5-fold coordination environment around the lanthanide ion.

Among the advantages that polyoxometalate chemistry offers for the design of molecular nanomagnets one can remark that: (i) the geometry around the magnetic ion is not restricted to D_{4d}, they can provide different rigid and highly symmetrical coordination environments; (ii) the diamagnetic polyoxometalate framework protects the lanthanide; and, (iii) they can in principle be prepared as nuclear spin-free systems, which is interesting to minimise decoherence when designing a POM-based spin qubit.[58]

Since the discovery of SMM behaviour in ErW_{10}, the impact of this class of molecular nanomagnets has been dramatically increased and now hundreds of SIMs have been reported.[66] These SIMs have shown very different coordination environments and different types of coordinated ligands.[67] Some relevant examples are the organometallic double-decker Er^{3+} compound[68,69] (Figure 1.4(a)) and the acetylacetonate lanthanoid complexes (Figure 1.4(b)),[70,71] both studied by the group of Prof. Song Gao, as well as the $Na[Dy(DOTA)(H_2O)]\cdot 4H_2O$ complex, (Figure 1.4(c)) where H_4DOTA = 1, 4, 7, 10-tetraazacyclododecane-N, N', N'', N'''-tetraacetic acid, reported by Prof. Roberta Sessoli *et al*.[72] Beyond the routine magnetic characterisation, the molecular magnetic easy axis of $Na[Dy(DOTA)(H_2O)]\cdot 4H_2O$ was determined by single crystal X-ray diffraction. The combination of these experimental results with *ab initio* theoretical calculations lead to evidence the significant impact that the capping coordinated molecule of water has over the calculated anisotropy axis.[73,74] The manipulation of the hydrogen atoms of the water molecule around the C_4 axis envisaged the large effects that minor modifications may have over magnetic anisotropy. This means that one must be very careful when assuming that the easy axis of magnetisation is oriented along the same direction as the molecular (pseudo-)symmetry axis using simple

magneto-structural correlations.[66] Nevertheless, this is still a topic under discussion, as it was contradicted in a more recent work (2013) where the same rotation of the apical water molecule using *ab initio* calculations was performed by Chilton *et al*. finding no dependence on the orientation of the ground state anisotropy axis.[75]

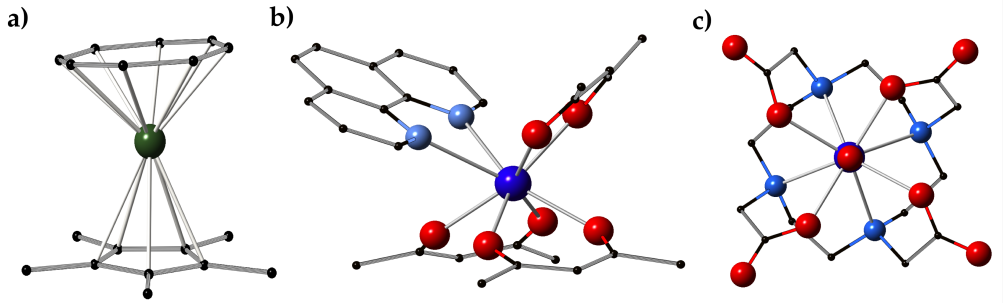

Figure 1.4: Molecular structures of the lanthanide-based SIMs: (a) Cp*ErCOT; (b) $[Dy(acac)_3(phen)]$; (c) $[Dy(DOTA)(H_2O)]^-$. Hydrogens are omitted for clarity.

On the other hand, the concept of SIMs is not limited to molecular materials. In fact, the first mononuclear lanthanide system displaying slow relaxation of the magnetisation was reported by Barbara *et al*. in the doped crystal $LiY_{0.998}Ho_{0.002}F_4$, observing a staircase-like hysteresis loop that was attributed to a nuclear spin driven quantum relaxation.[76] Also, the isostructural series of lanthanide-substituted scheelites of general formula $Ca_{(1-x)}Er_xWO_4$ exhibited coherent Rabi oscillations –quantum oscillations that result from the coherent absorption of photons driven by an electromagnetic wave–, which are indicative of high quantum coherence, behaving as a spin qubit.[77]

More recently it has been shown that mononuclear d-transition metals can also display SMM behaviour; these SIMs are beyond of the scope of this thesis, which is focused in f-element complexes. The origin of SMM behaviour in cobalt(II) ions with non-uniaxial anisotropy has been

investigated, being attributed to time-reversal symmetry that blocks direct spin–phonon processes independently of the sign of the magnetic anisotropy.[78] Examples of the most quoted cases of mononuclear d-transition complexes include the Fe-pyrrolide molecules,[79] a two-coordinate complex of iron(I) $[Fe(C(SiMe_3)_3)_2]^-$ that exhibits an effective spin-reversal barrier of U_{eff} = 226 cm^{-1},[80] a $Co(SPh)_4$ salt,[81] and for example, the recently investigated $(PPh_4)_2[Cu(mnt)_2]$ that shows an extraordinary potential for quantum computing presenting room temperature quantum coherence (~ 1 μs) with a coherence time at low temperatures of ~10 μs.[82]

Currently, the obtention of new molecules with larger energy barriers and the understanding of the quantum tunnelling processes are the two major challenges in molecular nanomagnetism.[17] In this context, actinoid-based SIMs are attracting a growing attention and their study is considered an emerging topic.[83] In fact, due to higher spin-orbit coupling and higher exposure of the f-electrons to the surroundings, actinides exhibit larger magnetocrystalline anisotropy, stronger spin–orbit coupling interactions and enhanced exchange interactions. As the *J*-ground state splitting caused by the crystal field is expected to be higher, they can be considered to be better candidates to provide SIMs than lanthanides. Those features are related to the 5f electrons, which are more extended than the 4f electrons on lanthanoids and interact more with the electrons of the ligands.

Although some examples have been reported in the last few years, SIMs based on actinides are still scarce and mainly restricted to U^{3+} species.[84] The Long group published the first two examples of uranium-based SIMs. The first one was measured in 2009 in a diphenylbis(pyrazolylborate) uranium(III) complex formulated as $U(Ph_2BPz_2)_3$,[85] previously isolated in 1999 by Santos *et al*.[86] A year later, a second example of the same family was reported in the

dihydrobis(pyrazolylborate) derivative $U(H_2BPz_2)_3$[87] (Figure 1.5) and the list was extended with the discovery of SMM behaviour in the UTp_3 complex (Tp^- = trispyrazolylborate).[88] Independently, Almeida *et al*. reported two further examples closely related of U^{3+} SIMs: the cationic complex $[U(Tp^{Me2})_2(bipy)]^+$, where Tp^{Me2}=hydrotris(3,5-dimethylpyrazolyl),[89] its precursor $[U(TpMe_2)_2I]$,[90] first prepared and characterised by Takats *et al*.,[91] and the $[U(Tp^{Me2})_2(bipy^*)]$ complex, which contains a radical ligand.[92] In this context, we performed the first attempt to rationalise the magnetic properties of these related complexes.[93] A few months later, the first uranium(V) SIM, based in triamidoamine, was published.[94] In this thesis, we will be focused on the modelling of uranium nanomagnets in Chapter 8.

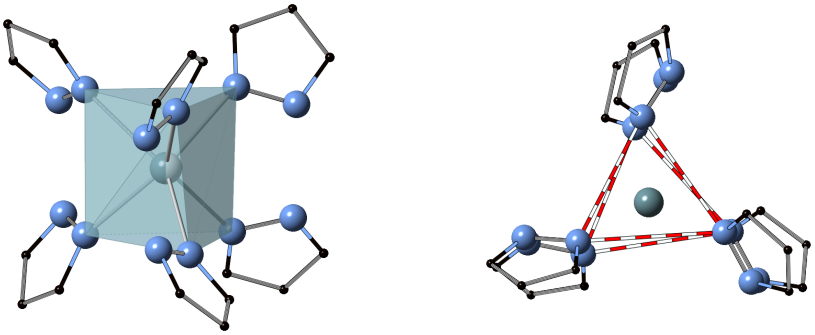

Figure 1.5: (left) Molecular structure of the $U(H_2BPz_2)_3$; (right) eclipsed view highlighting the trigonal prismatic coordination environment around U^{3+}. Hydrogens are not considered for clarity.

Other actinoid-based SMMs that are not going to be treated in this dissertation are a mononuclear complex based on neptunium, $[Np(COT)_2]$ ($COT = C_8H_8^{2-}$),[95] and two polynuclear complexes: the trimetallic cluster $\{Np^{VI}O_2Cl_2\}\{NpVO_2Cl(THF)_3\}_2$,[96] also known as Np_3, and the delocalised arene-bridged diuranium SMM of formula $[(U(BIPMTMSH)(I))_2(\mu\text{-}\eta_6\text{:}\eta_6\text{-}C_6H_5CH_3)]$, where BIPMTMS = $C(PPh_2NSiMe_3)_2$.[97]

1.1.2 Multifunctional materials

The interest in the design and development of novel materials that simultaneously combine different properties has increased for the past three decades. This has been motivated by the creation of future systems with a new level of functionality, adaptability, sustainability, higher efficiency and cost reduction. Multidisciplinary studies towards this direction have lead to materials that can be especially engineered to intimately incorporate electrical conductivity, magnetism and optical properties, together with other functionalities as mechanical properties and power generation. Often, the combination of these multiple capabilities in a particular material offers advantages beyond the sum of their individual physical properties. Their industrial applications include nowadays sensors, renewable energies, medicine, nanoelectronics, advanced defense, and automotive and aerospace technologies.[98]

In this context, materials chemistry plays a key role in the design and fabrication of these next-generation materials. The many possibilities of tuning the physical properties of the systems *à la carte* via conventional chemical synthesis make this molecular approach a promising way to obtain the targeted materials. One particular case of multifunctional materials are the multifunctional magnetic materials, which are those that combine magnetism with at least a second property. Multifunctional magnetic materials based on molecules offer a great potential for technological applications because they can present features that have traditionally been considered exclusive of solid-state materials. These characteristics include the combination of cooperative magnetism with conductivity, superconductivity or ferroelectricity.[11]

A particularly attractive class of multifunctional magnetic materials are the *switching magnetic materials*. These are characterised by the possibility of modifying the magnetic properties by the application of external stimuli such as light, pressure or temperature. The most known examples are molecular spin-crossover compounds[99,100] and 3D magnets based on Prussian Blue derivatives.[101,102] Another relevant property that can coexist with magnetic entities is that of chirality, which combined with ferromagnetism may lead to magneto-chiral dichroism (MCD).[103–105]

In recent years, the development of a molecular building block approach, which relies on the combination of different molecular entities carrying specific functionalities into an extended molecule-based solid, has proven to be a very effective synthetic route.[101,106,107] This has marked a turning point in the research of multifunctional materials. A particular class of materials following this approach are the *dual-function materials*. These hybrid materials are often prepared by combining inorganic and organic components, each of them with a different property, which can be incorporated into the final product. Relevant examples of such hybrid materials are the magnetic molecular conductors. Typically, these hybrids combine anionic inorganic building blocks showing ferromagnetism with a cationic organic conducting network, typically based on donor tetrathiafulvalene (TTF) or their derivatives.[108,106]

Another class of hybrid materials is constituted by those that incorporate a molecular unit into a solid-extended host. A successful example of that was reported by our group in a system formed by layered TaS_2 (superconductor) with intercalated SMMs[109] (Figure 1.6) or spin-crossover molecules.[110] This hybrid approach may be useful to investigate the influence of these SMMs on the properties of the material. For example, owing to their advantageous chemical, structural and electronic features

that make them suitable as spin qubits, mononuclear f-block complexes based on POMs are an attractive option to design the molecular part of such hybrid analogues.[58] Further analysis of the vortex dynamics of hybrid materials combining superconducting surfaces with molecular magnetism will be necessary to bring light to the possible vortex pinning character of these nanomagnets.[111,112] In addition, superconducting substrates have been reported as prime candidates for spin manipulation, increasing the lifetime due to the depletion of electronic states around the Fermi level in the superconductor.[113] Hence, we can envisage that superconducting surfaces will play a key role in the design of systems where spin dynamics can be controlled. This will enable surface-state spintronics[114,115] and quantum devices[116] based on the above-mentioned hybrid materials.

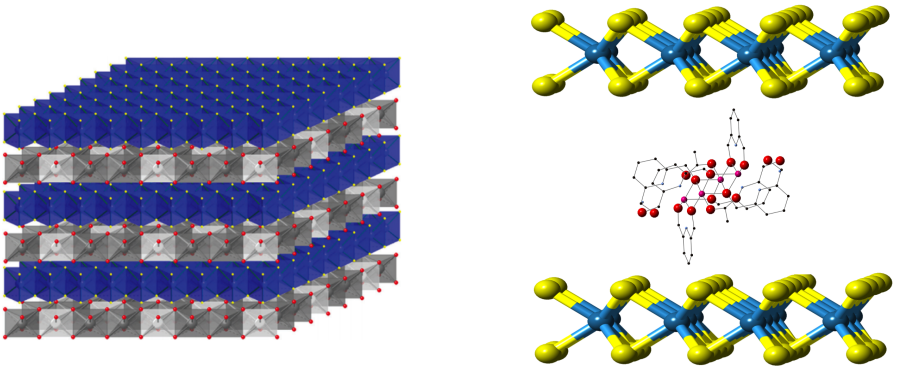

Figure 1.6: (left) Representation of the restacked material formed by $[TaS_2]^{-0.33}$ and $[Ni_{0.66}Al_{0.33}(OH)_2]^{+0.33}$, superconducting and magnetic layers respectively; (right) structural representation ascribed to the powder patterns observed in the hybrid material $[Mn_4(OAc)_2(pdmH)_6]_{0.15}[TaS_2]$.

A different approach to enhance multifunctionality towards lanthanoid-based materials is that based on the incorporation of these lanthanide complexes into metal-organic frameworks (Ln-MOFs). The performance of these structures as multifunctional systems has been

reviewed by Rocha *et al*.[117] Ln-MOFs can combine light emission with several properties such as microporosity, magnetism, chirality, molecule and ion sensing, catalysis and activity as multimodal imaging contrast agents. These materials are suitable to show synergy between these properties, such as the coupling between photoluminescence and magnetism. A particular class of Ln-MOFs are those based on bimetallic oxalate complexes, where the intrinsic magnetism of the MOF is combined with additional properties provided by different organic/inorganic functional cations.[118] Also, it is worth to mention the work of Schmitt and co-workers based on a highly augmented trivalent holmium-based MOF whose tridimensional network structure gives rise to porosity after desolvation.[119] In that recent work, the authors outlined a synthetic approach intended to tune the photophysical properties of the framework to obtain ligand-sensitised near-infrared (NIR) and visible light emitters in the Eu, Nd and Sm homologous cations.

In this context, we are going to present a lanthanide-based MOF formed by nodes that display SMM behaviour in section 6.6 of this thesis. That work, reported in 2014, opened the possibility of incorporating non-innocent POMs that would yield multifunctional MOFs in which the properties of the polyoxometalate can be combined with those of the lanthanoid framework.[120]

1.2 Theoretical modelling

The rapid development and growing interest in f-block SIMs over the past twelve years has been possible thanks to the advances in the experimental and theoretical techniques.[17] Such advances have motivated a high volume

of research and a steady output of publications, including the work to be described in this dissertation. As a result, the theory that was developed for trivalent lanthanide ions embedded in solid-state matrices or in highly symmetric inorganic crystal environments,[121] required the expansion to a new theoretical paradigm in order to investigate the properties of these low-symmetry entities with interest in molecular magnetism. Also, the theoretical methods used in molecular magnetism, specialised in transition metal clusters, had to be adapted to deal with the large number of parameters required in these molecules. This has given rise to new software packages and simple models, as we will describe in chapters 2 and 4. Throughout this process, the theoretical framework has allowed the identification of the key factors that are needed to guide the efforts for the synthesis of these molecules with magnetisation blocking and to facilitate the interpretation of their magnetic properties.[53,122]

To put this in perspective, let us recall that the theoretical analysis of classical molecular clusters evolved from the study of a reduced number of exchange-coupled transition metal ions, considering special spin topologies, to the development of the generalised spin Hamiltonian[123,124] intended to deal with high nuclearity systems.[125] Research towards this direction resulted in the development of the computational package MAGPACK, which has had a great impact in the field.[126] In general, the discovery of novel derivatives with SMM behaviour was focused on the optimisation of a large ground state spin S and a large negative zero field splitting (ZFS) parameter D as main factors.[27] These studies considered: (i) the importance of isolating the ground spin S from the first excited state S^*,[127] creating a strong negative uniaxial anisotropy ($D < 0$), and (ii) the influence of the transverse anisotropy term E and higher-order terms in the spin-Hamiltonian as an origin of the magnetisation tunnelling.[128] As

mentioned in 1.1, the inherent difficulties to optimise simultaneously these two requirements were also discussed.[34] Thus, the key point was to understand the intricate relations between the molecular structures and these parameters.[129]

In contrast, the magnetic properties of lanthanide SIMs depend primarily on the anisotropy of a single ion.[53,61] This in turn results from a strong spin-orbit coupling and an adequate ligand field. Thus, the design of new coordination complexes capable of displaying SMM properties requires the development and use of predictive theoretical models using their geometric structures.[122] For that there are mainly two options that have been proven to be useful for modelling the properties of lanthanide coordination compounds, namely the CF electrostatic approaches, which consider a point-charge distribution around the central ion, and *ab initio* calculations based on the complete active space self-consistent field (CASSCF).

The present section briefly describes the main features of both approximations. As this Ph.D. thesis is focused on the development of computational tools and models for the inexpensive rationalisation and prediction of novel SIMs, we will be centred on the development of the point-charge electrostatic approach adding the necessary covalent corrections.

1.2.1 Crystal field approaches

The unique spectroscopic and magnetic properties of lanthanide ions have excited researchers for decades.[130] These systems present more complex spectra than those of transition metals, which are usually characterised by a few broad bands. In this context, CF theory is essential to analyse and

simulate the energy level schemes of f-element complexes,[131] providing an accuracy level of about 10 cm^{-1}.[132–134] CF theory describes the perturbation of the electron cloud of the central ion produced by a surrounding charge distribution which breaks the orbital states degeneracies.[121] This quantum mechanical theory was first developed in 1929 by Hans Bethe.[135] In this section we aim to provide an overview of this theory. The crystal field Hamiltonian (H_{CF}) may be defined as:

$$H_{CF} = -e\sum_{i=1}^{n} V(r_i) = -e\sum_{i=1}^{n} \int \frac{\rho(R)}{|R - r_i|} \partial\tau \qquad (1.1)$$

where $V(r_i)$ is the potential, caused by a time-independent charge distribution $\rho(R)$, that the electron feels; e is the elementary charge; R and r_i are the position vectors of a general point of the environment and the electron respectively, and $\partial\tau$ is a volume element. The summation runs over all the electrons i of the central metal ion. The integral acts over the entire space.

There are several alternatives to parameterise the CF Hamiltonian presented in Equation 1.1. The main differences between them are related to the normalisation of tensor operators or the combinations applied by them. These parameterisations can be splitted into two types: those related to tesseral harmonics (whose parameters are always real) and those related to spherical harmonics (whose parameters are in general complex numbers). In this context, two different formalisms to calculate the matrix elements of H_{CF} are available in the literature, namely the formalisms of Stevens and Wybourne.[136,137] The former notation uses tesseral-tensor operators, whereas the latter applies spherical-tensor operators.

According to Stevens formalism,[136] proposed in 1952, the electrostatic potential around the lanthanide ion for a given J-multiplet can be expressed

by a sum of equivalent angular momentum operators, the extended Stevens operators O_k^q:[138]

$$\hat{H}_{CF}(J) = \sum_{k=2,4,6} \sum_{q=-k}^{k} B_k^q O_k^q = \sum_{k=2,4,6} \sum_{q=-k}^{k} a_k A_k^q \left\langle r^k \right\rangle O_k^q \qquad (1.2)$$

where k (for f-elements, k = 2, 4, 6) is the order (also called rank or degree) and q is the operator range, that varies between k and $-k$. The Stevens operator equivalents O_k^q are defined by Ryabov in terms of the angular momentum operators $J_\pm$ and J_z (see Table 2.2),[139] where the components $O_k^q(c)$ and $O_k^q(s)$ correspond to the ESOs with q ≥ 0 and q < 0 respectively. Note that all the Stevens CFPs B_k^q are real,[140] whereas the matrix elements of O_k^q (q < 0) are imaginary. a_k are the tabulated α, β and γ Stevens coefficients[136] for k = 2, 4, 6, respectively, which depend on the number of f electrons. $\langle r^k \rangle$ are the corrected expectation values of the radius. The symmetry elements of the B_k^0, B_k^q and B_k^{-q} are the same as those for the tesseral harmonics Z_{k0}^c, Z_{kq}^c and Z_{kq}^s. These are linear combinations of the spherical harmonics in the form: $Z_{kq}^c = \frac{1}{\sqrt{2}}\left[Y_k^{-q} + (-1)^q Y_k^q\right]$ and $Z_{kq}^s = \frac{i}{\sqrt{2}}\left[Y_k^{-q} - (-1)^q Y_k^q\right]$.[141]

This formalism has been especially successful when dealing with individual electronic terms such as the ground $^{2S+1}L_J$ multiplet in lanthanide trivalent ions. In this case, the CF splitting is typically one order of magnitude smaller than that of the spin–orbit coupling (as can be seen in Figure 1.7). Hence, one can consider the effects of the excited states practically negligible over the ground $^{2S+1}L_J$ multiplet. As long as we are

interested in the theoretical modelling of the magnetic properties of lanthanide SIMs, the Stevens formalism is suitable because there is no need to take into account the effects of the excited *J* multiplets. This formalism has been dominant in EPR studies.[142] This situation differs when we are interested in optical properties, where the more general formalism of Wybourne that naturally takes into account excited states dominates.[143]

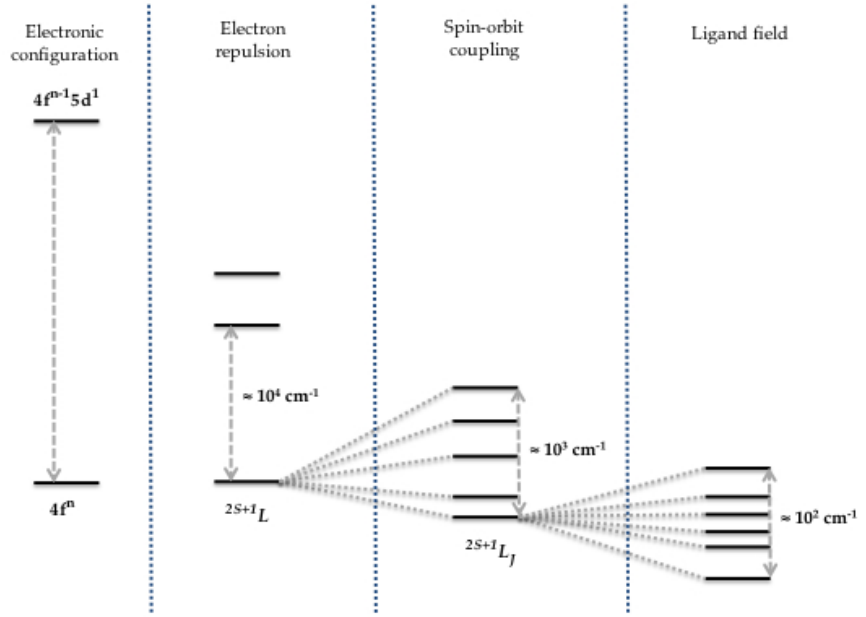

Figure 1.7: Schematic representation of the approximate sizes of the corresponding energy splittings in a lanthanide system.[17]

The parameterisation by Wybourne formalism can be expressed using the following equation, which is consistent with the CF parameterisations adopted by Görller-Walrand and Binnemans[144]:

$$\hat{H}_{CF} = \sum_{k}\left[B_{k0}C_0^{(k)} + \sum_{q=1}^{k}(\mathrm{Re}\,B_{kq}(C_{-q}^{(k)} + (-1)^q C_q^{(k)}) + i\,\mathrm{Im}\,B_{kq}(C_{-q}^{(k)} - (-1)^q C_q^{(k)})) \right] \quad (1.3)$$

where B_{kq} are the CFPs in Wybourne notation, which are in general complex (with the exception of B_{k0}). Their real and imaginary parts are expressed as ReB_{kq} and ImB_{kq} respectively. $C_0^{(k)}$, $C_q^{(k)}$ and $C_{-q}^{(k)}$ are the corresponding irreducible-tensor operators, which belong to the class of the spherical-tensor operators. The principal disadvantage of this formalism is that one has to deal with imaginary CFPs because their operators are not Hermitian. The tensor operators are related to the spherical harmonics by:

$$C_q^{(k)} = \sqrt{\frac{4\pi}{2k+1}} Y_k^q \quad (1.4)$$

The existence of different parameter notations and the inconsistent use of the phase convention between $C_q^{(k)}$ and $C_{-q}^{(k)}$ have caused confusion in researchers interested in CF theory.[141] Also, the CFPs depend of the coordinate system, requiring the development of conventions to choose the proper reference framework. In this sense, one needs to remark the work of C. Rudowicz and co-workers who have identified and corrected the pitfalls of a large amount of articles with the aim of standarising the CFPs according to the prevailing conventions.[140,145–148] This is very important to enable the comparison between different sets of parameters.

The calculation of the CF splitting can be performed by diagonalisation of the corresponding CF matrix. For that, one needs to determine the non-vanishing CFPs (B_k^q or B_{kq}, depending on the employed formalism). This is a non-trivial task with only a few alternatives

nowadays. The first approach to deal with this, which has been broadly used by spectroscopists, is the extraction of phenomenological CFPs from a direct fit of UV/visible spectroscopic experimental data. Although not predictive, this method has permitted the reproduction of the spectroscopic energy level scheme with great accuracy using a small set of parameters in high-symmetry systems. Useful information of lower lying magnetic levels can also be obtained from the far infrared (FIR) or from inelastic neutron scattering spectra (INS). Experimental advances in the field aiming to address this issue include the high resolution luminescence spectroscopic method, which has been applied to determine the fine electronic structures of lanthanide complexes.[73,149] Also, thermodynamic techniques, especially those based in single-crystal measurements,[73] including torque magnetometry,[150] can provide useful information about molecular anisotropy at different temperatures in order to obtain a reliable set of CFPs.

This phenomenological approach was adapted by Ishikawa *et al.* when modelling the $LnPc_2$ family for the first time.[55] In the absence of UV/visible spectroscopic data, the authors proposed a model to determine the CFPs of a set of isostructural lanthanide compounds. This method consists in the simultaneous fit of the temperature dependence of powder magnetic susceptibilies and ^1H NMR spectra, thus ensuring the correct orientation of the anisotropy axis, for the Tb, Dy, Ho, Tm and Yb derivatives. The molecular geometry was assumed to be strictly D_{4d}, i.e. the two Pc rings placed parallel and staggered 45º with respect to each other. This allowed the simplification of the CF Hamiltonian to only the three diagonal CFPs per derivative, being expressed as: $H_{CF}(J) = B_2^0 O_2^0 + B_4^0 O_4^0 + B_6^0 O_6^0$. In order to further limit the parameter space,

a key restriction was imposed, defining each parameter as a linear function of the number of f electrons, n:

$$A_k^q \left\langle r^k \right\rangle (n) = a_k^q + b_k^q (n - n_0) \tag{1.5}$$

where n_0 was fixed to 10.5, the mean value of n for the lanthanide ions included in the collective fit. This procedure was able to describe the static magnetic properties of the family. It was later applied to the series LnW_{10}, LnW_{22} and LnW_{30} relying merely on χT data.[62,63] This could provide an estimation of the CFPs, energy levels and wave functions of these three lanthanide polyoxometalate families with some of their derivatives exhibiting SMM behaviour. It is now widely recognised that a major shortcoming of this approach was to assume a linear dependence of the diagonal parameters on the number of f-electrons, which conveniently but arbitrarily restricts the degrees of freedom. Crucially, this sometimes results in unphysical evolution of the parameters, e.g. a change of the sign of the second-order aniosotropy parameter for a given coordination geometry.

From the computational point of view, a substantial advance was the development of the CONDON program by Kögerler *et al.*,[151] which uses the full Hamiltonian and determines the phenomenological CFPs from a fitting of the magnetic susceptibility data and/or energy levels.[152] However, when dealing with molecular systems, this strategy requires the determination of a large number of CFPs, resulting in overparameterisation. Low-symmetry is clearly the bottleneck of the phenomenological approach. For example, in C_i symmetry the number of parameters to be determined is as high as 27, which makes their determination meaningless. Furthermore, in these cases, the idealisation of the chemical structure is often unreasonable. Since such

procedures involve a function of many variables which have to be fitted, starting from a good trial set of CFPs is necessary in order to reach good convergence with a minimum of error.

A different strategy that involves the direct calculation of CFPs using very simple equations that relate the molecular structure with these parameters was proposed in the first third of the past century. The simplest procedure is based on the point charge electrostatic model (PCEM), subsequently improved by several *semi-empirical* models. These models, while very useful for quick predictions of the properties and for obtaining an initial set of CFPs, also need parameterisation to take into account covalency to provide a more realistic description of the observed properties of the system. We discuss here the differences between the most important of electrostatic models:

- The Point Charge Electrostatic Model (PCEM)[135] is the simplest approximation. The model parameterises the electrostatic field generated by the charge distribution around the metallic centre as a sum of Coulomb fields created by point charges placed at the crystallographic atomic positions. In its simplest form, it only considers the first coordination sphere. The value of the point charges is assumed to be that of the formal charges of the coordinated atoms, e.g. $Z_i = 1$ for F^-, Cl^-, OH^-, or $Z_i = 2$ for O^{2-}. The fundamental equations which determine the CFPs in the PCEM will be described with more detail in the next chapter (Equations 2.1). The model completely disregards covalency and it can only be considered as a rough approximation for ionic systems, predicting the correct sign of the parameters in these complexes. When comparing with the experimental values, the CFPs calculated by PCEM are considerably overestimated for $k = 2$, reasonable for $k = 4$ and greatly underestimated for $k = 6$.[131]

- The Effective Charge Model (ECM)[153] has offered more promising results (see for example the work of Klokishner *et al.*).[154,155] It has been able to reproduce sets of CFPs in many cases, being a more limited approximation in systems with a higher covalent character. The model reproduces the covalent effects by changing both the position and the magnitude of the charges. The ECM includes as effective charges all atoms that are placed in a 100 Å radius sphere.

- The Simple Overlap Model (SOM)[156–158] was designed to deal within 4f↔4f transitions in lanthanide complexes. The developers of the model used the PCEM as a starting point and suggested the delocalisation of the charge density between the lanthanide ion and the nearest neighbour atoms. The SOM postulates: (i) the potential energy of the 4f electrons is produced by charges uniformly distributed over small regions located around the middle distance between the lanthanide ion and the ligands, and (ii) the total charge in each region is proportional to the magnitude of the total orbital overlap between the lanthanide-ligand pair. As a major advantage compared with ECM, SOM only needs to consider the first coordination sphere and does not include free parameters. The input distance r_i is related to the crystallographic distance R_i by $r_i = R_i \cdot (1 \pm \rho_j)/2$ with $\rho_j = 0.05 \cdot (R_0/R_\mu)^{3.5}$, where ρ_j is the overlap between a 4f orbital and the valence orbitals of the ligand, and R_0 and R_μ are the smallest among the distances metal-ligand and the metal-ligand distance for each donor atom, respectively. The effective charges Z_i are related to a tabulated charge g_i by $Z_i = |g_i| \cdot \rho_i$, they are very similar to the ones of ECM.[158]

- The Angular Overlap Model (AOM)[159] is a general method that includes specific parameters to describe the interaction between the lanthanoid ion and the ligand. These parameters are directly linked with

the σ, π, δ and φ-bonding character of the ligands. The model discriminates the angular part and the electrostatic effects. According to their postulates, (i) the energies of the f-orbitals are determined as a perturbation that is proportional to the squares of the metal-ligand overlap integrals. (ii) the perturbation matrix generated by an apical ligand is diagonal if the basis of the f-orbitals is defined from a coordinate system *xyz*, and (iii) the contributions from different ligands are additive. Like SOM, it allows to classify the ligands in terms of their relative covalence, and allows an interpretation of the CF parameters in terms of the nature of the ligands and their coordinates. Note that the three previous models all shared the signs of the CFPs established by PCEM. However, in the AOM the signs of the CFPs depend on an angular paramater. This is an advantage of this approach, which can be considered more versatile, allowing the rationalisation of systems with rigid polyhapto ligands.

The models that we are going to introduce in this dissertation are framed within this type of CF models derived from the PCEM. All of them are relatively easy to apply, as they only require crystallographic positions as input. These approaches are necessarily oversimplified, leaving a large part of the physics out of the picture. However, they can produce a reasonable magnitude order in the CFPs calculation and a key advantage is that they have an inexpensive computational cost. This is of crucial importance, if we keep in mind there is no general and realistic solution to deal with low-symmetry real complexes. Thus, there is a value in effective electrostatic models which reduce the degrees of freedom for the simulation of a $4f^N$ configuration energy level scheme.

1.2.2 First principles

Post Hartree-Fock multi-configurational calculations have for some years been the default option for the theoretical characterisation of lanthanide SIMs, as first principles methods are expected to be more exact compared with the more intuitive electrostatic methods. These calculations are commonly called *ab initio*, which is a Latin term that translates as 'from the beginning', meaning in this case 'from the first principles'. Unlike *semi-empirical* methods, the *ab initio* approach does not use experimental data to be fitted. Thus, their results are derived from the fundamental constants introduced by the applied quantum physical laws. The great strength of this computationally expensive approach is the possibility of progressively and objectively improving the quality of the method. The systematic procedure of increasing the quality of the basis set, enlarging the embedding and the active space -within reason- and, most importantly, including more correlation effects,[160] should consistently produce a convergent set of results.

The most broadly employed *ab initio* multi-configurational approach in lanthanides is based on the complete active space self-consistent field (CASSCF).[161–163] Nowadays, CASSCF is implemented in several computational packages such as MOLCAS (the most used in molecular magnetism),[164] Gaussian,[165] Orca[166] and MOLPRO[167]. The basics of this approach lies in the splitting of the molecular orbitals into three main classes when building the CASSCF wave function. These are the inactive (double-occupied), active space and virtual (empty) blocks. The method computes a full configuration-interaction (full-CI) in the active space, within the mean field created by the inactive block. Based on this variational approach, the wave function is written as a linear combination

of all possible configurations (Slater determinants). The energy minimisation procedure is self-consistent with the coefficients of the configuration state functions and the molecular orbitals. The description of electronic near-degeneracies and excited states makes the model adequate to estimate ligand-field states in lanthanoid SIMs. The bottleneck of this approach is the increase of the computational cost which is proportional to the number of Slater determinants created by a particular subspace. Between the attemps to restrict the set of these functions, one can mention the restricted active space self-consistent field (RASSCF) method that reduces the number of electrons in specific active spaces.[168] On the other hand, CASSCF wave functions take only into account the static correlation. Dynamical correlation energy, which is necessary to obtain accurate results, may be calculated using the perturbative method CASPT2.[169] This approach provides a second-order perturbation on the CASSCF input states.

In molecular magnetism, the standard procedure when studying trivalent lanthanoid complexes using the *ab initio* approach is the CASSCF/RASSI-SO method. It is based on the restricted active space state interaction (RASSI),[170] which is included in the MOLCAS package[164] and considers spin-orbit coupling as non-perturbately. The active space includes all f-electrons and the seven 4f orbitals. The spin-orbit interaction is considered according to the Douglas-Kroll-Hess Hamiltonian in the mean-field approximation, which accounts for relativistic effects.[171] The energy levels are calculated after diagonalising the spin-orbit coupling using the CASSCF wave functions that have previously been optimised for each spin. As in lanthanides the spin-orbit is an order of magnitude larger than the CF effect, one needs to optimise and include the maximum number of CASSCF spin states as possible in the spin-orbit diagonalisation. This is a consequence of the fact that this procedure applies spin-orbit

coupling after, rather than before, the ligand field. With this regard, the best possible calculation concerning this limitation is the CASSCF optimisation of every Russell-Saunders state and their inclusion in the diagonalisation matrix. Because it is a computationally demanding method, the calculation of the maximum number of spin states originated by the $4f^N$ configuration needs the application of state-averaged CASSCF. Within this strategy the energy average of the demanded configuration-interaction roots is minimised by molecular orbital optimisation. An interesting review concerning the extraction of the magnetic Hamiltonian by different computational methods has been reported by Guihéry *et al*.[172]

In a second step, experts in the CASSCF/RASSI-SO method who deal with the modelling of lanthanide SIMs use the SINGLE_ANISO program.[173] This routine permits to compute the static magnetic properties (van Vleck susceptibility tensor and function, molar magnetisation vector and function) and the 27 CFPs. The CFPs are determined by a descomposition of the CF matrix in irreducible tensor operators (ITOs) and in extended Stevens operators working in the ground $^{2S+1}L_J$ multiplet. In the meanwhile, the projections of the total angular momentum with respect to the reference coordinate frame are also calculated.

In spite of the great popularity of this approach –one can find near a hundred of relevant results from Web of Science concerning the application of MOLCAS in f-element molecular magnetism–, and its success in the prediction of magnetic molecular anisotropy, Kögerler *et al*. recently pointed out the main issues derived from the application of CASSCF/RASSI-SO and how their results are interpreted in lanthanide and actinide systems.[152] That work also remarked the better performance of full vs. effective models in the description of the observables. Benchmarking of *ab initio* correlated methods goes back to a pioneering paper of Hirao *et*

al.,[174] where it was shown that CASSCF wavefunctions overestimate Coulomb repulsion, while ligand field restricted active spaces underestimate the CF splitting. Other articles using high-quality spectroscopic measurements have encountered some deviations between *ab initio* calculations and experimental data in the low-lying energy levels.[175–177] In a few examples, *semi-empirical* scale factors have been employed to bridge this gap,[176,177] which were attributed to either the thermal evolution of the molecular structures upon temperature variation, the limited size of the employed basis sets or unaccounted dynamical correlation. In this context, Mulak and Gajek concluded that "nowadays except the passive-phenomenological description of the crystal field effect we have at our disposal no effective crystal field theory based on reliable microscopic model which would be enough rigorous and simultaneously useful and handy for experimentalists", emphasising the great challenges that still exist in the study of f-element coordination complexes.[178] A full assessment of the accuracy of both effective and *ab initio* methods remains an open problem and will require systematic further efforts from both the experimental and theoretical side. In section 6.4 and Chapter 9 of this thesis, we will come back to these relevant issues, benchmarking the capabilities of the models and analysing the effects of the thermal-dependent structural effects over the energy levels.

1.3 Applications

Since the discovery of the first SMM in the early 1990s,[20] molecular nanomagnets have been proposed as promising candidates for the development of high-density magnetic memories,[179] magnetic refrigeration[180] and several applications in molecular spintronics,[181]

nanotechnology[182] and quantum computing devices[183]. These molecular entities combine the macroscale properties of classical magnets with the quantum ones arising from their nanoscale size. In this section we are going to overview the potential applications of these systems in nanomagnetism, in particular in quantum computing and molecular spintronics.

1.3.1 Quantum computing

One of the most encouraging potential applications of SMMs and SIMs is their integration as the building blocks of quantum computers. Quantum computing is a new paradigm in computer science based on the explicit use of quantum-mechanical phenomena to implement logic operations for the purposes of information technology.[184] The key difference when compared to conventional computers is that rather than store information in one of the two definite states '0' or '1', the basic units of a quantum computer are quantum bits (qubits) which can be a superposition of the basis states. A qubit is a quantum two-level system that may be represented as a linear combination of $|0\rangle$ and $|1\rangle$: $|\psi\rangle = \alpha|0\rangle + \beta|1\rangle$, where α y β are probability amplitudes and can be complex numbers.

As of the end of this thesis, the design of a real quantum computer is still in an embryonic stage. In recent years, a load of effort has been expended on finding physical systems to build such computers by applying the famous quantum circuit model of quantum logic gates established by DiVincenzo.[185] Since then, several alternative approximations to quantum computation have arisen.[186,187] The requirements are apparently simple. According to DiVincenzo, we need: (i) to initialise the qubit to a pure state, (ii) to perform any one-qubit gate, (iii) to prepare a superposition of states,

(iv) to read the final state with a projective measurement, and it is indispensable (v) to have a sufficiently long decoherence time. This is why most works focus precisely on the experimental determination and theoretical rationalisation of relaxation times and the design of strategies for minimising decoherence.[188]

Qubits may be embodied in a large variety of physical and chemical systems.[17] For many years, physicists have suggested a large range of quantum bits, such as trapped ions or trapped atoms,[189–192] photons in quantum optical cavities,[193,194] quantum dots[195,196] and superconducting quantum interference devices (SQUIDs).[197–199] Each of them has its strenghts and weaknesses.[116] More recently, condensed matter systems have demonstrated a great suitability, entangling spin qubits separated by three metres,[200] or showing room-temperature entanglement with storage times of the order of 1 ms.[201] These exceptional results have been reported using nitrogen-vacancy (NV) defects in a diamond matrix, which –in contrast with trapped atoms or photons in cavities– are systems in the domain of chemistry and materials science.[202]

In parallel, the 'bottom-up' approach based on chemical design was proposed, experiencing a fast development of the field of molecular spin qubits. This has been covered by several reviews covering both theoretical and experimental results.[39,186,203–205] The chemical approach is centred on the study of individual spin qubits and their use as model systems for the implementation of quantum gates. Still, experimental results are in a very preliminary stage compared with the above-mentioned hardware candidates proposed by the physics community. The final goal is the organisation of these molecular spin qubits to aim for scalability.[206,207] The main advantage that molecules present as hardware types to build up a quantum computer is that they can be tailored to give the targeted physical

behaviour. In this context, molecular nanomagnets are very attractive candidates. At low temperatures, SMMs function as an effective S = 1/2, i.e. a single qubit. Recently, it has been demonstrated that SMMs acting as single qubits can achieve strong and ultrastrong coupling regimes with superconducting circuits.[208] Furthermore, the main strategies for the implementation of quantum algorithms in such nanomagnets were described by Ardavan *et al*.[205] These propositions were followed by experiments utilising pulsed ESR techniques, showing that the phase relaxation times in at least some molecular magnets are long enough to permit multiple qubit operations. These operations can also take place via EPR pulses. Also, Landau-Zener transitions to enhance spin coherent manipulation in SMMs were discussed from a theoretical angle.[209] Interesting examples about the deployment of SMMs in quantum computing have been performed in Cr_7M heterometallic wheels (T_2 = 3.8 μs), with M = Ni and Mn, where phase-coherence relaxation is dominated by the coupling of the d electron spin to protons within the molecule.[205] Other examples of spin qubit candidates based on magnetic clusters include the antiferromagnetic V_{15} POM (T_2 = 0.1 μs) and Fe_8 (T_2 = 0.5 μs at 1.2 K).[210–213] The evolution of molecular spin qubits is rising very fast thanks to the design of increasingly coherent transition metal complexes. This is achieved, among other strategies, by employing ligands that are nuclear spin free and as rigid as possible. In this context, it has been demonstrated that the organic semiconductor copper phthalocyanine can provide T_2 times as long as 2.6 μs at 5 K and 1 μs at 80 K, just above the boiling point of liquid-nitrogen, being an excellent candidate for quantum information processing.[214] A spectacular success of this strategy was the Cu(II) monomer $(PPh_4)_2[Cu(mnt)_2]$ by the group of prof. van Slageren with

decoherence times in the order of decades of microseconds in the right conditions. again the $(PPh_4)_2[Cu(mnt)_2]$ complex, which shows an extraordinary potential for these purposes.[82] During the final stage of this thesis, we have witnessed yet another significant breakthrough: a CS_2 solution of $[V(C_8S_8)_3]^{2-}$, where neither the ligands nor the solvent present nuclear spins, displayed T_2 times aproaching the millisecond.[215] This has changed the playing field by introducing "solubility in CS_2" as an extra requirement to obtain new records in coherent molecular spin qubits. The molecular structures of the Cr_7M wheel and the $(PPh_4)_2[Cu(mnt)_2]$ complex are shown in Figure 1.8, whereas the evolution of T_1 and T_2 vs. temperature for different spin qubits is plotted in Figure 1.9.

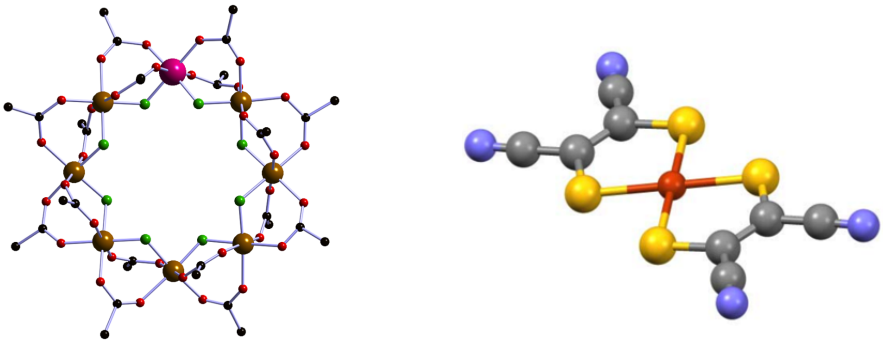

Figure 1.8: Molecular structure of: (left) the Cr_7M heterometallic wheel; (right) $(PPh_4)_2[Cu(mnt)_2]$.

On the same direction, several studies have been developed considering lanthanide single-ion magnets. Indeed, there exist full quantum computing proposals, including interactions between spin qubits in solid-state, which would also be applicable to a molecular crystal of lanthanoid SIMs.[216] We can mention the determination of coherence times and the observation of Rabi oscillations in $Ho_xY_{(1-x)}LiF_4$[77] and the discovery

of qubits based on Er^{3+} diluted in a single crystalline matrix of $CaWO_4$, isomorphic with $YLiF_4$.[217]

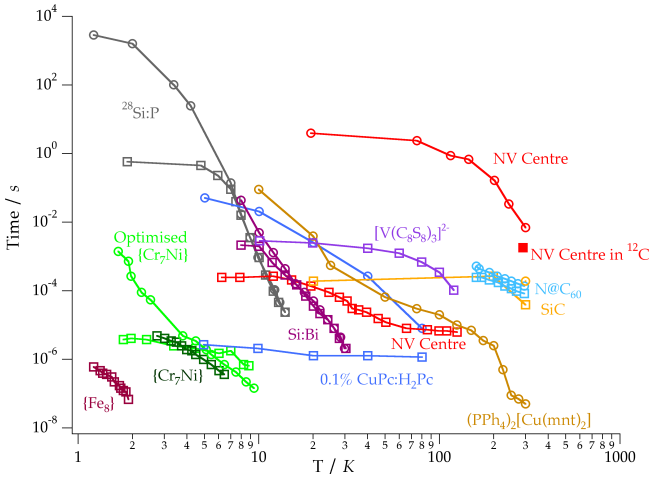

Figure 1.9: Relaxation times T_1 (circles) and T_2 (squares) for different solid state spin qubit candidates, including magnetic molecules, versus temperature. Long T_2 times i.e. coherent systems, are difficult to achieve at high temperatures, but lately both chemistry and solid-state physics have been making quick progress.

From a molecular perspective, the study of the mechanism of spin-lattice relaxation of Er^{3+} ions encapsulated in polyoxometalate clusters was also considered.[218] As the interaction with nuclear spins is a major source of decoherence for electron spins, such polyoxometalate-based molecules are in a privileged position to function as model spin qubits for sophisticated experiments aiming to address fundamental problems in quantum computing.[219] Also of great interest for quantum computing is the case of HoW_{10}, where a very effective way to eliminate decoherence based on atomic clock transitions, at which the quantum spin dynamics become protected against dipolar decoherence, has recently been discovered

(Coronado, E. & Hill, S. *et al.*, *Nature*. *In press*). Continuing with lanthanide POM-based complexes for quantum information, the trivalent gadolinium ion of both the series LnW_{10} and LnW_{30} was investigated. In this thesis (Chapter 11) we describe the main characteristics of the GdW_{30} SIM,[220] in which the number of coherent rotations was increased by a factor of 10 by matching the Rabi frequency with the frequency of the proton.[221] In the same chapter, we theoretically discuss the possibilities of $HoPd_{12}$ as a molecular spin qubit.[222] In these systems, it is essential to understand the CF splitting and especially the quantum tunnelling splitting. In that sense, both the computational and theoretical tools developed throughout this Ph.D. work are intended to help in the understanding and further development of this molecular approach for quantum information purposes.

Beyond single-qubit systems, several works have been focused on the synthesis and characterisation of molecular architectures which can embody more than one qubit. Many of these structures do possess weakly coupled electron spins.[223–225] An attractive research line focuses on the preparation of actual entanglement, what means the existence of non-trivial superpositions between more than one qubit. The full process of initialisation, gating and readout would be a fundamental task to apply to the entangled qubits in the next decades. So far, universal single-qubit gates applying a time-dependent magnetic field on the spin cluster have been developed on a simpler and more feasible scheme. Molecular clusters with two Tb^{3+} ions showed the capability to implement a C-NOT quantum logic gate, which also provided a method to realise a SWAP gate in the same cluster (Figure 1.10).[226] Later on, an introduction to the requirements for a coordination compound to act as a two-qubit quantum gate was proposed in a tutorial review published by Aromí *et al*.[225] In that work two

successful synthetic chemical strategies were presented, preparing a family of asymmetric dinuclear lanthanide complexes with weak magnetic coupling in which most of the analogues satisfy the requirements to act as 2-qubit C-NOT or SWAP quantum gates. This was latterly extended to treat heterometallic [LnLn'] complexes,[227] where the individual qubit properties of the lanthanide ions could be investigated by fabricating derivatives where one of the two centres (Ln or Ln') is a diamagnetic ion. Evidence for a proper definition of qubit states at low temperatures for each individual ion of the [Tb_2] and [CeEr] analogues could be obtained and magnetic coupling was also determined.

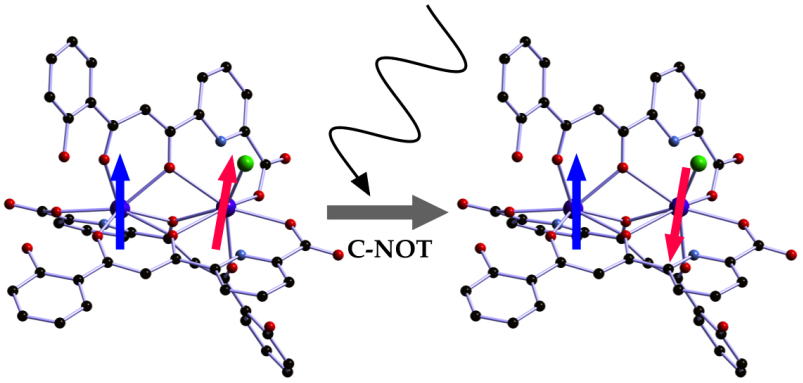

Figure 1.10: An EPR pulse can reverse the orientation of the magnetic moment of a Tb^{3+} ion, provided its neighbour is pointing ''up''. This selective switching is equivalent to the quantum logic gate Controlled-NOT (C-NOT).

1.3.2 Molecular spintronics

Spintronics (spin-based electronics) is a relatively new research field whose main goal is the active manipulation of the electron spin degrees of freedom in solid-state systems for carrying information.[114] The origin of this area goes back to the discovery of the "giant magnetoresistive" (GMR)

effect independently by Fert and Grünberg in the late 1980s.[228,229] Unlike the conventional electronic devices, which rely on the electrons motion and their charge, spintronic devices also aims at controlling the electron spin states. This additional degree of freedom is expected to improve the speed and storage capacity with respect to electronic devices. Spintronic systems have experienced a fast development and currently are used in a range of applications. These include read-heads devices, non-volatile magnetic memories (MRAM),[230,231] spin-transfer nano-oscillators (STNOs)[232] and quantum bits in a quantum computer.[233] These systems, based on inorganic metals and semiconductors, are considered the first real application of nanotechnology.

At present, the evolution of molecular electronics and molecular magnetism has led to the emergence of molecular spintronics,[234,235] which combines the ideas and concepts developed in spintronics with the singular possibilities offered by molecular electronics and molecular magnetism. This field can be divided into two major areas: molecule-based spintronics, commonly known as organic spintronics (especially by the physics community), and single-molecule spintronics.[236] The first one relies on the fabrication of novel devices that replace inorganic metals and semiconductors by molecular-based materials with the aim of enhancing the properties of conventional spintronics devices and reducing their price. The second intends to study individual magnetic molecules as main components of nanospintronic devices. This approach has a series of advantages, such as: (1) the possibility of designing devices at a molecular-scale limit, (2) the use of organic molecules (weak spin-orbit and hyperfine interactions) that can preserve their spin over times and distances much longer than in conventional semiconductor systems, and (3) the formation

of self-organised nanostructures based on previously designed molecules that are in addition easy to manipulate.

In the early stages of spintronics, molecules were used as model systems to study and determine the underlying mechanisms at a fundamental level.[125] Within this regard, POMs were suggested as interesting model systems due to their advantageous chemical, structural and electronic features.[125,58] In particular, mixed-valence POMs were investigated in order to understand the possibilities that these systems offer for electrical control of the spin state.[237,238] Subsequently, ambitious projects from a theoretical point of view were conducted on electrically switchable magnetic POMs: $[PMo_{12}O_{40}(VO)_2]^{q-}$ (Figure 1.11),[239,240] $[PMo_{12}O_{40}\{Ni(phen)_2(H_2O)\}_2]$ and $K_2Na_6[GeV_{14}O_{40}]_{10}H_2O$ (in short, V_{14}).[241–243] These included multiconfigurational studies involving big matrices, DFT calculations and vibronic coupling. Although most of the work developed until now remains theoretical, these theoretical advances pave the way for developing experimental realisations of these proposals.[244]

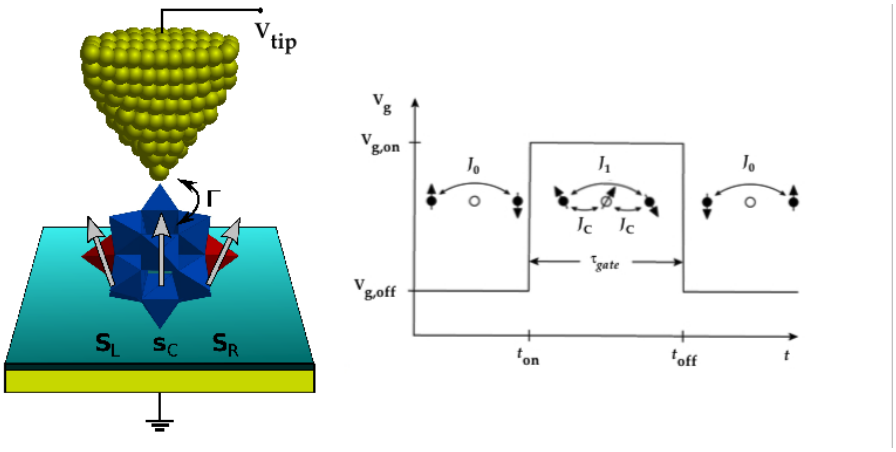

Figure 1.11: (left) Proposed setup to implement two-qubit gates onto $[PMo_{12}O_{40}(VO)_2]^{q-}$; (right) during τ_{gate} the voltage is $V_{g,on}$ and the Keggin structure hosts an extra electron, which induces a rapid exchange of the vanadyl spins.

In 2008, Bogani and Wernsdorfer reported an excellent progress article where the challenges in single-molecule spintronics were outlined.[245] The authors proposed three different schemes to build up spintronic devices with one or a few molecules. These are: (1) a molecular spin-transistor, where a magnetic molecule is embedded between two non-magnetic electrodes, (2) a molecular spin-valve, which is similar to the former but containing at least two magnetic elements, and (3) molecular multidot devices, based on a controlled number of molecules or multiple centres inside the molecule. The proposed building-blocks for these devices were individual SMMs such as Mn_{12},[246] $Co(TerPy)_2$[247] and the divanadium molecule [(*N*,*N*′,*N*′′-trimethyl-1,4,7-triazacyclononane)$_2V_2(CN)_4(\mu$-$C_4N_4)$].[248] Unfortunately, the practical construction of these SMM-based spintronic devices was not achievable due to several shortcomings within these particular molecular systems.

More recently, the performance of a SIM combined with an organic radical to design such spintronic devices has been conceived in order to overcome the obstacles presented by the above-mentioned SMMs.[249] Groundbreaking results have been obtained with the neutral trivalent terbium complex [$TbPc_2^0$].[33,250–252] Beyond its robust character and the high anisotropy barrier, the advantages that this nanomagnet does possess are: (i) the conjugated structures of the phthalocyaninato ligands with a delocalised S = 1/2 radical, (ii) the flat 'double-decker' structure, showing uniaxial anisotropy that favours the absorption of the molecule on surfaces, and (iii) the sublimability under UHV conditions.[253] In addition, the presence of the molecule in the junctions can be identified owing to the strong couplings between the electron and the nuclear spins in the $TbPc_2$ complexes. These characteristics permitted the practical achievement of the molecular schemes proposed a decade ago through the fabrication of

spintronics devices such as spin transistor, spin valve and spin resonator. They are fabricated using new hybrid devices based on carbon nanotubes coupled to a molecule of bis(phthalocyaninato) terbium(III) SIM.[254,255] This was inspired by the successful encapsulation of Mn_{12} in carbon nanotubes, yielding this type of hybrid nanostructures that combine the SMM properties of the guest molecules with the functional properties of the host nanotube.[256] Also, magnetic bistability of individual iron(III) SMMs grafted to carbon nanotubes has been reported.[257]

Other examples of lanthanide complexes with interest in molecular spintronics include $NdPc_2$ adsorbed on Cu(100), whose 4f orbitals can be directly accessed by scanning tunnelling microscopy, contributing to charge transport.[258] On the other hand, systems incorporating a radical, which can be interesting in the future for these purposes, are those based on the nitronyl nitroxide (NIT) ligand,[259,260] as for example the $\{Ln(hfac)_3(NIT\text{-}R)_n\}$ analogues.[261–263] A related interesting compound is the terbium derivative of $[Ln(NIT\text{-}pic)_3]$, which is coordinated by the radical NIT-picolinate, and also exhibits slow relaxation of the magnetisation.[264]

Nevertheless, in spite of the success obtained using the $TbPc_2$ analogue,[265] there are still very important challenges to be overcome. These include the design of SMMs with higher operating temperatures at which magnetic phenomena occur, the further exploration of the behaviour of SMMs deposited on surfaces, as most of the molecules are very fragile and react with the metallic surface, the study of the ability of SMMs to retain their magnetic properties when they are linked to electrodes, and finally the creation of specific and reproducible contacts between the molecule and the surface.

1

Development of the theoretical framework

2 Development of the computational package

The first objective of this thesis was the development of a computational package intended to calculate the spectroscopic and magnetic properties of lanthanide complexes using their chemical structures. At the beginning of this project, only a few examples of SIMs had been reported (see section 1.1.1 for details).[52] Hence, a general requirement in molecular magnetism was the setting up of a software package capable to rationalise the conditions that could favour slow relaxation of the magnetisation.

The first families of SIMs had been studied using an effective crystal field Hamiltonian, where the phenomenological ligand field parameters were extracted by simultaneous optimisation of static magnetic susceptibility and ^{1}H-NMR paramagnetic shift data.[55] To avoid overparameterisation, this approach makes two key simplifications: (1) the chemical structure is idealised, determining which CFPs are non-negligible in terms of the point group of the idealised molecule, and (2) each ligand-field parameter is treated as a linear function of the atomic number of the lanthanoid. Because the actual molecular structure is not taken into account in such a phenomenological ligand field model, its predictive power is in general limited. To overcome this problem, a different approximation introducing the real structure as an input was needed. As starting point,

the point-charge electrostatic model (PCEM) was chosen due to its simplicity and versatility.[135] The main advantage of this model is that it permits the estimation of the CFPs using the chemical structure in an inexpensive way. An additional advantage is that it can be deeply improved by adding minor modifications, overcoming most limitations of the initial model, in order to provide an initial set of CFPs for further explanations using the full Hamiltonian.[131,266]

In this chapter, the developed software package is presented and described, exemplifying its use. The program, called SIMPRE (Single-Ion Magnet PREdiction),[267,268] has been completely written in standard portable *Fortran 77*. It is important to remark that SIMPRE is the main tool of this thesis and that has been applied to the vast majority of examples presented herein.

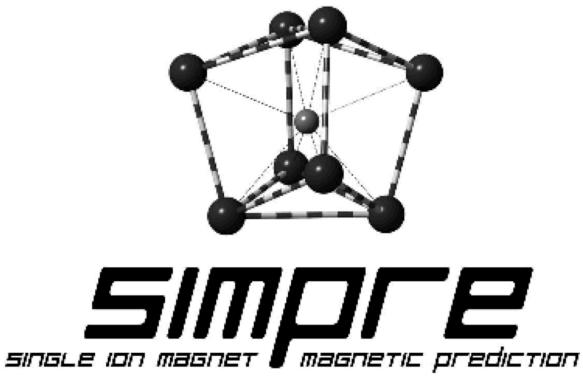

Figure 2.1: Logo of the freely distributable SIMPRE Computational Package: designed by Dr. Salvador Cardona-Serra.

2.1 Methods

As introduced above, SIMPRE uses an additive CF model, where the contributions of each ligand are taken into account separately. The oldest and simplest model of this kind is the point charge electrostatic model (PCEM) introduced by Bethe in 1929.[135] Within this model, the CFPs can be calculated placing formal charges of the coordinated atoms in the atomic coordinates of the system. However, this approach does not take into account covalence effects and does not offer reliable sets of CFPs capable to predict and reproduce the observed magnetic and spectroscopic properties.[121] These limitations could subsequently be improved by developing several related *semi-empirical* models.[156–159,269]

In the program, the environment in which the spin carrier is surrounded is represented by the CF potential, which is built from spherical harmonics. The Russell-Saunders (or *LS*) coupling scheme is adopted, where spin-spin coupling > orbit-orbit coupling > spin-orbit coupling. Such an approximation, widely used in the description of the magnetic properties of lanthanide compounds,[270] neglects excited multiplets and inter-multiplet interactions. A comparison between the results of the ground multiplet CF splitting obtained with the full Hamiltonian versus the ones using the *LS* coupling scheme in the complex Er(trensal) showed differences in the energy scheme of less than 2 cm^{-1} in each level. [268] These slight differences, that are accompanied by a too high computational cost when using the full Hamiltonian approach, justify the assumption that has been taken in the development of the package, which is compatible with the main goal of SIMPRE: the prediction of new derivatives as simple, and computationally inexpensive, as possible.

The CF Hamiltonian is applied to the total angular momentum components of a given centre and resolved after deriving the CFPs of the ground *J*-multiplet. The code parameterises the electric field effect produced by the surrounding ligands, acting over the central ion, by using the CF Hamiltonian expressed in terms of the Extended Stevens Operators (ESOs) (see Chapter 1, Equation 1.2).[138] According to the Stevens formalism[136] the CFPs are expressed as $B_k^q = a_k A_k^q \left\langle r^k \right\rangle$. In SIMPRE, the expectation values $\langle r^k \rangle$ have been corrected by the product $\langle r^k \rangle_{cal} \cdot (1-\sigma_k)$, taking into account the Sternheimer shielding parameters (σ_k) of the 4*f* electronic shell.[271] All this tabulated coefficients are reported in Table 2.1. They are introduced as constants in the subroutine LANTA of the main code.

Table 2.1: Stevens operators (α, β, γ), expectation value of r^k and Sternheimer shielding parameters (σ_k) for the series of lanthanoids included in the package.

Ion	α	β	γ	$\langle r^2 \rangle_{cal}$	$\langle r^4 \rangle_{cal}$	$\langle r^6 \rangle_{cal}$	σ_2	σ_4	σ_6
Ce^{3+}	$-5.71\cdot10^{-2}$	$6.35\cdot10^{-3}$	0	1.456	5.437	42.26	0.515	0.0138	-0.0301
Pr^{3+}	$-2.10\cdot10^{-2}$	$-7.35\cdot10^{-4}$	$6.10\cdot10^{-5}$	1.327	4.537	32.65	0.515	0.0138	-0.0301
Nd^{3+}	$-6.43\cdot10^{-3}$	$-2.91\cdot10^{-4}$	$-3.80\cdot10^{-5}$	1.222	3.875	26.12	0.518	0.0130	-0.0310
Pm^{3+}	$7.71\cdot10^{-3}$	$4.08\cdot10^{-4}$	$6.08\cdot10^{-5}$	1.135	3.366	21.46	0.519	0.0109	-0.0314
Sm^{3+}	$4.13\cdot10^{-2}$	$2.50\cdot10^{-3}$	0	1.061	2.964	17.99	0.519	0.0077	-0.0317
Tb^{3+}	$-1.01\cdot10^{-2}$	$1.22\cdot10^{-4}$	$-1.12\cdot10^{-6}$	0.893	2.163	11.75	0.523	-0.0107	-0.0318
Dy^{3+}	$-6.35\cdot10^{-3}$	$-5.92\cdot10^{-5}$	$1.04\cdot10^{-6}$	0.849	1.977	10.44	0.527	-0.0199	-0.0316
Ho^{3+}	$-2.22\cdot10^{-3}$	$-3.33\cdot10^{-5}$	$-1.29\cdot10^{-6}$	0.810	1.816	9.345	0.534	-0.0306	-0.0313
Er^{3+}	$2.54\cdot10^{-3}$	$4.44\cdot10^{-5}$	$2.07\cdot10^{-6}$	0.773	1.677	8.431	0.544	-0.0427	-0.0310
Tm^{3+}	$1.01\cdot10^{-2}$	$1.63\cdot10^{-4}$	$-5.61\cdot10^{-6}$	0.740	1.555	7.659	0.554	-0.0567	-0.0306
Yb^{3+}	$3.18\cdot10^{-2}$	$-1.73\cdot10^{-3}$	$1.48\cdot10^{-4}$	0.710	1.448	7.003	0.571	-0.0725	-0.0300

Regarding the notation of the CFPs, as mentioned in the preceding chapter, there are numerous parameterisation schemes for the effective H_{CF} and it is essential to be consistent with the prevailing conventions reported in the literature to avoid confusion.[268] Interesting works that clarify the notations of these conventions are those of Mulak and Gajek,[178,272] Hutchings[273] and Rudowicz.[147,148] ESOs were chosen due to its adequacy to the L-S coupling scheme programmed into the software.[17] The definitions of $O_k^q(J)$ operators are consistent with Hutchings, Mulak and Gajek and Stevens, but for clarity all the definitions of the positive and negative operator ranges (q) of the Stevens operators are reported with their explicit forms in Table 2.2.

Table 2.2: Explicit list of the extended Stevens operators $O_k^q(J)$ used in the SIMPRE computational package, *X = J(J+1).*

$O_2^0 = [3J_z^2 - X]$
$O_2^1 \equiv O_2^1(c) = \frac{1}{4}[J_z(J_+ + J_-) + (J_+ + J_-)J_z]$
$O_2^{-1} \equiv O_2^1(s) = \frac{-i}{4}[J_z(J_+ - J_-) + (J_+ - J_-)J_z]$
$O_2^2 \equiv O_2^2(c) = \frac{1}{2}[J_+^2 + J_-^2]$
$O_2^{-2} \equiv O_2^2(s) = \frac{-i}{2}[J_+^2 - J_-^2]$
$O_4^0 = [35J_z^4 - (30X - 25)J_z^2 + 3X^2 - 6X]$
$O_4^1 \equiv O_4^1(c) = \frac{1}{4}[(J_+ + J_-)(7J_z^3 - (3X+1)J_z) + (7J_z^3 - (3X+1)J_z)(J_+ + J_-)]$
$O_4^{-1} \equiv O_4^1(s) = \frac{-i}{4}[(J_+ - J_-)(7J_z^3 - (3X+1)J_z) + (7J_z^3 - (3X+1)J_z)(J_+ - J_-)]$
$O_4^2 \equiv O_4^2(c) = \frac{1}{4}[(J_+^2 + J_-^2)(7J_z^2 - X - 5) + (7J_z^2 - X - 5)(J_+^2 + J_-^2)]$
$O_4^{-2} \equiv O_4^2(s) = \frac{-i}{4}[(J_+^2 - J_-^2)(7J_z^2 - X - 5) + (7J_z^2 - X - 5)(J_+^2 - J_-^2)]$

$O_4^3 \equiv O_4^3(c) = \frac{1}{4}[(J_+^3 + J_-^3)J_z + J_z(J_+^3 + J_-^3)]$
$O_4^{-3} \equiv O_4^3(s) = \frac{-i}{4}[(J_+^3 - J_-^3)J_z + J_z(J_+^3 - J_-^3)]$
$O_4^4 \equiv O_4^4(c) = \frac{1}{2}[J_+^4 + J_-^4]$
$O_4^{-4} \equiv O_4^4(s) = \frac{-i}{2}[J_+^4 - J_-^4]$
$O_6^0 = [231J_z^6 - (315X - 735)J_z^4 + (105X^2 - 525X + 294)J_z^2 - 5X^3 + 40X^2 - 60X]$
$O_6^1 \equiv O_6^1(c) = \frac{1}{4}[(J_+ + J_-)\{33J_z^5 - (30X - 15)J_z^3 + (5X^2 - 10X + 12)J_z\} + \{33J_z^5 - (30X - 15)J_z^3 + (5X^2 - 10X + 12)J_z\}(J_+ + J_-)]$
$O_6^{-1} \equiv O_6^1(s) = \frac{-i}{4}[(J_+ - J_-)\{33J_z^5 - (30X - 15)J_z^3 + (5X^2 - 10X + 12)J_z\} + \{33J_z^5 - (30X - 15)J_z^3 + (5X^2 - 10X + 12)J_z\}(J_+ - J_-)]$
$O_6^2 \equiv O_6^2(c) = \frac{1}{4}[(J_+^2 + J_-^2)\{33J_z^4 - (18X + 123)J_z^2 + X^2 + 10X + 102\} + \{33J_z^4 - (18X + 123)J_z^2 + X^2 + 10X + 102\}(J_+^2 + J_-^2)]$
$O_6^{-2} \equiv O_6^2(s) = \frac{-i}{4}[(J_+^2 - J_-^2)\{33J_z^4 - (18X + 123)J_z^2 + X^2 + 10X + 102\} + \{33J_z^4 - (18X + 123)J_z^2 + X^2 + 10X + 102\}(J_+^2 - J_-^2)]$
$O_6^3 \equiv O_6^3(c) = \frac{1}{4}[(J_+^3 + J_-^3)(11J_z^3 - (3X + 59)J_z) + (11J_z^3 - (3X + 59)J_z)(J_+^3 + J_-^3)]$
$O_6^{-3} \equiv O_6^3(s) = \frac{-i}{4}[(J_+^3 - J_-^3)(11J_z^3 - (3X + 59)J_z) + (11J_z^3 - (3X + 59)J_z)(J_+^3 - J_-^3)]$
$O_6^4 \equiv O_6^4(c) = \frac{1}{4}[(J_+^4 + J_-^4)(11J_z^2 - X - 38) + (11J_z^2 - X - 38)(J_+^4 + J_-^4)]$
$O_6^{-4} \equiv O_6^4(s) = \frac{-i}{4}[(J_+^4 - J_-^4)(11J_z^2 - X - 38) + (11J_z^2 - X - 38)(J_+^4 - J_-^4)]$
$O_6^5 \equiv O_6^5(c) = \frac{1}{4}[(J_+^5 + J_-^5)J_z + J_z(J_+^5 + J_-^5)]$
$O_6^{-5} \equiv O_6^5(s) = \frac{-i}{4}[(J_+^5 - J_-^5)J_z + J_z(J_+^5 - J_-^5)]$
$O_6^6 \equiv O_6^6(c) = \frac{1}{2}[(J_+^6 + J_-^6)]$
$O_6^{-6} \equiv O_6^6(s) = \frac{-i}{2}[(J_+^6 - J_-^6)]$

The A_k^q CF parameters, presented in Chapter 1 (Equation 1.2), are determined by the following relations[268,274,275]:

$$A_k^0 = \frac{4\pi}{2k+1}\sum_{i=1}^{N}\frac{Z_i e^2}{R_i^{k+1}} Z_{k0}(\theta_i,\varphi_i)\, p_{kq} \qquad (2.1a)$$

$$A_k^q = \frac{4\pi}{2k+1}\sum_{i=1}^{N}\frac{Z_i e^2}{R_i^{k+1}} Z^c_{kq}(\theta_i,\varphi_i)\, p_{kq} \qquad q < 0 \ (2.1b)$$

$$A_k^q = \frac{4\pi}{2k+1}\sum_{i=1}^{N}\frac{Z_i e^2}{R_i^{k+1}} Z^s_{k|q|}(\theta_i,\varphi_i)\, p_{k|q|} \qquad q > 0 \ (2.1c)$$

where R_i, θ_i and φ_i are the effective polar coordinates of the point charges, and Z_i is the effective point charge, associated to the *i*-th donor atom with the lanthanoid at the origin. N is the number of ligands; e is the electron charge, Z_{kq} are the tesseral harmonics expressed in terms of the polar coordinates for the i-th donor atom and p_{kq} are the prefactors of the spherical harmonics.

From the relations[141] between the ESOs and Wybourne operators, the Stevens CFPs and the Wybourne CFPs are obtained via the following conversion relations[274]:

$$\lambda_{k0}A_k^0\langle r^k\rangle = B_{k0}\ ,\ \lambda_{kq}A_k^q\langle r^k\rangle = \mathrm{Re}\,B_{kq}\ \text{for q} < 0,\ \lambda_{k|q|}A_k^q\langle r^k\rangle = \mathrm{Im}\,B_{k|q|}\ \text{for q} < 0 \qquad (2.2)$$

The conversion factors λ_{kq} between the Stevens CFPs and the Wybourne CFPs can be found in Table 2.3. [141]

Table 2.3: Conversion factors λ_{kq} for the relation in the expressions 2.2.

k \ q	0	1	2	3	4	5	6
2	2	1/ √6	2/ √6				
4	8	2/ √5	4/ √10	2/ √35	8/ √70		
6	16	8/ √42	16/ √105	8/ √105	16/3 √14	8/3 √77	16/ √231

The non-negligible CFPs are determined by the symmetry of the molecule. Often, the assumed point group symmetry only takes into account the first coordination sphere. In SIMPRE, it is a general procedure to calculate the CFPs using the first coordination sphere of real structures, yielding the full set of CFPs. The ground *J* multiplet energy level scheme is calculated by the diagonalisation of the Hamiltonian.

To calculate the magnetic properties, SIMPRE introduces the interaction between the electron spin and an external magnetic field along the *z*-direction via a Zeeman term $\hat{H}_{ZEE}$:

$$\hat{H}_{ZEE} = g_J \mu_B B_z \cdot \hat{J}_z \tag{2.3}$$

where g_J is the Landé *g*-factor for the ground *J*-multiplet, μ_B is the Bohr magneton, B_Z is the external magnetic field along the z-direction and $\hat{J}_z$ is the z-component of the total electronic angular momentum operator.

Once we have the eigenvalues of the system at different magnetic fields or temperatures, one can evaluate the partition function *Z* and the different thermodynamic poperties of the system, such as magnetisation and magnetic susceptibility by the following fundamental definitions[2,276]:

$$M = NkT \frac{\partial \ln Z}{\partial H} \tag{2.4}$$

$$\chi = \left(\frac{\partial M}{\partial H} \right)_{H \to 0} \tag{2.5}$$

2.2 Organisation of the code

The organisation of the whole program is shown as a schematic chart in Figure 2.2. It can be briefly described as follows: The main program starts by calling the READ subroutine, which reads the include files *simpre.par* and *simpre.dat*. The information of both files is verified and the program proceeds to initialise a large common block area containing the data needed to run a calculation. The file *simpre.par* contains the options yes or no that the user switches for the calculation, e.g. calculation of the magnetisation. *simpre.dat* contains the basic data: magnetic centre, cartesian or spherical coordinates, effective charges and conditions for the calculation of the magnetisation and magnetic susceptibility.

In subsequent steps the main program calls ROTA, BKQ and ENER, which together solve the Hamiltonian problem. Subroutine ENER creates the main output file (*simpre.out*) containing in a schematic way all the information concerning the system definition, the errors and warnings generated at the different steps of the initialisation process. Last but not least, if the corresponding option is activated in *simpre.par*, SUS and MAG are called to calculate the magnetic susceptibility and the magnetisation. The rest of this subsection analyses this scheme with more detail.

At the beginning the program accepts as main input *simpre.par*, where the user specifies the following points:

- the dimension of the full energy matrix
- the units of the output CFPs and energy levels: kelvin (K), millielectronvolts (meV) or wavenumbers (cm^{-1})
- spherical (R, θ, φ) or cartesian (x,y,z) input coordinates
- the use of the Sternheimer shielding parameters (yes/no)
- rotation for a compact ground-state wave function (yes/no)

- calculation of the magnetic susceptibility (yes/no)
- calculation of the magnetisation (yes/no)
- eigenvalues reported in the output file (yes/no)
- the maximum number of charges

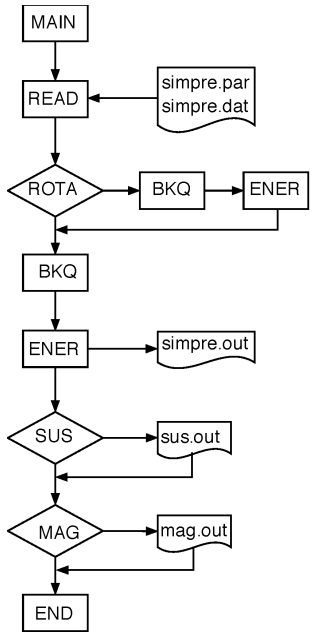

Figure 2.2: General organisation of the SIMPRE package showing the different subroutines.

In the second external input file, called *simpre.dat*, the user may define:

- the lanthanide ion code
- the number of coordinated charges
- the coordinates (either cartesian or spherical) and the charge value of each atom in the first coordination sphere

- if the user wants to calculate the magnetic susceptibility: the conditions (range of temperatures, magnetic field and number of points) for the calculation of the temperature-dependent magnetic susceptibility.
- if the user wants to calculate the magnetisation: the conditions (temperature, maximum value of the magnetic field, field increment and the number of angles in the integration procedure) for the calculation of the magnetisation.

After the initialisation process, the main program enters in ROTA, which may be used to determine the most compact description of the ground state wave function according to the charge distribution introduced as an input. If the corresponding option has been activated in *simpre.par*, ROTA performs rotations around the Euler angles[277] (see Figure 2.3 and Expressions 2.6) and in each step calls BKQ and ENER.

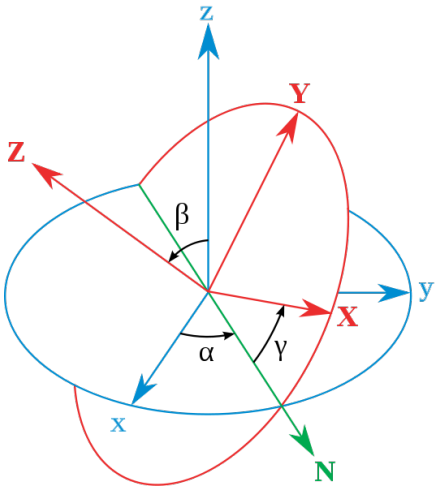

Figure 2.3: Euler angles (Image by Lionel Brits /CC BY 3.0).

Each set of coordinates (x,y,z) are calculated from the input coordinates (X,Y,Z) using the following expressions[142]:

$$X = x(\cos\alpha\cdot\cos\beta\cdot\cos\gamma - \sin\alpha\cdot\sin\gamma) + y(-\cos\alpha\cdot\cos\beta\cdot\sin\gamma - \sin\alpha\cdot\cos\gamma) + z(\cos\alpha\cdot\sin\beta) \quad (2.6a)$$

$$Y = x(\sin\alpha\cdot\cos\beta\cdot\cos\gamma + \cos\alpha\cdot\sin\gamma) + y(-\sin\alpha\cdot\cos\beta\cdot\sin\gamma + \cos\alpha\cdot\cos\gamma) + z(\sin\alpha\cdot\sin\beta) \quad (2.6b)$$

$$Z = x(-\sin\beta\cdot\cos\gamma) + y(\sin\beta\cdot\sin\gamma) + z(\cos\beta) \quad (2.6c)$$

where α, β and γ are the Euler angles represented in Figure 2.3.

Subsequently, BKQ calculates the CFPs, and ENER determines the wave functions and wave vectors of each energy level for each set of coordinates. The matrix Hamiltonian is diagonalised by a standard subroutine ZHPEV of the LAPACK Mathematical Library.[278]

The criterion for ROTA is the following: the selected orientation will be the one that results in the purest wave function, measured by the addition of the highest squared coefficient for each energy level. Of course, the orientation of the coordinate axis is rather arbitrary and it certainly does not alter the calculated averages properties. So, this step can be skipped for certain applications, e.g. when calculating the χT product of a powder sample, or if the desired orientation is known beforehand. For example, for ideal or nearly ideal systems, an external program may be used to orient the molecule, so that the z axis is aligned with the main symmetry axis. At this point it is important to stress that the state basis depends on the orientation. Thus, a random orientation produces in general a higher number of parameters and more complicated wave functions, and is thus not suited for meaningful comparisons.

If the magnetic properties of the lanthanoid complex are to be evaluated, the corresponding options have to be marked in *simpre.par*. As a

consequence, the different subroutines associated to these properties are called from ENE. These subroutines are MAG and SUS and they calculate magnetisation and magnetic susceptibility, respectively. To calculate the magnetisation and the susceptibility a new evaluation of the energy matrix that includes the additional interaction of the system with the external field (Zeeman effect) is required. This new contribution is evaluated in the secondary subroutine ZEE (not included in the diagram). To obtain a proper evaluation of these properties for powder samples, MAG and SUS subroutines assure a correct integration of the properties over the different orientations of the external magnetic field. SIMPRE returns from SUS and MAG different output files containing the evaluated properties in a column text type format that allows an easy plot for graphic package: *sus.out* and *mag.out*.

Regardless of whether or not *sus.out* and *mag.out* are produced, an execution of SIMPRE will generate at least one output file, namely *simpre.out*. Such file contains the result of the final coordinates and the diagonalisation of the Hamiltonian problem, i.e. the basis function set and the list of eigenvalues and eigenvectors. Additionally, it may include different messages of warnings and errors to help checking the coherence in the system definition, resulting in a guide to follow the different steps in the calculation.

Throughout the progress of this Ph.D. thesis, several patched versions of the package have also been developed to solve concrete problems. These versions include the determination of the easy axis orientation, the evolution of the energy level scheme under an applied magnetic field, the simulation of single-crystal rotations and the fitting of experimental data such as magnetic susceptibility or spectroscopic energy levels.

2.3 Application to an ideal cube

In this subsection, the application of the program to an ideal cube (LnX_8) is described. This particular geometry is attractive from a theoretical point of view, due to its high symmetry. Many of the coordination polyhedra for octa-coordinated systems can be considered as derived from a distorted cube. Hence, the spherical coordinates of eight identical charges (Z_i = 1) placed on the vertices of an ideal cube are introduced in *simpre.dat*. The distance between the lanthanide and the donor atoms (X) is fixed to 2.5 Å. The lanthanide ion is located at the origin of the system of coordinates. The coordinate axes coincide with the fourfold rotation axes, making the directions *x*, *y* and *z* equivalent. The input coordinates are reported in Table 2.4 as follows:

Table 2.4: Spherical coordinates (R_i, θ_i, φ_i) and charges (Z_i) for the ligands in a cube (O_h).

	R_i / Å	θ_i / °	φ_i /°	Z_i
1	2.5	54.7356103	45	1
2	2.5	54.7356103	135	1
3	2.5	54.7356103	225	1
4	2.5	54.7356103	315	1
5	2.5	125.2643897	45	1
6	2.5	125.2643897	135	1
7	2.5	125.2643897	225	1
8	2.5	125.2643897	315	1

In *simpre.par* ROTA is switched off, since we are only interested in the CFPs, energy levels, magnetisation and magnetic susceptibility in this first calculation. The program is run under these conditions and the procedure is repeated six times, specifying in *simpre.par* the six later lanthanoids: Tb, Dy, Ho, Er, Tm, Yb.

Tables 2.5 and 2.6 contain a summary of the results reported in *simpre.out*. The cubic symmetry eliminates second order contributions, so the only terms that survive are the diagonal parameters A_4^0, A_6^0 and the extradiagonal ones A_4^4, A_6^4. The expressions for the non-negligible CFPs, deduced from Equations 2.1, are the following:

$$A_4^0 \left\langle r^4 \right\rangle = -\frac{7}{18} Ze^2 \frac{\left\langle r^4 \right\rangle}{R^5} \tag{2.7a}$$

$$A_4^4 \left\langle r^4 \right\rangle = -\frac{35}{18} Ze^2 \frac{\left\langle r^4 \right\rangle}{R^5} \tag{2.7b}$$

$$A_6^0 \left\langle r^6 \right\rangle = \frac{2}{9} Ze^2 \frac{\left\langle r^6 \right\rangle}{R^7} \tag{2.7c}$$

$$A_6^4 \left\langle r^6 \right\rangle = -\frac{42}{9} Ze^2 \frac{\left\langle r^6 \right\rangle}{R^7} \tag{2.7d}$$

Due to this special symmetry, there are two fixed relations: one for the fourth rank parameters, $A_4^4 / A_4^0 = 5$ and, another for the sixth rank ones, $A_6^4 / A_6^0 =$ -21. Both relations are independent of the metal and of the metal-ligand distance. [121]

Of course, the smooth progression of the A_k^q parameters produces a more complex evolution of B_k^q, since the latter include the Stevens coefficients. The downward trend of the absolute value of A_k^q from TbX_8 to YbX_8 is easy to explain according to the values of $\langle r^k \rangle$ and $(1-\sigma_k)$ reported in Table 2.1.

Table 2.5: CFPs expressed as $A_k^q < r^k >$ for the series Ln = Tb, Dy, Ho, Er, Tm and Yb.

	TbX_8	DyX_8	HoX_8	ErX_8	TmX_8	YbX_8
$A_4^0 < r^4 >$	-79.2856	-73.1274	-67.8768	-63.4173	-59.5933	-56.3224
$A_4^4 < r^4 >$	-396.4280	-365.6368	-339.3842	-317.0867	-297.9667	-281.6122
$A_6^0 < r^6 >$	5.6286	5.0001	4.4744	4.0356	3.66465	3.3488
$A_6^4 < r^6 >$	-118.2014	-105.0028	-93.9623	-84.7475	-76.9576	-70.3251

Table 2.6: Energy level scheme (in cm^{-1}) of the series of lanthanides included in SIMPRE for the ideal cubic structure with R=2.5 Å and $Z_i = 1$

TbX_8	DyX_8	HoX_8	ErX_8	TmX_8	YbX_8
0	0	0	0	0	0
0	0	0	0	5	0
5	0	0	10	5	135
5	0	4	10	5	135
5	31	4	10	7	135
17	31	11	10	7	135
102	31	11	23	110	182
102	31	11	23	110	182
102	36	82	92	110	
120	36	82	92	121	
120	138	82	92	121	
120	138	95	92	121	
137	142	95	104	137	
	142	102	104		
	142	102	104		
	142	102	104		
		111			

In Table 2.6, we can appreciate the ground multiplet CF splitting of this series of lanthanoids surrounded by a perfect cube. We may observe that, as is well-known, in cubic symmetry the non-Kramers ions present degeneracies one, two and three while the states of the Kramers ions are

either doubly or four times degenerated. The largest gap with the first excited state (135 cm^{-1}) and the largest CF splitting (about 182 cm^{-1}) have been found for the Yb derivative. The near-degeneracy at low temperature observed in the calculated Stark sublevels of HoX_8 indicates the possibility of obtaining a favourable situation to study quantum coherence in lanthanide complexes displaying near-cubic symmetry. We will perform this kind of analysis in the last chapter of this thesis (see Section 11.2 for details).

As an example, the magnetic properties for the second-half series of lanthanoids (from Tb^{3+} to Yb^{3+}) were calculated. Figure 2.4 shows the magnetisation between 0 and 5 T with the temperature fixed at 2 K and the temperature-dependent magnetic susceptibility between 2 and 300 K under a magnetic field of 0.1 T.

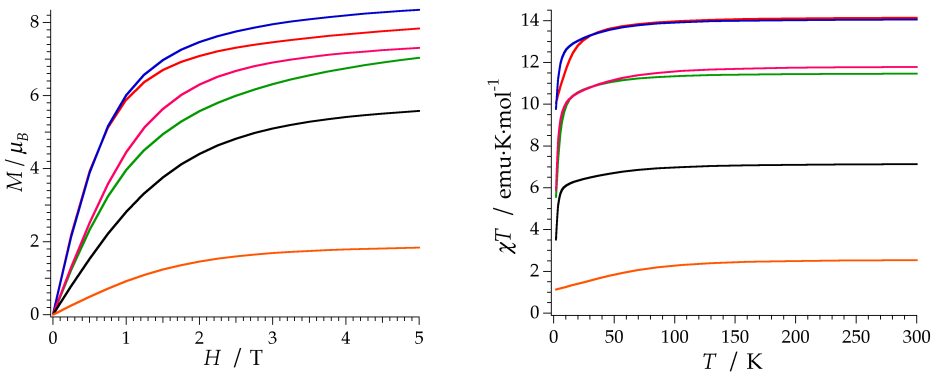

Figure 2.4: (left) Temperature-dependent magnetic susceptibility between 2 and 300 K; (right) magnetisation between 0 and 5 T of the series of lanthanides for the ideal cubic structure with R=2.5 Å and Z_i = 1. Dy (red), Ho (blue), Tb (pink), Er (green), Tm (black) and Yb (orange).

2.4 Conclusions

In this chapter, the main tool of this thesis has been presented: the SIMPRE computational package. This software package allows the calculation of the CFPs, energy levels and eigenvectors of mononuclear rare earth complexes. The user can either select as a magnetic centre one of the lanthanoids Ce, Pr, Nd, Pm, Sm, Tb, Dy, Ho, Er, Tm and Yb, or introduce the coefficients of a different rare earth ion. The program is based on a point charge electrostatic model to estimate the parameters of a general effective crystal field Hamiltonian. This approach is compatible with a series of related *semi-empirical* models. SIMPRE is designed as a tool to obtain a prediction of some static and dynamic magnetic properties for a given molecular structure, to guide the experimental effort before performing any sophisticated characterisation. This program also restricts the parameter space once experimental data are available, and this allows for physically meaningful fits.

The package has been used in preliminary attempts to rationalise the conditions a mononuclear rare earth molecule needs to meet to act as a nanomagnet, as we will see in the next chapter. It has also been applied to a large variety of lanthanide (and even actinide) complexes.

3 Rational design of single-ion magnets

As described in the introduction of this thesis, the design of single-molecule magnets is a major challenge in the field of molecular magnetism. Until a decade ago, the known recipes to achieve magnetisation blocking at low temperatures were mainly based on applying two rules: the first one was to design a polymetallic molecule with a high spin ground state (S), generally by coupling as many magnetic ions as possible in the same magnetic cluster. The second condition was a compelling negative zero-field splitting (D) in order to stabilise the highest M_S sublevel leading to an energy barrier (U) for the magnetisation reversal.[20] The ultimate source of the magnetisation blocking, however, is the anisotropy of the single ion. It is the sum of multiple individual anisotropies, via magnetic exchange, that created a giant anisotropic spin.

In 2003, a second generation of SMMs came out, in which a mononuclear lanthanide complex was sufficient to exhibit slow relaxation of the magnetisation and magnetic hysteresis.[51] The discovery by Ishikawa *et al*. of such a behaviour in the series $(NBu_4)[Ln(Pc)_2]$ (Pc^{2-} = phthalocyaninato anion, Ln = Tb^{3+}, Dy^{3+}) opened the door for obtaining new derivatives based on mononuclear rare earth coordination compounds.[52] This new approximation, using a single lanthanide complex as the sole source of high spin and anisotropy, was extremely efficient.[66]

The real explosion of the field, however, only started five years after this seminal discovery when our group reported the second example of mononuclear lanthanide SMM: the erbium derivative of the family of polyoxometalates $[Ln(W_5O_{18})_2]^{9-}$ (in short, LnW_{10}).[59] Despite the different type of ligands in these two families of SIMs, both exhibit the same coordination number (CN) around the central ion and a slightly distorted D_{4d} coordination symmetry, i.e. the magnetic centre is sandwiched between two square moieties that are staggered with a torsion angle of approximately 45º. This was known to be almost equivalent to a cylindric or pseudo-axial coordination environment, which at that time was thought to be the requirement of SIM behaviour.

Despite this similarity, a clear difference between the two families is obvious if one pays attention to which lanthanoid ion gives the targeted behaviour in each case. In the Ishikawa example, Tb^{3+} is the magnetic ion with the highest blocking temperature and largest energy barrier in the family, whereas in the second series, the Er^{3+} derivative was the most promising candidate. Preliminary studies about this question were focused in the opposite sign of the Stevens coefficient α (α<0 for Tb^{3+} and α>0 for Er^{3+}),[62] which implies that for a given coordination geometry, terbium and erbium are expected to show opposite magnetic behaviour. This can be related with the fact that the distance between the coordinating oxygen planes (LnW_{10}) is shorter than the distance between the nitrogen planes in the series $(NBu_4)[Ln(Pc)_2]$. Thus, it seems that the more compressed situation in the polyanion favours the stabilisation of the $M_J = \pm 13/2$ in the erbium ion, whereas the phthalocyaninate sandwich, which can be considered axially elongated, is an adequate environment for the terbium ion to show the reported behaviour ($M_J = \pm 6$).

At this point, it is important to remark that this kind of hand-waving magneto-structural reasoning can be made in f-element mononuclear complexes because the electronic spectrum and thus the magnetic properties are depending primarily on the magnetic anisotropy that results from the CF splitting. To improve on that, a quantitative methodology based on the analysis of the interaction between the lanthanide ion and the coordination environment of these systems was needed to be developed. Research along this line resulted in a basic guide to synthetic chemists aiming at the discovery of new SIM derivatives,[122] and allowed us to give the first insights to rationalise the observed properties. Nevertheless, one should be aware that the model that was used at the beginning of this work is inherently limited and this guide has to be understood just as a first foray into the theoretical design of this class of complexes. In the following chapters, we are going to develop new strategies that will be applied to different f-block complexes with the aim of addressing the rational design and modelling of these systems.

An initially accepted guideline, supported by the previous knowledge of the SMM phenomenon, is that a mononuclear lanthanoid coordination complex will exhibit slow relaxation of the magnetisation if the ligand field splits the ground state of the lanthanoid, J, in such a way that the ground-state magnetic doublet has a dominant contribution of a high M_J value, $\pm M_J$.[52] In this context, Long *et al.* remarked that double degeneracy is indispensable because the ground state bistability defines the properties of these magnetic entities.[61] Similar to transition metal SMMs, the second requirement will be to have the ground doublet well separated in energy from the first excited state through which a rapid relaxation is possible. Such a splitting will be determined by several factors including the ion itself, the charge distribution around the rare earth and the distortion of the

coordination environment. Nonetheless, simple magneto-structural correlations between the most common f-element coordination environments, CFPs and their magnetic properties were developed and they are reported in the present chapter.

3.1 Influence of the lanthanide

Lanthanides share many common characteristics. These include coordination numbers greater than six (usually eight or nine), a tendency for lanthanide contraction across the series which limits the CN, the adoption of the +3 oxidation state, the very small CF effects and the preference to form complexes with more electronegative elements (such as O or F) as donor atoms. Nevertheless there are important differences in their magnetism to take into account when rationalising their magnetic properties.

The first attempts to rationalise the magnetic behaviour of the free lanthanide ions have been recently summarised by Sorace *et al*.[17] These start with the work of Hund,[279] who could obtain a remarkable agreement between predictions using old quantum theory with the measured room temperature magnetic moment, with the exception of Eu^{3+} and Sm^{3+} derivatives. Subsequently, Laporte[280] included the contribution of excited multiplets for these ions but still was unable to correctly estimate the magnetic properties at room temperature for these two ions. Second-order effects introduced by Van Vleck could finally explain the magnetic behaviour for all the metals of the series.[281,282]

Concerning the rational design of SIMs, the first condition to be satisfied by a molecule with a lanthanoid as a magnetic centre is to possess

a high-M_J ground-state doublet. For that, a large J value is recommended. The values of the total angular momenta J, as well as L and S, of the lanthanide tripositive ions are reported in Table 3.1. One may observe that the ions of the second half of the lanthanoid series do present negative spin–orbit coupling, thus stabilising the states with maximum J values. According to this, Ho^{3+}, Dy^{3+}, Er^{3+}, Tb^{3+} and Tm^{3+} will be the best choices as magnetic ions, with Nd^{3+}, Pr^{3+}, $Pm^{3+}$and Yb^{3+} coming next.[122]

Table 3.1: Relevant magnetic information for free Ln^{3+} ions and Stevens coeficients sign.

Ion	Ground multiplet	S	L	J	α	β	γ
Ce^{3+}	$^2F_{5/2}$	1/2	3	**5/2**	-	+	0
Pr^{3+}	$^3H_4$	1	5	**4**	-	-	+
Nd^{3+}	$^4I_{9/2}$	3/2	6	**9/2**	-	-	-
Pm^{3+}	$^5I_4$	2	6	**4**	+	+	+
Sm^{3+}	$^6H_{5/2}$	5/2	5	**5/2**	+	+	0
Eu^{3+}	$^7F_0$	3	3	**0**	0	0	0
Gd^{3+}	$^8S_{7/2}$	7/2	0	**7/2**	0	0	0
Tb^{3+}	$^7F_6$	3	3	**6**	-	+	-
Dy^{3+}	$^6H_{15/2}$	5/2	5	**15/2**	-	-	+
Ho^{3+}	$^5I_8$	2	6	**8**	-	-	-
Er^{3+}	$^4I_{15/2}$	3/2	6	**15/2**	+	+	+
Tm^{3+}	$^3H_6$	1	5	**6**	+	+	-
Yb^{3+}	$^2F_{7/2}$	1/2	3	**7/2**	+	-	+

For each lanthanoid, the *J* states can be described mathematically by the quadrupole moment of the f-electron charge cloud, which is either prolate (axially elongated), oblate (equatorially expanded), or isotropic (spherical). The shapes of these electrostatic charge distributions were calculated using the total angular momentum quantum number (*J*), the Stevens coefficient of second order (α) and the radius of the 4f-shell squared $\langle r^2 \rangle$ (see Figure 3.1).[61]

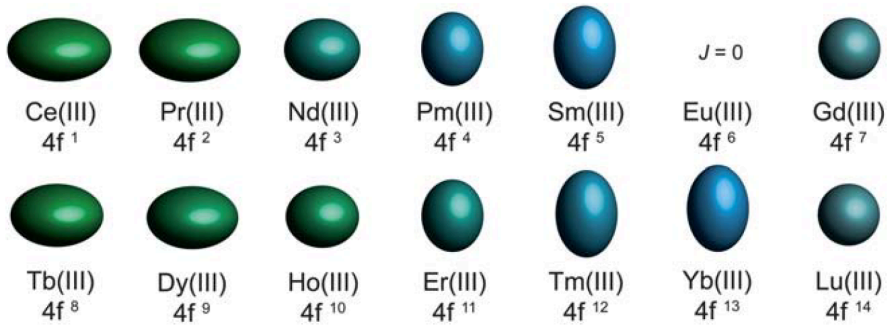

Figure 3.1: Quadrupole approximations of the 4f-shell electron distribution for Ln^{3+} as reported by Long *et al*.[61]

These quadrupole approximations are directly related to the second order Stevens coefficient: the sign of these coefficients (reported in Table 3.1) is determining the shapes.[142] It is obvious, then, that lanthanide ions with a negative second order Stevens coefficient present an equatorially expanded quadrupole moment, whereas the ones with a positive one are showing an axially elongated f-electron charge distribution. The different shapes of the 4f-shell electron distribution (as well as the sign of α) provide a simple way to get an intuitive idea of which coordination sphere is more adequate to stabilise a major contribution of a high M_J value in the ground

doublet. This key question is analysed with a few quantitative examples in the following section.

3.2 Influence of the coordination sphere

When a lanthanide ion is placed in a ligand environment with symmetry lower than spherical, the degeneracies of its partly filled 4f orbital states are broken due to the electrostatic field produced by the surrounding charge distributions of the ligands. The result is the splitting of the $2J+1$ degeneracy of the free ion states. The effect of the coordinating ligands over the magnetic properties of lanthanides becomes important at low temperatures, as the ground multiplets are split by an amount comparable to thermal energy. As a consequence, depopulation of the sublevels occurs, and deviation from the Curie law[283] is observed.

Regarding the question of choosing the most adequate coordination sphere to obtain SMM behaviour, it is always recommended to have highly symmetric axial sites in systems where all the coordinated atoms are similar. This is because they often provide the most favourable situation to have pure M_J wave functions. On the other hand, the level splitting produced by strong diagonal terms can avoid the mixture with low M_J states even for non ideal geometries. If the high-rank parameters are not taken into account, one can expect that α-negative lanthanoids (Tb^{3+}, Dy^{3+}, Ho^{3+}, Pr^{3+}, and Nd^{3+}) will stabilise a high-M_J ground-state doublet when they are in an axially elongated coordination environment, whereas α-positive lanthanoids (Er^{3+}, Tm^{3+}, and Yb^{3+}) will need equatorial or axially compressed coordination environments to achieve this. This can be better

illustrated after carrying out the following simple calculations, placing Dy^{3+} (oblate) and Er^{3+} (prolate) as magnetic centres:

- a linear molecule LnX_2, where Ln = Dy^{3+}, Er^{3+}.

In this first example, the two charges introduced in the program (Z_i = 1) are contained in the z axis (θ = 0º and 180º) at a distance of 2.5 Å between the electrostatic charges and the central ion. The coordination environment is perfectly axial, thus favouring SMM behaviour in lanthanide ions with an equatorially expanded 4f electronic distribution. This is the case of Dy^{3+} (Figure 3.2 (left)), which shows a ground state composed by $M_J = \pm 15/2$ with a barrier for the reversal of the magnetisation of about 900 cm^{-1}. This ideal situation almost exactly inverted for the Er^{3+} example, which presents an easy plane with a ground doublet formed by $M_J = \pm 1/2$ (Figure 3.2 (right)) with the main difference being the energy scale. In both ideal examples the second-rank CF parameter B_2^0 is governing the CF splitting with calculated values of -5.30 and +1.86 cm^{-1} for Dy and Er, respectively.

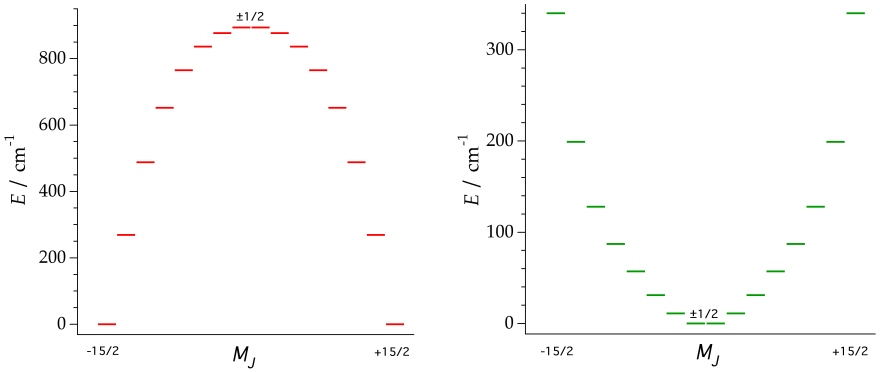

Figure 3.2: Calculated ground multiplet energy levels and main M_J contributions to the wave functions in z for the linear ideal system DyX_2 (left) and ErX_2 (right) with R_i = 2.5 Å and Z_i = 1.

- a square-planar molecule LnX_4, where Ln = Dy^{3+}, Er^{3+}.

The second example presented herein consists of a lanthanide ion compressed into an ideal square-planar crystal field. In this case, the lanthanide is coordinated by four electrostatic charges that are located in the edges of a square contained in the *xy* plane, i.e. $\theta = 90^{o}$. This equatorial charge distribution results in a ground doublet determined by $M_J = \pm 15/2$ in the erbium derivative (Figure 3.3 (right)). In contrast, for the Dy analogue the situation is completely different, with a ground doublet characterised by $M_J = \pm 1/2$ (Figure 3.3 (left)). The calculated values of B_2^0 are 5.30 and -1.86 cm^{-1} for Dy and Er respectively, i.e. the same value of the second-rank parameters in the example (a) but with the opposite sign. The total splitting of the ground multiplet in the Er^{3+} example is about 330 cm^{-1}.

Owing to the presence of the extradiagonal CF parameters B_4^4 and B_6^4 the wave functions are not pure. This results in contributions of about 3% of $M_J = \pm 1/2$ in the third excited doublet. If we compare the energy level scheme of the ErX_4 example (Figure 3.3 (right)) with the calculated one for ErX_2 (Figure 3.2 (right)), one can notice the difference between the two inverse shapes: in the case of DyX_2 the distribution of ground state M_J contributions is practically an inversion of the U shape of ErX_2. This situation is different for ErX_4, which presents a more triangular shape with the two Kramers doublets that are higher in energy more separated to the rest of energy doublets. This points out the importance of having the full set of CFPs determined, as all of them are playing a role in the energy levels distribution. Of course, it will be impossible to have an accurate determination of them in systems will low symmetry due to the

overparameterisation problem, but an approximation can be found using geometrical considerations.

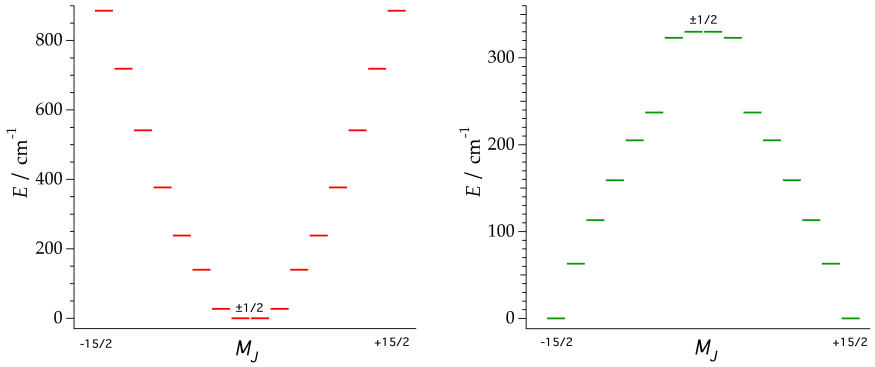

Figure 3.3: Calculated ground multiplet energy levels and main M_J contributions to the wave functions in z for the square-planar ideal system DyX_4 (left) and ErX_4 (right) with $R_i = 2.5$ Å and $Z_i = 1$.

These results may also be easily understood when observing the shapes of the quadrupole approximations of the 4f electron distributions in Figure 3.1. An oblate quadrupole f-electron charge distribution will present a more pronounced repulsion in an equatorially expanded crystal field, preferring a coordination sphere similar to the linear molecule of the first example ($\theta = 0^o$), with the electron density near the z axis. In the case of prolate ions as erbium, the tendency to stabilise a high M_J value in the ground doublet will appear for ligands located at $\theta = 90^o$ as in the second example.

Lanthanides form compounds with a greater diversity in coordination polyhedra than the d-block transition metals, with the most observed coordination numbers being 8 and 9,[284] although many systems with a lower or higher CN are known.[285,286] Symmetry around the cation determines the non-vanishing CF parameters, which are listed in function

of the different coordination polyhedra in Table 3.2. In the vast majority of these ideal polyhedra, assuming strictly ionic bonding, B_2^0 plays a dominant role determining the height of the barrier. This parameter in Stevens notation is related to the A_2^0 parameter by the following expression: $B_2^0 = \alpha \langle r^2 \rangle A_2^0$. Thus, for the obtention of a SIM, $B_2^0 < 0$ will require α < 0, because A_2^0 is positive when the charge distribution is axially elongated, or $\alpha > 0$ for a compressed environment, because in this case A_2^0 is negative. In Table 3.2 other particular symmetries where B_2^0 does not dominate (e.g., tetrahedral, octahedral or icosahedral symmetry) are also listed. In these examples the higher-order B_4^0 parameter usually dominates the CF splitting. In these cases, β-positive lanthanoids (Tb^{3+}, Er^{3+}, and Tm^{3+}) should have ligands on the *z* axis and/or on the *xy* plane, whereas β-negative lanthanoids (Pr^{3+}, Nd^{3+}, Dy^{3+}, Ho^{3+}, and Yb^{3+}) should have them placed at polar angles (θ) of around 50 and 60° in order to favour the stabilisation of the medium-to-high M_J compared with the lowest M_J states.

Table 3.2: Coordination polyhedra and point group symmetry for coordination numbers (CN), 6-12. Non-forbidden CFPs that a group of point charges may contribute collectively.

Polyhedron	Symmetry	CN	CFPs
Octahedron (Oct)	O_h	6	$B_4^0, B_4^4, B_6^0, B_6^4$
Trigonal prism (TP)	D_{3h}	6	$B_2^0, B_4^0, B_6^0, B_6^6$
Trigonal antiprism (TAP)	D_{3d}	6	$B_2^0, B_4^0, B_4^3, B_6^0, B_6^3, B_6^6$
Tetragonal bipyramid (TBP)	D_{4h}	6	$B_2^0, B_4^0, B_4^4, B_6^0, B_6^4$
Capped trigonal prism (CTP)	C_{2v}	7	$B_2^0, B_2^2, B_4^0, B_4^2, B_4^4, B_6^0, B_6^2, B_6^4, B_6^6$
Monocapped octahedron (MO)	C_{3v}	7	$B_2^0, B_4^0, B_4^3, B_6^0, B_6^3, B_6^6$
End-capped trigonal prism (ETP)	C_{3v}	7	$B_2^0, B_4^0, B_4^3, B_6^0, B_6^3, B_6^6$
Cube	O_h	8	$B_4^0, B_4^4, B_6^0, B_6^4$

Square prism (SP)	D_{4h}	8	$B_2^0, B_4^0, B_4^4, B_6^0, B_6^4$
Square antiprism (SAP)	D_{4d}	8	B_2^0, B_4^0, B_6^0
Dodecahedron (Dod)	D_{2d}	8	$B_2^0, B_4^0, B_4^4, B_6^0, B_6^4$
Bicapped octahedron (BOct)	C_{2v}	8	$B_2^0, B_2^2, B_4^0, B_4^2, B_4^4, B_6^0, B_6^2, B_6^4, B_6^6$
Bicapped trigonal prism (BTP)	C_{2v}	8	$B_2^0, B_2^2, B_4^0, B_4^2, B_4^4, B_6^0, B_6^2, B_6^4, B_6^6$
End-bicapped trigonal prism (EBTP)	D_{3h}	8	$B_2^0, B_4^0, B_6^0, B_6^6$
End-bicapped trigonal antiprism (EBTAP)	D_{3d}	8	$B_2^0, B_4^0, B_4^3, B_6^0, B_6^3, B_6^6$
Hexagonal bipyramid (HBP)	D_{6h}	8	$B_2^0, B_4^0, B_6^0, B_6^6$
Tricapped trigonal prism (TTP)	D_{3h}	9	$B_2^0, B_4^0, B_6^0, B_6^6$
Monocapped square antiprism (MSAP)	C_{4v}	9	$B_2^0, B_4^0, B_4^4, B_6^0, B_6^4$
Bicapped square antiprism (BSAP)	D_{4d}	10	B_2^0, B_4^0, B_6^0
Tetracapped trigonal prism (FTP)	C_{3v}	10	$B_2^0, B_4^0, B_4^3, B_6^0, B_6^3, B_6^6$
Pentagonal antiprism (PAP)	D_{5d}	10	B_2^0, B_4^0, B_6^0
Pentagonal prism (PP)	D_{4h}	10	$B_2^0, B_4^0, B_4^4, B_6^0, B_6^4$
Bicapped square prism (BSP)	D_{4h}	10	$B_2^0, B_4^0, B_4^4, B_6^0, B_6^4$
Pentacapped trigonal prism (PTP)	D_{3h}	11	$B_2^0, B_4^0, B_6^0, B_6^6$
Monocapped pentagonal prism (MPP)	C_{5v}	11	$B_2^0, B_4^0, B_6^0, B_6^5$
Monocapped pentagonal antiprism (MPAP)	C_{5v}	11	$B_2^0, B_4^0, B_6^0, B_6^5$
Icosahedron	I_h	12	B_6^0, B_6^5
Cuboctahedron	O_h	12	$B_4^0, B_4^4, B_6^0, B_6^4$
Truncated tetrahedron	T_d	12	$B_4^0, B_4^4, B_6^0, B_6^4$
Hexagonal prism (HP)	D_{6h}	12	$B_2^0, B_4^0, B_6^0, B_6^6$
Hexagonal antiprism (HAP)	D_{6d}	12	B_2^0, B_4^0, B_6^0
Bicapped pentagonal prism (BPP)	D_{5h}	12	B_2^0, B_4^0, B_6^0
Anticuboctahedron	D_{3h}	12	$B_2^0, B_4^0, B_6^0, B_6^6$

In the following section, the influence of the coordination environment on the splitting of the *J* ground multiplet in three of the most common coordination environments in lanthanide complexes, namely, the square antiprism, triangular dodecahedron, and trigonal prism, is discussed in detail. The effect of these CF environments and some general

guidelines for the choice of the most adequate geometry are provided. The approximation obtained by applying the PCEM to the ideal structures is more reasonable for homoleptic compounds, and may provide an initial quantitative guess before the experimental work starts. The modelling of the properties of the real systems will need more complex first principles calculations or the use of *semi-empirical* models accompanied by experimental techniques as we will see along this dissertation.

3.2.1 Square antiprismatic versus cubic geometry

In this subsection, a comparison between the square antiprismatic geometry (D_{4d} ideal symmetry) and the cubic geometry (O_h ideal symmetry) is developed. As examples of both octa-coordinated symmetries, two families of POMs are selected, where all the coordinated atoms are almost equivalent. Good examples of ideal geometries are: in the case of square antiprism, the series $[Ln(W_5O_{18})_2]^{9-}$,[59] and for the cubic structure the family of polyoxopalladates $[LnPd_{12}(AsPh)_8O_{32}]^{5-}$ reported by Kortz *et al*.[287] The chemical structures are shown in Figure 3.4. Comparing the experimental magnetic data measured in these two families, it is intriguing that whereas some derivatives of the polyoxowolframate series could exhibit SMM behaviour, all the derivatives of the second family showed a fast spin relaxation at low temperatures.[222] This may indicate that D_{4d} symmetry is more suitable for the design of SIMs than the O_h symmetry is. Let us now discuss and rationalise the origin of such a difference in the observed behaviours using the crystal structures. In the erbium derivative of $[Ln(W_5O_{18})_2]^{9-}$, the ratio between the interplanar distance d_{pp} = 2.47(1) Å, calculated as the distance between the upper and lower planes containing the four oxygen atoms, and the average distance between the four

neighbouring oxygen atoms placed in each plane, d_{in} = 2.86(5) Å, reveals an axial compression of the square antiprism. Within this geometry, the main CF parameters to be considered are B_2^0, B_4^0, and B_6^0, i.e. those allowed by an ideal D_{4d} system (see Table 3.2), but in the real example the slight distortion of the site will also make appear non-negligible values for B_4^3, B_4^4 and B_6^4. The sign of B_2^0 is positive in Tb^{3+}, Dy^{3+}, and $Ho^{3+}$and negative for Er^{3+}. In general, the sign of B_2^0 for a given lanthanoid complex is determined by the combination of the axial ($\theta < 54.7°$) or equatorial character ($\theta > 54.7°$) of the sites, as defined by the ligand position. In fact, at θ = arccos[$(1/3)^{-2}$] ≈ 54.7°, which corresponds to an axially non-distorted antiprism (defined by $d_{in} = d_{pp}$) or to a perfect cube, the point charge is placed on a node ($B_2^0 = 0$, as Z_{20}(arccos[$(1/3)^{-2}$], φ_i) = 0) and contributes to B_4^0 and B_6^0 (see Expression 2.1a).

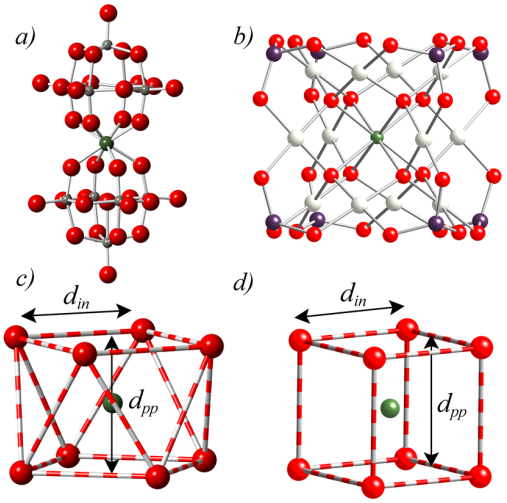

Figure 3.4: Schematic structure of two different POM complexes with interesting coordination symmetry, (a) $[Ln(W_5O_{18})_2]^{9-}$ and (b) $[LnPd_{12}(AsPh)_8O_{32}]^{5-}$, and their coordination polyhedra: (c) square antiprism and (d) cube.

In order to test the effect of the cubic symmetry over the ground state wave functions, calculations using the PCEM on the erbium derivative of the $[LnPd_{12}(AsPh)_8O_{32}]^{5-}$ series were performed. Electrostatic charges of Z_i=2 were placed in the crystallographic positions. Results show a mixed ground-state doublet, with the most important contribution being M_J = ±1/2, followed by ∓ 15/2, ∓ 7/2, and ±9/2. The first 4-fold degenerate excited state is located at 13.1 cm^{-1}, where the majority of the M_J values are contributing to the wave function. This extensive mixing of the sublevels yields a fast quantum tunnelling of the magnetisation and, in addition, the high presence of ±1/2 (52%) in the ground state explains why this molecule does not display SMM behaviour. Owing to the well-known relations for cubic symmetry, $B_4^4 / B_4^0 = 5$ and $B_6^4 / B_6^0 = -21$, this system is defined only by two CF parameters, B_4^0 and B_6^0 . The absence of B_2^0 reduces the possibilities of using a different lanthanoid (e.g., Tb^{3+}, Dy^{3+}, or Ho^{3+}) to obtain a higher barrier and/or stabilise a high M_J value in the ground state. This explains why D_{4d} symmetry (axially elongated for Tb^{3+}, Dy^{3+}, or Ho^{3+} or equatorially compressed for Er^{3+}) is much more favourable than cubic (O_h) symmetry, as the later symmetry does not satisfy the general criteria to obtain slow relaxation of the magnetisation. This system will be revisited in Chapter 6, where the spectroscopic and magnetic properties of the second-half lanthanide derivatives will be analysed in terms of effective electrostatic models.

This conclusion can be better illustrated by performing a magneto-structural study in which the D_{4d} symmetry is taken as a distorted case of the O_h symmetry when the two squares are staggered rather than eclipsed. This situation is defined by the torsion angle between the upper and lower squares, φ, which goes from 0° in the O_h symmetry to 45° in the D_{4d}

symmetry (see Figure 3.5). To perform this calculation, the coordinates of the four point charges forming the upper square are rotated with respect to those of the lower square around the z axis in the Dy derivative. While rotating the planes, typical distortions of the D_{4d} symmetry are obtained by slightly deviating φ from 45°. In this procedure, the crystal field parameters B_4^0 and B_6^0 are invariant with respect to the torsion angle. Additionally, B_4^4 and B_6^4 are different than zero, except for φ = 45°, and they evolve as a function of φ. Thus, the exact cancelation of these two parameters occurs for ideal square-antiprismatic symmetry, while the maximum values are reached for the cubic structure. In conclusion, one can anticipate that for an ideal D_{4d} symmetry the wave functions can be described by pure $\pm M_J$ values, while for an O_h symmetry, the presence of the parameters B_4^4 and B_6^4 will result in an extensive mixing of functions with different M_J values: in particular, those that differ by four units.

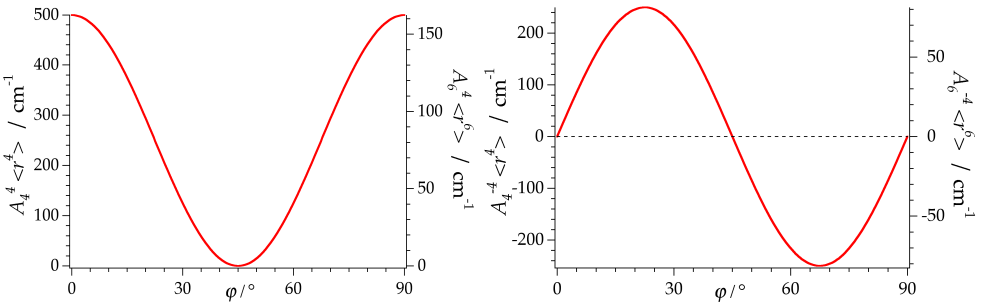

Figure 3.5: Magneto-structural correlation of (left) $A_4^4\langle r^4\rangle$ and $A_6^4\langle r^6\rangle$, and (right) $A_4^{-4}\langle r^4\rangle$ and $A_6^{-4}\langle r^6\rangle$ with φ, which is the torsion angle that describes the rotation of a cube from O_h ($\varphi = 0°$) to D_{4d} ($\varphi = 45°$) symmetries.

On the other hand, as we have explained before, in these particular examples with θ = 54.7°, B_2^0 is cancelled. In general, this second-rank parameter plays a remarkable role for creating a gap between the ground-state doublet and the excited states. Thus, it seems that the possibility of having an energy barrier will only appear if the antiprism is axially distorted (elongated or compressed) and will determine which lanthanide ion is the most adequate. The distortion of the real structures can be analyzed using the SHAPE package[288] developed by Álvarez *et al.*

3.2.2 Triangular dodecahedron

Another common lanthanide coordination environment is the triangular dodecahedron, which presents D_{2d} symmetry, closely related to S_4 (Figure 3.6). In this case, two very nice examples are found in the solid-state salts $LiHo_xY_{1-x}F_4$ and $Er_xCa_{1-x}WO_4$, with a CN of 8 around the lanthanoid ion.[77,217] Both of them show a scheelite structure with tetragonal distortion from the cubic symmetry. This arises from the displacement of two opposite edges in opposite directions, leading to a symmetry reduction from O_h to S_4. In this case, the presence of non-negligible extradiagonal parameters B_4^4 and B_6^4 yields an extensive mixture of M_J. Indeed, both CFPs are one and two orders of magnitude larger than the corresponding diagonal terms (B_4^0 and B_6^0), respectively,[289] resulting in ratios that are even higher than those of cubic geometry. This means that in general the triangular dodecahedron, similarly to cubic environments, does not seem to be ideal for generating SMM behaviour.

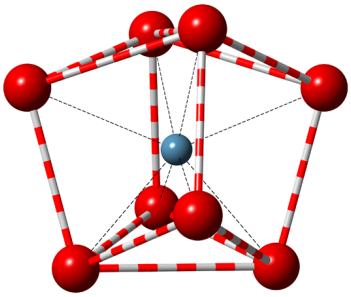

Figure 3.6: Schematic structure of a triangular dodecahedron site with D_{2d} symmetry.

3.2.3 Trigonal prism

Trigonal prismatic molecular geometry describes the shape of compounds where six ligands are arranged around a central atom, defining the vertices of a triangular prism (Figure 3.7). Such a point group is also very common in lanthanoid coordination chemistry, either bare or with up to three vertices in the centre of the rectangular faces. It has to be remarked that, in general, these complexes show low-symmetry highly distorted geometries (often seen as distorted D_{4d} complexes), which are not easy to model.

In any case, if one intends to approach this problem as a rational design process, one should first take into account that an ideal trigonal prism (D_{3h} symmetry) can only present B_2^0, B_4^0, B_6^0, and B_6^6 terms (Table 3.2). The presence of the extradiagonal CF parameter B_6^6 means mixing between M_J values differing by ±6. It is crucial to note that this will produce direct tunnelling only for doublets that involve states with M_J = ±3 or ±6, and even in these cases, the compound may show slow relaxation of the magnetisation if B_2^0 is large enough. This also indicates that an ideal D_{3h} coordination symmetry may be as good as a pseudoaxial one for getting SMM behaviour for half-integer spins like Nd^{3+}, Sm^{3+}, Dy^{3+}, Er^{3+}, and Yb^{3+}

because it is not possible to have direct mixing between $+M_J$ and $-M_J$ values. In fact, even though actinoids cannot be precisely described by the Russell–Saunders scheme like lanthanoids, due to the mixing with excited J states, examples of U^{3+} ($J = 9/2$) in this coordination environment have also been reported exhibiting SMM properties (see Chapter 1, section 1.1). Such examples will be discussed with more detail in Chapter 8.

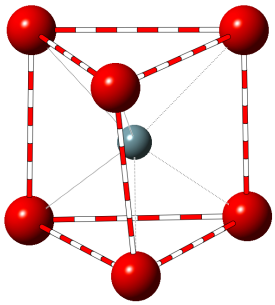

Figure 3.7: Schematic structure of a trigonal prism site with near D_{3h} symmetry.

3.3 Conclusions

The initial approach presented in this chapter, applying the old Point Charge Electrostatic Model with the SIMPRE package, provided some insights to take into account for the rational design of lanthanide SIMs. In this chapter we have observed that the energy level splitting of the ground J manifold depends mainly on the lanthanide ion, the charge distribution symmetry and the distortion of the coordination environment. As far as the lanthanide is concerned, both the ground state J and the Stevens coefficients (α, β and γ) are fixed and are specific for each lanthanide. The sign of these coefficients determines which kind of charge distribution around the central ion is desired to obtain slow relaxation of the magnetisation. Symmetry and distortion of the coordination site decide

which crystal field terms are active and thus the mixing conditions between the M_J sublevels. Taking into account these factors, the main rules that need to be known for the design of this kind of nanomagnets can be summarised as follows.

Lanthanide-based SIMs –as most SMMs- require (a) a high M_J ground state, (b) an energy barrier leading to slow thermal relaxation, and (c) low mixing in the ground doublet wave functions, to minimise fast quantum tunnelling processes. In the simplest case, this can be achieved with an ideal pseudoaxial symmetry such as D_{4d}, C_{5h}, D_{6d}, or any symmetry of order six or higher (such as, for example, in organometallic sandwich-type complexes). Notice that the chemical inequivalence of the ligands or chelating groups needs to be taken into account because it will usually lower the overall symmetry. In any symmetry, the most suitable case is achieved when the absolute value of the second-order uniaxial anisotropy, accounted for by the B_2^0 parameter, is maximised.

Not all of the molecular symmetries are equally suited for favouring SMM behaviour. For example, in the case of octacoordinated complexes, the simplest cases are the antiprismatic D_{4d} symmetry and the cubic O_h symmetry. However, as the cubic coordination lacks second-order uniaxial anisotropy, B_2^0, this geometry is not well suited to exhibit a large energy barrier for the magnetisation reversal. On the contrary, an axially distorted D_{4d} symmetry typically shows high B_2^0 values (either positive or negative), and this is why it has provided the first examples of mononuclear lanthanide SMMs. Axially elongated sites with electron density near the symmetry axis are favourable for Tb^{3+}, Dy^{3+}, and Ho^{3+}, as exemplified by $LnPc_2$, while axially compressed sites with electron density near the basal plane are favourable for Er^{3+}, as exemplified by POMs.

In addition to a thermal barrier, quantum tunnelling should be minimal for a slow relaxation of the magnetisation. Tunnelling is caused by the presence of an extensive mixture of M_J values in the ground-state; extradiagonal terms and the nature of the ground doublet are critical in this context (additionally, phonons allow transitions with $\Delta M_J = \pm 1$). If the two wave functions do not present any overlap, relaxation through tunnelling is forbidden.

To sum up, in this chapter it has been shown that the major electronic features that determine the spin dynamics of SIMs based on lanthanoids can be correlated with the local coordination environment around the f-metal ion. By using a simple point-charge model, a quick estimation of the splitting of the ground state, *J*, of the lanthanoid into M_J sublevels can serve at least as starting point to guide the adequacy of choosing a particular lanthanide ion for a particular geometry. This simple approach proposes general magneto-structural correlations and pieces of advice for the discovery of new derivatives, after examining three of the most common lanthanoid geometries: square antiprism, trigonal prism, and triangular dodecahedron. However, due to the inherent limitations of the PCEM, the problem of a realistic description of the magnetic and spectroscopic properties of rare earth SIMs cannot be addressed in this chapter. The development of *semi-empirical* models and their application to real systems is reported in the following chapters, offering a more complete and well-tested tool for the future rational design of these interesting systems. Finally, note that many rare earth SIMs will also be useful as spin qubits; this will be discussed in Chapter 11.

4 Development of two effective electrostatic models

In the previous chapter, initial considerations for the rational design of lanthanide SIMs have been presented. Although the model employed is attractive because of its simplicity and is helpful in predicting the sign of the CFPs, one need to be aware that the PCEM is only a crude approximation if one aims to describe the properties of f-block mononuclear complexes.[121] It is well known that the agreement between the calculated CFP values obtained by PCEM and the CFPs fitted from spectroscopic data is very poor.[144,290] Usually the second order term predicted by PCEM is too large, whereas the fourth- and sixth- order terms are considerably smaller in comparison to the phenomenological ones.[291] For a more realistic description of f-bock complexes one needs to take into account the character of the ligand and the magnetic and spectroscopic information that can be measured experimentally. Thus, a main question at this point is: can we overcome the limitations of the PCEM keeping its simplicity?

According to studies along this direction (e.g. Newman),[292,293] the overall two-electron interactions can be parameterised in the same manner as a classical, one-electron point charge electrostatic potential or approximated to it with quite fair accuracy. This means that there exist

possibilities of improving the PCEM which would not be in conflict with quantum mechanical principles.

To overcome the difficulties arising from the simplifications of the point charge model, two new effective electrostatic models are proposed in this Ph.D. thesis, and concretely presented in this chapter. Such effective electrostatic models depend on the bond character and the donor atoms: a Radial Effective Charge (REC) model, for compounds coordinated by σ-type bonding, as for example compounds coordinated by halogen or oxygen atoms due to their spherical character, and a Lone Pair Covalent Effective Charge (LPEC) model in the case of π-bonding systems, where the lone pair is not pointing directly to the metal ion, as occurring, for example, in aromatic rings coordinated to an f-element.[294]

4.1 Radial Effective Charge (REC) model

The Radial Effective Charge (REC) approach is based on a modification of the classical point charge electrostatic model. The main aim of the proposed approach is to remove the main drawbacks of the PCEM by introducing two essential changes. First, the formal charges are replaced by effective charges (Z_{eff}) attributed to the electron charge of the σ-type metal-ligand bonding, thus $Z_i = Z_{eff}$. Secondly, the metal-ligand distance from the crystal structure is replaced by an effective distance (R_{eff}), which is smaller than the real metal–ligand distance. For that, a radial displacement vector (D_r), also known as covalent correction, is defined, in which the effective distance is varied: $R_i = R_{eff} = r_i - D_r$, being r_i the original crystallographic position (see Figure 4.1). This allows to simulate the position of the electron charge maximum with respect to the metal origin, accounting for the effect of

covalent electron sharing. At the same time, the charge value (Z_i) is scanned in order to achieve the minimum deviation between calculated and experimental data (magnetic susceptibility, magnetisation and/or energy level scheme), whereas θ and ϕ remain constant. The displacement of the point charge has remarkable consequences in the values of the second-, fourth- and sixth- rank CFPs, correcting the deviations encountered in the PCEM. This model provides improved ratios between the different rank CFPs when compared with the phenomenological ones extracted from spectroscopy as we will see in the following chapter. Within this approximation, we are able to keep both the physics of the system and the simplicity of the PCEM, adding its chemical nature. As reported in the work entitled 'Modeling the properties of lanthanoid single-ion magnets using an effective point-charge approach' in 2012, in this model the crystal field potential is generated by electrons that are participating in the chemical bonds.[294]

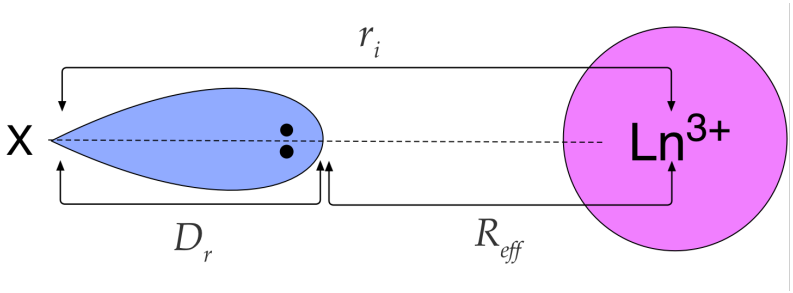

Figure 4.1: Electronic pair of a ligand X oriented towards the nucleus of a trivalent lanthanoid cation. The effective charge is located between the lanthanoid and the donor atom at $R_{eff} = r_i - D_r$.

As an example of the effects of the charge displacement, the evolution of the CFP values in a perfect D_{4d} system, varying the effective distance

from 2.5 Å to 1 Å, is reported. The input coordinates are displayed in Table 4.1 as follows:

Table 4.1: Spherical coordinates (R_{eff}, θ_i, φ_i) and effective charges (Z_i) for the ligands in a perfect D_{4d} system. R_{eff} is varied between 2.5 and 1 Å.

	R_{eff} / Å	θ_i / °	φ_i /°	Z_i
1	2.5 - 1	57	0	1
2	2.5 - 1	57	90	1
3	2.5 - 1	57	180	1
4	2.5 - 1	57	270	1
5	2.5 - 1	123	45	1
6	2.5 - 1	123	135	1
7	2.5 - 1	123	225	1
8	2.5 - 1	123	315	1

In Figure 4.2 (left) one can observe that at 2.5 Å, $A_2^0\langle r^2\rangle > A_4^0\langle r^4\rangle > A_6^0\langle r^6\rangle$. As D_r is increasing (i.e. R_{eff} decreasing), the value of $A_4^0\langle r^4\rangle$ is incremented faster with respect to the growth of $A_2^0\langle r^2\rangle$, overtaking it at about 1.5 Å. This different increase of the higher rank CFP is more accused in the case of $A_6^0\langle r^6\rangle$, which passes $A_2^0\langle r^2\rangle$ if $R_{eff} < 1.1$ Å. Of course, in a real study –fitting experimental data– as soon as D_r increases, Z_i would decrease. Logically, the CFP values presented in this example will give unreasonably high CF splittings. Figure 4.2 (right) is showing the relative ratio between the different diagonal CFPs: the blue line is equal to ($A_2^0\langle r^2\rangle$ / $A_6^0\langle r^6\rangle$), the green line ($A_4^0\langle r^4\rangle$ / $A_6^0\langle r^6\rangle$) and the red one represents ($A_2^0\langle r^2\rangle$ / $A_4^0\langle r^4\rangle$).

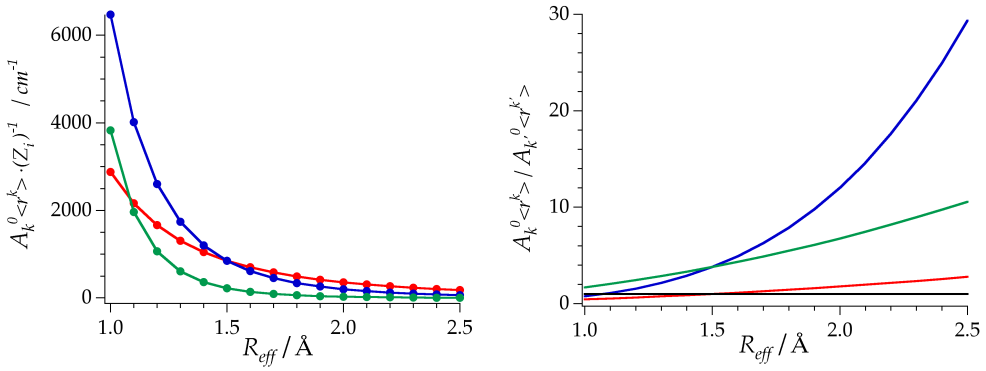

Figure 4.2: (left) Evolution of the values of $A_2^0\langle r^2\rangle$ (red), $A_4^0\langle r^4\rangle$ (blue) and $A_6^0\langle r^6\rangle$ (green); (right) ratio ($A_2^0\langle r^2\rangle$ / $A_6^0\langle r^6\rangle$) (blue), ($A_4^0\langle r^4\rangle$ / $A_6^0\langle r^6\rangle$) (green) and ($A_2^0\langle r^2\rangle$ / $A_4^0\langle r^4\rangle$) (red).

The horizontal black line in Figure 4.2 (right) plot marks the relation $A_k^0\langle r^k\rangle / A_{k'}^0\langle r^{k'}\rangle = 1$, which means that both CFPs are identical. As commented above, the two crosses appear at 1.5 Å, between $A_2^0\langle r^2\rangle$ and $A_4^0\langle r^4\rangle$, and at 1.1 Å, between $A_2^0\langle r^2\rangle$ and $A_6^0\langle r^6\rangle$.

The evolution of the CFPs with R_{eff} is easily explained if one pays attention to Equation 2.1a, where $A_2^0 \propto \frac{1}{R^3}$, $A_4^0 \propto \frac{1}{R^5}$ and $A_6^0 \propto \frac{1}{R^7}$. The CFPs are thus inversely proportional to the effective distance to the k+1 power, increasing their value as R_{eff} diminishes, being more pronounced this increment in the case of A_6^0, followed by A_4^0, due to their higher exponents.

The two simple assumptions of the REC model presented herein improve significantly one of the main inherent limitations of the PCEM reported in the literature: the underestimation of the four- and sixth- rank CFPs. The improvement of the PCEM makes necessary the use of two

parameters for each kind of ligand, making the model especially promising for homoleptic complexes coordinated by halogen or oxygen atoms.

4.2 Lone-Pair Effective Charge (LPEC) model

The second effective electrostatic model that is presented here is more adequate for systems with π-coordinating bond, where the spin polarisations of the negative charges are not individually shifted along the ligand-metal vector, but integrally along the normal of the aromatic plane. Thus, for a more realistic description of these systems, it is necessary to define a new displacement vector. This vector can be named horizontal (D_h) or vertical (D_v) displacement, depending on the orientation of the π cloud. In the case of $LnPc_2$ (see Chapter 7, section 7.1), the chemical structure forces the lone pair to point to the centre of the perpendicular to the lanthanide plane defined by four nitrogen atoms.[294] Thus, for that family of lanthanide-based SIMs, two vectors (D_h and D_r) should be applied to the original position of each nitrogen atom in order to determine the position of the effective centre of charge (Figure 4.3). Vector D_r simulates the attraction of the lone pair by the lanthanoid cation. Note that this latter displacement reflects, like in the REC model, the effective charge resulting from the sharing of the ligand electron density by the lanthanide ion. This correction does possess physical sense due to the fact that the nearest part of the electron cloud to the lanthanoid induces a more marked effect than the areas placed further away. A schematic representation of the orientation of the electronic pair in a lanthanide ion linked to a nitrogen atom in $LnPc_2$ is plotted in Figure 4.3.

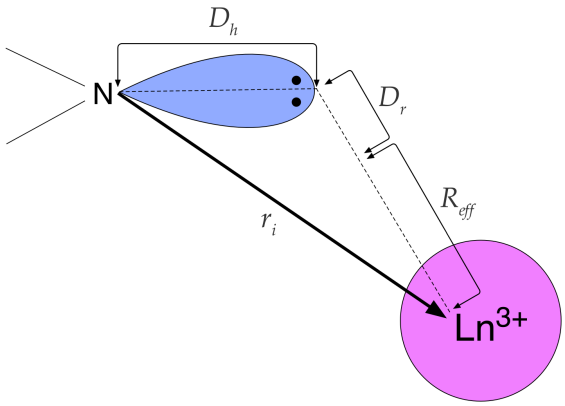

Figure 4.3: Orientation of a lone pair of a nitrogen donor atom that is not pointing directly towards the lanthanoid cation.

As commented above, this effect is especially easy to observe in the double-decker bisphthalocyaninato complexes, by the position of the nuclei of nitrogen. PCEM or REC models could never explain the negative sign of B_2^0 obtained by a fit of the magnetic susceptibility data. This would change the resulting energy level scheme, making more complicated the compatibility of the ground state wave function with the SMM behaviour shown by the Tb^{3+} complex. However, when considering the direction in which the nitrogen lone pairs point, the B_2^0 term changes in sign naturally. Then, an LPEC fit in $TbPc_2$ situates the effective charge on the other side of the B_2^0 node as we will see in section 7.1. This change in the sign of the second order uniaxial anisotropy does have dramatic consequences for the magnetic energy level scheme and ground state wave functions, making them compatible to the experimentally observed behaviour. Using the real structure, with only three LPEC parameters the full CF Hamiltonian is produced. The model, once the effective distances and charges are calculated and introduced in SIMPRE, provides the whole set of diagonal

and extradiagonal parameters as an output. Thus, tunnelling splittings and minor M_J contributions can be directly obtained.

Finally, it is worth to mention that a derived model from REC and LPEC was recently proposed by Jiang *et al.* to determine the quantised axis of lanthanide complexes.[295] These authors provided an inexpensive electrostatic model to provide an estimation of the easy axis orientation based on charge displacement, the approach also depends on the nature of the coordination σ- or π-bonds. The main objective of that work has been to overcome the drawbacks of the classical electrostatic model, adding minor covalent corrections, in order to improve the determination of magnetic anisotropy of this type of complexes.

4.3 Conclusions

The predictive power of the Radial Effective Charge and the Lone-Pair Effective Charge models is due to the possibility of associating to each type of ligands with a reduced set of effective parameters (two or three). These parameters are specific of the ligands and therefore can be used for many lanthanoid complexes. Series of analogous compounds, such as those provided by POM chemistry, as we will see in Chapter 6, are of special interest for the goal of building a general reusable library of ligands for the rational design of magnets based on lanthanoid complexes. In order to obtain a trustable library upon which one can firmly found further work, the desiderata are[17]:

(1) A high quality of the experimental data to be fitted, e.g. magnetic data (χT vs. T curves) and spectroscopic data, in order to obtain an accurate picture of the energy level scheme.

(2) Systematic studies: simultaneous fits of a series. In this case, a handful of parameters can be used to reproduce the experimental behaviour of a large quantity of compounds. This reduces the possibilities of numerical artifacts and also the propagation of experimental errors into the final parameters.

(3) The use of homoleptic compounds, where all coordinating atoms are as chemically indistinguishable as possible. Indeed, with heteroleptic complexes it can easily be the case that the error in the parameterisation of the effect of a type of ligand can be compensated and thus shadowed by another error in the parameterisation of a different ligand, resulting in flawed parameters for both of them. We will attack this problem in chapter 10, analysing the challenges and perspectives of this approach when dealing with complexes with different atoms coordinated to the lanthanide.

(4) Finally, the REC model will almost always be more trustable than the LPEC model, as it is simpler. Of course, in complexes where the effect of the lone pair is crucial, e.g. in the case of the phthalocyaninate sandwiches or systems with aromatic rings, REC has to be abandoned in favour of LPEC.

The REC and LPEC models presented in this chapter, as well as the computational package described in Chapter 2, are the foundations of this Ph.D. thesis. In the following part of this dissertation, these models will be applied using the SIMPRE package to understand the ligand field and the properties of different families of lanthanoid SIMs. This will complete the initial attempt for the rational design of single-ion magnets that we have presented in Chapter 3, distinguishing between different type of ligands and pointing out the current challenges of this kind of approaches.

2

Application of the effective electrostatic models to lanthanide homoleptic complexes

5 Lanthanide complexes coordinated by halogen atoms

In this chapter, a systematic application of the REC model to different series of the later lanthanide ions in crystal hosts is performed. The four families that have been chosen for this analysis are halogenide metal complexes in which the ligands are either fluoride or chloride anions. The spectroscopic studies and the CFPs determination carried out a few decades ago on these systems[121] serve as a benchmark to test whether it is possible to obtain reliable D_r and Z_i parameters that describe the crystal field effects of these halogen donor atoms. Moreover, we aspire to extract some insight on D_r and Z_i that can be extrapolated for non-halogenide complexes.[296]

The general formulas of the studied lanthanide ions in crystal hosts are: $LiYF_4:Ln^{3+}$ (coordination number = 8), $LaCl_3:Ln^{3+}$ (coordination number = 9) and $Cs_2NaYCl_6:Ln^{3+}$ (coordination number = 6), where Ln = Tb, Dy, Ho, Er and Tm, and the isostructural hexacoordinated family, $Cs_2NaYF_6:Ln^{3+}$, in which only the data of Ho and Er compounds are used in the fit. In general, lanthanides adopt coordination numbers greater than 6, usually 8-9.[297] Thus, the coordination environment of the selected examples is in principle adequate to extract useful information that can serve for predictions in other homoleptic lanthanide-based compounds.

The strategy proposed in this chapter is based on the fitting of high-quality spectroscopic data using modified versions of the SIMPRE package that integrate two nested loops that explore the parameter space for D_r and Z_i. In fact, two different procedures will be applied, as described below, fitting either the energy levels or the spectroscopic set of CFPs. These strategies based on spectroscopic information should be considered as the "gold standard", as they provide more reliable parameters compared with fitting of less informative magnetic experimental data. Unfortunately, it cannot be of general application, as most of the complexes of interest in molecular magnetism have not yet been fully characterised by spectroscopy.

The first procedure consists in the fitting of the ground multiplet energy level scheme for each lanthanoid in a given series using the available spectroscopic data for these sublevels. The description of the effect of the ligating atom in the whole family requires the collective fit of all metal complexes in the same coordination environment as a second step. This is carried out in a homemade code that searches for the best combination of D_r and Z_i and thus achieves the collective minimum deviation between calculated and experimental data.

The second procedure involves the direct fitting of the phenomenological CFPs of each lanthanide complex. These phenomenological CFPs were extracted by spectroscopy, using photoluminescence measurements on all the excited J states of the compounds.[298–304] Hence, it is interesting to compare the results of our CFPs calculations using a model that uses only the ground J energy level schemes with the phenomenological CFPs. This offers a good opportunity to benchmark the capabilities of the REC model in the understanding of the properties of these complexes.

In the fitting of the spectroscopic energy levels, the quantity to be minimised is the relative error E_Δ which is defined as:

$$E_\Delta = \frac{1}{n}\sum_{i=1}^{n}\frac{\left[\Delta_{theo,i} - \Delta_{\exp,i}\right]^2}{\left[\Delta_{\exp,i}\right]^2} \qquad (5.1)$$

where $\Delta_{exp,i}$ and $\Delta_{theo,i}$ are the experimental and theoretical energy values, respectively, and n is the number of points considered in the fit. When fitting CFPs, the quantity to be minimised is the absolute error E_{Bkq} which is defined as follows:

$$E_{Bkq} = \sum_{k=2,4,6}\sum_{q=-k}^{k}\frac{\left[B_{kq,theo} - B_{kq,phen}\right]^2}{\left[B_{kq,phen}\right]^2} \qquad (5.2)$$

where $B_{kq,phen}$ and $B_{kq,theo}$ are phenomenological CFPs (fitted from all the available spectroscopic information using the full Hamiltonian) and the theoretical CFPs (also in Wybourne notation) as calculated by the REC model, respectively.

5.1 Fluorides

To determine the REC parameters that simulate the ligand field effects of the fluorine atoms, the series of lanthanide crystal hosts $Cs_2NaYF_6:Ln^{3+}$ and $LiYF_4:Ln^{3+}$ are considered. Lanthanide ions in a hexafluoroelpasolite lattice ($Cs_2NaYF_6:Ln^{3+}$) occupy a high symmetry (O_h) site.[302–304] In this structure, each lanthanoid ion is coordinated to six F^- ions, and each has a second coordination sphere comprised of eight Cs^+ ions located at the vertices of a regular cube and a third coordination sphere comprised of six Na^+ ions

occupying the vertices of a regular octahedron. In $LiYF_4:Ln^{3+}$, which crystallises in the tetragonal scheelite C_{4h}^6 structure, the trivalent lanthanide ions substitute for trivalent yttrium with S_4 point symmetry. In practice, it has been found that the $4f^N$ energy level structures in these systems could be effectively modelled by a H_{CF} of D_{2d} symmetry.[305] The coordination environment for each family is illustrated in Figure 5.1:

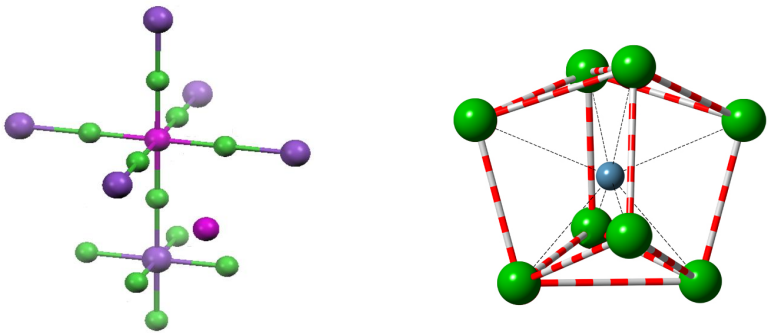

Figure 5.1: (left) An asymmetric unit of $Cs_2NaYF_6:Er^{3+}$, showing the relative positions of Er (magenta, octahedral), F (green), Na (violet), Cs (pink); (right) coordination environment around the Ho ion (blue) in LiYF4:Ho^{3+}, F (green).

As one can observe, the rare earth is coordinated by six and eight fluorine atoms respectively. Because of that, an independent collective fit for each family is performed. This allows us to analyse the effects of the coordination number over the parameters of the REC model.

After applying the fitting procedures described above to every particular system, the D_r and Z_i values with the minimum relative error for the fluorine atoms are plotted in Figure 5.2. The dispersion of the circles that represent each individual fit in $Cs_2NaYF_6:Ln^{3+}$ are distributed between 0.46 and 0.68 Å for D_r, and 0.46 and 1.00 for Z_i. This situation is different in the case of $LiYF_4:Ln^{3+}$, where D_r varies between 0.68 and 0.95 Å, and the effective charge varies between 0.14 and 0.25. In the second family the

effective charges are smaller but they are placed closer to the lanthanoid. The collective fit of each series is represented by a black cross (D_r = 0.51 Å and Z_i = 0.85, for Cs_2NaYF_6:Ln^{3+}; D_r = 0.84 Å and Z_i = 0.17, for $LiYF_4$:Ln^{3+}). For each coordination number, there is a coincidence of the parameter range for the individual fits of the energy levels, for individual fits of the phenomenological CFPs and, naturally, for the collective fit. The differences in the REC parameters depending on the coordination number will be deeply analysed in section 5.4.

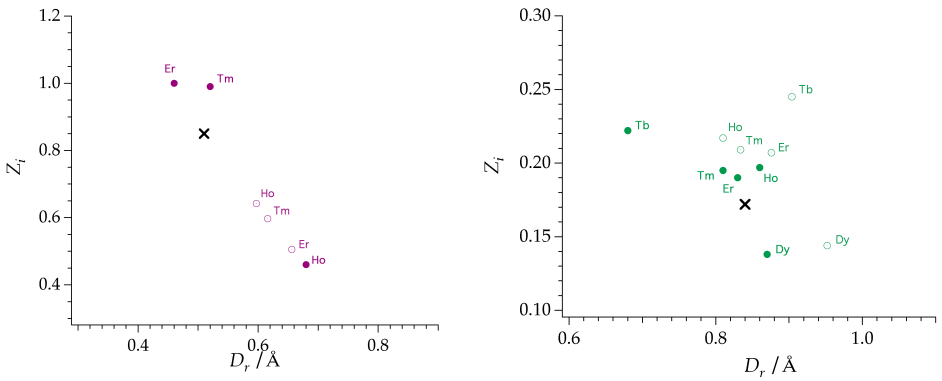

Figure 5.2: Dispersion of the D_r and Z_i values obtained by fitting: (1) the experimental energy levels (circles) and, (2) phenomenological CFPs (open circles) of: Cs_2NaYF_6:Ln^{3+} (right: purple) and $LiYF_4$:Ln^{3+}(left: green). The black cross represents the collective fit of energy levels solution for each family.

Note that due to the smaller number of ground multiplet energy levels reported for the Cs_2NaYF_6:Tm^{3+}derivative,[304] only the information of the Ho and Er complexes has been included in the collective fit. This means that the quantitative information is of limited value if one aims to extract further conclusions. However, a qualitative comparison with the trends

observed in $LiYF_4:Ln^{3+}$, where the collective fit takes into account all the information determined in the Tb-Tm complexes,[299] reflects a smaller radial displacement and a larger effective charge in the hexacoordinated systems.

A summary of these results is reported in Table 5.1. The REC parameters extracted in the elpasolite family using the energy levels information show drastic variations compared with the ones obtained by fitting the CFPs. This situation is different for the lanthanide ions in the scheelite structure and can be attributed to the larger number of CFPs in the second case. In general, this individual effect is corrected by the collective fit, where the evolution of the CFPs along isostructural lanthanide complexes has to be taken into account. Again, the results on $Cs_2NaYF_6:Ln^{3+}$ are to be trusted less, because the collective fit is only considering information from the two derivatives that presented full spectroscopic information.

Table 5.1: Systematic D_r and Z_i calculation from fitting of the experimental ground multiplet energy levels and the reported CFPs for the 8 complexes coordinated by fluorides studied in this section.

	Ln^{3+}	**Energy levels individual fit**		**CFPs individual fit**	
		D_r	Z_i	D_r	Z_i
$Cs_2NaYF_6:Ln^{3+}$	Ho^{3+}	0.68	0.46	0.51	0.66
	Er^{3+}	0.46	1.00	0.62	0.60
	Tm^{3+}	0.52	0.99	0.60	0.64
	Collective	**0.51**	**0.85**	-	-
$LiYF_4:Ln^{3+}$	Tb^{3+}	0.68	0.22	0.90	0.25
	Dy^{3+}	0.87	0.14	0.95	0.15
	Ho^{3+}	0.86	0.20	0.81	0.22
	Er^{3+}	0.83	0.19	0.88	0.21
	Tm^{3+}	0.81	0.20	0.83	0.21
	Collective	**0.84**	**0.17**	**-**	**-**

The REC parameters obtained for each family are applied to the first coordination sphere using the crystallographic positions. This allows the obtaining of the following set of energy level schemes, plotted using green horizontal lines in Figure 5.3. The resulting ligand field splitting is compared with the experimental energy levels for each metal (red horizontal lines).[299,300,302–304] The question mark appears when a particular energy level could not be accessed by photoluminescence. As one can observe, the agreement is excellent for both families, providing a simple picture of the potential of the REC model to reproduce and simulate the observables of this kind of homoleptic compounds coordinated by halogens. The understanding of the obtained REC parameters using this systematic approach will allow the inexpensive prediction of new derivatives. In the following section, we are extending the interpretation of the spectroscopic observables based on the REC model to two families of lanthanoids coordinated by chlorine atoms.

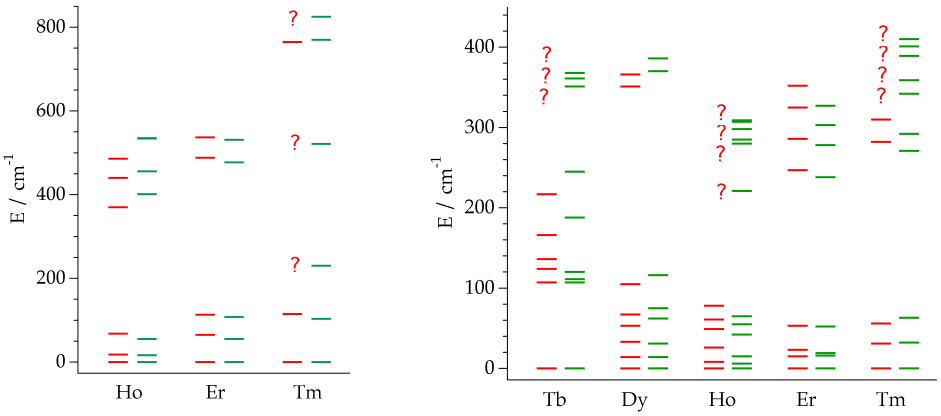

Figure 5.3: Experimental ground multiplet energy levels (red) and calculated ones using the collective fitting value for D_r and Z_i (green) in $Cs_2NaYF_6:Ln^{3+}$ (left) and $LiYF_4:Ln^{3+}$ (right); non-determined levels are marked with the question mark.

5.2 Chlorides

Following the same procedure, we determine the REC parameters that best reproduce the ligand field effects of chlorine atoms coordinated to the later lanthanides in two different crystal host lattices. The first family that is presented herein is isostructural with $Cs_2NaYF_6:Ln^{3+}$, i.e. a perfect octahedron coordinated by chlorides: $Cs_2NaYCl_6:Ln^{3+}$.[301] This allows a comparison between these two isostructural positions occupied by two different anions. The second family is a classical host for trivalent lanthanides, whose optical spectroscopic properties have been studied in detail. $LaCl_3$ crystallises in the hexagonal space group $P6_3/m$ with C_{3h} point symmetry for the La^{3+} site.[298]

The D_r and Z_i values with the minimum relative error for the chlorine atoms coordinated to each lanthanoid are represented in Figure 5.4. The dispersion of the circles that represent each individual fit in $Cs_2NaYCl_6:Ln^{3+}$ are dispersed across a larger area: between 0.45 and 1.49 Å for D_r, and between 0.04 and 0.99 for Z_i, with a clear inverse relation between D_r and Z_i. Despite that, the collective solution for the family (D_r = 0.86 Å and Z_i = 0.36) provides a result that is close to the individual fits of D_r and Z_i obtained from the phenomenological CFPs determined by Richardson *et al.*,[306] which display a much smaller dispersion (red open circles in Figure 5.4).

In the case of $LaCl_3:Ln^{3+}$, the obtained D_r values are placed between 1.16 and 1.30 Å, with the effective charges varying between 0.12 and 0.18. The collective fit of this family is represented by a black cross in Figure 5.4 (D_r = 1.25 Å and Z_i = 0.14). Again, the collective fit of the energy levels is very close to the individual fits of CFPs. Furthermore, as in section 5.1, there are clear differences between the REC parameters determined for

each families, which permits to intuit a direct relation with the coordination number.

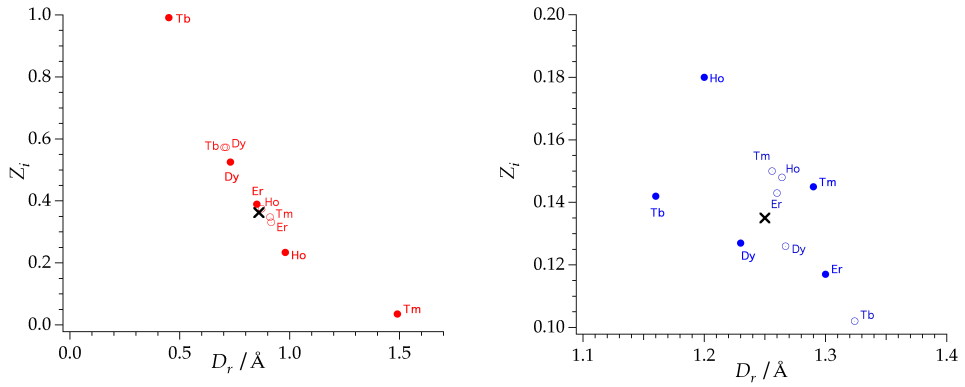

Figure 5.4: Dispersion of the D_r and Z_i values obtained by fitting: (1) the experimental energy levels (circles) and, (2) the phenomenological CFPs (open circles) of the family Cs_2NaYCl_6:Ln^{3+} (red) and $LaCl_3$:Ln^{3+} (blue). The black cross represents the collective fit of energy levels solution for this family.

A summary of the parameter set determined for the different families that have been modelled in this section is reported in Table 5.2. It is interesting to notice that in both families, the parameters are presenting larger variations between the different ions when they are extracted from the Stark sublevels. This is clearly seen in the elpasolite family, due to the low number of CFPs allowed by the octahedral symmetry. This means that the REC model used for an individual fit can sometimes satisfy the description of the ground multiplet M_J sublevels via a set of CFPs that does not coincide with the ones determined using information from the whole set of excited states. In contrast, the collective solution takes advantage of the implicit evolution of the CFPs along the series of later lanthanides using the equations presented in Chapter 2, offering a more adequate description

of the ligand field effects of the donor atom (chlorine in this case), as well as a good starting point for further phenomenological fittings.

Table 5.2: Systematic D_r and Z_i calculation from fitting of the experimental ground multiplet energy levels and the reported CFPs for the 10 complexes coordinated by chlorides studied in this section.

	Ln^{3+}	**Energy levels individual fit**		**CFPs individual fit**	
		D_r	Z_i	D_r	Z_i
$Cs_2NaYCl_6:Ln^{3+}$	Tb^{3+}	0.45	0.99	0.74	0.57
	Dy^{3+}	0.73	0.53	0.68	0.57
	Ho^{3+}	0.98	0.23	0.92	0.38
	Er^{3+}	0.85	0.39	0.96	0.33
	Tm^{3+}	1.49	0.04	0.95	0.35
	Collective	**0.86**	**0.36**	**-**	**-**
$LaCl_3:Ln^{3+}$	Tb^{3+}	1.16	0.14	1.32	0.10
	Dy^{3+}	1.23	0.13	1.27	0.13
	Ho^{3+}	1.20	0.18	1.26	0.15
	Er^{3+}	1.30	0.12	1.26	0.14
	Tm^{3+}	1.29	0.15	1.26	0.15
	Collective	**1.25**	**0.14**	**-**	**-**

Analogously to the results reported for fluorides, the Stark sublevels of each compound are calculated using the collective REC parameters of each family. The calculated energy level scheme is plotted together with the observed optical transitions measured at low temperature in Figure 5.5. For visual simplicity, in the plot we are not distinguishing between singlets, doublets, triplets or quadruplets.

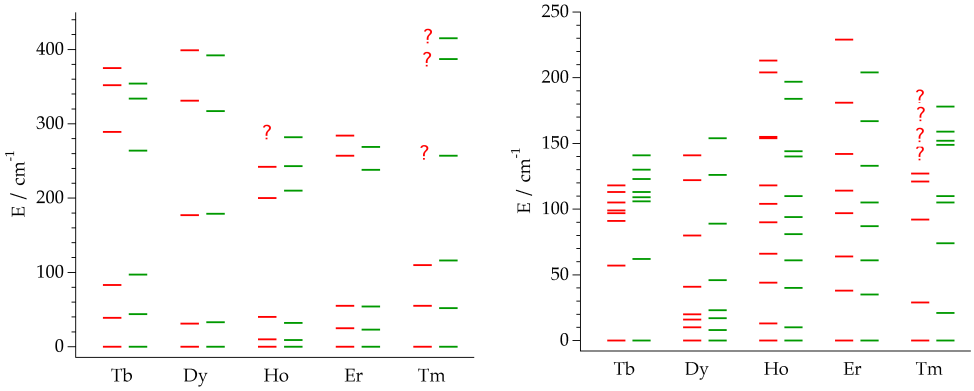

Figure 5.5: Experimental ground multiplet energy levels (red) and calculated ones using the collective fitting value for D_r and Z_i (green) in $Cs_2NaYCl_6:Ln^{3+}$ (left) and $LaCl_9:Ln^{3+}$ (right); non-determined levels are marked with the question mark.

This picture remarks the capacity of this simple model to describe the spectroscopic properties of a set of ground multiplet energy levels for these two families of lanthanide complexes coordinated by chlorine atoms. As the error is weighted inversely to the level energy (Equation 5.1), the agreement between theory and experiment is particularly good for the lower excited states. The distribution of these levels and the total crystal field splitting is also reproduced.

To put the potential of the REC model in perspective, it is useful to compare a selected example with the crystal-field energy levels that can be obtained using the PCEM. For that, we chose the Er derivative of the $Cs_2NaYCl_6:Ln^{3+}$ series, where all the Stark sublevels are spectroscopically determined and most of them are placed under 100 cm^{-1}. The ground state has quadruple degeneracy and the first excited doublet is located at 25 cm^{-1}. The total crystal field splitting is of 284 cm^{-1}.

The calculations using the PCEM were performed using the atomic coordinates: a perfect octahedron of six point charges placed at 2.57 Å of

the lanthanoid. The value of the charges where set to 1, according to the formal charge of chlorides. This resulted in B_{40} = 476.8 cm^{-1} and B_{60} = 21.8 cm^{-1}, which are clearly different to the CFPs obtained with the REC model for this complex using the collective fit (B_{40} = 1380.0 cm^{-1} and B_{60} = 140.8 cm^{-1}) and the phenomenological CFPs determined by Tanner (B_{40} = 1492 cm^{-1} and B_{60} = 163 cm^{-1}).[301] The effects of the two parameters of the REC model over the basis of the PCEM yield a ratio B_{40}/B_{60}(REC) = 9.8, which is pretty similar to the phenomenological fit, B_{40}/B_{60}(FIT) = 9.15, especially if we compare with the one obtained by the PCEM, B_{40}/B_{60}(FIT) = 21.9. Of course, the difference in the ratio B_{40}/B_{60} between the PCEM and the phenomenological determination has severe consequences in the energy level scheme. The PCEM predicts and scheme formed by 4+4+2+2+4 energy levels. On the contrary, the experiment and the REC model indicate a 4+2+4+2+4 scheme, as it is illustrated in Figure 5.6:

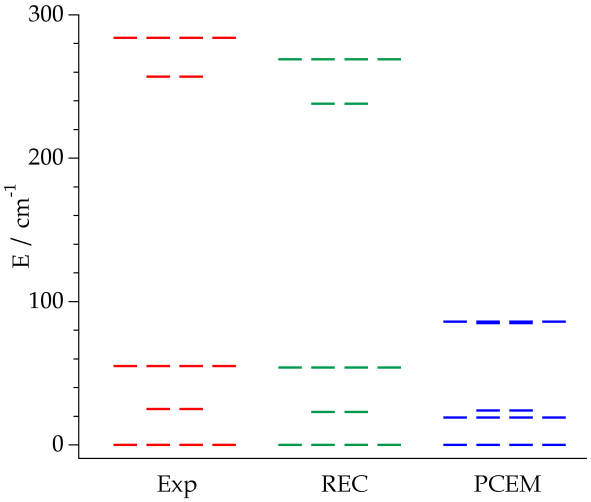

Figure 5.6: Experimental (red) and theoretical ground multiplet energy level scheme calculated by the REC model (green) and the PCEM (blue) for $Cs_2NaYCl_6:Er^{3+}$.

5.3 Comparison between calculated CFPs and phenomenological CFPs

Now, we can move on to perform a comparison between (a) the crystal field parameters calculated in the SIMPRE package, using the real structures and the REC parameters determined by the collective fits reported in this chapter, and (b) the phenomenological crystal field parameters used by spectroscopists in previous works, which fit all the available spectroscopic data.[298–302] When applying the REC model, the CFPs are varied indirectly because they result from the effective coordinates that are modified according to the model. Thus, for each set of coordinates, a set of CFPs emerges as an output. Differently, the non-negligible CFPs for each point group, which are extracted by the spectroscopists, are scanned directly in order to obtain the set that describes better the data. As in the REC approach the information from excited states is not considered, it is necessary to compare the results with each set of phenomenological CFPs.

The evolution of the B_{20}, B_{40} and B_{60} CFPs in Wybourne notation for each family of compounds are plotted in Figures 5.7-5.9. Note that for the two trivalent lanthanide elpasolite lattices B_{20} is equal to 0, due to the octahedral symmetry, which cancels this term. As one can observe, the calculated CFPs using the REC model are in the same magnitude order that the ones extracted directly from the experiment and the agreement is, in general, very good. This reflects that this strategy overcomes the inherent limitations of the PCEM, obtaining a set of CFPs compatible with the phenomenological ones, and in particular obtains the correct ratios between CFPs. Furthermore, this comparison demonstrates the potential of the REC

model for the obtaining of an initial set of CFPs that can be used for a fitting of the energy level scheme including excited states.

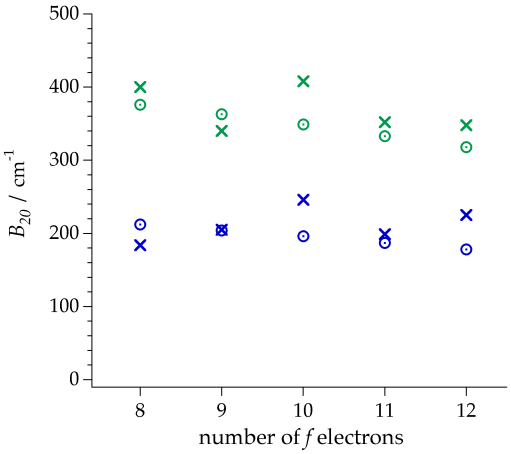

Figure 5.7: Phenomenological (crosses) and calculated B_{20} (open circles) in Wybourne notation, using the collective fitting value for D_r and Z_i, in $LiYF_4$: Ln^{3+} (green) and $LaCl_3$:Ln^{3+} (blue).

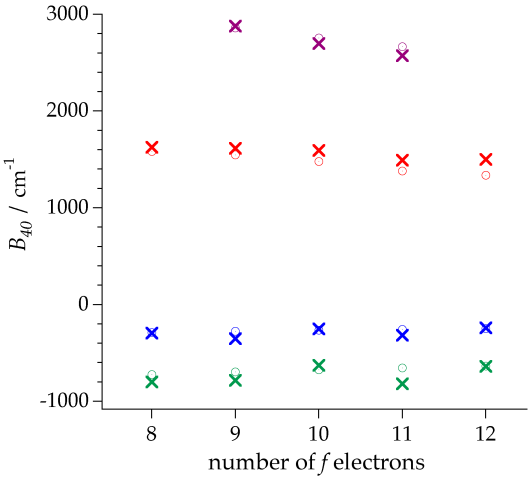

Figure 5.8: Phenomenological (crosses) and calculated B_{40} (open circles) in Wybourne notation, using the collective fitting value for D_r and Z_i, in Cs_2NaYF_6:Ln^{3+} (purple), $LiYF_4$:Ln^{3+} (green), Cs_2NaYCl_6:Ln^{3+} (red) and $LaCl_3$:Ln^{3+} (blue).

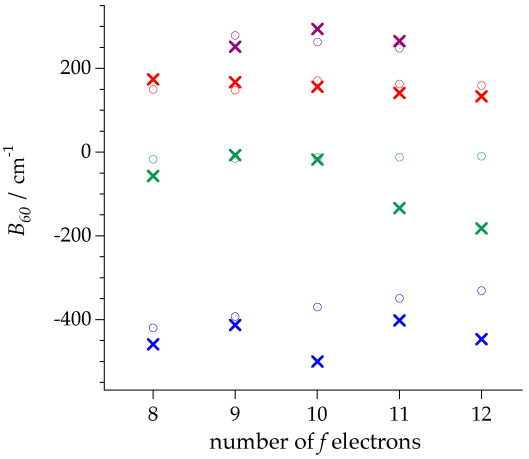

Figure 5.9: Phenomenological (crosses) and calculated B_{60} (open circles) in Wybourne notation, using the collective fitting value for D_r and Z_i, in Cs_2NaYF_6:Ln^{3+} (purple), $LiYF_4$:Ln^{3+} (green), Cs_2NaYCl_6:Ln^{3+} (red) and $LaCl_3$:Ln^{3+} (blue).

5.4 Relation of the REC parameters with Pauling electronegativity and coordination number

The results of every individual fit, taken together with the collective fits for each family, reveal at first glance some trends that can be related both with the Pauling electronegativities of the ligands and with the coordination numbers (see Figure 5.10). For instance, for a given coordination number (CN), e.g. CN=6, D_r is higher for the ligand with a lower electronegativity ($E_{Cl} < E_F$). Additionally, for a given donor atom, D_r is higher for a higher coordination number. This is verified both for F^- and Cl^-. This means that as far as the coordination number increases, the effective charges are placed closer to the lanthanoid. On the other hand, a more electronegative donor atom requires a weaker covalent correction, and thus the effective charge will be less displaced from the crystallographic position of the ligand.

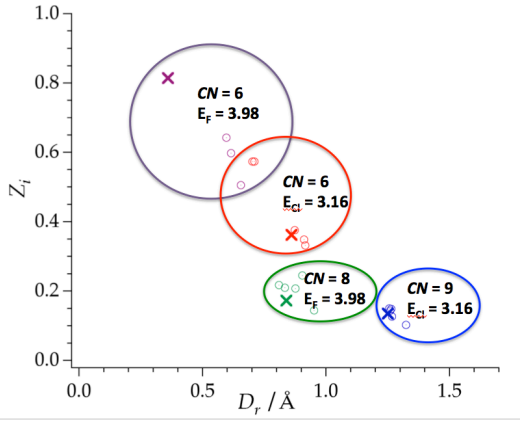

Figure 5.10: D_r and Z_i parameters obtained for each CFPs individual fit (open circles), collective fitting of the energy levels (cross) for the families $Cs_2NaYCl_6:Ln^{3+}$ (red), $LiYF_4:Ln^{3+}$ (green), $LaCl_3:Ln^{3+}$ (blue) and $Cs_2NaYF_6:Ln^{3+}$ (purple).

If the REC model is to be used as a predictive starting point as stated above, one needs to go beyond these qualitative arguments and search for an empirical mathematical relation. We found that the collective fits of the different families studied in this chapter are compatible with the following approximate relation[296] between the radial displacement (D_r), the coordination number (CN), the valence of the metal (V_M) and the Pauling electronegativities of the ligand and of the metal (E_L and E_M, respectively):

$$D_r \approx \left(\frac{CN}{V_M}\right) \cdot \frac{1}{E_M(E_L - E_M)} \qquad (5.3)$$

Table 5.3 allows a comparison between the approximation offered by Equation 5.3 and the collective fit of the ground multiplet energy level scheme of each family. Also, in Table 5.3, the averages of the D_r obtained

within the individual fits of the four families, based on ground multiplet energy levels and crystal field parameters, are reported.

Table 5.3 D_r (Å) estimated either from Equation 5.3, by a collective fit of each family or as an average of the individual fits of the energy levels and of the CFPs. (*): see text.

	Eq. 5.3	**Collective fit**	**Fit energy levels (ave.)**	**Fit CFPs (ave.)**
Cs_2NaYF_6:Ln^{3+}	0.6	0.51 (*)	0.57 (*)	0.57 (*)
$LiYF_4$:Ln^{3+}	0.8	0.84	0.8	0.88
Cs_2NaYCl_6:Ln^{3+}	0.85	0.86	0.90	0.85
$LaCl_3$:Ln^{3+}	1.28	1.25	1.24	1.27

As can be observed, the agreement is reasonable for the four families. Note that for the Cs_2NaYF_6:Ln^{3+} family, marked with (*) in Table 5.3, the collective fit uses only the data of Ho^{3+} and Er^{3+},[302,303] and this value is expected to change if more derivatives are taken into account.

Regarding the obtained effective charges of these complexes, an inverse proportional relation respect to the D_r values may be observed in both fluoride and chloride-based families (Figure 5.11). As we will see through the results presented in this Ph.D. thesis, this is indeed a general trend in all the systems fitted using this model: as far as the effective charge is getting closer to the lanthanoid ion, its value decreases (Figures 5.2 and 5.4). The reason for this is obvious: if a solution is already in the right parameter region, pushing the charges closer to the metals and simultaneously rising their effective values will produce a completely incorrect total crystal field splitting. In Figure 5.11, we have plotted the individual D_r and Z_i values obtained when fitting the ground multiplet sublevels, the ones obtained when fitting the CFPs directly and the lowest

relative error combination that describes the ground multiplet energy levels of the whole series. As an approximation, the following relation can be extracted:

$$f_{X,CN} = D_r \cdot Z_i \tag{5.4}$$

where f is a factor which depends on the coordination number and on the coordinated atom (X).

The resulting values of $f_{X,CN}$ are calculated using the REC parameters of the collective fit. Such values are: $f_{F,6}$ (CN=6) = 0.434, $f_{F,8}$ (CN=8) = 0.144, $f_{Cl,6}$ (CN=6) = 0.311 and $f_{Cl,8}$ (CN=9) = 0.169. For the two pairs of families coordinated by fluorides and chlorides, the relations $Z_i = f_F / D_r$ and $Z_i = f_{Cl} / D_r$ are calculated keeping the averaged $f_F = (f_{F,6}+f_{F,8})/2$ and $f_{Cl} = (f_{Cl,6}+f_{Cl,9})/2$ constant. These functions are represented by the dashed black lines in Figure 5.11. They are an approximation of the inverse relation empirically determined that exist between the two parameters of the REC model.

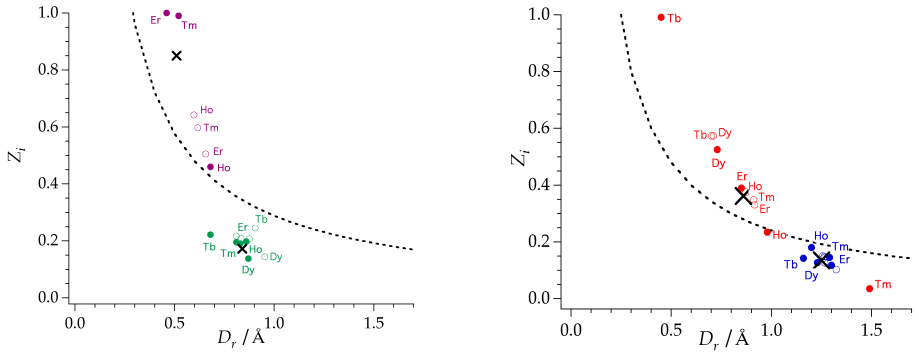

Figure 5.11: Radial displacement (D_r) and effective charge (Z_i) values obtained fitting the ground multiplet energy levels (circles) and CFPs (open circles); (left) Cs_2NaYF_6:Ln^{3+} (purple) and $LiYF_4$ $^{3+}$ (green); (right) Cs_2NaYCl_6:Ln^{3+} (red) and $LaCl_3$:Ln^{3+} (blue). Collective fit (black cross). Function $Z_i = f_X / D_r$.

Assuming the relations 5.3 and 5.4 presented in this chapter are not specific for fluorine and chlorine, they would allow an initial estimation of the CFPs, energy levels, magnetic and optical properties for homoleptic later lanthanide complexes when working in absence of experimental data.[296] In principle, we will assume that they should work better for ligands with a marked ionic character. Moreover, they can be especially useful to obtain an initial trial of CFPs for spectroscopic studies in f-element complexes using the full Hamiltonian. Also, the calculated REC parameters can be used as inexpensive initial values for D_r and Z_i in the fitting procedures when modelling the properties, either spectroscopic or thermodynamic, of this kind of systems.

For perspective, it is worth to compare the approximations presented in Equations 5.3 and 5.4 with previous efforts by other researchers towards the same direction. There are several similarities between the estimation of the effective charge by Zolnierek in 1984, where a modified point-charge model was presented, and the present one.[307] In both approaches, the effective charge:

(a) is directly proportional to the valence of the metal

(b) is inversely proportional to the number of ligands

(c) goes to zero as the electronegativity of the ligand approaches the electronegativity of the metal

(d) can be written as a negative number plus a term that depends linearly on the electronegativity of the ligand.

Furthermore, in a recent work by Tanner *et al.*,[308] (c) is exactly true and (d) is approximately true if one considers small differences in electronegativity, as one then can look at the linear approximation of a negative Gaussian function. As Ref. 308 considers a constant radius depending only on the metal ion, it also supports the proportionality

between the radial displacement and coordination number. This means that crystallographic radii increase with the coordination number, thus a rising radial displacement is needed to compensate for this if an invariant effective radius is to be obtained.

5.5 Conclusions

In this chapter, 18 different compounds where a lanthanide is coordinated by halides have been modelled. The collective fit using two parameters for each of the four families have provided a good reproduction of the measured energy levels in all cases. The comparison with the PCEM in the study of $Cs_2NaYCl_6:Er^{3+}$ shows how the covalent correction and the attributed effective charge can improve significantly the description of the properties of a lanthanide complex. The CFPs calculated using the collective fit of the REC parameters to the Stark sublevels are also in a reasonable agreement with the ones extracted by a fitting of the REC parameters to the phenomenological CFPs. This systematic study demonstrates that one can keep the simplicity of the electrostatic model but reproducing experimental properties with a fair accuracy.

The collective study of the four isostructural families has allowed the extraction of two approximative equations that permit an estimate of the Radial Effective Charge model parameters by relating them to chemical concepts such as Pauling electronegativity and the coordination number. The parameters obtained with these equations are expected to be a very useful tool to address the widespread need for an inexpensive estimation of a starting parameter set in more sophisticated CF determinations, as well as a route for an inexpensive qualitative prediction of the magnetic properties of f-block compounds.

Of course, one expects that the calculated REC parameters will be closer to the actual ones in complexes coordinated by ionic donor atoms (like halides) with coordination numbers between six and nine, being less exact for oxygen donor atoms and offering worse predictions for complexes coordinated by nitrogens or organometallic compounds. It is also important to note that the compounds presented in this chapter are all homoleptic. Thus, an open problem is to deal with heteroleptic complexes (as will be described in Chapter 10). However, in any case, the aforementioned equations offer a starting point for a more accurate description of these systems.

6 Lanthanide complexes coordinated by oxygen atoms

In this part of the thesis, we are going to continue with the application of the Radial Effective Charge model to mononuclear lanthanide homoleptic complexes. In this case, we will describe the properties of different families of lanthanide compounds coordinated by oxygen atoms. This is a relevant test of the REC model, since stable rare earth compounds coordinated by oxygen-donor ligands are very common in coordination chemistry, trivalent ions being "hard" acceptors.[309] Unlike the systems presented in the previous chapter, for most of the examples described here there is no high-quality spectroscopic information available up to now. Thus, for their rationalisation, we are forced to be restricted to magnetic susceptibility experimental data. The employed procedure will aim to predict the magnetic properties of similar derivatives of the same families and to get some clues for the discovery of new complexes with SMM behaviour. To facilitate this task, the parameters obtained throughout the work will be integrated in the general library of ligands developed during this thesis, that parameterises the most common ligands in terms of the REC model.[310]

The first three subsections (6.1, 6.2 and 6.3) will deal with eight-coordinated polyoxometalate (POM) compounds. As potentially nuclear spin free systems offering different rigid and highly symmetrical coordination environments, POMs are in a nearly unique position for the

design of both SIMs and model spin 1/2 systems (spin qubits), minimising decoherence and unwanted relaxation processes.[58] In these examples, the REC parameters are extracted by a collective fitting of the magnetic properties of derivatives with a similar oxo-based coordination environment. In 6.4, we will proceed with the analysis of a nine-coordinated oxydiacetate family, where the analysis of existing spectroscopic data stimulated the synthesis of the Er and Dy derivatives, obtaining field-induced slow relaxation of the magnetisation in both of them. The experimental data will enable the benchmarking of the capabilities of the REC model in systems coordinated by oxygen donor atoms. We will also include *ab initio* calculations in the description of these oxydiacetate-based compounds, critically discussing the limitations of each approach. The subsection 6.5 will include the study of two layered dysprosium hydroxides, revealing single-molecule magnetic behaviour with slow relaxation processes ascribed to the different Dy sites.[311] This investigation puts into evidence the evolution from to single ion towards 2D and 3D interaction effects between dysprosium ions. Before the conclusions, this chapter will include the description of the first example of a metal-organic framework (MOF) having as nodes lanthanoid SIMs.[120] The synthesis of this SIM-MOF was guided by rational design using the SIMPRE computational package and the REC model.

6.1 Polyoxowolframates: series LnW_{10} and LnW_{22}

The characterisation of LnW_{10} and LnW_{22} permitted the description of the magnetic behaviour of the first two families of lanthanoid POM-based SIMs reported in the literature.[59,31262] In particular, the erbium derivative of the series LnW_{10} was the second example of a mononuclear SMM. The

magnetic theoretical characterisation offered useful additional information about the Stark sublevels and ground multiplet wave functions.

Regarding the chemical structures, in both families the lanthanoid metal is encapsulated between two monolacunary polyoxometalate anions that act as tetradentate ligands. They present a square antiprismatic environment around the Ln^{3+} centre, with a near D_{4d} symmetry (Figure 6.1). In complexes $[Ln(W_5O_{18})_2]^{9-}$ (short: LnW_{10}, where Ln = Tb, Dy, Ho and Er, each anionic moiety is twisted 44-45º with respect to the other, whereas in $[Ln(\beta_2\text{-}SiW_{11}O_{39})_2]^{13-}$ (short: LnW_{22}, where Ln = Tb, Dy, Ho, Er, Tm and Yb, they display a more pronounced distortion, with a rotation angle between the two moieties of about 41º.

To quantify the deviation of both real structures from the ideal square antiprism, the SHAPE software was used, where a Continuous Shape Measure S_P is mathematically defined in a way that is independent of the size and orientation of the system.[288] By definition, the resulting value of S_P is zero when the real coordinates of the metal site (problem structure, P) show exactly the desired ideal shape. Then, S_P increases with the degree of distortion of the structure. According to the manual of the program, values below 0.1 represent chemically insignificant distortions in the structure. Values larger than 3 mean important distortions, with the highest possible values in the order of 40. Using the corresponding idealised D_{4d} square antiprism as target structure, one obtains values of S_P = 0.047 for the Er derivative of the family LnW_{10} and S_P = 0.122 for ErW_{22}. In both cases we have used the atomic coordinates of the erbium derivatives. Here it is important to note that although these calculated S_P values mean chemically insignificant structural distortions in ErW_{10} and slight distortions in ErW_{22}, the non-exact ideality of the structures yield all possible terms of the CF Hamiltonian. This occurs because the CFPs, calculated with the expressions

2.1, cannot be cancelled if the chemical structure deviates (even a few degrees) from the point group. These distortions from the point group symmetry are the responsible of the mixing in the wave functions.[122] Moreover, they can generate non-negligible tunnelling splitting in the non-Kramers derivatives. For example, a variation of only 3º in the twist angle can signify a difference of an order of magnitude between the HoW_{10} and HoW_{22} tunnelling splittings.

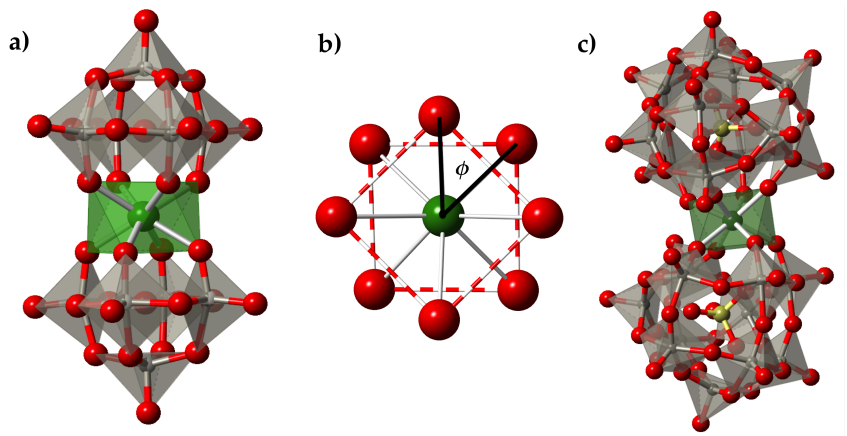

Figure 6.1: (a) Molecular structure of $[Ln(W_5O_{18})_2]^{9-}$; (b) view of its square antiprismatic coordination sphere, ϕ is the skew angle; (c) molecular structure of the series $[Ln(\beta_2\text{-}SiW_{11}O_{39})_2]^{13-}$.

As we may observe in Figure 6.1, a well-defined magnetic axis is expected for the different derivatives because of the near pseudo-axial symmetry of the compounds. Thus, in the calculations our coordinate system was referred aligned with the main symmetry axis of the square antiprism. As the eight oxygen atoms are chemically equivalent, a simultaneous fit of the magnetic susceptibility data of LnW_{10} and LnW_{22} from 2 to 280 K was performed. This substantially reduces the parameter space and allows an interpretation of the ligand field effects of

polyoxowolframates. A satisfactory fitting of the χT product was obtained when D_r = 0.895 Å and Z_i = 0.105 with a relative error of $E = 3.56 \cdot 10^{-3}$. The validity of these two REC parameters can be tested with the prediction of the magnetic susceptibility of TmW_{22} and YbW_{22}, which are described successfully with the same two parameters. As one can see, the agreement between the model and all the experimental data is excellent (Figure 6.2), even for the Tm^{3+} and Yb^{3+} derivatives which have been described with the same parameters and were not included in the collective fit.

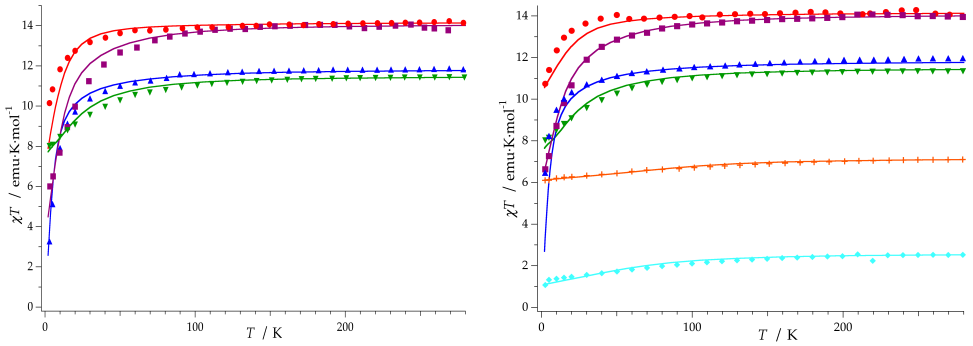

Figure 6.2: Fitting of the experimental χT product of the series of (left) $[Ln(W_5O_{18})_2]^{9-}$ and (right) $[Ln(\beta_2\text{-}SiW_{11}O_{39})_2]^{13-}$ using the REC model: Dy (●), Ho (■), Tb (▲), Er (▼), Tm(+) and Yb (◆). Markers: experimental data; solid line: theoretical fit for Dy-Er and prediction for Tm and Yb.

The energy level schemes and ground state descriptions of the ten lanthanide-based polyoxowolframate complexes modelled in this chapter are reported in Figures 6.3 and 6.4. It is remarkable the difference between the most compact description of the Tb and Er derivatives in both families. In the case of Tb, a diamagnetic ground state (98% of $M_J = 0$) is obtained, whereas a 99% and 98% contribution of a high M_J value (±13/2) in ErW_{10} and ErW_{22} explains the SMM behaviour exhibited by both analogues. The

measurement of the tunnelling splitting of the HoW_{10} by Hill *et al.*,[313] with a value of 0.3 cm^{-1}, permitted to study the more probable distortions at low temperatures which are compatible with this value.

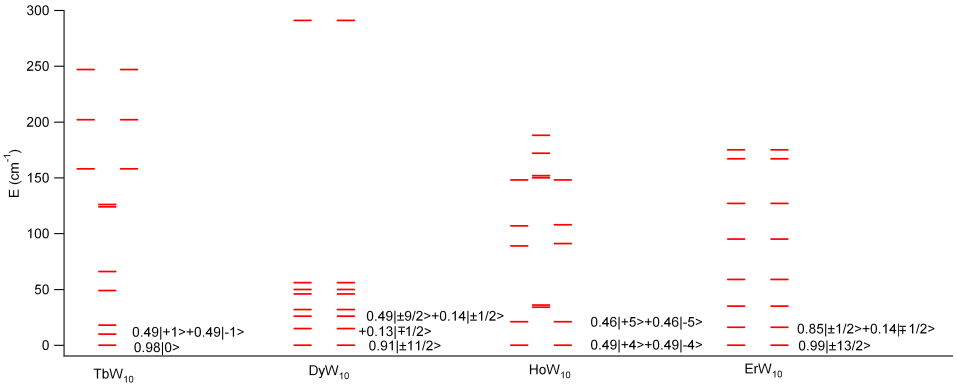

Figure 6.3: Energy level scheme and main contributions to the wave function for the ground and first excited states for $[Ln(W_5O_{18})_2]^{9-}$

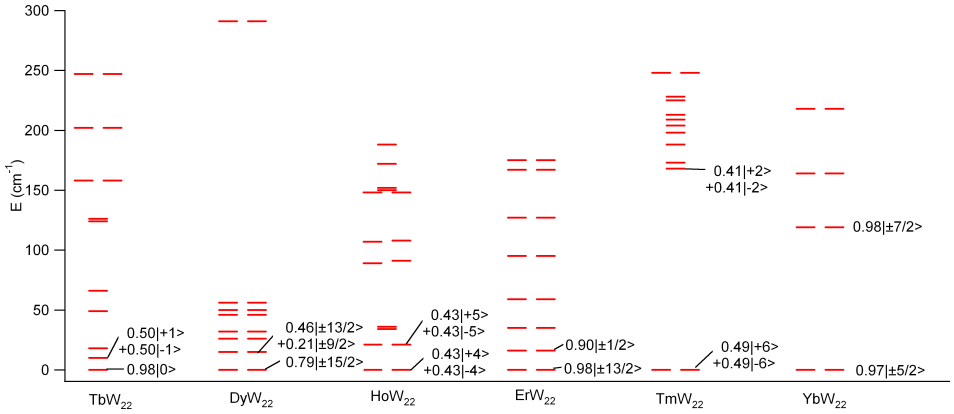

Figure 6.4: Energy level scheme and main contributions to the wave function for the ground and first excited states for $[Ln(\beta_2\text{-}SiW_{11}O_{39})_2]^{13-}$

To have a closer look, the energy level schemes and main contributions to the wave functions of compounds ErW_{10} and YbW_{22} are shown in Figure 6.5. One may observe the high contribution of a high M_J in both cases (99% of ±13/2 and 97% of ±5/2 for ErW_{10} and YbW_{22} respectively), which are compatible with the SMM behaviour reported in the work of AlDamen *et al*.[62] It is worth to mention that in the case of ErW_{10} the calculated first excited state yields at 16 cm^{-1}, whereas the experimental one, which was determined by EPR and specific heat, is located at 17 cm^{-1}.[218] This description improved the previous explanation[62] of the CF splitting of the ErW_{10} compound, where the first excited level (with a main contribution of ±1/2) was placed at 2 cm^{-1}.

In a second step, the possibility of having novel SIMs in other derivatives of these two series was explored. The SIMPRE package was acting as a spyglass and the most promising results were identified for NdW_{10}.[314] Then, the real structure of the Nd derivative and the REC parameters obtained in the study of both polyoxowolframate families were combined to obtain a prediction of the energy level scheme and the contributions to the wave functions (Figure 6.5). The theoretical calculations describe a ground state with 95% of contribution of M_J = ±5/2, which is very similar to the mononuclear SMM YbW_{22}. Furthermore, the main M_J contribution to the ground state wave function of NdW_{10} coincides with the one of the first Nd-based single-ion magnet reported by Long *et al*. in 2012.[88] This encouraged us to prepare the sample and measure its properties. With this objective, we had a meeting at the end of 2013 with Yan Duan, a Ph.D. student at ICMol with experience in the synthesis of polyoxometalates. She proceeded with the synthesis and magnetic characterisation of this derivative.

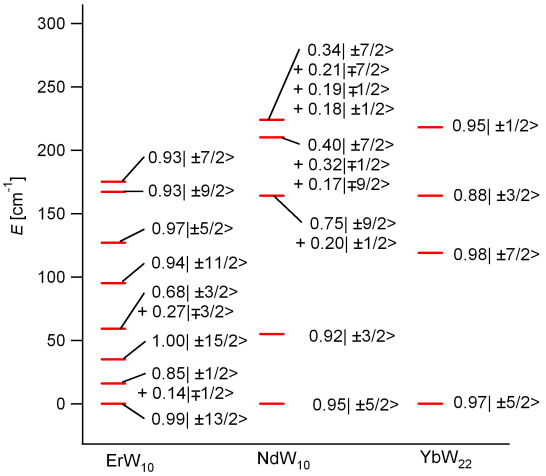

Figure 6.5: Energy level schemes and main M_J contributions for ErW_{10}, NdW_{10} and YbW_{22}. Note that all levels are Kramers doublets.

The magnetic measurements were performed by José M. Martínez Agudo on previously ground crystals of NdW_{10} in the range 2-300 K with an applied field of 1000 Oe. Alternate current (*ac*) data were collected in the range 2-15 K with an applied alternating field at different frequencies in the range 1500 – 10000 Hz, detecting a maximum that was varying with the frequency.

The temperature dependence of the χT was successfully predicted.[310] The results of this thermodynamic property are plotted and compared with the experimental results in Figure 6.6. An almost perfect agreement may be found between the prediction and the experiment, showing the great possibilities that this strategy can provide to the community by checking new candidates with interesting properties.

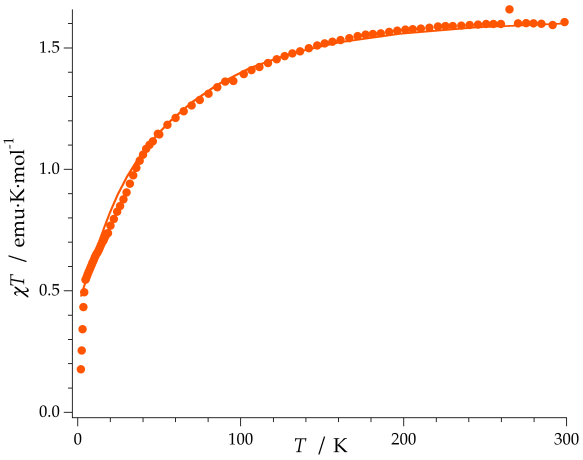

Figure 6.6: χT product of NdW_{10}. Circles: experimental data, solid line: theoretical prediction using the REC model.

The *ac* magnetic properties reveal the typical features associated with SMM behaviour for a system with some mixture and thus the possibility of avoided hyperfine crossings and quantum tunnelling (Figure 6.7). Thus, in the absence of a *dc* field there is a weak frequency-dependent signal in χ'' but no clear χ' signal. When applying an external field of 1000 Oe, the system is taken beyond the hyperfine crossing region and as a result both χ' and χ'' show strong frequency dependencies, which indicate the presence of a slow relaxation process involving an energy barrier for the reversal of the magnetisation. Depending on the frequency of the applied *ac* field, χ' presents a maximum between 6.8 and 7.9 K, while χ'' has also a maximum between 5.9 and 6.9 K for 1500 and 10000 Hz, respectively (Figure 6.7 (right)).

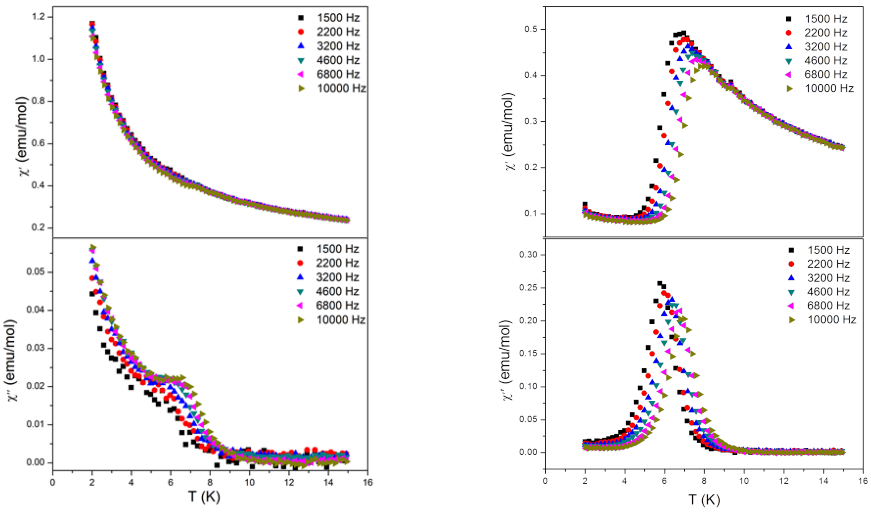

Figure 6.7: In-phase (top) and out-of-phase (down) dynamic susceptibility of NdW_{10}: without an external field (left), and with an applied field of 1000 Oe (right). The frequencies are shown in the legend.

Analyses of the frequency dependence of the χ'' peaks through an Arrhenius plot allowed the estimation of the magnetisation-relaxation parameters in this system (Figure 6.8).[310] The best fitting affords a barrier height (U_{eff}) of 51.4 cm^{-1} with a pre-exponential factor (τ_0) of $3.55 \cdot 10^{-10}$ s. Given the good insulation of the Nd^{3+} ions provided by the diamagnetic polyoxowolframate framework (the shortest Nd⋯Nd distance is 11.221 Å), the slow relaxation process exhibited by the complex should be considered as a single-molecule property.

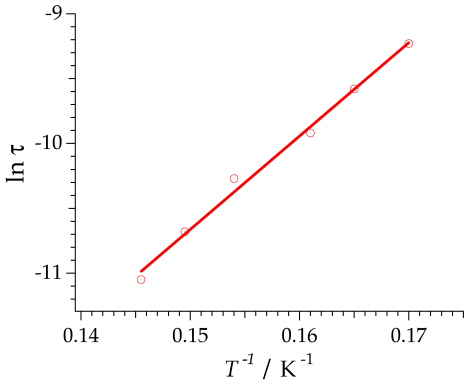

Figure 6.8: Relaxation-time fitting to the Arrhenius law in the 1500-10000 Hz interval for NdW_{10}.

6.2 Polyoxomolybdates: series $LnMo_{16}$ and $LnMo_{10}$

The chemical similarity of the coordination environment of the two families of polyoxowolframates rationalised in the preceding section motivated us to study the magnetic properties of polyoxomolybdates encapsulating lanthanides.[315] An interesting aspect compared with the series LnW_{10} and LnW_{22} is the possibility of making them more easily reducible by one or more electrons, allowing the coexistence of localised f electrons with a number of delocalised d electrons. As has already been demonstrated with transition metal ions, this kind of systems are unique model systems which favour the appearance of novel phenomena and possibilities in nanotechnology.[316]

The first family under study was prepared by Dr. Salvador Cardona-Serra and Yan Duan, supervised by Dr. Carlos Giménez-Saiz, by reacting $[(n\text{-}C_4H_9)_4N]_4[Mo_8O_{26}]$ with lanthanide nitrate salts. The rare earths metals, which are highly oxophilic, were connecting two $[\beta\text{-}Mo_8O_{26}]^{4-}$ moieties to

produce a new family of polyoxomolybdate-based mononuclear single-molecule magnets formulated as $[Ln(Mo_8O_{26})_2]^{5-}$ (with Ln = Tb, Ho, Dy, Er, Yb and Tm) (Figure 6.9). One example of this kind, encapsulating a diamagnetic ion (La^{3+}), had previously been reported by Ozeki, Yagasaki *et al.*,[315] demonstrating the synthetic feasibility of this proposal. Unlike the previous series of heteropolyoxowolframates, this new series of heteropolyoxomolybdates is soluble in organic solvents. This means that besides the possibility of reduction, the change in the main metal of the polyoxometalate opens new paths for processability. This will allow the preparation of hybrid materials that may combine both SMM behaviour and other properties like conductivity, optical activity and spin-crossover.[317,318]

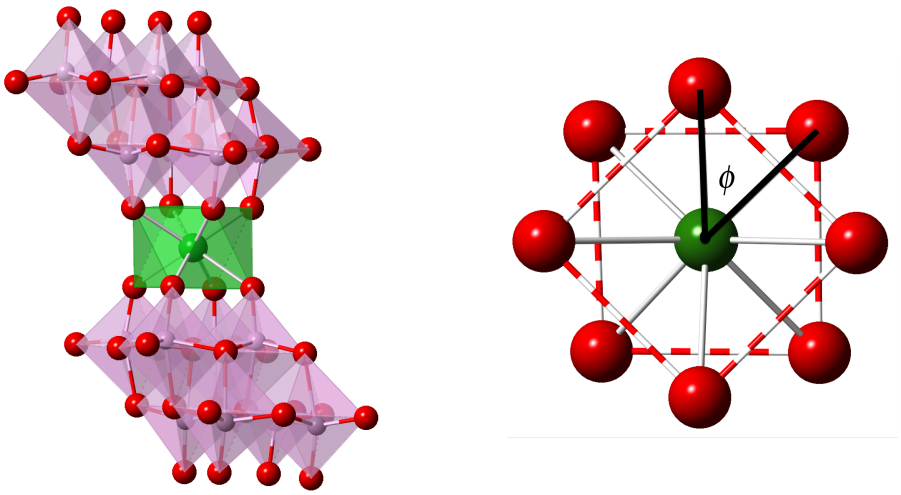

Figure 6.9: (left) Molecular structure of $[Er(Mo_8O_{26})_2]^{5-}$ and (right) projection of the first coordination sphere showing the square antiprismatic coordination site. ϕ is the skew angle.

According to the results from X-ray diffraction measurements, this family of compounds crystallise in two different space groups: monoclinic

($P2_1/c$) for Tb^{3+} and orthorhombic (*Pbca*) for the rest of the series. Because of the rigidity of the polyoxometalate, this difference in the crystallography is in practice not noticeable in the vicinity of lanthanide ion: in all cases, the structure exhibits the presence of a lanthanide ion sandwiched between two $[\beta\text{-}Mo_8O_{26}]^{4-}$ units. The octamolybdate unit is composed of two Mo_4O_{13} subunits stacked together by relatively elongated molybden-oxygen bonds. The lanthanide ions which are bonded to the terminal oxygen atoms of the two octamolybdate units show eight-fold square antiprismatic coordination (Figure 6.9).

Magnetic static and dynamic measurements were performed in fresh powdered samples of $LnMo_{16}$. Those data were measured (by José M. Martínez-Agudo) between 2 and 280 K under an applied magnetic field of 1000 G with a commercial magnetometer equipped with a SQUID sensor. The four magnetic susceptibility curves of the Tb, Dy, Ho and Er polyanions were used to carry out a simultaneous fit based on the REC model. This procedure provided the two parameters that describe the ligand field effects of these eight chemically equivalent polyoxomolybdate ligands. The most satisfactory agreement with the experimental χT product was obtained when D_r = 0.72 Å and Z_i = 0.253. If we compare with the obtained parameters for the heteropolyoxowolframate family,[310] the radial displacement is smaller in this case. This means that the effective point charge needs a smaller covalent correction to produce an adequate relation between the CFPs that describe the experimental data. This difference can be related to the different Pauling electronegativity of the Mo and W atoms (2.16 and 2.36 respectively). The larger difference in E_M between Mo (2.16) and O (3.44) enhances the ionic character of oxygen as a donor atom to the lanthanide, decreasing the covalent character of the coordination bond, which results in smaller corrections: smaller D_r and larger Z_i. On the

contrary, a smaller difference in electronegativity between W (2.36) and O (3.44) diminishes the ionic character of oxygen as a donor atom to the lanthanide, increasing the covalent character of the coordination bond, which results in larger corrections: higher D_r and lower Z_i.

As done in LnW_{10} and LnW_{22}, the validity of the determined collective two parameters is tested with the application of them to the real coordinates of the Tm and Yb derivatives and comparison with the experimental results. The predicted magnetic behaviour shows an excellent agreement with the experimental data (Figure 6.10).

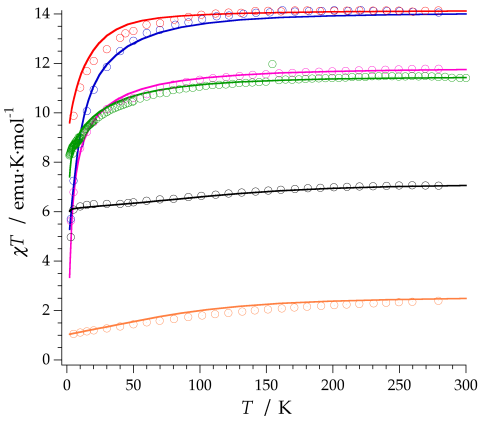

Figure 6.10: Fitting of the experimental product of the series $[Ln(Mo_8O_{26})_2]^{5-}$ using the REC model: Dy (red), Ho (blue), Tb (blue), Er (green), Tm (black), Yb (orange). Markers give experimental data, and the solid lines theoretical fits for Tb-Er and predictions for Tm and Yb.

The resulting energy levels are reported in Figure 6.11. A general trend for this family compared with the previous POM-based ones is the slightly larger crystal field splitting observed. This has to be understood as a more pronounced effect of the ligands as the average Ln-O distance is practically identical between ErW10 and $ErMo_{16}$ (2.367(7) Å and 2.367(3) Å).

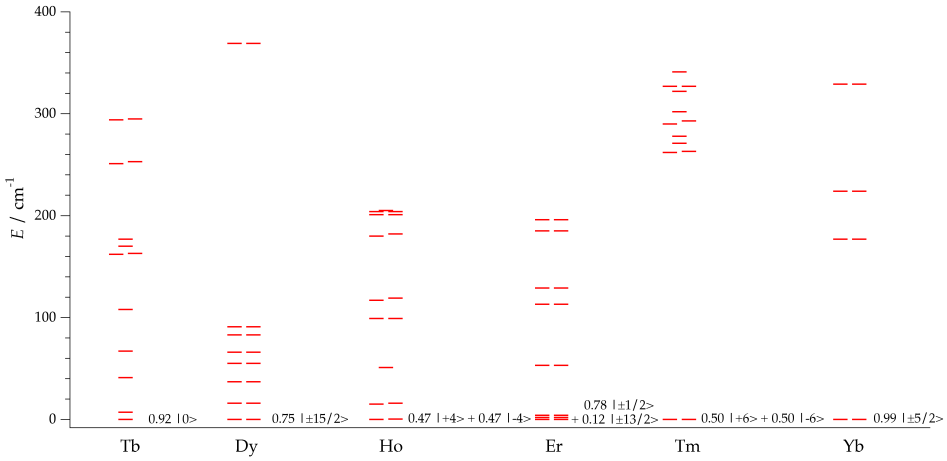

Figure 6.11: Energy level scheme and main contributions to the wave function of the ground state for $[Ln(Mo_8O_{26})_2]^{5-}$.

Ac measurements have been collected in the range 2-12 K with an applied alternating field of 3.95 Oe at different frequencies in the range 1-10000 Hz. In the case of the $LnMo_{16}$ family, the Er and Ho derivative show frequency dependent out-of-phase signals at very low temperatures. In neither complex a clear peak is observed even applying an external field of 1000 Oe. This feature is a characteristic of the fast relaxation process that take place at low temperatures. In any other derivative, there appears no increase in the out-of-phase signal down to 2 K (Proust, A., Coronado, E. *et al*. *In preparation*).

Subsequently, another series of mono-lanthanide containing polyoxomolybdates was synthesised by the group of Anna Proust in Paris. For that, they used the hybrid lacunary Lindqvist-type pentamolybdate $[Mo_5O_{13}(OMe)_4(NNC_6H_4\text{-}p\text{-}NO_2)]^{3-}$ as ligand.[319] The advantage of this approach is that the substitution of organic ligands in the POM opens an avenue for chemical functionalisation, and thus is a promising advance

towards functional molecule-based nanostructures. The coordination environment of the lanthanide in the thus prepared $[Ln\{Mo_5O_{13}(OMe)_4(NNC_6H_4\text{-}p\text{-}NO_2\}_2]^{3-}$ species (from now on: $LnMo_{10}$, where Ln = Tb, Dy, Ho, Er, Yb and Nd) is very close to that observed in the previously reported $[Ln(W_5O_{18})_2]^{9-}$, although polyoxomolybdate frameworks are known to be more flexible than polyoxowolframates. The chemical structures of the Tb, Ho and Er derivatives were also determined by X-ray. The crystal structures show the lanthanoid ion coordinated by eight oxygen atoms that are bonded to molybdene atoms. The POM complex is formed by two anionic $[Mo_5O_{13}(OMe)_4(NNC_6H_4\text{-}p\text{-}NO_2)]^{3-}$ moieties sandwiching the magnetic centre (Figure 6.12). These anionic clusters are surrounded by tetrabutylammonium cations, thus balancing the total charge of the system. Each anionic moiety is twisted around 44º ($TbMo_{10}$), 39º ($HoMo_{10}$) and 40º ($ErMo_{10}$) with respect to the other. In the case of the $LnMo_{16}$ family, the skew angle is about 40º for the Tb analogue and 44º for the Dy-Yb derivatives. As the ideal D_{4d} skew angle is 45º, the coordination site may be roughly described, as in previously studied cases, as slightly distorted square-antiprismatic. In a more detailed comparison with the families of polyoxowolframates exhibiting SMM behaviour, the skew angle ϕ of $TbMo_{10}$, $DyMo_{16}$, $HoMo_{16}$, $ErMo_{16}$, $TmMo_{16}$ and $TmMo_{16}$ is comparable with the measured one for ErW_{10} (44.2º), whereas the Ho and Er derivatives of $LnMo_{10}$, as well as $TbMo_{16}$, are more distorted, being comparable with the ErW_{22} derivative (41.4º). It is clear that there is so far no fine chemical control on the skew angle, which depends on a number of subtle crystal packing interactions.

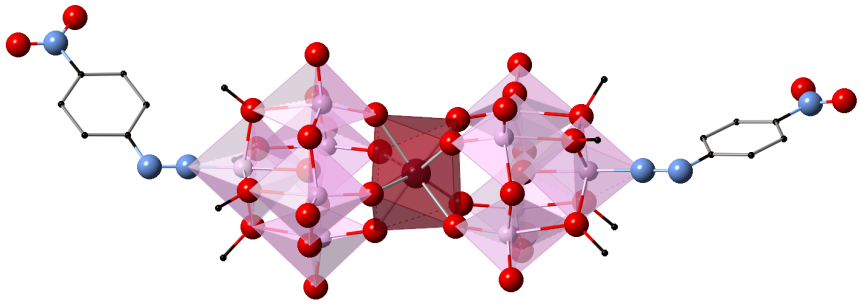

Figure 6.12: Structure of the $(TBA)_3[\{Mo_5O_{13}(OCH_3)_4(N_2C_6H_4\text{-}p\text{-}NO_2)\}_2Tb]$ POM.

At the time of our first contact with this family, we had not yet investigated the $LnMo_{16}$ derivatives with the REC model, and thus a quick first estimation of the possibility of obtaining SMM behaviour in some of the derivatives of this series was performed. Then, we used the REC model introducing the available crystal structures of the Tb, Ho and Er derivatives as input in SIMPRE, applying the two REC parameters (D_r = 0.895 Å and Z_i = 0.105) determined in 6.1 for the heterooxopolywolframate complexes. The prediction of the properties for the different derivatives illustrated the possibility of having SMM behaviour in the Dy derivative (95% of M_J = ±11/2). This was confirmed after the magnetic characterisation, where slow relaxation of the magnetisation in the Dy and Yb derivatives from the *ac* measurements was observed (Proust, A., Coronado, E. *et al*. *In preparation*).

Owing to the chemical similarity of the two families of polyoxomolybdates presented in this section, especially in the coordination environment and the kind of oxygen donor atoms, the parameters D_r = 0.72 A and Z_i = 0.253 obtained in the study of $LnMo_{16}$ were applied. This allowed the calculation of the CFPs, energy levels, wave functions and magnetic properties of this new family of polyoxomolybdates. The result of the χT product prediction is presented in Figure 6.13.

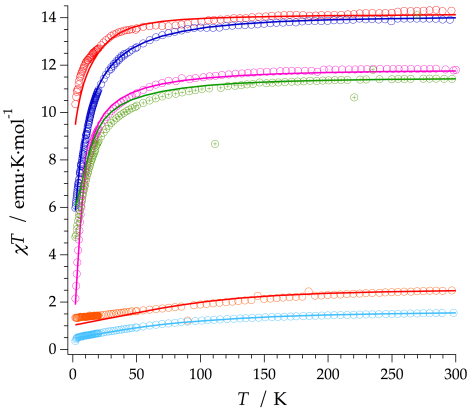

Figure 6.13: Experimental (circles) and predicted (solid lines) χT product of the series $LnMo_{10}$: Tb (pink), Dy (red), Ho (blue), Er (green), Yb (orange), Nd (sky blue) from 2 to 300 K.

One can observe that the agreement between the prediction and the experiment is excellent for the Tb, Ho and Nd derivatives, and the calculations reproduce quite well the magnetic susceptibility temperature dependence of Dy, Er and Yb. The calculated energy level scheme and the magnetisation of the different compounds are represented in Figure 6.14 and Figure 6.15, respectively.

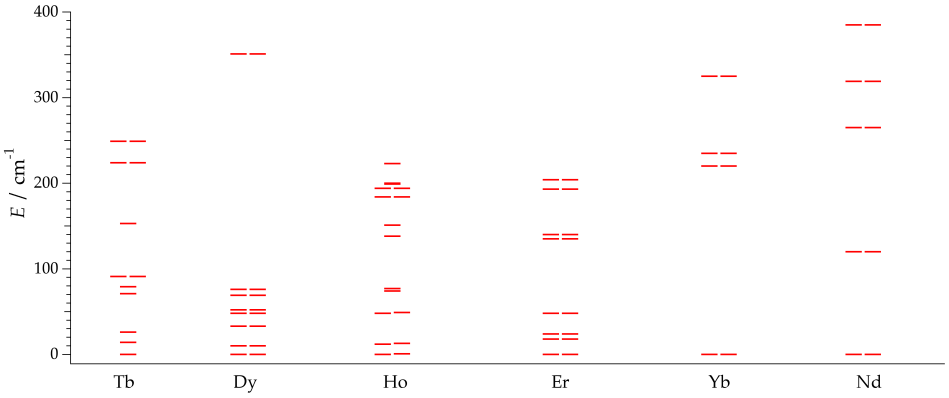

Figure 6.14: Calculated energy levels of the series $LnMo_{10}$.

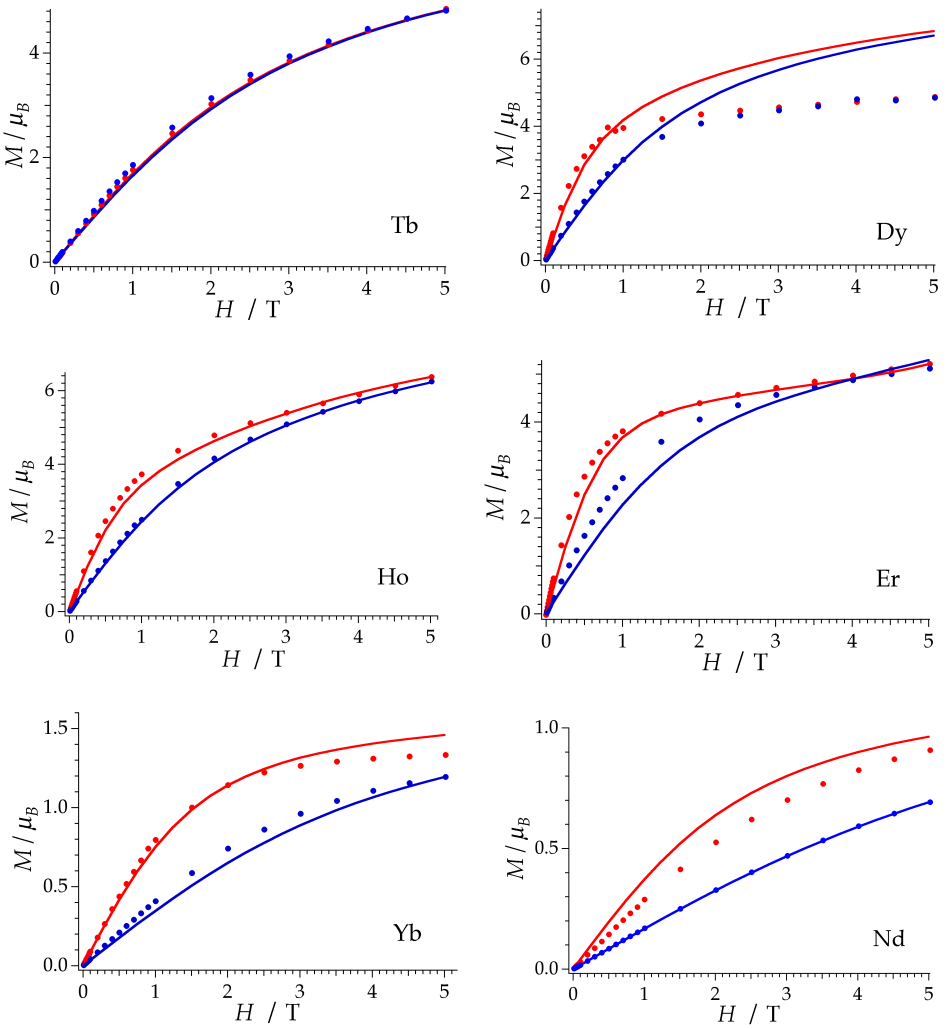

Figure 6.15: Experimental (circles) and predicted (solid lines) field dependence magnetisation of $LnMo_{10}$ at 2K (red) and 5 K (in blue) from 0 to 5 T.

The main deviation between experiment and theory is encountered for the Dy analogue in this case. This can be due to the proximity of the first excited state –about 10 cm^{-1} according to the prediction–, which can be

located at lower energy, contributing to the magnetisation at 2 K and 5 K under a magnetic field stronger than 1 T.

For a deeper analysis of the compounds exhibiting SMM behaviour in both families, in Figure 6.16, the Stark sublevels of the $HoMo_{16}$ and $ErMo_{16}$ derivatives are plotted and commented below.

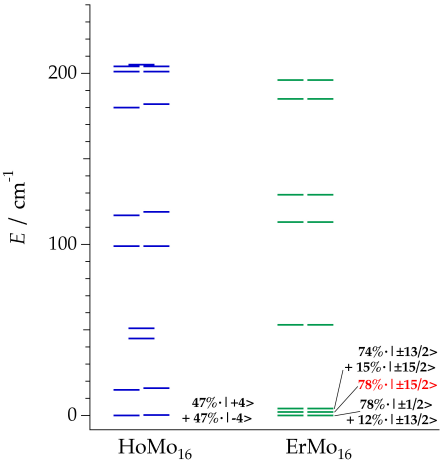

Figure 6.16: Energy level scheme and main contributions to the ground state wave function for the Ho and Er derivatives of $LnMo_{16}$.

Regarding the lower states wave functions, one can observe that in the case of the $HoMo_{16}$ the ground state is defined by a mixture of 47% of |+4> and 47% of |-4>. In this case, the crystal field operators correlate the projection of the moment and its inverse, thus concluding that in absence of an external magnetic field this wave function prevents the system to get blocked. Nevertheless when a transversal external field is applied, the purity of the M_J = +4 and M_J = -4 is recovered and the route to relaxation becomes more tough so the single molecule blocking is permitted. For $ErMo_{16}$ the wave function for the ground state appears to be M_J = 0.78|±1/2> + 0.12|±13/2> with a two very near states above it (at about 1.6

and 3.7 cm^{-1}). Those are described by $M_J = 0.78|\pm15/2>$ –marked in red in Figure 6.16– and $M_J = 0.74|\pm13/2> + 0.15|\pm15/2>$ respectively. The low energy difference between the ground and the first excited state (and even the second) is definitively below the precision of the method. Also, thermal effects over the chemical structure can slightly affect the energy level description, becoming significant at this level of proximity of the energy levels. So one can suggest, according to the experimental results, that the Kramers doublet described by 78% of $\pm15/2$ is the actual ground doublet. Within this assumption, the ground wave function would show a high M_J projection compatible with a single ion magnet property. The calculated energy level scheme of $DyMo_{10}$ and $YbMo_{10}$ (Figure 6.17) are represented as follows.

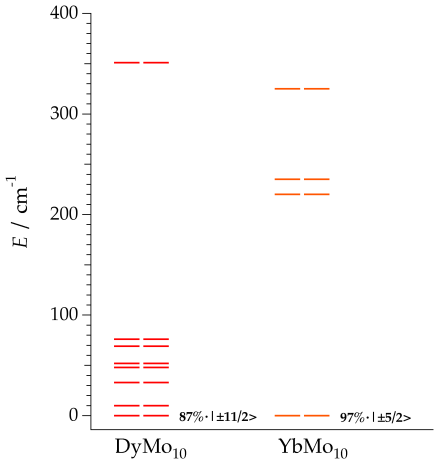

Figure 6.17: Calculated energy levels of the Dy and Yb derivatives of $LnMo_{10}$.

According to the REC prediction, $DyMo_{10}$ possesses a ground state dominated by $M_J = \pm11/2$ (87%) with an excited state of $M_J = 0.87|\pm9/2>$, which is placed at about 10 cm^{-1} above it. Such scheme is compatible with the observed SMM behaviour. One can notice that in this example all the M_J

states are bunched below 100 cm^{-1} with the exception of the highest M_J = 15/2 which is located at 350 cm^{-1}. In the case of $YbMo_{10}$, the level scheme is quite clear and the possibility of relating the ground-state wave function M_J = 97% of |±5/2> with the single-molecule property. The rest of the energy levels appear at 220 cm^{-1} above it, starting with the M_J = 0.97|±3/2>. The absence of mixing provides a quasi-pure M_J function without a clear path to invert its moment, thus the system can be blocked at low temperatures.

Now, it is worth to compare the results of a particular lanthanide ion placed in the different families of POMs that we have theoretically characterised until this point. For that, we will focus in the erbium analogue because its crystal structure has been determined for ErW_{10}, ErW_{22}, $ErMo_{16}$ and $ErMo_{10}$. Regarding the lowest energy levels, we found a ground state characterised by ±13/2 in both heteroxopolywolframates, and a first excited state dominated by ±1/2 (placed at ~16 cm^{-1} in ErW_{10} and 11 cm^{-1} in ErW_{22}). In contrast, this picture is totally different in the case of $ErMo_{10}$, where the ground doublet is dominated by ±1/2 (96%) and the first excited state (located at about 18 cm^{-1}) presents 96% of ±15/2. In this family the best candidate is the Dy analogue due to the more axial coordination environment. The explanation of such a different behaviour can be attributed to the slight differences in the first coordination sphere. The interplanar distance, d_{pp}, was measured to be 2.46 Å in ErW_{10}, 2.48 Å in ErW_{22} and 2.61 Å in $ErMo_{10}$, presenting a more favourable coordination environment –to exhibit SMM behaviour using erbium as a magnetic ion– in the case of the two series of polyoxowolframates. $ErMo_{16}$ shows an intermediate situation, having d_{pp} = 2.55 Å and a skew angle comparable to that of ErW_{10}. As we have mentioned above, according to our calculations $ErMo_{16}$ has three Kramers doublets very close in energy, two of them dominated by high M_J values and one dominated by ±1/2.

6.3 Polyoxopalladates: the series $LnPd_{12}$

The next series of lanthanide ions coordinated by oxygens that has been investigated in this thesis is a family of cubic heteropolyoxopalladate-based complexes.[287] These polyanions were prepared by the group of Prof. Ulrich Kortz in Jacobs University and present the general formula $[LnPd_{12}(AsPh)_8O_{32}]^{5-}$ (in short: $LnPd_{12}$), where Ln = Tb, Dy, Ho, Er and Tm. They consist of a cuboid framework of twelve Pd^{2+} ions with eight phenylarsonate heterogroups located at the vertices and a central guest ion Ln. The molecule is very attractive from the point of view of the symmetry as it presents exact O_h symmetry with the eight oxygen atoms being chemically equivalent (Figure 6.18), all coordinated to the Ln and three Pd^{2+} atoms each. This is a very unusual situation since due to steric reasons two squares of atoms coordinating a spherical lanthanide tend to be more stable close to a skew angle of 45º. Additionally, changing the main metal comparing with previous series (Pd instead of W or Mo) allows us to study the influence of atoms beyond the first coordination sphere.

The family has been magnetically characterised by Naresh Dalal and co-workers in Florida State University and theoretically described in this Ph.D. thesis using the REC model.[222] In the meanwhile, the polyoxopalladate oxygen atoms are parameterised and added to the general library of ligands. Subsequently, the calculated CFPs will be used as input for a second fitting via a phenomenological crystal field approach using the full Hamiltonian in the CONDON package.[151] The high symmetry of the compounds provides only two non-vanishing crystal field parameters (CFPs) B_{40} and B_{60}. This situation is highly beneficial to perform a phenomenological fit, allowing to obtain a more accurate description of the ground state of the derivatives of the family.

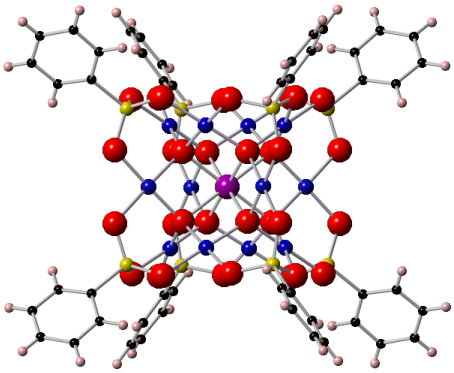

Figure 6.18: Ball and stick representation of $LnPd_{12}$. Color code: Ln (violet), O (red), Pd (blue), C (black), As (yellow) and H (pink).

The cubic symmetry also results in highly degenerate energy levels. This lack of anisotropy allows us to explore the breaking of degeneracy by reducing the symmetry around the lanthanide, or through the application of a magnetic field in a non-Kramers magnetic ion, such as Ho^{3+}, on the quantum coherence of the molecular spin qubit. This systematic study will be explained in Chapter 11, where a quantitative and inexpensive estimate of decoherence times in this family of cubic polyoxopalladates is described. In any case, this requires as a first step an understanding of the unperturbed system, which follows.

The magnetic susceptibility data of the series from 2 to 300 K have been simultaneously fit using the two parameters of the REC model in SIMPRE. A satisfactory fitting of the χT product is obtained when D_r = 0.8 Å and Z_i = 0.197, with a relative error of $E = 3.02 \cdot 10^{-3}$. Theoretical and experimental curves are represented in Figure 6.19. The two parameters, although similar to the ones obtained for the LnW_{10} and LnW_{22} families in section 6.1 (D_r = 0.895 Å and Z_i = 0.105) and for $LnMo_{16}$ in 6.2 (D_r = 0.72 Å and Z_i = 0.235), show small differences. Again, this can be attributed to the

different electronegativity of the neighbour atoms: wolfram (2.36), palladium (2.20) and molybden (2.16). An intermediate electronegativity is translated into an intermediate need for covalent correction and consequently into intermediate REC parameters.

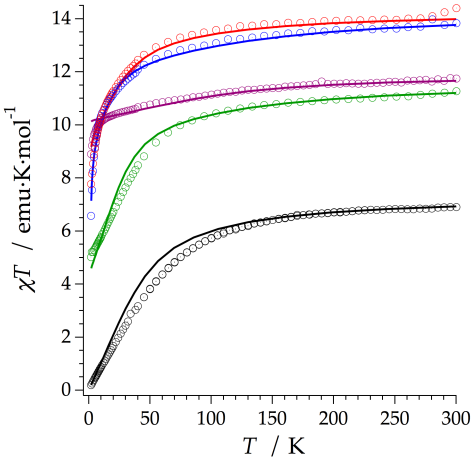

Figure 6.19: Fitting of the experimental χT product of the series of $LnPd_{12}$ using the REC model: Dy (red), Ho (blue), Tb (violet), Er (green), Tm (black). Open circles stand for experimental data and solid lines represent theoretical fit of $TbPd_{12}$, $DyPd_{12}$, $HoPd_{12}$ and $ErPd_{12}$ and prediction for $TmPd_{12}$.

The calculated CFPs, energy level schemes and magnetic properties for $DyPd_{12}$ (Figure 6.20) and $HoPd_{12}$ (Figure 6.21) are reported as an example. The energy level scheme and the magnetic susceptibility curves have been calculated by three different procedures: (i) calculated by the REC model (parameters from the collective fit) in the SIMPRE package using the Russell-Saunders approximation; (ii) calculated using the obtained CFPs in the CONDON package (full-Hamiltonian); and (iii) calculated from the individual fit of CFPs (phenomenological B_{40} and B_{60}).

In all three cases the magnetic susceptibility is well reproduced. The CFPs determined by the REC are close to the ones extracted from the fit. This emphasises the adequacy of using simple models as the REC one to define an initial set of CFPs that will allow the description of the system with accuracy.

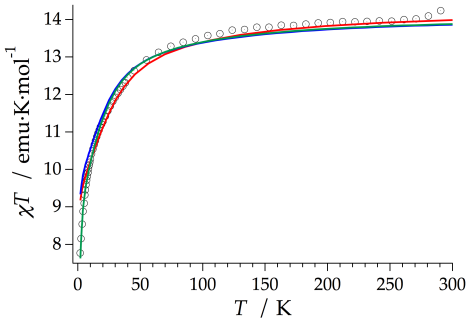

	REC SIMPRE E / cm^{-1}	REC CONDON E / cm^{-1}	FIT CONDON E / cm^{-1}
	0	0	0
	0	0.2	0.4
	0.8	0.4	4
	0.8	0.6	4
	0.8	7	4
	0.8	7	4
	68	57	56
	68	57	56
	68	57	56
	68	57	56
	288	278	251
	288	278	251
	347	328	304
	347	328	304
	347	328	304
	347	328	304
B_{40}	-1260	-1260	-1127
B_{60}	449	449	442

Figure 6.20: (left) Comparison of the χT value of $DyPd_{12}$ for powder from experiment (circles), REC model assuming Russell-Saunders scheme (red line), REC model using the full Hamiltonian (blue line) and phenomenological fit using the full Hamiltonian (green line); (right) energy levels of $DyPd_{12}$ calculated by the three differentes procedures (in cm^{-1}).

In both examples, the largest absolute difference between the three approaches is found in the most excited level within the ground *J* multiplet. In $DyPd_{12}$ there are important differences at lower temperatures, making more difficult the full interpretation of the spectroscopic properties of the

system. This picture is different in $HoPd_{12}$, where there is an exact coincidence between the collective fit of the REC model and the phenomenological determination under 2 cm^{-1} (Figure 6.21). The rich structure at low temperature of this complex makes it promising to perform a set of calculations that will investigate its possibilities as spin qubits.

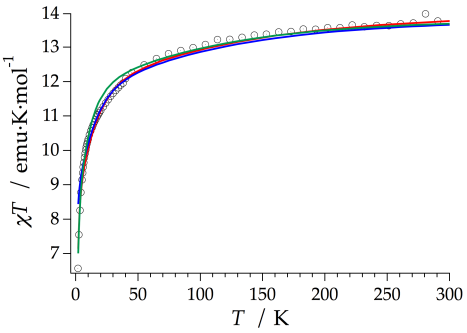

	REC SIMPRE E / cm^{-1}	REC CONDON E / cm^{-1}	FIT CONDON E / cm^{-1}
	0	0	0
	0	0	0
	2	0.9	2
	2	1	2
	2	1	2
	42	39	29
	42	39	29
	42	39	29
	311	280	260
	311	280	260
	325	294	276
	325	294	276
	325	294	276
	340	311	294
	382	347	314
	382	347	314
	382	347	314
B_{40}	-1224	-1224	-1219
B_{60}	428	428	384

Figure 6.21: (left) Comparison of the χT value of $HoPd_{12}$ for powder from experiment (circles), REC model assuming Russell-Saunders scheme (red line), REC model using the full Hamiltonian (blue line) and phenomenological fit using the full Hamiltonian (green line); (right) energy levels of $HoPd_{12}$ calculated by the three differentes procedures indicated above.

Finally, the magnetisation curves of the Dy and Ho derivatives measured at 5 K are represented in Figure 6.22, showing a reasonable agreement with the experiment. The ground doublet of $DyPd_{12}$ is

composed by a mixture of 40% |±13/2> + 34% |±5/2> + 20% |∓3/2> + 6% |∓11/2> and the first excited sublevel is a quadruplet at 0.8 cm^{-1}. For the same orientation, the wave function of the ground doublet is composed by 27% |±6> + 23% |±2> + 23% |∓2> + 27% |∓6> in $HoPd_{12}$, having a triplet at about 2 cm^{-1}. A transversal magnetic field or the distortion of the cubic symmetry unbreaks the degeneracy of the system.

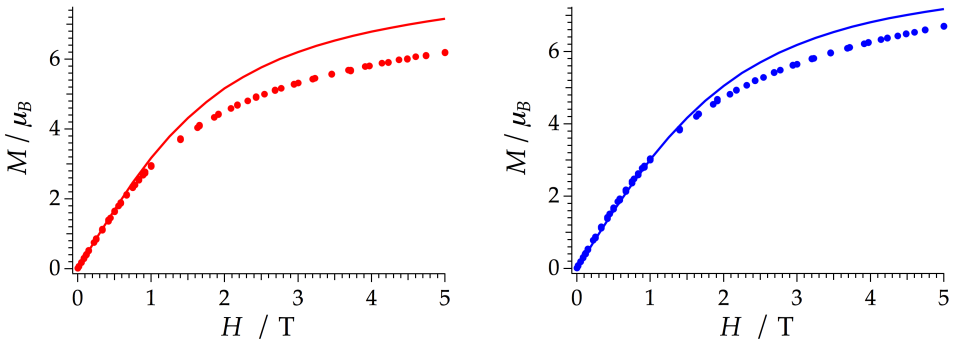

Figure 6.22: Experimental (markers) and calculated with the REC model in the SIMPRE package (solid line) magnetisation of $DyPd_{12}$ (left) and $HoPd_{12}$ (right) at 5 K with an applied magnetic field varying between 0 and 5 T.

6.4 Oxydiacetate: the series LnODA

The tris-terdentate coordination complexes formed by the chelation of the three oxydiacetate ligands to a trivalent lanthanide ion have been studied extensively.[133,320–323] Such studies have been useful to elicit information about the effects of ligand structural complexity on the details of $Ln^{3+}(4f^N)$ electronic state structure and optical properties. The series have the general formula $Na_5[Ln(oda)_3](H_2O)_6(BF_4)_2$, where Ln = Tb, Dy, Ho and Er and oda = oxydiacetate ($C_4H_4O_5^{2-}$), in short LnODA.[324] In these complexes, each

oxydiacetate ligand is coordinated to the lanthanide ion via two negatively charged oxygen atoms (one from each of the two carboxylate moieties in oda) and a neutral ether oxygen atom. The crystal structure can be refined in one of the Sohncke space groups (*R*32).[325] It has been reported[324] that the formation of hydrogen bonds involving BF_4^- anions could be essential in the packing of the homo-chiral complexes, resulting in the spontaneous resolution. The coordination geometry around the lanthanide ion is practically identical for both DyODA and ErODA. It may be described as slightly distorted tricapped trigonal prismatic (of D_3 symmetry). The upper and lower triangles are defined by carboxylate oxygen atoms and the capping positions (perpendicular to the near-C_3 symmetry axis) occupied by ether oxygen atoms (Figure 6.23). Thus, the coordination environment is not clearly axial nor equatorial,[61] being necessary to perform structure-based theoretical calculations to know which lanthanide ion is a better candidate to exhibit SMM behaviour.

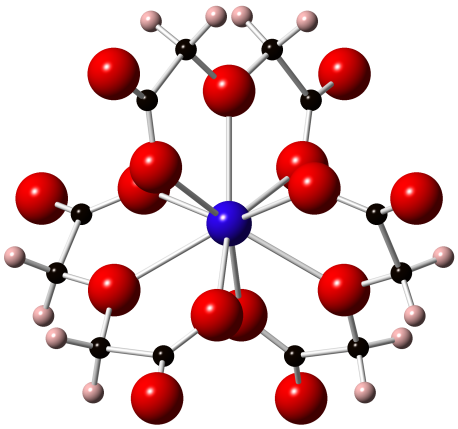

Figure 6.23: Vertical view of the three-blade-propeller molecular structure of $Na_5[Dy(oda)_3](H_2O)_6(BF_4)_2$ that emphasises the near-C_3 symmetry axis. The erbium derivative is isostructural.

The syntheses of the Dy and Er derivatives were proposed by the Ph.D. candidate because the ground doublet wave functions (previously calculated: 9/2 for DyODA and 15/2 for ErODA)[133,321] indicated the possibility of enhancing slow relaxation of the magnetisation in both complexes, in spite of the particular coordination environment of the complexes. These ground state wave functions were calculated using the CFPs of the phenomenological fit and the full Hamiltonian. The measured spectroscopic data in both compounds made them ideal to use as benchmark systems to test and compare the capabilities of our model.

Dealing with the modelling of this family with the REC model, we decided to test the possibilities beyond halogen atoms of the *semi-empirical* equations presented in Chapter 5 in the description of the Stark sublevels of the Dy and Er derivatives. This *semi-empirical* strategy allowed us to obtain a quick estimation of the energy levels and magnetic properties in the absence of any parameter, just utilising the previous knowledge in the study of the properties of lanthanide compounds coordinated by halogens. The availability of spectroscopic energy levels for the whole crystal field splitting in the case of DyODA and for most of the sublevels of ErODA gave us the opportunity to test the predictive power of the developed tools beyond the halides. Secondly, we followed the usual procedure using the energy levels of the Tb, Dy, Ho and Er derivatives and proceeding with the collective fit, giving priority to the lower-lying energy levels, i.e. accounting for the relative error instead of the absolute one.

On the other hand, for the same above-mentioned reason (availability of spectroscopic information beyond magnetic characterisation), we included an electronic structure *ab initio* study[173] performed by Roser Morales from the group of Prof. Eliseo Ruiz in the University of Barcelona. They carried out post Hartree-Fock calculations based on the relativistic

quantum chemistry method CASSCF+RASSI implemented in the MOLCAS 8.0 software package for the both compounds of interest.[164] CASSCF calculations were performed for three different multiplicities (sextet, quartet and doublet) for the Dy complex, and two multiplicities (quartet and doublet) for the Er complex. 21, 128 and 98 states for the sextet, quartet and doublet calculations of the Dy complex were included. Whereas for the Er derivative, 35 and 112 states for the quartet and doublet calculations were taken into account. Furthermore, CASPT2 calculations were performed in order to allow richer comparison between different models and experimental data.[169] CASPT2 calculations of the ground state multiplicities included 21 states for the sextet of Dy and 13 states for the quartet of Er. The effect of spin-orbit coupling on the basis of the converged wave functions obtained in the previous step (CASSCF or CASPT2) was added by the Restricted Active Space State Interaction (RASSI) method. Spin Hamiltonian parameters (such as g factors) were calculated from the wave functions resulting after the state interaction step employing the SINGLE_ANISO program, implemented in MOLCAS 8.0. The employed basis set has the following contractions: Dy [9s8p6d4f3g2h]; Er [9s8p6d4f3g2h]; O close [4s3p2d1f]; O distant [3s2p]; C [3s2p]; H [2s]. The structure of the model was extracted from the corresponding X-ray structure without any ligand simplification.

Regarding the experimental part, Yan Duan proceeded with the synthesis of the Dy and Er derivatives and the diluted samples of both compounds ($Y_{(1-x)}Ln_{(x)}$ with x=0.01 for Dy, x=0.05 for Er). José M. Martínez recorded the magnetic data, performing *dc* susceptibility measurements for the pure and diluted samples of both compounds under an applied field of 0.1 T. In the pure compound, the χT values at 300 K are near the expected values for the $^4I_{15/2}$ and $^6H_{15/2}$ multiplets of Er^{3+} (11.27 (exp.) vs. 11.48 emu·

K/mol) and Dy^{3+} (14.08 (exp.) vs. 14.17 emu· K/mol). To avoid dipolar interactions that are not included in the theoretical model, the experimental χT products of the diluted samples of DyODA and ErODA are to be compared with the theoretical results. In both cases the temperature-dependent magnetic susceptibility gradually decreases upon cooling due to depopulation of the electronic fine structure, reaching values close to 6 emu·K/mol (Figure 6.24).

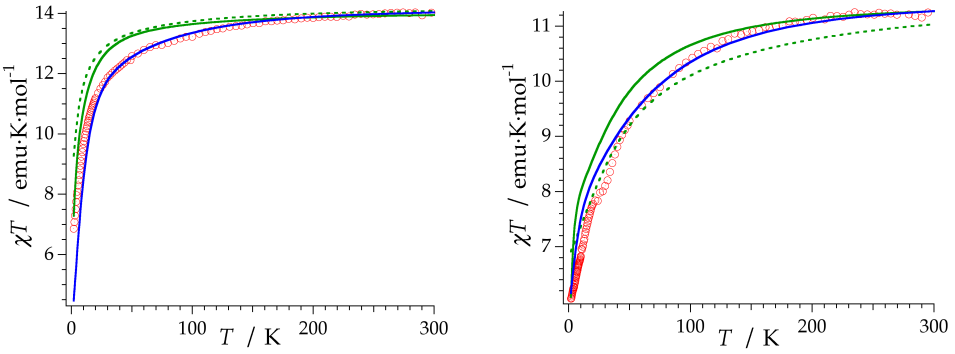

Figure 6.24: Comparison of the $\chi_m T$ product for the magnetically diluted powder samples of $Y_{0.99}Dy_{0.01}ODA$ (left) and $Y_{0.95}Er_{0.05}ODA$ (right) at H = 1000 Oe. Red open circles: exp.; blue solid line: REC prediction, green solid line: CASSCF, green dashed line: CASPT2.

It can be observed that the overall shape of both experimental curves is in general well reproduced by all three methods (REC prediction, CASSCF and CASPT2 results), being the experimental results closer to the predicted ones using the REC model. It is remarkable that the electrostatic method (blue solid line) reproduces the χT curves with an almost excellent agreement with the experiment (red open circles) in both cases. In the case of the *ab initio* calculated χT product there is no improvement between CASSCF and CASPT2, being almost equivalent in the Dy derivative. There

are noticeable differences between CASSCF (green solid line) and CASPT2 (green dashed line) in the Er example (Figure 6.24 (right)), where CASPT2 seems to reproduce better the magnetic behaviour below 100 K, while at higher temperatures CASSCF is closer to the experiment. Dynamic correlation contribution seems to be more important for the erbium system, probably for the larger electron repulsion due to the presence of two extra electrons in the f orbitals in comparison with the Dy complex. Anyway, CASSCF method provides reasonable values, as expected taking into account the relatively large ionic character of the metal-ligand interactions. In particular, CASPT2 calculations predict a χT value of 11.03 emu·K/mol, which may indicate a total CF splitting larger than the one obtained by the CASSCF method. The better agreement of the electrostatic calculation allows us to think that, in these two particular examples, the energy level scheme should also be better reproduced by the *semi-empirical* method.

For both compounds, *ac* susceptibility measurements were performed above 2 K. In both cases, they reveal the typical features associated with the SMM behaviour for a system with some mixture of M_J components enabling the possibility of presenting avoided hyperfine crossings and quantum tunnelling. Hence, in the absence of a *dc* field there is a weak frequency-dependent signal in χ'' but no clear χ' signal. The system is taken beyond the hyperfine crossing region after applying an external field of 1000 Oe. As a result, both χ' and χ'' show strong frequency dependencies. This indicates the presence of a slow relaxation process involving an energy barrier for the reversal of the magnetisation. In the Dy derivative, a maximum is detected between 2.5 and 3.0 K in χ' (Figure 6.25 (top, left)), which is frequency dependent. In χ'', the maximum could not be observed in the measurements carried out between 2 and 10 K (Figure 6.25 (down,

left)). The upward trend from 4 K to 2 K permits to expect that the position of the maximum should appear between 1 and 2 K, but this is outside our operating range.

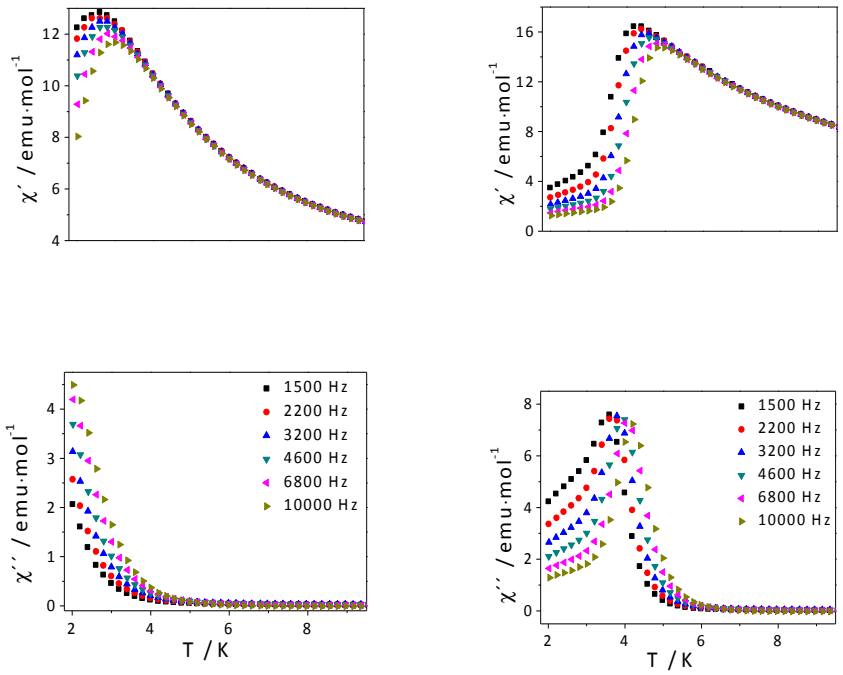

Figure 6.25: In-phase (top) and out-of-phase (down) dynamic susceptibility of DyODA (left) and ErODA (right) under an applied *dc* field of 1000 Oe at the frequencies shown in the legend.

On the other hand, the magnetic properties of ErODA reveal the typical features associated with SMM behaviour. Thus, both χ' and χ'' under an applied magnetic field of 1000 Oe (Figure 6.25 (right)) show strong frequency dependencies, which indicates the presence of a slow relaxation process involving an energy barrier for the reversal of the

magnetisation. Depending on the frequency of the applied *ac* field, χ' presents a maximum between 4.3 and 4.9 K, while χ'' has also a maximum between 3.5 and 4.2 K for 1500 and 10000 Hz, respectively (Figure 6.25 (right, down)).

In references 133 and 321, a large number of energy levels were located and assigned for both members of the LnODA family (65 for Er, 152 for Dy) by a combination of spectroscopic techniques, which in both studies consisted of optical absorption (unpolarised, linearly and circularly polarised), and was also extended to optical emission (also including all polarisations) for DyODA. Fits assumed a trigonal CF symmetry, thus in each case six CF parameters (B_{20}, B_{40}, B_{60}, B_{43}, B_{63} and B_{66}) were varied in order to find a complete description of the experimental properties. In both derivatives, the root-mean-square deviation between the fit and the experimental data is below 10 cm^{-1} for the whole spectrum, and below 7 cm^{-1} for the ground *J* manifold, so this is the expected accuracy for the missing experimental levels in the case of the erbium derivative. Note that this accuracy is maintained for energies in the tens of thousands of cm^{-1}, accounting for the power of this approach and justifying its use as benchmark or "gold standard" to judge the quality of theoretical calculations when not all the experimental energy levels are available.

In Figure 6.26, we compare these reference data with different sets of theoretical energy levels using the real structures of both complexes, by three different strategies. We have to stress that, in this case, the application of the REC model does not rely on any free fitting parameters: we used Equation 5.3 (Chapter 5), the relation $f = Z_i \cdot D_r$ and previous results on polyoxowolframate oxygen-based ligands (Chapter 6, section 6.1) to obtain an effective distance of $D_r \approx 1.1$ Å and an effective charge of $Z_i \approx 0.085$. Such a procedure has been described in Chapter 5.

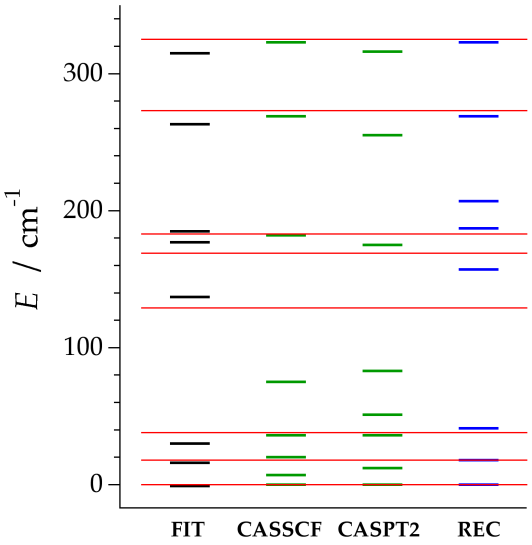

Figure 6.26: Crystal field energy level scheme of the ground *J* multiplet of DyODA. Thin red lines: experimental optical spectrum. Thick lines: spectroscopic fit, CASSCF/CASPT2 energies including spin-orbit effects and REC model prediction, as indicated at the axis (details in the text).

The experimental energy level scheme of DyODA can be described as a bunching of levels in three groups 3+3+2, where each group has a width of about 50 cm^{-1} and there is a gap with no levels of about 80 cm^{-1} between every two groups.[321] This 3+3+2 description is well reproduced by the *semi-empirical* REC prediction. In contrast, both CASSCF and CASPT2 respond rather to a 5+1+2 scheme, that is, the fourth and fifth energy levels, that experimentally are found near 150 cm^{-1}, are predicted to be about a 50% lower in energy, around 75 cm^{-1}. The total energy level splitting, of about 320 cm^{-1}, is adequately reproduced by all methods. The CASPT2 method improves CASSCF results for the low-lying state energies, which are crucial for the theoretical determination of the anisotropy barriers. On the other hand, the prediction provided by the REC model using Equation 5.3 offers

a remarkable reproduction of the scheme, as confirmed in the correct prediction of the χT product. In addition, one can observe that following this methodology the total CF splitting is perfectly determined and the scheme 3+3+2 is also obtained. In this particular case, this predictive electrostatic approach results in a very satisfactory description of the energy levels.

In the case of the Er derivative, five of the eight CF Kramers doublets split out of the $^4I_{15/2}$ (ground) multiplet were reported.[133] Taking the spectroscopic fit as a reference for the whole set of levels (black thick line in Figure 6.27), a slightly different 2+3+3 bunching is observed, with bunches that are at the same time increasingly wider (40, 70 and 110 cm^{-1}) and more separated than in the Dy case (over 100 cm^{-1} for each of the inter-bunch separation). In this case, the CASSCF calculation qualitatively predicts the 2+3+3 bunches, but underestimates all energies, so that in general the CASSCF levels are situated in the energies between the experimentally found energy bunches. Interestingly, while in this case an overall increase in CASSCF energies of about 50% that would improve the agreement, the factor would be of the order of 400% if only the first excited state is considered, highlighting the risk of using these type of factors with partial information. As reflected in the χT curve (Figure 6.24 (right)) in the case of CASPT2 the difference between the calculated energy levels with respect to CASSCF is striking, but also pretty far from the experimental result with no clear improvement. In this case, a 1+6+2 bunching is found with a total splitting of about 740 cm^{-1}, which is a 68% higher than the results of the phenomenological fit (441 cm^{-1}). Such a total splitting seems unreasonable and is key to understand the deviation of the χT product respect to the experiment (see Figure 6.24 (right), green dashed line). On the other hand,

the REC prediction is not as accurate as the one calculated in DyODA, but still respects the 2+3+2 scheme. The total splitting calculated by the REC model is very close to the one calculated with the phenomenological fit and thus is expected to be close to the actual energy levels.

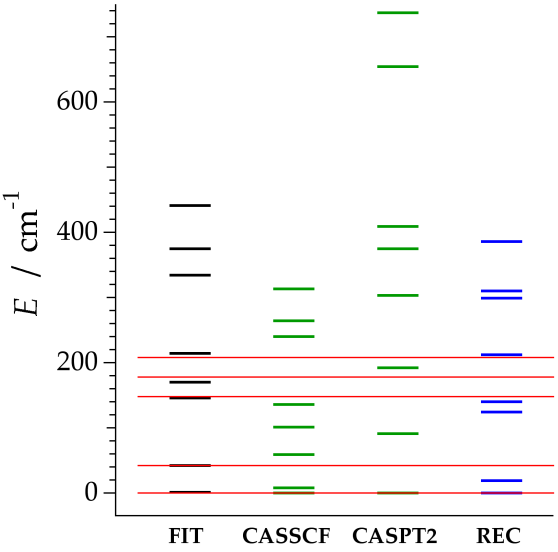

Figure 6.27: Crystal field energy level scheme of the ground *J* multiplet of ErODA. Thin red lines: experimental optical spectrum. Thick lines: fit, CASSCF/CASPT2 energies including spin-orbit effects and REC model prediction, as indicated at the axis (details in the text).

After the analysis of these two particular examples, one can critically review general limitations of *ab initio* calculations and the electrostatic approach presented in this thesis. For clarity, one can briefly enumerate the limitations of each approach, and then go into some detail. In this regard, Complete Active Space *ab initio* calculations:

(1) consider a single complex (the results should be compared with those obtained with magnetically dilute samples),

(2) apply perturbations in the wrong order, in CASPT2 both dynamic correlation and spin-orbit effect are included perturbatively.

(3) are limited by large computacional requirements.

Even when more than a single metal is considered, dipolar interactions within the crystals are also outside the scope of this approach. More crucially, the fact that the SINGLE_ANISO procedure applies spin-orbit coupling after, rather than before, the ligand field, has fundamental, limiting consequences in the accuracy of the method that have not yet been adequately evaluated. On top of that, there are the non-fundamental limits posed by large computational requirements, especially in the case of the CASPT2 method. Because it is a computationally demanding method, it can happen that the end results have not converged, that is, that using a larger basis set, active space or contraction would produce results that are closer to the experimental data. Again, an extra theoretical effort will eventually overcome (2), but it will require programming new calculation procedures. However, electronic structure methods provide several useful pieces of information (g components, energy of the states, probability of the different spin relaxation mechanism between states and so on) and tools for the understanding of the magnetic properties (electrostatic potential of the ligands, shape of the electron density).

The *semi-empirical* REC model considers:

(1) a single metal,

(2) the first coordination sphere

(3) the ground *J* multiplet

(4) it is a parametric (*semi-empirical*) method that often relies on low-quality data (powder χT) data and assumes parameters are re-usable.

As it considers a single metal, this method is inappropriate for cluster-type complexes. Limiting the point charges to the first coordination sphere

can have severe consequences for the prediction of the easy axis of magnetisation, while limiting the treatment to the ground *J* means the upper levels, even within the ground *J*, are less well described, and their energies are often overestimated. Being *semi-empirical* means there is no systematic method to obtain more accurate CF parameters, other than fitting higher-quality (spectroscopic) experimental data. That includes the risk of assuming that parameters extracted from a compound can be used on a different one. Some of these points can be improved by some extra theoretical effort. For example (3), is solved by considering the full single-ion Hamiltonian, while (4) is continuously being improved as the number of examples studied by this method grow, which provide a better understanding of the adequate parameterisation of each kind of ligand.[310]

Finally, as expected, the spectroscopic fit offers a perfect description of the measured levels. Nevertheless, it is important to point out that such a phenomenological approach can only be carried out after the energy level scheme is properly determined and it is only adequate when the symmetry of coordination environment is comparable to a point group, thus reducing the number of CF parameters. In real molecules, when 27 crystal field parameters are non-negligible, models based on the prediction of the properties from the real structure, such as the two approaches that have been compared and discussed here are necessary.[152]

6.5 Hydroxide: a layered lanthanide hydroxide

The particular combination of properties that can be achieved by inserting a diversity of anions in between the host inorganic layers have revitalised the interest in layered metal hydroxides. These lamellar hosts offer a broad range of possibilities,[326,327] such as introducing a stimulus responsive

molecule that control the physical properties of the host.[328,329] In this context, a particular class of materials are the so-called layered lanthanide hydroxides (LLHs),[326] which are compounds with a general chemical formula of $Ln_2(OH)_5A{\cdot}nH2O$. In these compounds A represents interlayer anions such as Cl^-, NO_3^-, Br^-, etc. and n is 1.5–1.8. The unit cell of these materials contains three crystallographic distinct lanthanide sites, with two different Ln coordination environments, as can be seen in Figure 6.28. The three crystallographic sites are labelled as Ln1, Ln2 and Ln3.

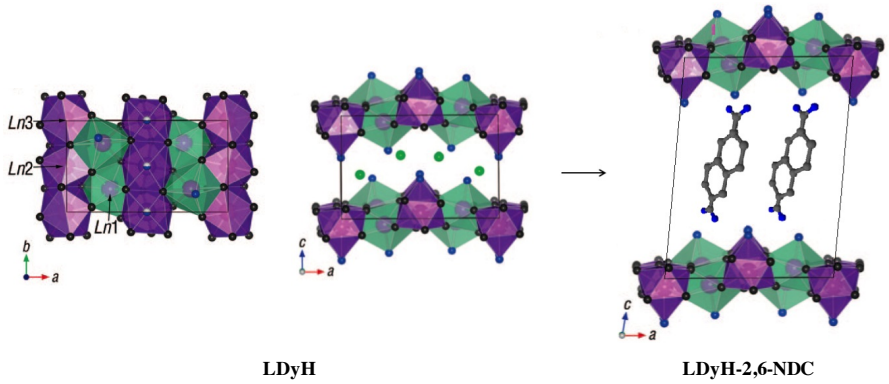

Figure 6.28: $Ln_8(OH)_{20}Cl_4{\cdot}nH_2O$ crystal structure viewed along the *c* axis (left) and along the *b* axis (centre) and schematic representation of the LDyH-2,6-NDC structure viewed along the *b* axis (right). Ln ions are depicted as purple, hydroxyls as gray, water molecules as blue, chloride ions as green, and carbon as gray balls. The 8-fold dodecahedron and 9-fold monocapped square antiprism are in light green and purple, respectively. (adapted by L.C. Pereira from Ref. 311).

One of the lanthanide ions (Ln1) presents an 8-fold coordination, $[Ln(OH)_7(H_2O)]$, in a dodecahedron environment and the other two Ln ions (Ln2 and Ln3) present a 9-fold coordination, $[Ln(OH)_8(H_2O)]$, forming a monocapped square antiprism coordination geometry with the capping position occupied by the water molecule. The crystal structure is built up

along the *c*-axis via an alternating stacking of the host layer, composed of edge-shared $[Ln(OH)_7(H_2O)]$ and $[Ln(OH)_8(H_2O)]$ polyhedra, with each hydroxyl acting as a μ_3-bridge connecting the lanthanide centres and the anions which are intercalated between the layers ensuring charge neutrality.[330]

The small anions A in these structures can be easily replaced by more bulky ones, following an intercalation process that preserves the layered structure.[331] The compositional flexibility of such materials, where the identity of both cation and anion can be controlled to target a specific application, makes them extremely appealing for different possible applications, and studies have focused mainly on their optical properties.[332–338] The magnetic properties of these lanthanide compounds are also potentially interesting, but have been a lot more neglected in spite their potential namely for providing SMM behaviour with large anisotropy barriers[56] and high blocking temperatures[46].

With the aim of distinguishing between the different contributions, the group of Prof. Manuel Almeida prepared a dilution of the compound LDyH in the diamagnetic Y analogous matrix, and intercalated with 2,6-naphthalene dicarboxylate anions (LDyH-2,6-NDC). The first show the behaviour of the single Dy ions, while the intercalated material is expected to reveal the effects of isolated layer (purely 2-D) interactions.

The magnetic properties of these layered dysprosium hydroxides, both diluted in the diamagnetic Y analogous matrix (LYH:0.04Dy), and intercalated with 2,6-naphtalene dicarboxylate anions (LDyH-2,6-NDC) were measured. Both diluted and intercalated materials presented a perfect overlapping of zero-field-cooled (ZFC) and field-cooled (FC) magnetisation curves with no indication of any ordering down to 2 K.[311] This was also previously described for the undiluted compound (LDyH=

$Dy_8(OH)_{20}Cl_4{\cdot}6H_2O$) that had been reported in 2013.[339] As may be seen in Figure 6.29, the room temperature μ_{eff} values for Dy atom for LYH:0.04Dy and LDyH-2,6-NDC are comparable to that of the pure LDyH compound and close to the expected value of 10.6 μ_B/Dy for one non-interacting Dy^{3+} ion (S= 5/2, L= 5, J= 15/2, $^6H_{15/2}$, and g= 4/3). It can be observed that in all compounds there is a gradual decrease of μ_{eff} upon cooling, with no signs in the diluted compound of the sharp maxima observed in the pure LDyH. A reminiscence of this peak is observed in intercalated material as a small anomaly.

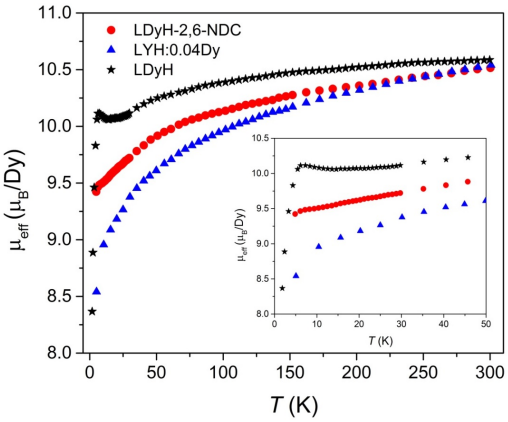

Figure 6.29: Effective magnetic moment of the dysprosium compounds in the temperature range from 5 to 300 K obtained under a magnetic field of 100 G.

In order to understand the single-ion effects, the Radial Effective Charge model was applied to the three different lanthanide centres of LYH:0.04Dy using the two REC parameters presented in 6.1 (D_r = 0.895 Å and Z_i = 0.105) and the software package developed in the thesis. The theoretical calculations clearly indicated a different energy level scheme and ground state wave functions for each magnetic centre, especially between the two different coordination of the Dy ions, as can be observed

in Figure 6.30. This is compatible with the two different relaxation processes that had been encountered experimentally, which may be attributed to the different coordination environments. The two *semi-empirical* REC parameters could provide an estimation of the ligand field effects of every oxygen atom coordinating each magnetic centre. In this case a collective fit taking into account other derivatives with the same crystal structure was not possible to carry out, as all the experimental work was based in the Dy centres. However, the polyoxowolframate-based corrections offered reasonable results for the purpose of understanding the magnetic properties. Such corrections seem reasonable according to the similar character of the hydroxides and the oxygen donor atoms in molecular metal oxide clusters.

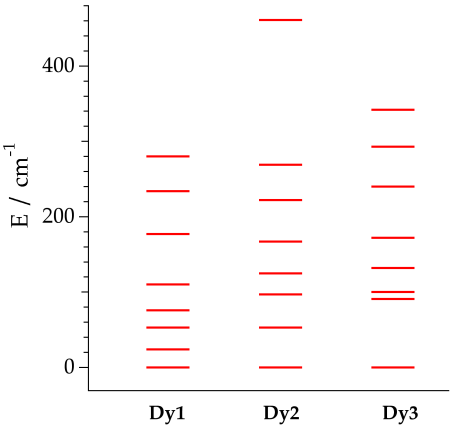

Figure 6.30: Calculated ground multiplet crystal field splitting illustrating the Kramers doublets for the three different Dy centres.

The averaging of the contributions of all three different Dy centres, allowed to estimate the magnetisation curves expected for the diluted sample at different temperatures. The results were found in surprising good agreement with experimental data, as may be observed in Figure 6.31.

As the shape of the curves was practically coincident with the theoretical prediction, a scale factor of +1.0885 was applied to the experimental data for better agreement which can be translated into a 0.037 of Dy instead of 0.04 after the dilution procedure.

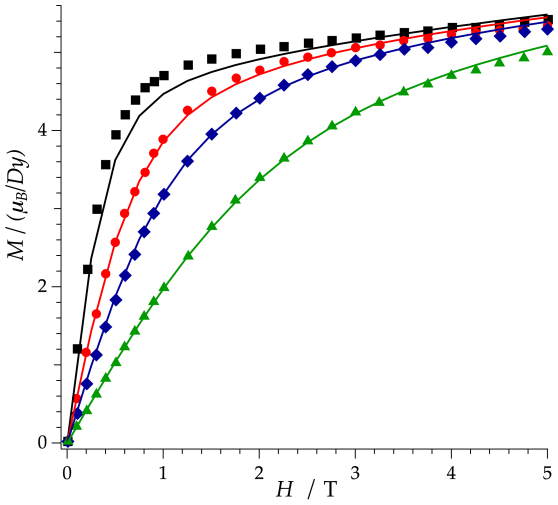

Figure 6.31: Experimental (symbols) and predicted average (lines) magnetisation M versus field H of LYH:0.04Dy at 1.7 K (black), 3.3 K (red), 5 K (blue) and 10 K (green).

The same two parameters offered a fair reproduction of the experimental χT product, where, in addition to the above mentioned correction scale factor 1.088, a TIP correction of $7.2 \cdot 10^{-3}$ emu/mol was introduced (Figure 6.32).

These calculations show, as expected, that the ground doublet is different for the different crystallographic sites, being composed by 0.76 |±13/2>, 0.98 |±15/2> and 0.99 |±15/2>, with the g_z values equal to 16.2, 19.79 and 19.91 for Dy1, Dy2 and Dy3 respectively. The results are

compatible with the observed SMM behaviour that present two relaxation processes corresponding to the 8- and 9-fold coordinated Dy ions.

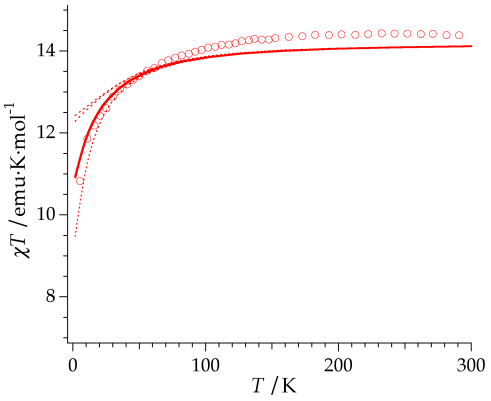

Figure 6.32: Experimental (symbols) and predicted (lines) χT product versus temperature of LYH:0.04Dy. The dashed lines show the χT product of each individual magnetic centre.

In order to test the effect of the water molecule of each centre, which is chemically different from all the coordinated OH^- and differs more from the polyoxowolframate atoms, the program was run again without considering the water molecule at all (i.e. assuming an effective charge Z_i=0). Results showed that, in this case, the absolute effect of the water molecule is very limited in terms of removing the water molecule from the input file did not yield significant differences concerning magnetic properties, energy levels, wave functions and easy axis orientations.

Concerning the magnetic easy axis orientation of each centre, it was found again that they are very similar in the case of Dy2 and Dy3, but almost perpendicular to Dy1. The easy axis of Dy2 and Dy3 are along the *b*-axis corresponding to the slightly zigzagging line (α = 170°), connecting these ions in the crystal structure. It should be noted that even in the

absence of ferromagnetic superexchange, this alignment of the easy axes is expected to promote a ferromagnetic coupling via dipolar interaction within these spin chains. In contrast, the easy axis of Dy1 is perpendicular to the *ab* plane. This alignment favours ferromagnetic coupling via dipolar interaction between spin chains of different layers, possibly explaining the slower decrease of effective magnetic moment upon cooling of the non-diluted material as shown in Figure 6.29. Because of the ferromagnetic superexchange, the near-perpendicular orientation of the easy axes between Dy1 chains and Dy2-Dy3 chains should favour a strongly canted arrangement of magnetic moments with an overall ferromagnetic coupling, both within and between the layers. Such canting arrangement is also denoted by the previously described two-step shape of the low temperature magnetisation curve for the undiluted compound.[339]

The magnetisation dynamics of both complexes were probed by using *ac* susceptibility measurements at low temperatures with an *ac* field of 5 G at different frequency values. The LYH:0.04Dy presents strong frequency-dependent signals below 6 K under both zero (Figure 6.33 (a,b)) and 1000 G (Figure 6.33 (c,d)) static magnetic fields, with the appearance of two resolved maxima in both real, χ', and imaginary, χ'', components of susceptibility at 1000 G. The intensities of the signals increase with decreasing temperature and frequency. Such performance clearly indicates slow relaxation of the magnetisation due to single ion effects originating from two relaxation processes. As we have shown according to the theoretical calculations, these two relaxation processes are most likely associated with the two different types of coordination of the Dy ions in the structure. The process at lower temperatures with a more intense *ac* susceptibility could therefore be ascribed to the $[Dy(OH)_8(H_2O)]$ polyhedron (corresponding to 2/3 of the total Dy^{3+} ions), and the higher

temperature one with weaker *ac* susceptibility would then be associated with $[Dy(OH)_7(H_2O)]$ (corresponding to 1/3 of the total Dy^{3+} ions). It should be noted that in the pure Dy compound only one relaxation process was observed.[339] The absence of two processes of relaxation in the nondiluted LDyH compound is probably due to the ferromagnetic interactions between the Dy ions.

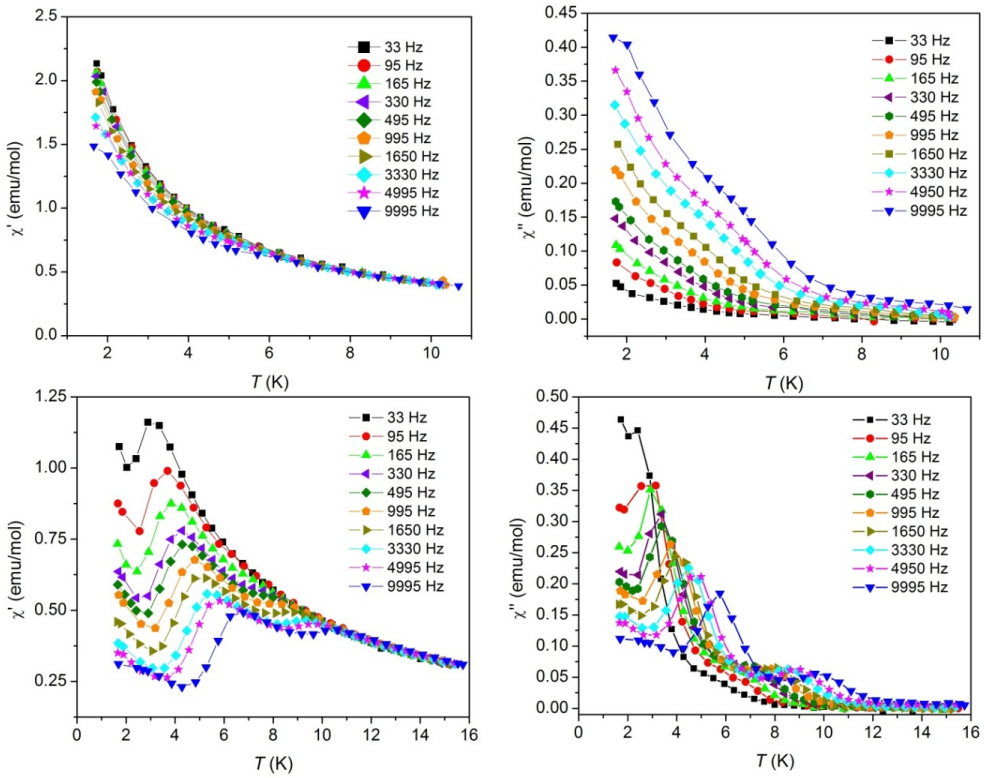

Figure 6.33: Temperature dependence of the real (χ', left) and imaginary (χ'', right) components of the *ac* susceptibility for LYH:0.04Dy under different static fields: (top) B = 0 G and (bottom) B = 1000 G, measured at different *ac* frequencies.

6.6 N,N′-dioxide: a SIM metal-organic framework

In this section we present the rational design of a family of metal-organic frameworks (MOFs) in which the nodes are formed by mononuclear lanthanide SIMs.[120] The proposed family has the general formula $[Ln(bipyNO)_4](TfO)_3 \cdot x$solvent (Ln = Tb, Dy, Ho, Er; bipyNO = 4,4′-bypyridyl-N,N′-dioxide; TfO = triflate), in which the lanthanoid centres have an square antiprismatic coordination environment suitable for SMM behaviour.[340–342]

This system lies between two major areas within the field of coordination chemistry that are currently attracting much interest: the development of SMMs and MOFs.[343,344] The combination of both fields, that is, the formation of SMM-MOFs has been largely pursued to develop new types of molecular magnetic materials. In addition, the conjunction of accessible pores in which different guest species can be stored with the magnetic bi-stability provided by the SMMs would result in a dynamic magnetic coordination polymer.[328] This could add further functionalities in the hybrid material through the incorporation of different guest species into the cavities.

An inspection of the Cambridge Structural Database (CSD) by Dr. Guillermo Mínguez revealed the presence of 73 crystal structures containing Ln and bipyNO, but only six of them were found to have eight-coordinated nodes with only bipyNO as ligands, the others containing a mixture of ligands and/or coordinated solvent molecules. These six crystal structures present suitable coordination environments for SMM behaviour, that is, a square-antiprismatic coordination of eight oxygen atoms, although an appropiate lanthanoid centre needs to be chosen for magnetic purposes.[340–342] For that, the chemical structures of the different complexes

were introduced in the SIMPRE package by the Ph.D. candidate. The REC parameters of the families LnW_{10} and LnW_{22} were utilised for this purpose, as they are the only oxygen-donor atoms that had been modelled at that time. Such predictions marked the Dy derivative as the most promising one for the design of a SIM-MOF, envisaging the possibility of obtaining such behaviour in the Tb and Er derivativaes. However, to obtain a set of more accurate calculations by a collective fit of magnetic susceptibility data, Christoph Gamer synthesised at the ICMol the four derivatives of the 3D MOFs IXEDUK and IXEFAS (see CSD).[120] The coordination environment around the Ln and the view of the eight bipyNO ligands are reported in Figure 6.34.

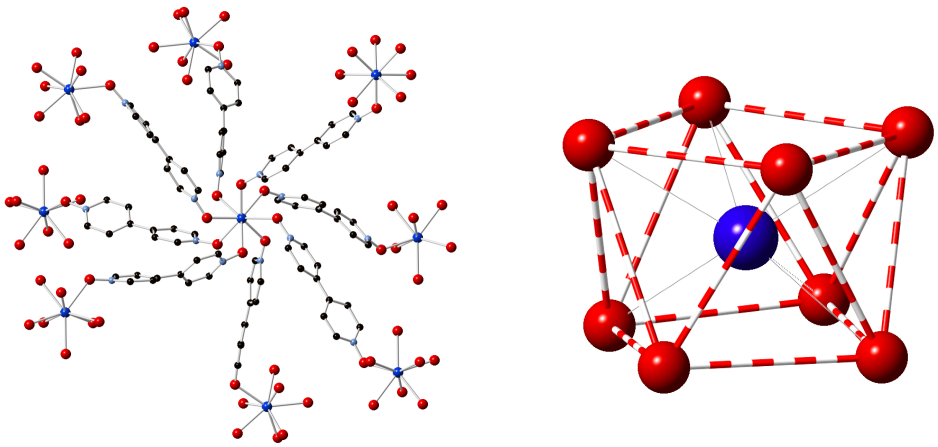

Figure 6.34: (left) View of the eight bipyNO ligands that form bridges between lanthanoid centres. Only one of the three crystallographically independent Ln is shown; Hydrogen atoms are removed for clarity. Key: Ln (blue), C (black), N (blue) and O (red); (right) Near square antiprismatic coordination environment of the Dy^{3+} centres.

Due to the collapse of the crystals upon removal of the solvent molecules, the magnetic measurements have been performed immersing 60 mg of crystals in methanol. Static *dc* magnetic measurements of the Tb-Er derivatives are shown in Figure 6.35. The observed drop of χT at low temperature results primarily from the depopulation of the highest crystal-field levels, as commonly seen on anisotropic lanthanide ions, although some contribution from weak dipolar coupling between the lanthanoid centres could be present. This interaction has been discarded by examining the isotropic Gd analogue, which shows a constant χT value for all temperatures.

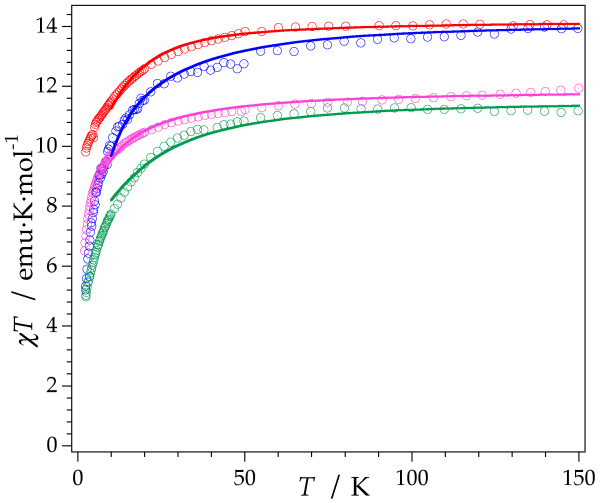

Figure 6.35: Fitting of the experimental χT product of $Tb(bipyNO)_4$, $Dy(bipyNO)_4$, $Ho(bipyNO)_4$ and $Er(bipyNO)_4$ using the REC model. Open circles: experimental data; solid line: theoretical fit from 10 to 150 K.

As can be seen in Figure 6.35, the χT curves are successfully reproduced until 10 K. A satisfactory simultaneous fit of the four curves (χT from 10 to 150 K) is achieved when D_r = 0.926 Å and Z_i = 0.073, having

a relative error of $E = 2.1 \cdot 10^{-4}$. The energy diagrams with the main contributions to the wave functions for the ground states of the three Dy centres (linear combination of M_J states) of $[Dy(bipyNO)_4](TfO)_3$ are shown in Figure 6.36. The lowest Kramers doublets for these systems correspond to a mixture between $M_J = |\pm 15/2>$ and $M_J = |\pm 13/2>$. The first excited doublet is in the vicinity of 20 cm^{-1} in all three cases, and is dominated by $M_J = |\pm 5/2>$, $M_J = |\pm 3/2>$ and $M_J = |\pm 7/2>$. Such description is compatible with slow relaxation of the magnetisation. Similarly, these calculations also show a predominant contribution of high M_J values for the Tb and Er derivatives which also favours SMM behaviour (see Figure 6.37), albeit in the case of $[Ho(bipyNO)_4](TfO)_3$ the ground state is formed by a heavy mixture of different M_J values (± 5, ± 3, ∓ 3, ∓ 5) which difficults this phenomena (see Ref. 120).

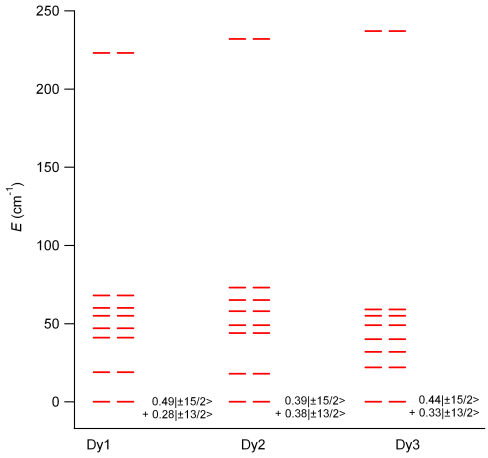

Figure 6.36: Energy level scheme and main M_J contributions to the ground state for three different Dy centres in $[Dy(bipyNO)_4](TfO)_3$.

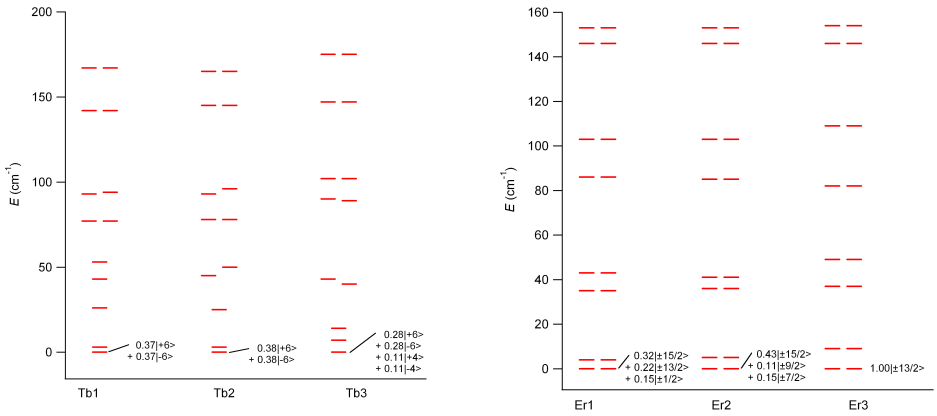

Figure 6.37: Energy level scheme and main M_J contributions to the ground state for three different Dy centres in $[Tb(bipyNO)_4](TfO)_3$ and $[Er(bipyNO)_4](TfO)_3$.

The theoretical calculation of the magnetisation for each Dy centre has also been calculated (Figure 6.38). The average of the three calculations is shown below. This result confirms the Ising-type nature (lager contribution of ±15/2 and ±13/2) of this mononuclear SMM.

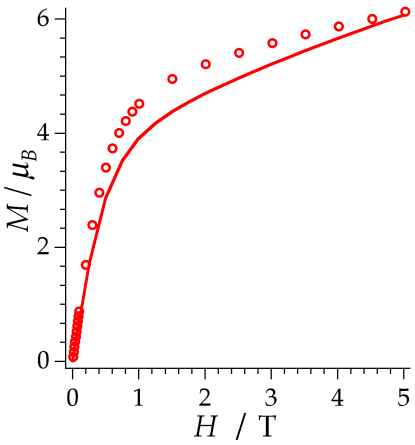

Figure 6.38: Magnetisation of $[Dy(bipyNO)_4](TfO)_3$ at 2 K. Open circles: experimental data; solid line: calculated values.

Dynamic magnetic measurements (*ac*) in the absence of an external field show the presence of an out-of-phase signal, χ'', that is frequency-dependent for the Dy derivative, although no maximum is observed, possibly due to the presence of a fast relaxation of the magnetisation through a quantum tunnelling mechanism. This fast tunnelling can be easily removed with the application of an external field that drives the levels away from the hyperfine avoided crossing region.[345–347] Thus, *ac* measurements performed in the presence of a small external *dc* field of 1000 G, both χ' and χ'' show a slower relaxation, and a maximum which is frequency dependent is observed (Figure 6.39). In addition, these maxima are further displaced to higher temperatures by increasing the external *dc* field to 2000 and 10000 G. The possibility of using a magnetic diluted sample to suppress the zero-field tunnelling of the magnetisation was unsuccessful, since *ac* susceptibility studies using a MOF with a Dy/Y molar ratio of 1:10 show a similar behaviour to $[Dy(bipyNO)_4](TfO)_3$. Analyses of the frequency dependence of the χ'' peaks through an Arrhenius plot permit estimation of the magnetisation-relaxation parameters in this system. Best fittings afforded a barrier height (U_{eff}/k_B) of 17.9 K with a pre-exponential factor (τ_0) of 1.86×10^{-7} s with an applied external field of 1000 G. Upon increasing the external field, these values become physically meaningless.

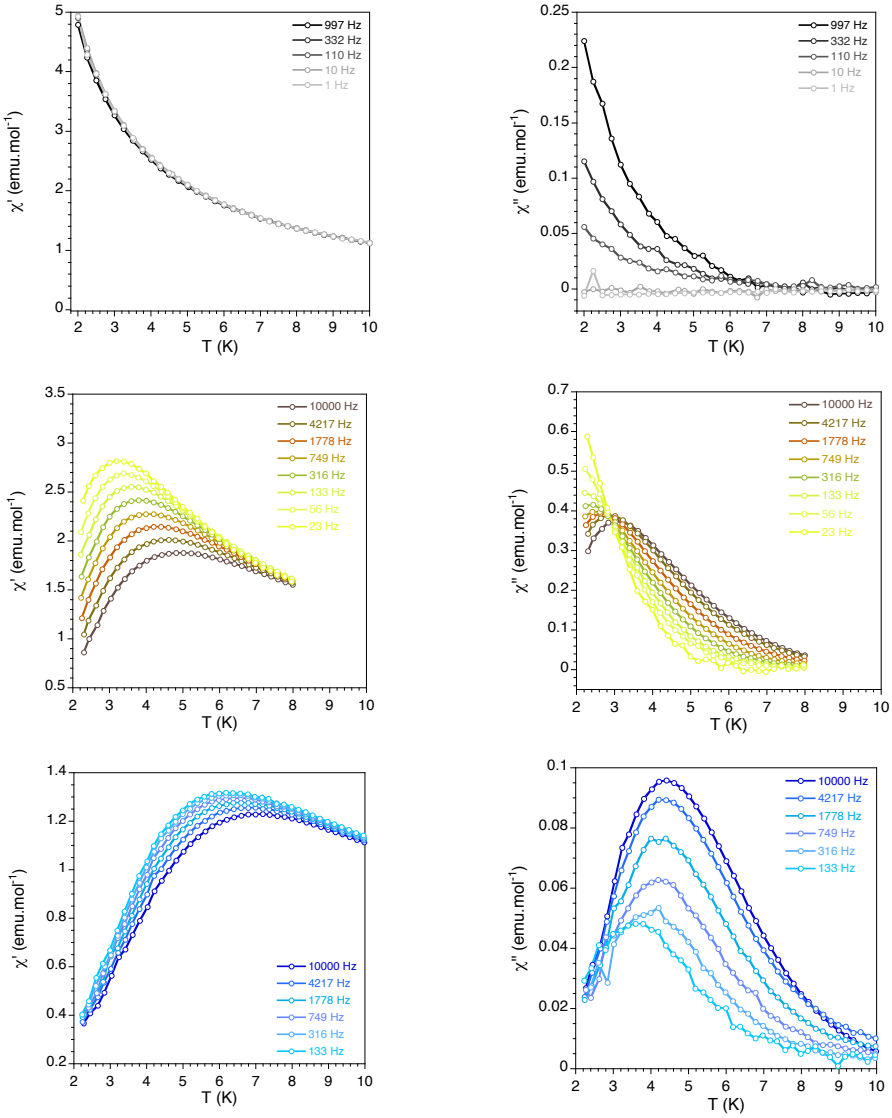

Figure 6.39: In-phase (left) and out-of-phase (right) dynamic susceptibility of 2 under different external *dc* magnetic fields (from top to bottom: 0, 2000 and 10000 G). Solid lines are included to guide the eyes.

Finally, we note that in addition to the interest of these magnetic frameworks in molecular magnetism, the dispersion of the POMs inside the big cavities provided by this porous structure leads to solids in which the polyoxometalates present an extraordinary surface area (Figure 6.40). This feature would facilitate the access of chemicals inside the framework and the interaction with POMs, making these POM-MOFs of interest in those applications in which the surface is a requirement (heterogeneous catalysis, for example).[348]

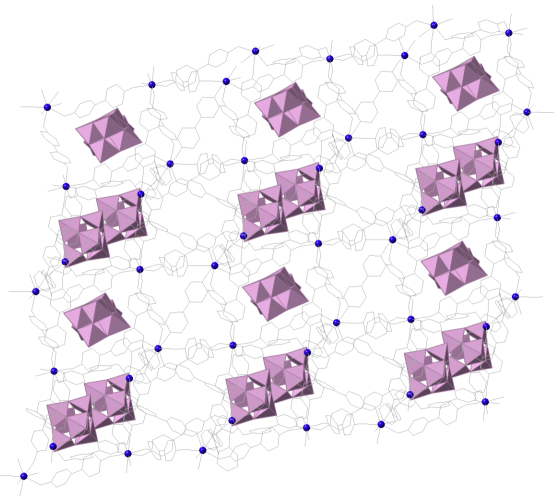

Figure 6.40: Crystal structure of $[Dy(bipyNO)_4](TfO)_3$-POM, showing the presence of the POMs in the pores. Dy atoms shown in blue, the organic ligands in grey and the POMs in purple.

6.7 Conclusions

In the previous chapter, we demonstrated the capabilities of the REC model and the SIMPRE computational package to reproduce the spectroscopic properties of lanthanide coordination compounds with halogens as donor atoms. Moreover, this served to obtain two *semi-empirical* equations that

offer an initial inexpensive prediction of the magnetic properties of new derivatives.

The works collected in the present chapter demonstrate that the REC model and the SIMPRE computational package are adequate for oxygen donor atoms. This is done by studying eight different families of complexes (LnW_{10}, LnW_{22}, $LnMo_{16}$, $LnMo_{10}$, $LnPd_{12}$, LnODA, $Ln_2(OH)_5A{\cdot}nH_2O$ and $Ln(bipyNO)_4$) with the same model. It is important to remark that demonstrating the validity of our approach for oxygen is a crucial point of the thesis. Lanthanide ions have a very high affinity for oxygen and thus complexes where the ligand coordinates by oxygen are by far the most numerous.

The first two families coordinated by oxygen atoms that have been analysed in this chapter were chosen due to their historical relevance. In particular, the family LnW_{10} is the second family of mononuclear SMMs. It was studied in 2008 due to their D_{4d} symmetry,[59] similar to the Ishikawa derivatives.[51] The process of revisiting this family via a more quantitative theoretical modelling has allowed the prediction of the second neodymium-based SIM.

In a second step, due to the similar chemical structures of the heteropolyoxowolframate (LnW_{10} and LnW_{22}) and the heteropolyoxomolybdate ($LnMo_{10}$ and $LnMo_{16}$) series, the later were proposed as interesting systems for experimental characterisation and theoretical study. In the first inspection using the REC parameters of the former families, some of the derivatives were signalled as good candidates to enhance slow relaxation of the magnetisation. Subsequently, this could be demonstrated experimentally in collaboration with researchers from the ICMol and the University of Pierre and Marie Curie in Paris. The theoretical study allowed us to explore the evolution of the properties and

the REC parameters between these structures that have different neighbours in the second coordination sphere. The efforts presented in this chapter could add two new families of POM-based mononuclear single-molecule magnets to the growing family of coordination compounds exhibiting slow relaxation of the magnetisation.

In the third section, the family of polyoxopalladates, which present a cubic coordination environment was magnetically and theoretically characterised. The lack of anisotropy makes these systems unsuitable as SMMs. However, the cubic symmetry results in an extraordinarily rich energy level structure at low temperatures. This study of the $LnPd_{12}$ family will be completed in Chapter 11 due to the potential of the Ho derivative to build a molecular spin qubit.

In spite of their historical importance, polyoxometalates are just a particular case within oxygen-donor coordination. In this aspect, it is particularly interesting to study the carboxylate ligand due to their great importance in coordination chemistry. In this study the litmus test is the determination of the spectroscopic energy levels of the LnODA series, where the spectra has been determined by photoluminescence. As we have seen, our theoretical model, when evaluated by this benchmark study, offers better results than the *ab initio* methods. This is shocking, considering *ab initio* methods in this case are computationally more expensive by at least six orders of magnitude: each single calculation with MOLCAS takes hours vs. milliseconds with SIMPRE.

Finally, we have explored other ligands that coordinate lanthanides via an oxygen atom, namely hydroxides and N-oxides. At the same time, we have increased the dimensionality of the targeted system. In 6.5 we have studied layered systems helping in the understanding of the evolution of the magnetic interactions with growing dimensionality. In 6.6 we have

predicted the magnetic behaviour of the first ordered SIM structure within a metal-organic framework.

The natural step to be taken in the next chapter, is the exploration of the next donor atom in terms of practical relevance, and the first one in historical importance: the nitrogen. It is not obvious that the present approach can offer reliable results in homoleptic systems coordinated by nitrogen atoms as we are going further away from the ionic bonding. Thus, in the next chapter we will be exploring a more challenging situation, where covalent effects are playing a key role and need to be accounted.

7 Lanthanide complexes coordinated by nitrogen atoms

The next step in the process of modelisation of different homoleptic lanthanoid coordination complexes is the study of systems coordinated by nitrogen atoms with interest in molecular magnetism. This means advancing up a steeper path in the description provided by these effective electrostatic approaches, as we are progressively moving from more ionic to more covalent coordination compounds.

In this chapter, the Lone Pair Effective Charge (LPEC) model, described in Chapter 4 (section 4.2), is applied for the first time in this dissertation. In the Ishikawa series, the trivalent cation is sandwiched between two moieties of phthalocyaninato ligands.[51] The rigid, planar structure of the phthalocyanine molecule determines the direction of the lone pair of the nitrogen donor atoms. As the electron density is not pointing towards the central ion, the LPEC correction over the REC model is necessary to simulate the crystal field effect.[294] To complete this study, we will take advantage of the spectroscopic data measured by Prof. Joris van Slageren and co-workers.[176]

It is important to remark that the LPEC model is not always required to model nitrogen donors. The seventh chapter of the thesis includes the description of the first neodymium-based single-ion magnet, which is based on pyrazolyl ligands. This study is extended to a similar example

based on dysprosium that is also coordinated by pyrazolyl ligands and shows slow relaxation of the magnetisation. In both cases there is no need to apply the LPEC model as the electron density points toward the lanthanide: these systems are modelled by the two parameters of the REC model.

7.1 Phthalocyaninato ligands

At this point we are going to navigate into the properties of the first family of mononuclear lanthanide ions exhibiting SMM behaviour, which was reported by Ishikawa *et al*. in 2003.[51] This family presents the general formula $(NBu_4)^+[LnPc_2]^-\cdot 2$ dmf (in short: $LnPc_2$, where Ln = Tb, Dy, Ho, Er; dmf = N,N-dimethylformamide), with a 'double-decker' structure and phthalocyaninato anions as ligands (Figure 7.1). That seminal work inspired a plethora of more complicated derivatives, e.g. triple-deckers,[349] oxidised double-deckers for enhanced magnetic anisotropy[350] or substituted double-deckers for processability,[351] among others. We chose this example because its large historical relevance in the field of molecular nanomagnetism. This family of complexes crystallises in the space group $P\bar{1}$, where the inversion centre is between two molecules. Hence the site symmetry is C_1. Describing the crystal field by means of the crystal field Hamiltonian up to 27 CFPs could be included. Nevertheless, the idealised symmetry is very close to D_{4d}.

As in this family the electron lone pair of nitrogen is not located along the radial Ln-N direction, it is necessary to include the horizontal displacement (D_h) vector (defined in Chapter 4, section 4.2).[294] Both vectors, D_h and D_r, were applied to the original position of each nitrogen nucleus,

determining the position of the effective centre of charge. Vector D_h is in the plane NCC containing the ligand atom N and its two covalently bonded C atoms. This vector is also parallel to the bisection of the NCC angle, and the resulting effective distance after applying such a displacement simulates the effective position of the centre of charge of a lone pair. For nitrogen lone pairs, the centre of charge is expected to be at a distance between 0.5 and 1.0 Å apart from the nucleus, but the effective "size" of this electron cloud can easily be more than three times larger.[352] As described in Chapter 4, vector D_r is applied to the effective distance once applied D_h. Note that D_r reflects, like in the REC model, the effective charge resulting from the sharing of the ligand electron density by the lanthanide ion. This correction does possess physical sense due to the fact that the nearest part of the electron cloud to the lanthanoid induces a more marked effect than the areas placed further away.

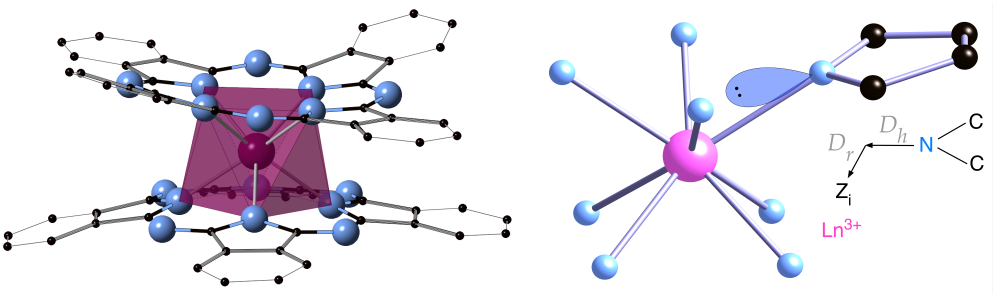

Figure 7.1: (left) Crystal structure of $[LnPc_2]^-$; (right) first coordination sphere around the lanthanide and lone-pair representation.

Then, we performed a *semi-empirical* study of the crystal field splitting of the later lanthanoid analogues reported by the group of Ishikawa. The theoretical characterisation was carried out in two different phases. The

first one was a preliminar study of these complexes, reported in 2012, using a set of idealised structures and the experimental magnetic susceptibility data (LPEC A).[294] In the second phase, we departed from the X-ray crystal structures determined for the Dy, Ho and Er derivatives in 2014.[176] For this more accurate description, we combined magnetic susceptibility data with observed CF transitions by FIR and INS spectroscopies within the ground Russell-Saunders multiplets (LPEC B).

Because of the lack of crystal structures for the whole series in our first analysis, we slightly idealised the structure by assuming a C_4 symmetry but keeping the experimental torsion angle between the two phthalocyaninato ligands. With this assumption and after applying the displacement vectors and charge scanning, the minimisation procedure found a reasonable good agreement with the experimental χT curves of the whole series (see Figure 7.2) when Z_i = 0.63, horizontal displacement D_h = 0.195 Å and radial displacement D_r = 0.48 Å.

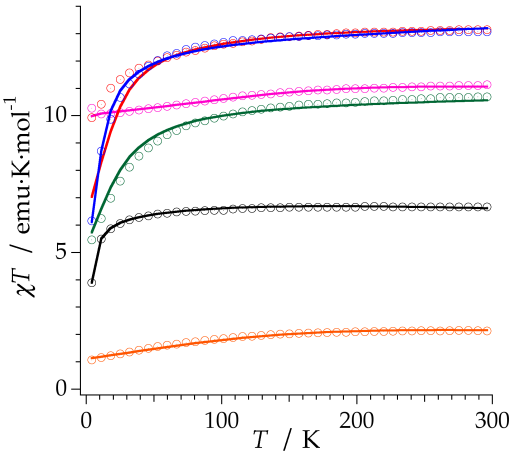

Figure 7.2: Fitting of the experimental magnetic properties of the series of [Ln(Pc)$_2$] SIMs from LPEC A model: Dy (red), Ho (blue), Tb (pink), Er (green), Tm (black) and Yb (orange).

The difference between this procedure based on the LPEC model and the original phenomenological model used by Ishikawa (CFPs and paramagnetic shift phenomenological fit) lies in the use of parameters that modify the effective coordinates instead of the use of CFPs as fitting parameters. To avoid overparameterisation, the model of Ishikawa assumes a linear dependence of all three diagonal parameters with the number of electrons.[55] Instead, the fitting parameters of the effective electrostatic models developed in this thesis are only the position and value of the point charges. That enables us to introduce a richer Hamiltonian without such overparameterisation problems and without assuming arbitrary variations of the ligand field terms.

Compared with the nuclear positions of the nitrogen atoms, the horizontal displacement of the LPEC model means that the effective barrier has crossed the node at the "magic" polar angle $\theta = \arccos[(1/3)^{-2})] \approx 54.7^{o}$. This translates into a sign change of the B_2^0 so that it is negative for Tb^{3+} accounting for the SMM behaviour observed in this compound, i.e. stabilising $M_J = \pm 6$ in the ground state. The total displacement of approximately 0.6 Å is well within the expected volume of the electron cloud, not very far from its charge centroid. In fact, for nitrogen lone pairs, the centre of charge is expected to be at a distance between 0.5 and 1.0 Å apart from the nucleus, but the effective "size" of this electron cloud, can easily be, depending on its definition, more than three times larger.

Applying the whole-series fit to the terbium derivative, a well-isolated ground state doublet composed by |+6> and |-6> was obtained, with the rest of sublevels excited by more than 300 cm^{-1} and bunched up in a window of less than 150 cm^{-1}. This picture offered by the model is coherent with its known SIM properties, allowing the slow relaxation of the

magnetisation. Ishikawa provided essentially the same description. In his study, the first excited sublevel lies at about 400 cm^{-1} and the lowest substrates are |+6> and |-6>. A crucial difference between both energy levels schemes is the effect of the fourth-order extradiagonal parameters (B_{44} and B_{64}), which enable a mixing between |+6> and |-6> doublet at zero field. This mixing arises from three consecutive steps when applying the fourth-order parameters: i.e. from |+6> to |+2>, to |-2> and finally, to |-6>, and analogously, from |-6> to |+6>, passing through the same M_J states. That is the reason why the mixing is very weak and cannot give rise to a noticeable tunnel splitting, as does occur in other examples of the literature. On a different manner, it also means that a minimal longitudinal magnetic field -necessary to find a level crossing where tunnelling is not forbidden by the nuclear spins- will recover the purity of the M_J states. Due to these peculiarities, $TbPc_2$ is an interesting example where the SIM behaviour is not destroyed by extradiagonal terms allowing a mixing within the ground state.

In a more recent approach to this family, we used the direct observation of CF excitations within the ground Russell-Saunders multiplets to study the Dy, Ho and Er derivatives. We took advantage of the article published by van Slageren *et al.*,[176] which is one of the first works performing inelastic neutron scattering, and the first far infrared spectroscopic investigation, of lanthanide-based SIMs. In that work, the crystal structures of the three derivatives were resolved. We scanned the three parameters of the LPEC model (D_h, D_r and Z_i) using the real structures in order to reach the minimum error in the determination of the magnetic susceptibility curves and the spectroscopically determined energy levels. This phenomenological way to model the system although not predictive, allowed a better reproduction of the observables. The collective

solution generated the following result: D_h = 0.3 Å, D_r = 0.2 Å and Z_i = 0.86. However, the individual parameters were varied around this solution to offer a better phenomenological explanation in terms of the LPEC model. The results of these updated calculations were compared with the experiment for the Dy, Ho and Er derivatives. In Figures 7.3-7.5, the results obtained by the LPEC with the idealised D_{4d} structure (LPEC Ideal (A)) fitting the magnetic data, the phenomenological fit of Ishikawa (FIT CFPs (B)) and the CASSCF calculations using the experimental crystal structure embedded in five layers of point charges and basis 2 (see supporting information of Ref. 176) are also included.

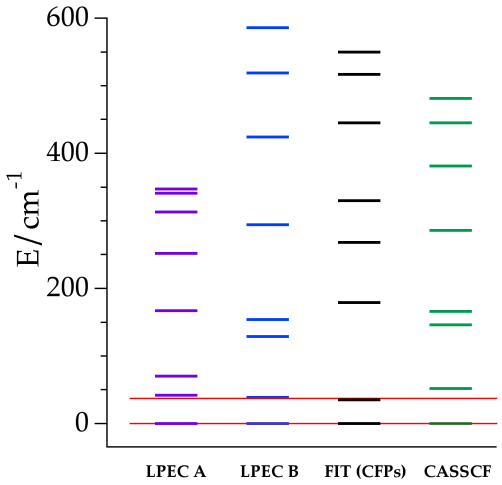

Figure 7.3: Crystal field energy level scheme of the ground *J* multiplet of $DyPc_2$. Thin red lines: experimental optical spectrum. Thick lines: LPEC model using the idealised D_{4d} structure and collective fit of magnetic data, LPEC model using the real structure and fitting magnetic and spectroscopic data, phenomenological fit of CFPs, CASSCF predicted energies including spin-orbit effects, as indicated at the axis (details in the text).

As can be observed in Figure 7.3, the four different approaches reproduce pretty well the first excited state of $DyPc_2$. This excited doublet was observed at 37 cm^{-1}. Logically, the LPEC methods (42 and 39 cm^{-1}) and the phenomenological fit (35 cm^{-1}) offer a better reproduction of the gap with that excited sublevel. Nevertheless, the three procedures include a fit of experimental properties, whereas the more expensive CASSCF calculations (52 cm^{-1}) are providing a prediction using the real structure as an input.

It is important to remark the discrepancy in the ground doublet wave function of the LPEC Ideal (A) with the rest of the calculations. This model described a ground doublet composed practically 100% of ±11/2 with the first excited doublet determined by ±13/2. The ground and excited Kramers doublets were inverted with respect to the phenomenological and *ab initio* approaches. The lower agreement of LPEC Ideal with the magnetic susceptibility data for the Dy derivative, especially at low temperature (Figure 7.2), indicates that the wave functions of the ground doublet are not correctly determined.[176] The LPEC X-Ray (B), which uses real structure and spectroscopic data, provides a description that coincides with the phenomenological and CASSCF calculations (ground state ±13/2), correcting the previous determination. Regarding the total CF splitting, LPEC Ideal generates a smaller one comparated with the results of the LPEC X-Ray and phenomenological fit, as well as with the CASSCF prediction. We can envisage that the total splitting of the ground *J* multiplet is between 500 and 600 cm^{-1}. According to the spectrochemical series of ligands it is expected that ligands with nitrogen as the donor atom create a stronger ligand field (they lie at the right end of the series compared with oxygen- or halogen-donor atoms) as they are π-acceptor ligands.

In the case of the Ho analogue (Figure 7.4), all the models also give an acceptable result for the first excited doublet. In this case, only the LPEC models correctly predicts that there are four doublets below 100 cm^{-1}. The second fitting using LPEC and X-Ray structure provides an excellent reproduction of the four determined excited sublevels (experimental: 19, 53, 92 and 189 cm^{-1}; LPEC X-Ray: 17, 53, 93, 189 cm^{-1}). In the case of the phenomenological fit, only three doublets appear at the region under 100 cm^{-1}, whereas, on the contrary, an aglomeration of six energy doublets appear in the predicted scheme using the MOLCAS package. A similar picture was observed in the study of Dy and ErODA (Chapter 6) where the results from this model were benchmarked with spectroscopic data. As in the preceding scheme, the phenomenological fit gives the largest total field splitting, whereas, in this case, such property is similar for LPEC Ideal and CASSCF.

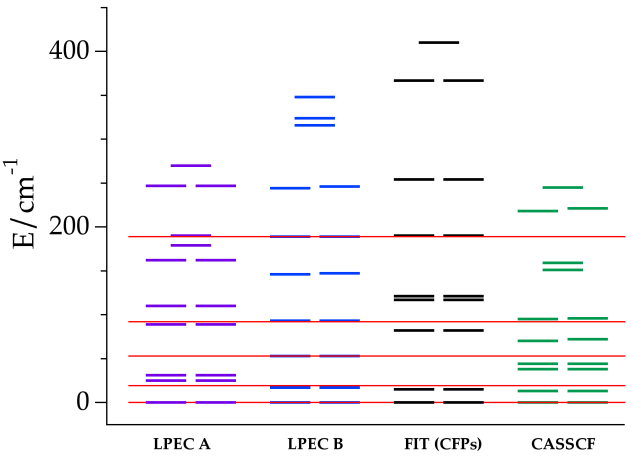

Figure 7.4: Crystal field energy level scheme of the ground *J* multiplet of $HoPc_2$. Thin red lines: experimental optical spectrum. Thick lines: LPEC model using the idealised D_{4d} structure and collective fit of magnetic data, LPEC model using the real structure and fitting magnetic and spectroscopic data,

phenomenological fit of CFPs, CASSCF predicted energies including spin-orbit effects, as indicated at the axis (details in the text).

For the Er derivative (Figure 7.5), only one state at 74 cm^{-1} was accessed by spectroscopic techniques. The energy of this excited doublet was perfectly matched by the LPEC X-Ray. The rest of the models: LPEC Ideal (58 cm^{-1}), phenomenological fit (102 cm^{-1}) and CASSCF (59 cm^{-1}) deviated between 20-30% up or down. The most deviated in this derivative is the determined by the Ishikawa method, probably due to intrinsic limitations derived by the assumption of the linear correlation of CFPs.

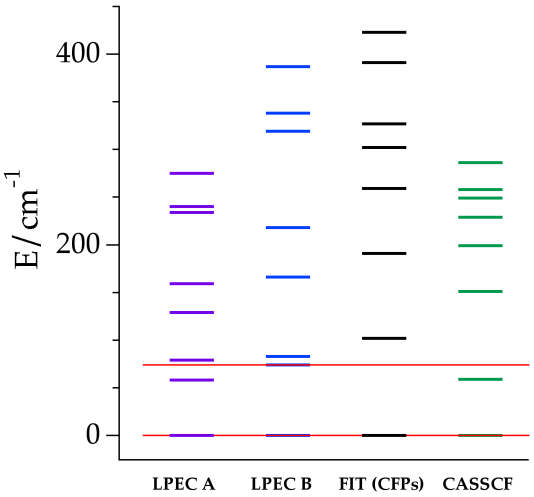

Figure 7.5: Crystal field energy level scheme of the ground J multiplet of $ErPc_2$. Thin red lines: experimental optical spectrum. Thick lines: LPEC model using the idealised D_{4d} structure and collective fit of magnetic data, LPEC model using the real structure and fitting magnetic and spectroscopic data, phenomenological fit of CFPs, CASSCF predicted energies including spin-orbit effects, as indicated at the axis (details in the text).

Finally, it is worth to plot the calculated temperature-dependence magnetic susceptibility curves of the three examples togheter with the theoretical calculations of LPEC X-Ray (Figure 7.6). As expected, due to the excellent reproduction of the spectroscopic transitions at low temperatures with the model, the theoretical lines perfectly reproduce the experimental data.

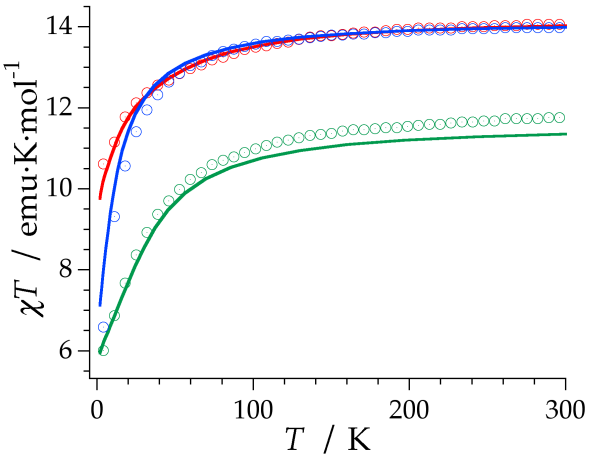

Figure 7.6: Experimental (circles) and fitted by the LPEC B (solid lines) χT product of the series $LnPc_2$: Dy (red), Ho (blue) and Er (green) from 2 to 300 K.

7.2 Pyrazolyl ligands

Now we will focus on two lanthanoid SIMs based on pyrazolyl ligands that were reported by the Long group in 2011-2012: $NdTp_3$ and $Dy(H_2BPz^{Me2}2)_3$.[88,353] Both complexes are coordinated by nitrogen donor atoms from pyrazole rings in a D_{3h} crystal field. The main objective of this analysis is to extend and prove the versatility of the REC model to estimate

the splitting of a lanthanide ion ground multiplet caused by the ligand field.[354]

$NdTp_3$ is the first neodymium mononuclear SMM reported in the literature.[88] The molecular system is formed by a neodymium trivalent ion surrounded by three trispyrazolylborate (Tp^-) ligands. The magnetic ion is directly coordinated to nine pyrazole rings in a crystallographically exact D_{3h} tricapped trigonal prism coordination environment (Figure 7.7).

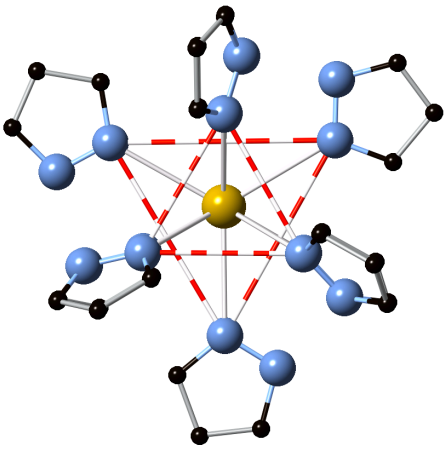

Figure 7.7: Eclipsed view of the tricapped trigonal prismatic coordination structure of $Nd(Tp)_3$; Hydrogen atoms are omitted for clarity.

For this example, two Kramers doublets into the Stark sublevels placed at 107 and 301 cm^{-1} had been determined, as the absorption spectrum was measured experimentally by Reddmann *et al*.[355] Those authors derived a truncated CF splitting patern, fitting the parameters of the phenomenological CF Hamitonian. Thus, as we did in the second procedure described in Chapter 5 with the systems coordinated by halogen atoms, we could use the phenomenological CF parameters extracted from the whole spectrum (r.m.s. deviation of 11 cm^{-1} for 48 assigments) to be

fitted. This allowed us to parameterise the ligand in terms of the effective electrostatic approach. Because the lone pairs of the nitrogen donor atoms are pointing almost toward the metal site, we employed the REC model.

Given the high symmetry of the coordination environment of $NdTp_3$, the crystal field splitting might be described by the simplified CF Hamiltonian:

$$H_{CF}(J) = \sum_{k=2,4,6} B_k^0 O_k^0 + B_6^6 O_6^6 \qquad (7.1)$$

The four CFPs that were determined from the phenomenological fit of experimental data are B_{20} = -512 cm^{-1}, B_{40} = -969 cm^{-1}, B_{60} = 153 cm^{-1} and B_{66} = 828 cm^{-1}, expressed in Wybourne notation. The collective fit of the four CFPs was carried out using the crystallographic coordinates of the nitrogen atoms bonded to the lanthanide ion and varying R_i (from the original postion until R_i-1.5 Å) and Z_i (between 0 and 1). The mininum relative error E_{Bkq} = 0.65 was reached when D_r = 1.378 Å and Z_i = 0.047. These parameters applied to the initial coordinates generated the following CFPs: B_{20} = -149 cm^{-1}, B_{40} = -1237 cm^{-1}, B_{60} = 112 cm^{-1} and B_{66} = 868 cm^{-1}. Here it is important to recall Equation 5.3 to compare the estimation of D_r based on this *semi-empirical* equation and the obtained value. For that, we must take into account the Pauling electronegativity of the neodymium (1.14) and the nitrogen (3.04) atoms, as well as the coordination number of the molecule (CN = 9) and the valence of the cation (+3). This results in a covalent correction of D_r = 1.385 Å, which is in excellent agreement with the fitted value. In spite of the difficulties that the effective electrostatic model may have when dealing with nitrogen-donor atoms, the model respects the trends detected in the halogens: direct relation between the coordination number and the radial displacement, and inverse relation between Pauling electronegativity of the donor atom and the radial displacement.

As mentioned above, due to the high symmetry of the system, the Hamiltonian only includes the diagonal terms and the symmetry-allowed CFPs (Equation 7.1). In particular, as a consequence of the symmetry-allowed B_{66}, one can understand that the mixing in the wave function occurs between M_J values that differ by six units i.e. between $M_J = \pm 7/2$ and $M_J = \mp 5/2$, or between $M_J = \pm 9/2$ and $M_J = \mp 3/2$. For this complex, according to this effective description, the ground doublet is a mixture involving $0.54|+5/2\rangle + 0.46\ |-7/2\rangle$ and $0.54|-5/2\rangle + 0.46\ |+7/2\rangle$. This is compatible with the reported SMM behaviour because there is no direct mixing between + M_J and – M_J in the ground state. The first excited state was determined at 103 cm^{-1} (experimental at 107 cm^{-1}), and it is a doublet mixed between $\pm 3/2$ (64%) and $\mp 9/2$ (36%). The calculated energy level scheme and the phenomenological one (Fit CFPs) reported in Ref. 355 are compared with the spectroscopic lines in Figure 7.8.

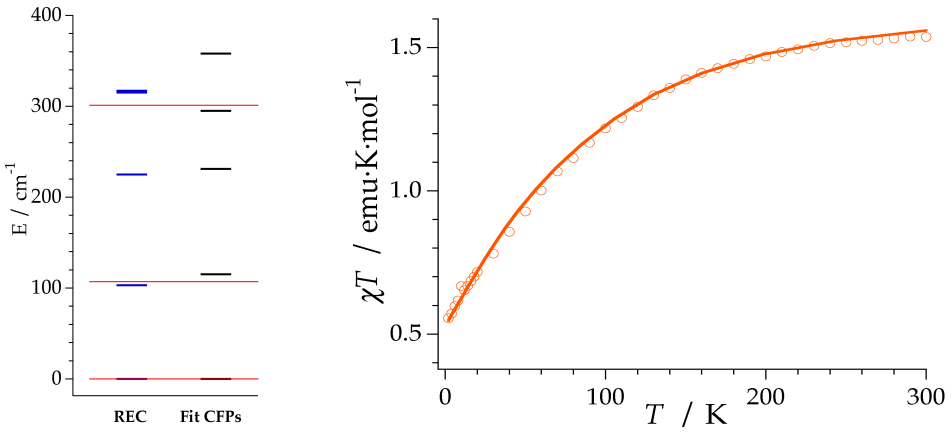

Figure 7.8: Energy level scheme of $NdTp_3$ determined by the REC model (left) and fitting the spectroscopic information by Reddmann *et al.*[355] (right); Experimental

energy levels: thin red lines; Temperature-dependent magnetic susceptibility: solid lines (REC model) and open circles (experiment).

Figure 7.8 also includes the temperature-dependence of the magnetic susceptibility calculated by the REC model and the experimental one. As can be seen, the agreement is excellent for all the range of temperatures.

Subsequently, we used the information provided by the fitting of the CFPs of $NdTp_3$ to study a SMM with a related molecular structure and similar ligands bonded to the metal ion. $Dy(H_2BPz^{Me2}{}_2)_3$ is coordinated by three dihydrobis-(dymethylpyrazolylborate) ligands (see Figure 7.9 (left)).[353] The environment of the trivalent dysprosium centre is trigonal prismatic with an approximate D_{3h} symmetry. To quantify the deviation of the real structure from an ideal trigonal prism, we used the SHAPE software.[288] Using the corresponding idealised D_{3h} trigonal prism as a target structure a value of $S_P = 0.040$ was obtained. Therefore, due to this excellent agreement between the real and the ideal structure with chemically insignificant distortions, we were able to use the ideal coordinates in order to explain the magnetic properties with only four CF parameters. The coordinate system was referred aligned with the main symmetry axis of the trigonal prism.

In the absence of more experimental information for $Dy(H_2BPz^{Me2}{}_2)_3$, the radial contraction D_r was calculated using the *semi-empirical* Equation 5.3, giving an approximated value of D_r = 0.90 Å. Owing to the related molecular nature of the ligands, which results in a similar electrostatic effect of the nitrogen donor atoms over the neodymium cation, the effective charge was estimated keeping the relation $f = D_r \cdot Z_i$ in the $NdTp_3$ complex as a constant. Then, we replaced the value of D_r obtained by solving the Equation 5.3. This yielded a value of $Z_i = 0.072$.

Within these two parameters and the chemical structure, we calculated the CFPs and the energy level scheme of this mononuclear SMM. The wave function that describes the ground doublet is a mixture between $M_J = \pm 15/2$ (75%) and $M_J = \pm 11/2$ (15%). The first excited level lies at about $\Delta = 11$ cm^{-1} with a wave function dominated mixed between $M_J = \pm 7/2$, $\pm 5/2$ and $\pm 11/2$. Thus, the description of the lowest levels of the compound supported the reported SMM behaviour of the complex.

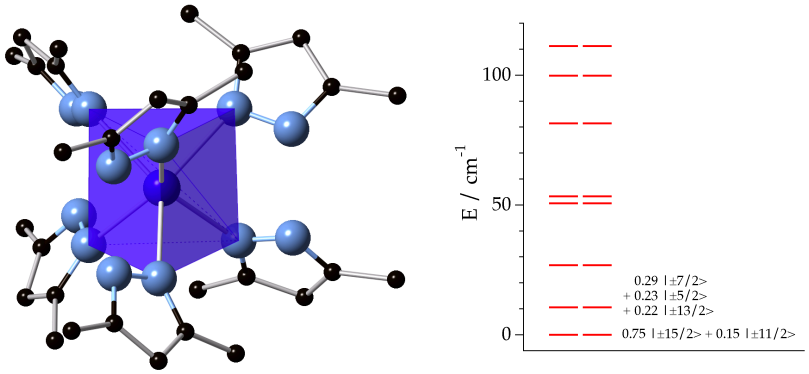

Figure 7.9: (left) Trigonal prismatic coordination structure of $Dy(H_2BPz^{Me2}_2)_3$; (right) its calculated energy level scheme and the weight of the M_J contribution to ground and first excited doublets wave functions determined by the REC model.

7.3 Conclusions

In this chapter, we have provided a theoretical description of the magnetic properties of the first family of lanthanoid SIMs, the series $LnPc_2$, and two pyrazolyl-based SIMs with neodymium and dysprosium trivalent ions as central ions. By doing so, we have shown that our model is adequate to predict the effect of nitrogen-donor ligands in the CF of lanthanide ions.

Due to the rigid, planar character of the phthalocyaninato ligands, in the first example, we have used the LPEC model. From it, we have successfully described the spectroscopic and magnetic properties of some of the derivatives of the family. This model has been applied two times. The first one uses idealised crystal structures and a collective fit of the magnetic susceptibility data of the Tb-Tm compounds. As a second alternative, we have taken advantage of the resolved crystal structures of the Tb, Ho and Er complexes and the INS and FIR experimental measurements performed recently to improve the description. The results have been compared (a) with the fit performed by Ishikawa, which assumed a correlation of the CFPs with the number of f-electrons, and (b) with the predictions provided by CASSCF methods. We have seen that the LPEC model has provided an inexpensive and fair description of these systems, simulating the covalent effects of the surrounding ligands.

In the second part of this chapter, we have studied two complexes in which the lanthanide is coordinated to pyrazolyl-based ligands. In this case, the lone pairs of the nitrogen donor atoms point toward the lanthanide ion, thus allowing their modelling in terms of the REC model. The first complex analysed herein is also the first neodymium-based single-ion magnet, which was reported by the Long group. The description offered by the model is fully compatible with the slow relaxation of the magnetisation observed in the compound. Furthermore, the radial displacement extracted from the fit of the phenomenological CFPs coincides with the calculated one using the Equation 5.3. This supports the capability of the REC model to obtain reliable inexpensive predictions for new derivatives in the future. As an example, we have applied the equations presented in Chapter 5 and the parameters gathered in the study of $NdTp_3$. This has allowed an estimation of the energy level scheme of a

Dy^{3+} bis(pyrazolyl)borate single-molecule magnet, achieving a ground doublet wave function which supports the observed SMM behaviour.

This chapter has completed the trilogy presented in this second part of the thesis, concerning the application of the developed electrostatic models to homoleptic lanthanide complexes coordinated by halogen, oxygen and nitrogen atoms. The great potential of these approaches has been shown exhaustively, especially when dealing with more ionic chemical bonds, but also offering promising results in systems where covalency plays a fundamental role. In the following part of the thesis, we will show that this model can also be used to study some of the main current challenges in the field: (i) the modelling of uranium SIMs, (ii) the study of molecular anisotropy in SIMs, (iii) the modelling of heteroleptic complexes combining oxygen and nitrogen donor atoms in the same molecule, and (iv) the use of these systems as molecular spin qubits.

3

Current challenges

8 Beyond the lanthanides: modelling of uranium SIMs

8.1 Introduction

The next step in the rationalisation and modelling of f-block mononuclear SMMs is to extend the study to those nanomagnets based on uranium as a magnetic centre.[84] These systems are very promising in molecular magnetism because they could combine the best features of 3d and 4f nanomagnets, since 5f electrons can lead to the simultaneous presence of strong ligand-field potential and magnetic superexchange coupling.[96,356–358] Unfortunately, this promise of extraordinary properties is hindered by the extraordinary theoretical problems they present for their modelling.

In lanthanides, the crystal field is the weakest interaction (not considering hyperfine coupling and external applied fields) due to the limited radial extension of the f-orbitals. This situation is different in actinide complexes because the 5f orbitals are more diffuse and both spin-orbit coupling and ligand field are stronger. Thus, interelectronic repulsion ($\approx 10^4$ cm^{-1}), spin-orbit coupling ($\approx 10^3$ cm^{-1}) and ligand field potential ($\approx 10^3$ cm^{-1}) are roughly of the same order in terms of energy. This has consequences in the modelling of actinides complexes, becoming more complicated than for most $3d^N$ and $4f^N$ systems, since a coupling scheme

based on the Russell-Saunders approximation provides poor outcomes.[152] In particular, intermediate coupling calculations have shown that for $5f^2$, $5f^3$ and $5f^4$ configurations the Russell-Saunders state makes up for around 80% of the true ground state.[359,360] This can be put in perspective by comparing it with the favourable case of lanthanides, e.g. 94% in the case of Er^{3+}, and with the worst scenario for other actinoids, Am^{3+} (44.9%). This means that for the U^{3+} the Russell-Saunders accounts for 84.1% of the ground state. The accuracy would be even worse for U^{4+}, with just a 77.5% of the ground state stemming from the Russell-Saunders wave function.[361] These limitations have to be taken into account, as they put an upper limit in the exactness of the results when using a computational package as SIMPRE that only considers the ground multiplet in the CF Hamiltonian. Hence, effects not included in the Russell-Saunders approximation should be included through effective corrections.

Because of experimental difficulties, only a handful of examples of SIMs based on actinoids have been characterised and reported so far (see Chapter 1, section 1.1). In the first step we will focus on the study of the first three reported uranium SIMs, $U(Ph_2BPz_2)_3$, $U(H_2BPz_2)_3$ and UTp_3, all based on pyrazolyl ligands.[93] Through this study, we will test the possibilities of the REC model for the description of these systems, within the above-mentioned fundamental limitations of the Russell-Saunders approximation. In a second step, we will describe the first attempt to model the magnetic behaviour of the tetravalent uranium compound with a radical azobenzene ligand $[\{(SiMe_2NPh)_3\text{-tacn}\}U^{IV}(\eta^2\text{-}N_2Ph_2^*)]$.[362] As the ground state wave function of tetravalent uranium is not properly described by the Russell-Saunders approximation, for this case we will use a Hamiltonian that includes both the spin-orbit coupling and the ligand field. As this coupling scheme is not yet included in SIMPRE, for this

particular task we used the CONDON package.[151] To facilitate the study of the tetravalent uranium complex, we will analyse the behaviour of its precursor, the trivalent uranium compound $[U^{III}\{(SiMe_2NPh)_3\text{-tacn}\}]$.[363]

8.2 Modelling the properties of uranium SIMs

The first complex we are going to deal with is the tris[hydrotris(1-pyrazolyl)borato]uranium(III), in short: UTp_3, which is formed by an uranium trivalent ion surrounded by three trispyrazolylborate (Tp^-) ligands.[88] The molecular structure is analogous to $NdTp_3$ (described in the preceding chapter), where the magnetic ion is directly bonded to nine pyrazole rings in a crystallographically exact D_{3h} tricapped trigonal prism coordination environment (Figure 8.1).

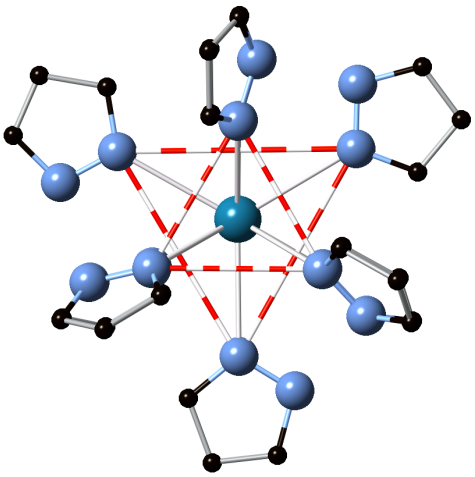

Figure 8.1: Eclipsed view of the tricapped trigonal prismatic coordination structure of $U(Tp)_3$; hydrogen atoms are omitted for clarity.

As in the case of $NdTp_3$, the experimental absorption spectrum was available in the literature. The energy level scheme was determined by

Apostolidis *et al*. in 2010.[364] We could use the phenomenological ground multiplet energy levels to parameterise the system in terms of the REC model. Such Stark sublevels were extracted from the diagonalisation of the full Hamiltonian taking into account high-quality data from all the *J* states. Again, the LPEC model was not necessary because the lone pairs point almost toward the metal site. Due to the high symmetry of this example, the CF splitting might be described by the simplified CF Hamiltonian (Equation 8.1):

$$H_{CF}(J) = \sum_{k=2,4,6} B_k^0 O_k^0 + B_6^6 O_6^6 \qquad (8.1)$$

The phenomenological CFPs are B_{20} = -1124 cm^{-1}, B_{40} = -2457 cm^{-1}, B_{60} = 440 cm^{-1} and B_{66} = 2529 cm^{-1}, expressed in Wybourne notation. Such CFPs have the same sign as the ones extracted for $NdTp_3$ (same coordination environment), but they are larger due to the more intense CF potential in $5f^N$ complexes. The fit of the energy levels calculated by Apostolidis *et al*. was performed using the crystallographic positions of the nitrogen atoms as an input. A satisfactory fitting is achieved (relative error E_{Bkq} = 0.91) when D_r = 1.353 Å and Z_i = 0.0223. For the radial displacement, the *semi-empirical* Equation 5.3, using the electronegativity of the uranium atom (1.38) gives $D_r \approx$ 1.310 Å, that is actually very close to the fitted value. These parameters are very similar to the ones we obtained for nine-coordinated $NdTp_3$. This is expected owing to the very similar character of the ligands, which results in a similar electrostatic effect of the nitrogen donor atoms over the uranium cation. The application of the REC parameters to the real coordinates yielded the following values for the CFPs: B_{20} = -50 cm^{-1}, B_{40} = -1960 cm^{-1}, B_{60} = 249 cm^{-1} and B_{66} = 1766 cm^{-1}. Compared with the phenomenological ones, the largest discrepancy is found for B_{20}. A similar

pattern was detected in the study of $NdTp_3$, but for uranium this discrepancy is more important as 5f orbitals are involved and the limitations of the model are more severe.[365] This indicates that a description based in the REC model should not be adequate for the modelling of the properties of the excited *J* states (e.g. optical properties of the system).

Both results (phenomenological and REC model) show that the diagonal B_{40} crystal-field parameter dominates the splitting. The extradiagonal parameter B_{66} plays a fundamental role as it is in the same order of magnitude. In particular, as a consequence of the symmetry-allowed B_{66}, one can understand that the mixing in the wave function occurs between M_J values that differ by six units i.e. between $M_J = \pm 7/2$ and $M_J = \mp 5/2$, or between $M_J = \pm 9/2$ and $M_J = \mp 3/2$.

The energy level scheme generated by the REC model is calculated with SIMPRE (Russell-Saunders approximation) and CONDON (full Hamiltonian). Then, the calculations are compared with the first excited level (determined experimentally at 270 cm^{-1}) and the results obtained with the phenomenological CFPs and the full Hamiltonian. In the CONDON package we have included the following assumptions: ζ_{5f} = 1516 cm^{-1}, F^2 = 36305 cm^{-1}, F^4 = 26462 cm^{-1}, F^6 = 23130 cm^{-1},[152] and D_{3h} ligand field. The results are plotted in Figure 8.2, as can be seen in this case, there is almost no difference between the calculations using the SIMPRE and CONDON packages for the same set of CFPs. This can be attributed to the character of the ligands and the molecular geometry, which generate a relatively small total CF splitting (358 cm^{-1} in $NdTp_3$ and 805 cm^{-1} in UTp_3, according to the phenomenological approach). The ground doublet of the first excited *J* multiplet in UTp_3 was determined at 4354 cm^{-1}. Thus, the spin-orbit coupling is larger than the ligand field potential, and that explains why the restricted and complete approach gives similar results in this particular

example. Of course this cannot be a general assumption for uranium coordination complexes. Molecular systems with a larger crystal field splitting will make the Russell-Saunders approximation not feasible, offering very poor results.

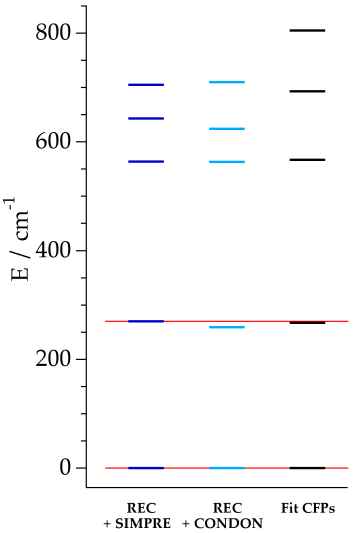

Figure 8.2: Kramers doublets for UTp_3 determined by the REC model in the SIMPRE (blue) and CONDON (sky blue) packages, phenomenological fit from Ref. 364 (black) and the experiment (red thin line).

Regarding the wave functions of these sublevels, the phenomenological approach based on the absorption spectrum of UTp_3, leads to a ground state dominated by $\pm 5/2$. The first excited state is calculated to lie at 267 cm^{-1} (very close to the experimental value determined at 270 cm^{-1}) with a predominance of $M_J = \pm 3/2$. The three Kramers' doublets that are placed upper in energy (labelled as $^1\Gamma_8$, $^2\Gamma_7$ and $^2\Gamma_9$) are dominated by $\pm 1/2$, $\pm 7/2$ and $\pm 9/2$ respectively. This coincides with the calculated wave functions using the REC model in the SIMPRE

package. Such ground multiplet sublevels, ordered from the lowest to the highest in energy, are governed by 53% of ±5/2, 62% of ±3/2, 100% of ±1/2, 53% of ±7/2 and 62% of ±9/2. These coincidences, in spite of the discrepancies observed in the determination of the CFPs, supported the use of these calculations as starting point for the understanding of the properties of uranium SIMs, as they are computationally inexpensive and may offer useful information about the lowest sublevels and ground state wave functions.[93] Of course, if we introduce the calculated parameters in a more complete Hamiltonian, including the appropriate free ion terms and the CF terms, and incorporating the intermediate coupling and the *J* mixing, the results will have more pronounced divergences, especially in the determination of the energy levels.[152] A complete methodology for the full understanding of the electronic structure of uranium coordination complexes is still an open problem in theoretical spectroscopy, molecular optics and molecular magnetism. Apart from the unsuitability of the two coupling schemes (Russell-Saunders and also jj coupling) to describe the properties of uranium, configuration interaction is also important in actinides. This leads to 20 free ion parameters and between 2 and 27 CFPs, depending on the molecular structure and total angular momentum *J*.

However, in spite of the approximations and limitations of the model, the experimental susceptibility curve of UTp_3 can closely be reproduced (shape and order of magnitude) using the previously reported set of CFPs (Figure 8.3), both in the SIMPRE and the CONDON packages. The model was also able to give a good estimation of the main contribution to the wave function for each sublevel when compared to the phenomenological description of the complex. As mentioned above, we attribute this success to the molecular symmetry and the character of the bis(pyrazolyl)borate ligands.

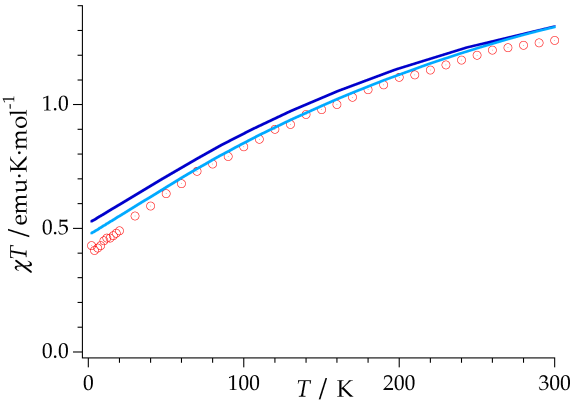

Figure 8.3: χT product for UTp_3. Open circles: experimental data; solid line: theoretical estimation of the REC model in the SIMPRE (blue) and CONDON (sky blue)

Following with the theoretical characterisation of uranium SIMs, we analysed the compounds $U(Ph_2BPz_2)_3$ and $U(H_2BPz_2)_3$,[85,87] which are structurally very similar and thus were studied together. Both are U^{3+} complexes coordinated by three bis(pyrazolyl)borate ligands (see Figure 8.4). The main difference between them lies in the ligands which are diphenylbis(pyrazolylborate) in the first case and dihydrobis(pyrazolylborate) in the second one. This fact produces important differences in the crystal structure but only minor distortions in the coordination sphere. Thus, in both cases the environment of the U^{3+} centre is trigonal prismatic with an approximate D_{3h} symmetry. To quantify the deviation of both real structures to the ideal trigonal prism, we used the SHAPE software.[288] Using the corresponding idealised D_{3h} trigonal prisms as target structures, one obtained values of $S_P = 0.268$ for $U(Ph_2BPz_2)_3$ and $S_P = 0.260$ for $U(H_2BPz_2)_3$. All other hexacoordinated target structures result in values of $S_P > 10$, supporting the view that these structures are slightly

distorted trigonal prisms. Therefore, we referred our coordinate system aligned with the main symmetry axis of the trigonal prism in both cases.

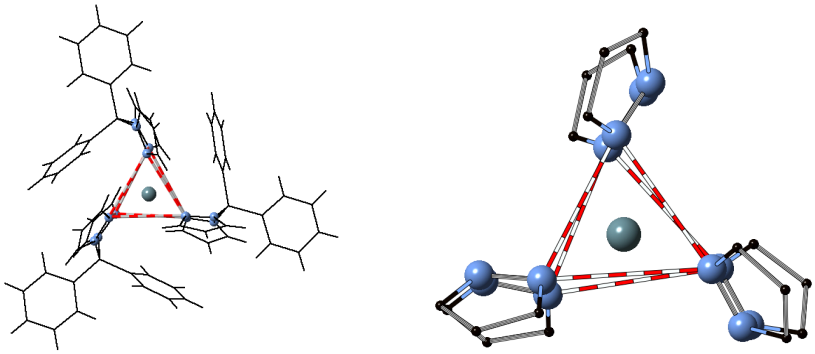

Figure 8.4: Molecular structure of: (left) $U(Ph_2BPz_2)_3$ and (right) $U(H_2BPz_2)_3$; the corresponding trigonal prismatic coordination centres are highlighted.

Given the coordination environment of both analogues, a clear magnetic easy-axis was expected for both cases. Owing to the small deviations from the point group of the two chemical structures, the Hamiltonian includes all possible terms. Unfortunately, both examples were not studied by spectroscopic techniques. This complicates obtaining a reliable description for both of them. Thus, a fitting of the magnetic susceptibility data of the two systems from 20 to 300 K was needed to determine the radial displacement, D_r, and the effective charge, Z_i. This provided an estimation of the whole set of CF parameters, related to the original atomic coordinates. These two parameters also reproduced magnetic susceptibility data (Figure 8.5). Note that the χT product under 20 K was not considered for the fitting due to the presence of dipolar interactions at lower temperatures, as evidenced by the drastic variation of the susceptibility between diluted and concentrated samples in

$U(H_2BPz_2)_3$.[353] A satisfactory fitting of the χT product was obtained for a D_r = 1.30 Å and Z_i = 0.0247 in $U(Ph_2BPz_2)_3$, while D_r = 1.40 Å and Z_i = 0.0203 in $U(H_2BPz_2)_3$. In both cases the same corrections were used, TIP= $-1.5 \cdot 10^{-3}$ emu/mol and F= 0.95.

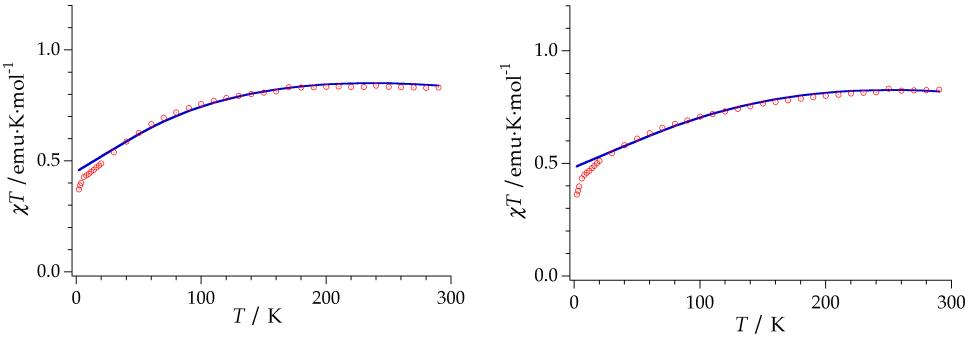

Figure 8.5: χT product for complex $U(Ph_2BPz_2)_3$ (left) and $U(H_2BPz_2)_3$ (right). Open circles: experimental data; solid line: theoretical fit.

In spite of the good agreement between the model and the experimental data from 20 to 300 K, regions where dipolar interactions are negligible, these results based on magnetic susceptibility data must be taken with extreme caution. In these systems we did not have information of the energy level scheme and the CF strength. It is known that assuming LS coupling in these conditions can lead to unreasonable results. Thus, further efforts such as those reported in Ref. 152 are necessary in order to provide a better understanding of these challenging issues.

Regarding the resulting full set of CF parameters, the key points that are worth discussing are: (a) among the diagonal parameters, B_{40} dominates, as expected considering the polar angle of the coordinating nitrogen atoms (Figure 8.6), and (b) among the extradiagonal parameters, B_{66} has a prominent role, as the coordination environment corresponds to a

trigonal prism. The deviations from ideality are mostly reflected in the high values of B_{65} in $U(Ph_2BPz_2)_3$, and the lower but also high values of B_{65} and B_{43} in $U(H_2BPz_2)_3$. Note that, because of the location of the boron-bound hydrogens, a significant amount of electron density may be found closer to the equatorial plane in $U(H_2BPz_2)_3$. It might then be described as tri-augmented trigonal prismatic. Although there are not enough data to quantify this effect, qualitatively it would lead to a smaller value of B_{20}.

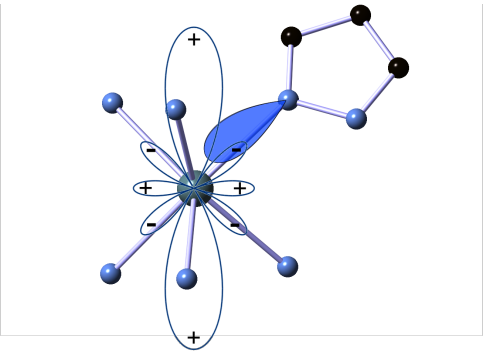

Figure 8.6: Orientation and electronic distribution of the lone pair in $U(Ph_2BPz_2)_3$ and representation of the shape of the spherical harmonic Y_4^0.

The energy level scheme for both compounds is depicted on Figure 8.7. Analogously to the above-mentioned UTp_3 complex, as a consequence of the symmetry-allowed extradiagonal parameter B_{66}, we found that the most important mixing in the wave function occurs between M_J values that differ by six units. In $U(Ph_2BPz_2)_3$ the ground level is a doublet mainly described by the wave functions: $0.79|+5/2\rangle + 0.17\ |-7/2\rangle$ and $0.79|-5/2\rangle + 0.17\ |+7/2\rangle$. The REC model also allowed to estimating the contamination of the ground state wave function by minor M_J components, which could not be addressed by only considering the major extradiagonal terms. The sum of all such terms is less than 4% for $U(Ph_2BPz_2)_3$. According

to these calculations, the first excited level lies at about $\Delta = 190$ cm^{-1} with a mixed wave function composed of $\pm 3/2$ and $\mp 3/2$ (66%) and 18% of $\mp 9/2$. The description of the lowest levels of $U(Ph_2BPz_2)_3$ is perfectly compatible with the reported SMM behaviour of the analogue, because there is not direct mixing between $+M_J$ and $-M_J$ in the ground doublet.

For $U(H_2BPz_2)_3$, and always according to this effective description, the ground doublet was defined as a mixture involving 0.68|+5/2> + 0.24 |-7/2> and 0.68|-5/2> + 0.24 |+7/2>. The sum of all terms that are not allowed in an ideal approximation of the coordination environment reached 8%, accounting for the small deviations from the ideal structure, which in this case is parameterised by a large B_{66} crystal-field parameter. Still, this description is compatible with SMM behaviour because there is no direct mixing between $+M_J$ and $-M_J$ in the ground state. The first excited state was estimated to be located at 230 cm^{-1}, and again, like in $U(Ph_2BPz_2)_3$, it is a doublet mixed between $\pm 3/2$ and $\mp 3/2$ (52%) and a 32 % of $\mp 9/2$.

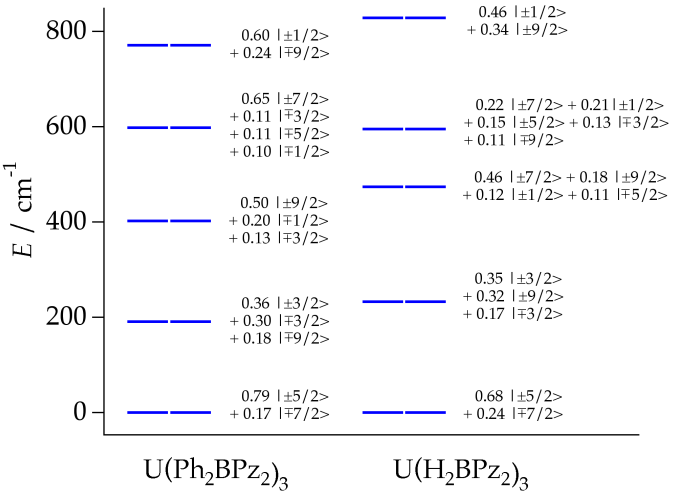

Figure 8.7: Energy level scheme and main contributions to the wave functions for $U(Ph_2BPz_2)_3$ and $U(H_2BPz_2)_3$.

To finish, the same procedure was applied to two closely related uranium complexes. These are the fourth and fifth mononuclear uranium complexes that were reported to display SMM behaviour: the cationic complex $[U(Tp^{Me2})_2(bipy)]^+$,[89] and its precursor $[U(Tp^{Me2})_2I]$.[90] As in the previous two examples, in both cases only magnetic susceptibility data was available. Satisfactory fits could be obtained with REC parameters for the pyrazole-based ligands that are within the range of those obtained the three U^{3+} examples reported herein.[93] Compared with the fitting procedures for such compounds, there are more free parameters for $[U(Tp^{Me2})_2(bipy)]^+$ and $[U(Tp^{Me2})_2I]$, because of the additional ligands (bipyridine and iodide respectively). This results in a slight overparameterisation, where minor improvements can be found in the low-temperature behaviour at the cost of an unrealistic increase in the crystal field splitting. The bipyridine ligand effect was reproduced with D_r= 1.25 Å and Z_i= 0.133 for the two coordinated nitrogen atoms, and the contribution of the iodine anion was parameterised with D_r= 1.88 Å and Z_i= 0.0843. The ground state doublet is formed by a combination of 0.31|+3/2> + 0.27|-5/2> +0.15|-7/2> and 0.31|-3/2> + 0.27|+5/2> +0.15|+7/2> in $[U(Tp^{Me2})_2(bipy)]^+$, whereas it is composed by 0.35|+9/2> + 0.34|+5/2> +0.28|-3/2> and 0.35|-9/2> + 0.34|-5/2> +0.28|+3/2> in $[U(Tp^{Me2})_2I]$. The resulting gaps with the first excited levels are 110 cm^{-1} and 136 cm^{-1} respectively, being compatible with the observed SMM behaviour.

In the above discussion, we have rationalised why the five U^{3+} complexes exhibit a SMM behaviour. In the following we will investigate the properties of an U^{4+} complex. This compound has been recently synthesised and magnetically characterised by the Almeida's group.[362] This group reported the U^{4+} compound formulated as $[\{(SiMe_2NPh)_3\text{-tacn}\}U^{4+}(\eta_2\text{-}N_2Ph_2^*)]$ and the U^{3+} precursor $[U^{3+}\{(SiMe_2NPh)_3\text{-tacn}\}]$ (Figure 8.8). For the

first time, the possibility of obtaining single-molecule behaviour in a U^{4+} complex was demonstrated. This encouraged us to collaborate with this research group in order to apply the methods described in this thesis to model the experimental data. In contrast to the U^{4+} derivative, the U^{3+} precursor did not exhibit slow relaxation of the magnetisation (a frequency-dependent out-of-phase magnetic susceptibility could not be observed in the *ac* magnetic measurements). In both cases, the REC model and the CONDON package were useful tools to provide useful information about the magnetic and spectroscopic properties of these systems, as we describe below.

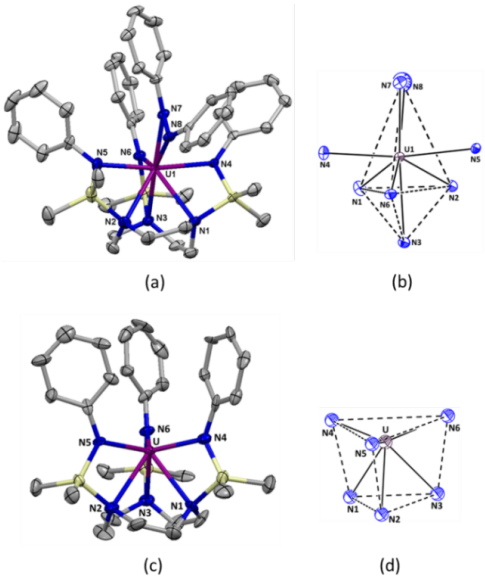

Figure 8.8: Molecular structures and coordination geometries of (a, b) [{$(SiMe_2NPh)_3$-tacn}$U^{4+}(\eta^2\text{-}N_2Ph_2)$] and (c, d) [$U^{3+}${$(SiMe_2NPh)_3$-tacn}] (thermal ellipsoids set at a 40% and 20% probability level respectively).

The procedure we followed in the study of both compounds started with the application of the REC model to the idealised structure (C_{3v}) of

$[U^{3+}\{(SiMe_2NPh)_3\text{-tacn}\}]$, introducing the coordinates of the donor atoms in the SIMPRE computational package. The structure was idealised to minimise the number of CFPs, as the second step involves a phenomenological fit. As the ligands had not been parameterised before, for this initial estimate of CFPs, the effective distances were calculated using the formula for D_r described in the fifth chapter (Equation 5.3).

Subsequently, the effective charge of the donor atoms was calculated assuming a similar relation $f = D_r \cdot Z_i$ than the observed between the REC parameters of different nitrogen-coordinated compounds studied by this model.

Thus, we introduced this initial trial of calculated CFPs in the package CONDON, which is suitable to model these systems due to the numerical approach that takes into account all the energetic effects of the free ion and the ligand field. The temperature-dependent magnetic susceptibility data were fitted using the full Hamiltonian approach with the assumptions: ζ_{5f} = 1516 cm^{-1}, F^2 = 36130 cm^{-1}, F^4 = 26000 cm^{-1}, F^6 = 21000 cm^{-1},[364] and C_{3v} ligand field. The symmetry approximation implies that the only non-vanishing ligand field parameters are B_{20}, B_{40}, B_{43}, B_{60}, B_{63} and B_{66}. The least-squares fit (S_Q = 0.31%) yields B_{20} = -4900 cm^{-1}, B_{40} = 1788 cm^{-1}, B_{43} = 2144 cm^{-1}, B_{60} = 4363 cm^{-1}, B_{63} = -7055 cm^{-1} and B_{66} = 8166 cm^{-1}.

The overall ligand field splitting of the ground multiplet is ca. 1805 cm^{-1}. The ground multiplet is separated from the lowest state of the following first excited multiplet only by 1744 cm^{-1}, which is located at 3549 cm^{-1}. This evidences the need of using a full approach instead of an effective one (assuming Russell-Saunders coupling) for a proper description of the system. This differs with the wave numbers determined in UTp_3, where the first excited *J* lies further from the highest doublet in the ground *J* multiplet. All 182 doublets covered by the application of the full

basis span an energy interval of ca. 65970 cm^{-1}. The ground doublet is mainly composed of M_J = 42% |±5/2> + 36% |±1/2> + 22% |±7/2> states. The presence of an important contribution of ±1/2 in the ground doublet explains the inability of displaying SMM behaviour of [U^{3+}{$(SiMe_2NPh)_3$-tacn}]. This was also evidenced when observing the crystallographic structure of the compound, the three nitrogen atoms of the group $SiMe_2NPh$ are placed at 77º in average from the polar coordinate in θ. Thus, the complex illustrates a situation where the electron density is distributed near the plane xy. Since U^{3+} is an oblate ion with the f-electron density equatorially distributed,[61] the repulsive contacts between ligand and f-electron charge cloud do not favour the stabilisation of a high M_J value in the ground doublet. The fitted χT product and the predicted magnetisation of [U^{3+}{$(SiMe_2NPh)_3$-tacn}] at different temperatures using the full Hamiltonian in the CONDON computational package are depicted in Figure 8.9.

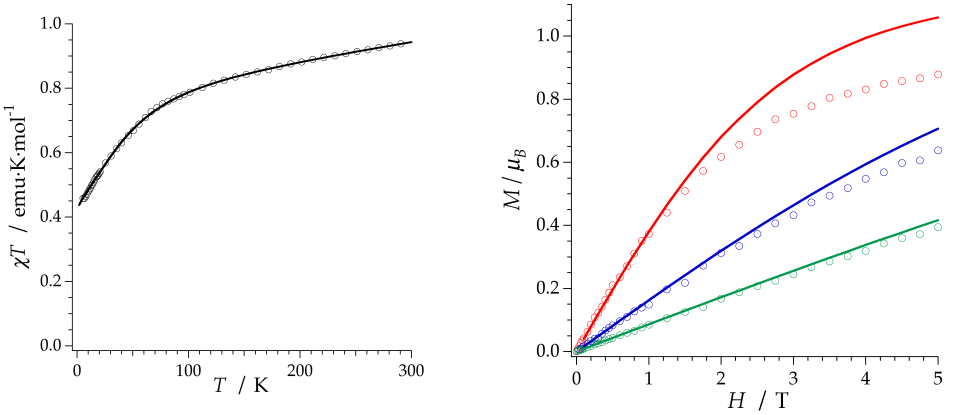

Figure 8.9: Temperature dependence of the magnetic susceptibility of [U^{3+}{$(SiMe_2NPh)_3$-tacn}] from 2 to 300 K, experimental (symbols) and calculated (solid line) using the CONDON package (left); Magnetisation, experimental (symbols) and predicted (solid lines), versus H at 2 K (red), 5 K (blue) and 10 K (green) from 0 to 5 T (right).

The χT product was fitted from 5 to 300 K, obtaining an excellent agreement between the theory and the experiment. The predicted magnetisation is essentially exact at low field/temperature ratios (at least until H/T = 0.5 T/K). One can observe that there are some deviations at higher fields or lower temperatures, where the predicted magnetisation rises above the experimental data. This can be due to small dipolar interactions between U^{3+} centres at very low temperatures.

In a second step, the REC model was applied again to obtain an estimation of the REC parameters D_r and Z_i of the groups tacn (D_r = 1.52 Å and Z_i = 0.04) and $SiMe_2NPh$ (D_r = 0.18 Å and Z_i = 2.64) by a direct fitting of the phenomenological CFPs from the idealised structure. These results, combined with an analogous study with pyrazolyl ligands in UTp_3 (D_r = 1.48 Å and Z_i = 0.023), allowed us to obtain an estimation of the CFPs of the tretravalent uranium compound. For that, we introduced the crystal structure of this compound and we used the SIMPRE package just to obtain a set of CFPs.

Finally, we moved on to CONDON in order to calculate the spectroscopic and magnetic properties arising from these CFPs after diagonalising the full Hamiltonian. It is important to note that in this case the presence of a radical and the lack of symmetry elements in the coordination environment mean it is unreasonable to directly fit the data, especially due to the overparameterisation that arises from the geometry of the system. It is clear that we are dealing with a particularly difficult system to be analysed. A full description of the magnetic and spectroscopic properties will require further treatments accompanied by novel techniques in the future. Up to now, the prediction obtained with the REC model and the full Hamiltonian allows a reproduction of the χT curve, as can be seen in Figure 8.10.

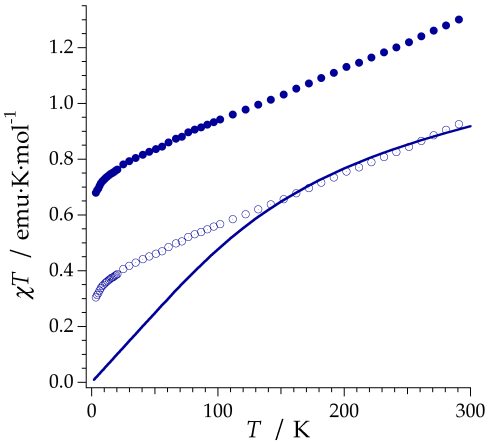

Figure 8.10: Temperature dependence of the magnetic susceptibility of [{($SiMe_2NPh)_3$-tacn}U^{4+}(η_2-N_2Ph_2*)] between 2 and 300 K (Experimental (blue circles), experimental substracting a radical contribution estimated as 0.375 emu·K·mol^{-1} (open circles) and prediction (solid line)) using the REC model and the CONDON package.

The agreement at high temperatures is remarkable, considering that the whole theoretical analysis up to this point was done in absence of any experimental magnetic data of [{($SiMe_2NPh)_3$-tacn}U^{4+}(η_2-N_2Ph_2*)] and is thus a structurally-guided effective charge electrostatic prediction. One should therefore not discard the possibility of this coincidence being, at least in part, accidental. If we accept the theoretical calculation as essentially correct for the U^{4+} ion, the observed deviation, which starts below 150 K and is already quite marked below 100 K, should be understood as a ferromagnetic direct exchange coupling between the electronic sp^2 spin of the radical, which practically overlaps with the 5f orbitals of U^{4+}. Here it is important to recall that actinide 5f orbitals are considerably more diffuse than lanthanoid 4f radicals. The end result is that the experimental χT product at the low temperature limit is of the order of

0.7 emu·K·mol^{-1}, while the calculated value for the U^{4+} ion in the absence of the radical would be practically zero. The calculations were performed using the full Hamiltonian approach with the default assumptions for U^{4+}: ξ_{5f} = 1926 cm^{-1}, F^2 = 76557 cm^{-1}, F^4 = 50078 cm^{-1}, F^6 = 36429 cm^{-1}, and C_s ligand field. The energy level scheme of the ground multiplet for [{(SiMe$_2$NPh)$_3$-tacn}U^{IV}(η_2-N$_2$Ph$_2$*)] without considering the interaction with the radical is reported in Figure 8.11.

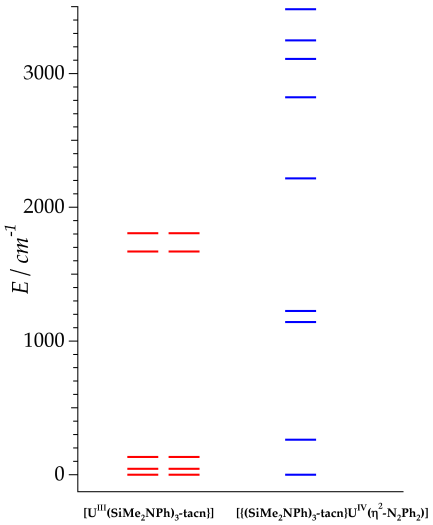

Figure 8.11: Energy level scheme of the ground multiplet for [U^{III}{(SiMe$_2$NPh)$_3$-tacn}] (red) and [{(SiMe$_2$NPh)$_3$-tacn}U^{IV}(η_2-N$_2$Ph$_2$*)] (blue).

According to our calculations, the ground state shows an important contribution of $M_J = \pm 4$ (74%) but also there is a presence of $M_J = 0$ (17%) in the easy axis. Thus, the interaction with the radical seems to play a key role in the slow relaxation of the magnetisation in [{(SiMe$_2$NPh)$_3$-tacn}U^{IV}(η_2-N$_2$Ph$_2$*)], while the mere presence of this axial ligand would not be enough.

In other words, an equivalent ligand field produced by a diamagnetic but otherwise similar coordination sphere would produce a magnetic behaviour very similar to that encountered in the U^{3+} precursor. The paramagnetic ligand switches the parity from non-Kramers to Kramers, offering a new route to obtain SIMs based on non-Kramers ions.

8.3 Conclusions

In this chapter, we have described the first theoretical attempt to analyse the magnetic behaviour of uranium-based SIMs, which are the next frontier in molecular nanomagnetism. We have found that theoretical tools that were originally designed for the study of lanthanoid SIMs can offer a starting point for the modelling of uranium SIMs. In particular, by combining the REC model with experimental data we can extract an initial trial of CFPs and information about the wave functions of the target analogues. This model may help in the design of new derivatives based on the same cation. We also have shown that the combination of the REC model using SIMPRE, limited to the ground *J*, with the *semi-empirical* approach included in the CONDON software package, that includes excited *J* manifolds, is useful to obtain information on the lowest-lying magnetic levels and the associated wave functions of the different nanomagnets.

Regarding the calculated wave functions with the effective charge approach in UTp_3, it has been shown that the calculated wave functions are in full agreement with the phenomenological ones. The ground state wave functions of the three first examples presented in this chapter (dominated by $\pm 5/2$) have been found to be compatible with the SMM behaviour observed in them.

In a second step, we have described the related systems $[U^{3+}\{(SiMe_2NPh)_3\text{-tacn}\}]$ and $[\{(SiMe_2NPh)_3\text{-tacn}\}U^{4+}(\eta_2\text{-}N_2Ph_2^*)]$. The model has been able to explain why the former does not exhibit slow relaxation of the magnetisation, presenting a major contribution of $\pm 1/2$ to the ground state wave function. In the meanwhile, the unprecedented behaviour among uranium(IV) has been discussed, explaining its origin from the interaction of the metal ion with the paramagnetic ligand which switches the parity from non-Kramers to Kramers. This latter approach may provide a novel strategy to design SIMs in non-Kramers ions. When considering the use of this strategy to extend relaxation times in rare earth complexes, it is important to consider that tunnelling can only be blocked for temperatures much smaller than the coupling energy. Therefore, in order to achieve a significant success in enhancing the blocking temperature, the exchange coupling to and via the radical must be significant, something that is exceptional for lanthanides but more common in actinides.

9 Molecular anisotropy in an organometallic SIM

9.1 Introduction

Magnetic anisotropy in molecular complexes means that the magnetic properties of the system depend on orientation.[366] Thus, a molecular material is anisotropic when the response to an external magnetic field is conditioned by the molecular direction along which the field is applied. Technically, this defines the hard, medium and easy axes of magnetisation of the crystal. The same effect is sometimes described as the magnetic moment lying preferentially along a certain direction to minimise the potential energy.

The measurement of the magnetic susceptibility on oriented single crystals (single-crystal magnetometry) is a powerful technique to analyse the anisotropic response of a coordination compound to an external field. This kind of information is needed to establish magneto-structural correlations between the coordination environment and the magnitude and orientation of the magnetic moment.[73] Nevertheless, a review of the SMM literature shows that most complexes have only been characterised by powder *dc* and *ac* susceptibility measurements. Even in single crystals, magnetic measurements provide an average over the different species that

are usually present in the crystal. In this context, triclinic structures presenting a single magnetically independent site become ideal candidates for getting information on the magnetic anisotropy.

From an experimental point of view, the group of Prof. Roberta Sessoli has been very active performing single-crystal magnetic experiments. A relevant case is that of the $Na[Dy(DOTA)(H_2O)] \cdot 4H_2O$, where H_4DOTA = 1,4,7,10-tetraazacyclododecane-N,N',N'',N'''-tetraacetic acid).[72,73] The angular dependence of the magnetisation was investigated by gluing a crystal on the face of a millimetric Teflon cube. The three orthogonal faces of the cube were indexed in the reference frame of the crystal with non-integer Miller indices. The normals to these faces defined the laboratory *xyz* reference frame. The cube attached to the crystal was then mounted on a horizontal rotator in a SQUID magnetometer. This permitted to extract the susceptibility tensor in the compound, as the crystal lattice only contains one molecular orientation. Other examples reported by this group include the study of the orthorombic organometallic Cp*ErCOT,[68] which provided the first reconstruction of the anisotropy tensor in a crystal lattice with two molecular orientations.[367] This could be achieved by collecting angular-resolved magnetic measurements under in- and out-of-equilibrium conditions.

In this chapter we will focus our attention precisely in this organometallic erbium single-ion magnet: Cp*ErCOT. We are going to perform a full theoretical analysis of the molecular anisotropy using the SIMPRE package. The additional challenge in this case is that the system is expected to have intense covalent effects that can hardly be simulated by simple point-charge ligands.[368] The erbium ion is sandwiched between two aromatic rings, Cp* and COT, where Cp* = pentamethylcyclopentadiene anion (C_5Me_5) and COT = cyclooctatetraene dianion ($C_8H_8^{2-}$), as can be seen

in Figure 9.1. The two aromatic rings are not exactly parallel to each other, with the two planes presenting a tilt angle of 8°. The crystalline structure containing this organometallic complex presents an additional difficulty because of the presence of two different crystallographic orientations, each occupied by two different conformers.

The main features that made this SIM an ideal benchmark system to test of the capabilities of an effective electrostatic approach in a limit case are: (i) the complex is based on aromatic rings, which are eminently covalent; (ii) a detailed study of the angular dependence of the magnetic susceptibility of Cp*ErCOT was available,[367] thus permitting the comparison with the predicted molecular anisotropy of the system using the calculated crystal-field parameters (CFPs), without the introduction of any extra parameter; and (iii) the availability of high-quality spectroscopic information of the crystal field splitting on a series of independent complexes with Cp* and COT rings combined with trispyrazolylborate (Tp^-) ligands, which had previously been parameterised by the REC model (see Chapter 7). This third point is probably the most exciting one because it paves the way towards the inexpensive modelling of these systems, which are in principle chemically far away from models based on purely electrostatic considerations. The inclusion of the effective charge information about the Cp* and COT rings in the general library of ligands could be very useful to predict the properties of different complexes in different crystal fields.

The delocalised electron density of the p_π orbitals that coordinate the erbium cation is modelled in this chapter by a sum of effective charges placed in a plane closer to the metal and parallel to the aromatic ring plane. We simulated this by defining a vertical displacement vector (D_v), one for each p_π orbital. D_v is perpendicular to the plane formed by the carbon atom

sp^2 plane, and it defines the angular coordinates θ_i and φ_i. of the effective charges. This is similar to the definition of D_h in the bis-phthalocyaninato series, but in the present case the vector simulates the π cloud and thus is perpendicular to the aromatic ring. Radial vector D_r was applied after D_v, pointing directly to the lanthanoid nucleus and defining the effective radial coordinate R_i. The radial correction, like in the REC model, accounts for the fact that averaging a spherical distribution to a point charge in the centre of a given distribution is not a good approximation when dealing with high order terms. Both sets of vectors, D_v and D_r, were applied to the original position of the aromatic carbon nuclei, determining the positions of the effective centres of charge that model the π cloud effects as represented in Figure 9.1.

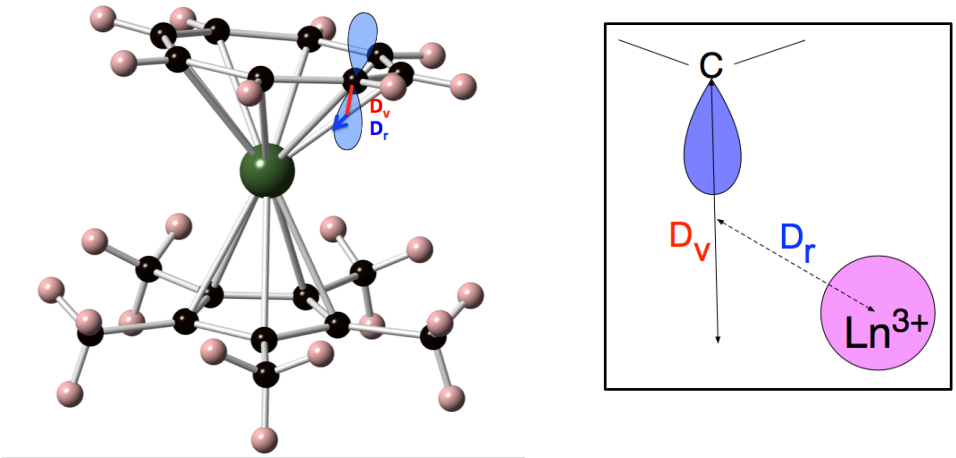

Figure 9.1: (left) Molecular structure of Cp*ErCOT at 10 K including the representation of the relation of D_v (red arrow) and D_r (blue arrow) with one of the p_π orbitals; (right) Schematic representation of D_v and D_r.

9.2 Molecular anisotropy analysis

In this part of the work, we are going to describe the results derived from the application of the LPEC model to the organometallic Cp*ErCOT. Following the standard procedure of the model, an excellent agreement (E = $4.4 \cdot 10^{-6}$) with the experimental magnetic behaviour -powder data- was obtained (Figure 9.2, red solid line) with the following set of parameters: D_v = 0.98 Å, D_r = 0.26 Å and Z_i (Cp*) = 0.4. To avoid overparameterisation, it was assumed that the π orbitals of Cp* and COT are very similar, and that the formal charge of the aromatic ligands is delocalised over all the C atoms. As a consequence, the formal charge on each Cp* carbon atom was fixed to 1/5=0.2 and 2/8=0.25 for COT carbon atoms. Thus, in the fitting we used the same LPEC parameters (D_v and D_r) to determine each the effective coordinates, and accounted for the different charges in the two rings by introducing a fixed ratio Z_i(COT) = 1.25· Z_i(Cp*) = 0.5. Of course, one could question the assumption that the ratio between the effective charges of Cp* and COT is equal to the actual charge ratio between Cp* and COT. Indeed, relaxing this condition and performing a full study with multiple complexes and spectroscopic information will yield a better effective charge description of both Cp* and COT as ligands.

As the angular dependence of the susceptibility was measured between 2 and 10 K,[367] we used the crystal data obtained at 10 K for all our calculations. Nevertheless, as a common problem with theoretical modelling is not knowing the effects in the properties of a structural change with temperature, we verified that only minor deviations in the χT product depend on the structure determined at different temperatures (10, 20 and

120 K) as shown in Figure 9.2. This concern will be analysed in depth in the next chapter in a dysprosium β-diketonate compound.

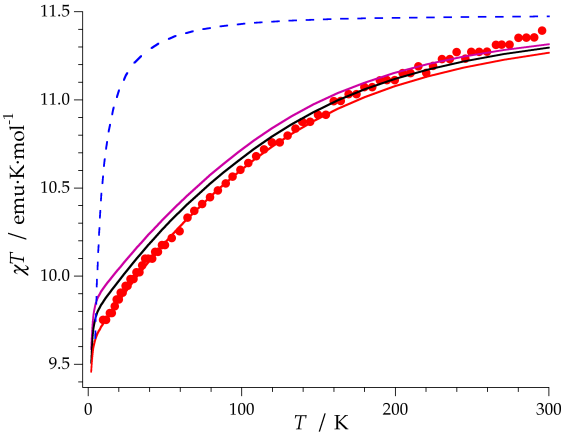

Figure 9.2: Fitting of the experimental χT product of Cp*ErCOT from 10 to 300 K using the LPEC model in the SIMPRE package with the structure at measured at 10 K (red solid line), 20 K (purple solid line) and 120 K (black solid line), and using a minimal PCE model (blue dashed line).

According to our calculations using the structure at 10 K, the ground state for both conformers of Cp*ErCOT is dominated by the highest M_J value (Ising-type). The contribution of $M_J = \pm 15/2$ is of 96% for conformer 1 and of 95% for the second one. The first excited state is placed at 156 cm^{-1} in the first conformer and 125 cm^{-1} in the second one. This description is fully compatible with the observed slow relaxation of the magnetisation in this organometallic single-ion magnet.

At this point, it is interesting to examine the effect of the π-cloud displacement that was simulated via the vertical displacement (D_v) of the effective charges. Calculations using the classical PCEM placing formal charges on the crystallographic positions of the carbon atoms were

performed in order to determine the influence of D_v. The χT product curve represented in Figure 9.2 gives a clear and expected evidence that a minimalistic PCEM is not able to predict a comparable magnetic behaviour (with deviations of the order of 10% at 20 K). As we know that fitting a single susceptibility curve to a number of free parameters often can lead to different solutions and that powder data is not very sensitive to anisotropy, this is a necessary but not sufficient condition to give a satisfactory answer to the first challenge of this chapter, i.e. the validity of a point charge description to describe the CF effects of a covalent ligand. Thus, we need to validate the parameterisation by predicting, without further fittings, independent properties of the same compound, and, if possible, also of different compounds, in order to test the validity of the three *semi-empirically* determined parameters. By doing so, we will also address second challenge.

First, we used the model and the parameters that we obtained from the powder susceptibility data fit, together with the crystal structure, to predict the magnetic anisotropy that was previously been determined experimentally. We used the real coordinates modified by D_v and D_r (from the powder χT LPEC fit) and simulate the experimental rotations labelled Rot1 and Rot2, which were performed by Sessoli *et al*.[367] Such experimental rotations are illustrated in Figure 9.3 where the magnetic field is vertically oriented in the paper plane and the crystal rotates around an axis perpendicular to the plane.

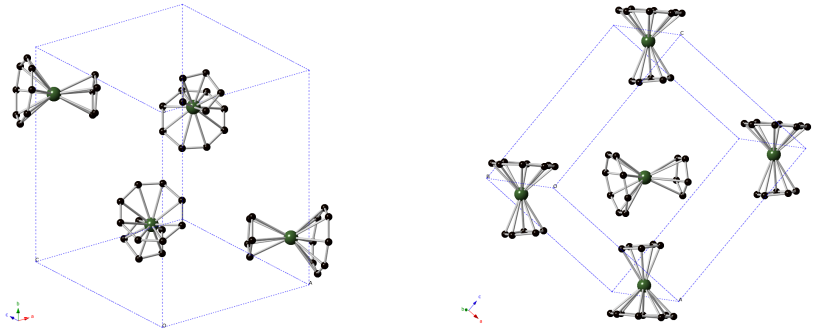

Figure 9.3: Orientation of the molecules in the two experimental rotations : Rot1 (left) and Rot2 (right). The magnetic field is vertically oriented in the paper plane and the crystal rotates around an axis perpendicular to the plane.

The predicted spherical angular dependence of the magnetic susceptibility at 10 K is plotted as a cylindrical map projection versus θ and φ in Figure 9.4.

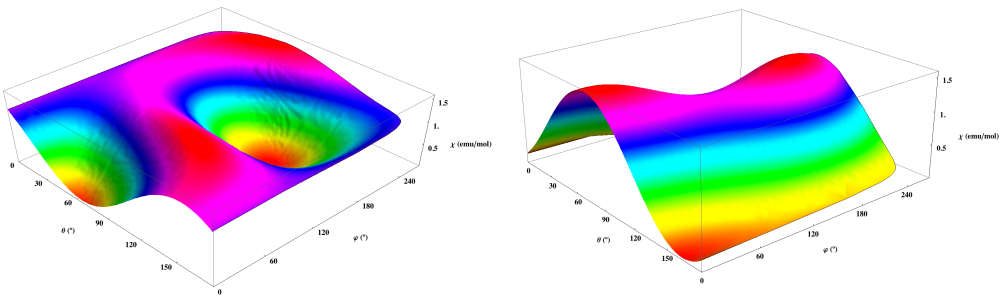

Figure 9.4: Cylindrical map projection of the calculated susceptibility angular dependence at 10 K and H = 1 kOe corresponding to Rot1 (left) and Rot2 (right).

For a comparison between the theoretical calculations using the LPEC and the PCEM, with the experimental results, the angular dependence of

the magnetic susceptibility of the two rotations is represented in Figure 9.5. Note that single-crystal experimental data needed to be scaled by a factor of 0.81 to be consistent with the experimental powder data reported in Ref. 367 at 10 K. The theoretical prediction was superimposed in Figure 9.5 without the use of any extra-parameter.

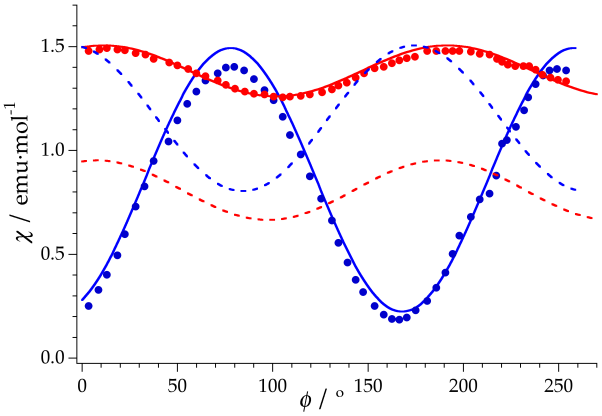

Figure 9.5: Angular dependence of magnetic susceptibility performed on a single crystal at H = 1 kOe for Rot1 (blue) and Rot2 (red) at 10 K. A scale factor of 0.81 need to be applied in order to match the single-crystal experimental data with the powder data. In solid line is plotted the theoretical prediction (no extra-parameters) using the LPEC model. Dashed line corresponds to the theoretical prediction with a minimal PCEM.

An almost perfect agreement in both phase and intensity for the two experimentally available rotations was obtained using the parameters extracted from the χT fit. For the powder χT curve, the theoretical curve results from the weighted average of the signals of the two different crystallographic orientations. Each one is occupied by two different conformers. The angular dependence of magnetic susceptibility for Rot1 and Rot2 of each conformer on each crystallographic orientation is reported

in Figure 9.6. This allowed a better understanding of how the actual magnetic anisotropy works in each single Er-ion frame.

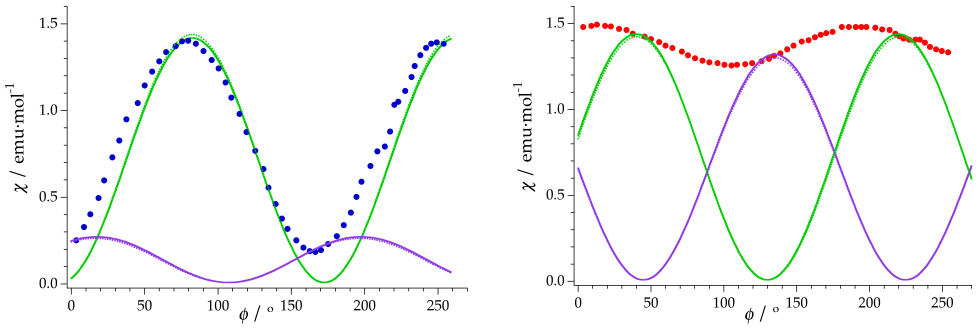

Figure 9.6: Experimental angular dependence of magnetic susceptibility performed on a single crystal at H = 1 kOe for Rot1 (left: blue dots) and Rot2 (right: red dots) at 10 K versus theoretical angular dependence of each orientation (Orientation 1, green; Orientation 2, purple; this work). Conformer 1: solid lines; conformer 2: dotted lines.

It is remarkable that a three-parameter LPEC model, which uses as sources of information the powder χT data and the low temperature crystallographic data, is enough to match, without any additional parameter, the magnetic anisotropy of this complex system. On the other hand, it is also important to notice that a minimal electrostatic model would be utterly unable to predict the experimental angular dependence of the magnetic susceptibility. The PCEM provided a ground state mainly determined by $M_J = \pm 1/2$ (more than 99%) in the experimentally determined direction of the main axis of anisotropy for each conformer. As can be seen in Figure 9.5, neither the phase nor the intensity are compatible with the behaviour measured in Ref. 362. These results underline the severe limitations of this simple electrostatic model to determine the easy axis in those cases in which the ligands have lone pairs (or π clouds), which are

not pointing directly towards the lanthanoid ion. From our experience applying the REC and LPEC models in other systems, we suggest that this correction is necessary to determine the ground state wave function and the easy axis of the magnetisation when dealing with rigid polyhapto ligands such as aromatic rings, including phthalocyaninato anions (Chapter 7).

Subsequently, the angular dependence of magnetic susceptibility for both rotations at different temperatures was calculated and plotted for comparison with the experimental results (Figure 9.7). Again, the experimental curves coincided with the calculations using the LPEC model without any further fitting. From Figure 9.7 (left) we were able to detect some kind of experimental deviation of the maximum position from around 80º to 67.5º in the data at 5 K. We could safely discard that this originates from a structural transition. It seems more probably connected with the hysteretic effects experimentally detected below this temperature.[367] The fact that such deviation of the maximum χ is not observed for Rot2 (Figure 9.7 (right)) supports this assumption.

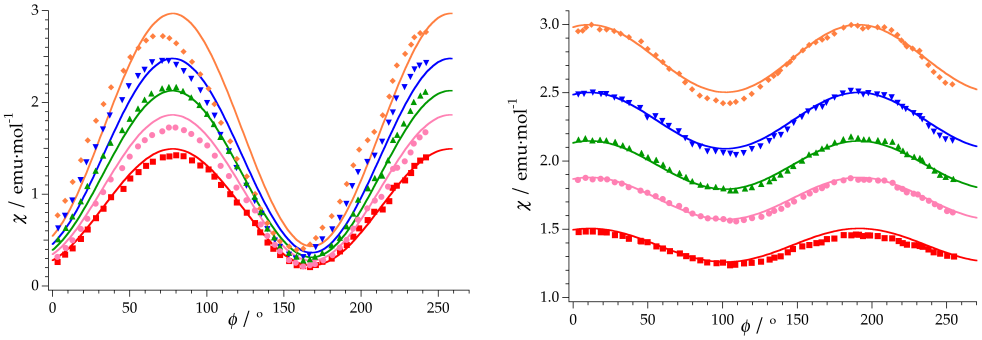

Figure 9.7: Angular dependence of the magnetic susceptibility at different temperatures for Rot1 (left) and Rot2 (right) at H = 1 kOe. From top to bottom: 5, 6, 7, 8 and 10 K. Comparison between experiment (solid circles) and theory (solid lines).

The second challenge we mentioned in the introduction of the chapter is arguably the most exciting. Has this model a predictive character when applied to organometallic lanthanide complexes? Can we extrapolate the specific parameters for each ring to other compounds that feature the same ligands? This possibility is related to the spectrochemical and nephelauxetic series of ligands in classical coordination chemistry, distinguishing quantitatively between 'weak' and 'strong' field ligands for lanthanoid complexes. In this part of the discussion, we want to link this challenge to yet another open problem in this field, namely the reliable estimation of the total CF splitting, i.e. the CF strength of the ligands.

Using the LPEC model, the calculated total splitting for both conformers is $\Delta = 630$ cm^{-1} and 513 cm^{-1}. These rather large Δ-values are in full agreement with the expected behaviour, as aromatic rings are known to produce very strong CF splitting, being as they are at the right of the spectrochemical series. In particular, spectroscopic isometallic results by Amberger *et al*. have indicated $\Delta = 861$ cm^{-1} for Nd(Cp*)$_3$,[369] $\Delta = 533$ cm^{-1} for [Nd(COT)[HB(3,5-Me$_2$pz)$_3$]],[370] and $\Delta = 358$ cm^{-1} for NdTp$_3$.[355] These results evidence that Δ is higher in compounds that are coordinated by aromatic rings than for those coordinated by nitrogenated ligands such as pyrazolylborate.[354] This is logically expected according to the ligand position in the spectrochemical series, ordered from weak to strong field ligands. It is to be noted that the other available models are unable to predict this strong CF splitting in the study of this complex. Thus, for the reported system, a previous fit using the CONDON software yielded a total CF splitting $\Delta \sim 380$ cm^{-1} (Figure 9.8),[69] whereas the CASSCF / RASSI model estimated Δ values of 276 cm^{-1} and 308 cm^{-1} when using the

crystallographic structure, and 235 cm^{-1} for both conformers with the DFT optimised structures.[367]

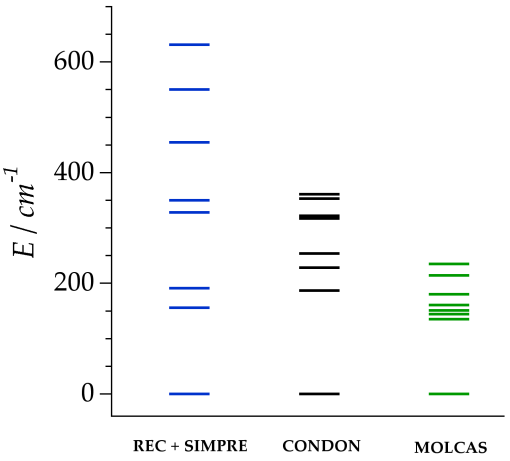

Figure 9.8: Calculated energy level scheme for Cp*ErCOT (conformer 1) in this work and previous calculations reported using MOLCAS (with DFT optimised structure) and CONDON.

Given that different theoretical tools strongly disagree in the values of the total splitting, we tested the predictions based on this *semi-empirical* effective electrostatic model in cases where spectroscopic data are available. We check the calculated energy levels using the effective charge description of ligands: Tp^{-}, Cp* and COT, against the real electronic structure determined by spectroscopy for [Nd(COT)[HB(3,5-Me_2pz)$_3$]] and Nd(Cp*)$_3$. For comparison with a direct fit using the REC model, in Figure 9.9 these energy level schemes are plotted together with the one reported for Nd(Tp)$_3$. The fitting of the spectroscopic energy levels by Amberger *et al.* gave a ground state wave function $M_J = \pm 5/2$. Taking into account the crystal structure of these complexes, we obtain a ground state formed by

0.54 |±5/2> + 0.46 |∓7/2>, 0.69 |±5/2> + 0.19 |∓5/2> and 0.89 |±5/2> + 0.11 |∓7/2> for $Nd(Tp)_3$, [Nd(COT)[$HB(3,5\text{-}Me_2pz)_3$]] and $Nd(Cp^*)_3$ respectively.

With these results, we encourage experimentalists working on molecular magnetism to measure the magnetic properties of both [Nd(COT)[$HB(3,5\text{-}Me_2pz)_3$]] and $Nd(Cp^*)_3$, because the M_J contributions to the ground state wave functions are completely compatible with SMM behaviour. This is the first time where the evolution of the total CF splitting of a series of rare earth complexes was successfully predicted using the contributions of each ligand taken into account separately. As can be seen in Figure 9.9, the accuracy of the predicted total CF splitting is striking, but there is clearly room for improvement in the fine details, specially in [Nd(COT)[$HB(3,5\text{-}Me_2pz)_3$]]. Such an improvement is expected with the full study using the spectroscopic data of multiple families.

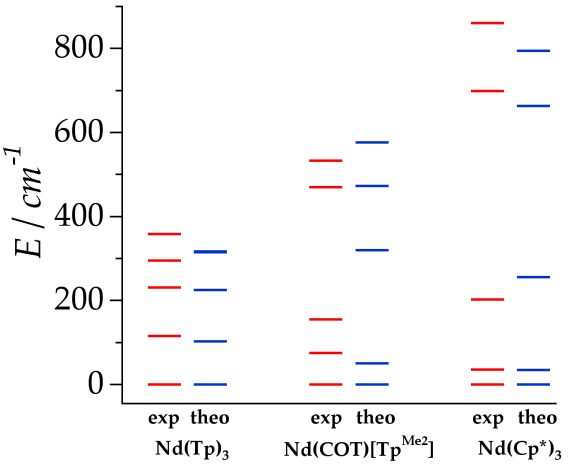

Figure 9.9: Experimental and calculated energy level scheme for $NdTp_3$ (fit), [Nd(COT)[$HB(3,5\text{-}Me_2pz)_3$]] (prediction) and $Nd(Cp^*)_3$ (prediction).

9.3 Conclusions

In this study the crystal field effect created by the Cp* and COT ligands is modelled by a *semi-empirical* effective electrostatic model that has been corrected to account for the covalent effects of the π clouds. This is done by a fit of the temperature dependence of the powder magnetic susceptibility of the compound Cp*ErCOT. To verify this model, a zero-parameter fit is performed that quantitatively reproduces the experimental full magnetic anisotropy analysis, i.e. two perpendicular rotations of the crystal in the presence of a magnetic field at temperatures ranging from 5 K to 10 K.

Subsequently, the obtained parameterisation for Cp* and COT ligands, together with analogous results for Tp^- from a previous study, are used for a zero-parameter fit of the spectroscopically determined crystal field splitting and magnetic properties of two further complexes, Nd(COT)[Tp^{Me2}] and Nd(Cp*)$_3$. Finally, the quantitative agreement of the prediction of the CF splitting emphasises the predictive character of this simple approach.

10 Heteroleptic complexes based on oxygen and nitrogen donor atoms

10.1 Introduction

Up to this point we have reported the application of the developed theoretical tools to homoleptic complexes. This has demonstrated the capabilities of the REC and LPEC models to interpret and predict the properties of this kind of systems, using two or three parameters respectively. Along this dissertation, it has been detailed how these models can simplify overparameterisation problems when determining CFPs.

Nevertheless, the beauty of chemistry involves many possibilities in the design of coordination complexes with a rare earth as a central ion. Indeed, literature offers a broad range of SIMs having more than one type of ligands, i.e. heteroleptic molecules that are interesting from the point of view of nanomagnetism. Under the REC approach, one has to introduce two parameters (D_r and Z_i) for each type of donor atom. This means that for a particular family of heteroleptic compounds, e.g. those coordinated to nitrogen and oxygen donor atoms, the problem is augmented to a total of four REC parameters: two of them for each ligand. If the donor atoms have to be treated in terms of the LPEC model, there is an increase in the number

of parameters to be fitted, as we have to consider D_h or D_v for each type of donor atom. The need of two or three parameters per donor atom is a clear limitation of the effective charge models in the description of heteroleptic compounds, as this leads to overparameterisation.

As examples of real heteroleptic systems behaving as mononuclear SMMs, molecular analogues containing a Dy^{3+} ion between three β-diketonate ligands in a 'paddle-wheel'-like arrangement are very common in molecular magnetism.[70] These systems are formed by two β-diketonate ligands trans- to each other and the third trans- to a neutral ligand, having an approximated square antiprism coordination geometry. Examples of them are the following related complexes: $[Dy(acac)_3(H_2O)]$,[70] $[Dy(acac)_3(phen)]$,[71] $[Dy(acac)_3(dpq)]$,[371] $[Dy(acac)_3(dppz)]$,[371] $[Dy(tfpb)_3(dppz)]$,[372] $[Dy(tta)_3(bipy)]$,[373] $[Dy(tta)_3(phen)]$,[373] $[Dy(tta)_3(pinene\text{-}bipy)]$[374] and $[Dy(hfac)_3(dme)]$,[375] where acac = acetylacetone; phen = 1,10-phenanthroline; dpq = dipyridoquinoxaline; dppz = dipyridophenazine; tfpb = 4,4,4-trifluoro-1-phenyl-1,3-butandionate; tta = 2-thenoyltrifluoroacetone; bpy = 2,2'-bipyridine, pinene-bpy = 4,5-pinene bipyridine; hfac = hexafluoroacetylacetonate and dme = dimethoxyethane. The easy axis of magnetisation of all these nine β-diketonates has been modelled by both *ab initio* and purely electrostatic methods and reported in the literature.[376,75] Its orientation has been found to be perpendicular to the 'paddle-wheel' axis, crossing the two trans-β-diketonate ligands.

In this chapter, we are going to apply the REC model to describe the properties of a system having these characteristics. For that, we are going to focus our attention on a new β-diketonate SIM published in 2015.[377] This is the $Dy(^tBu\text{-}acac)_3bpy$ complex, where ^{t}Bu-acac = 2,2,6,6-tetramethylheptane-3,5-dionate, studied by Dr. Shang-Da Jiang. In terms of

the REC model, one needs to account for four REC parameters: the radial displacements and effective charges of the O- and N-donor atoms. Within this process, we will describe the molecular magnetic anisotropy analysis that we performed in this SIM. This was possible because, beyond the routine magnetic characterisation, Dr. Jiang had determined the molecular magnetic easy axis by angular resolved magnetisation measurements on a single crystal.

Furthermore, we are going to report a study of the effects of the temperature over the crystal structure and its consequences in the magnetic anisotropy. This is interesting because most of the experimental and theoretical investigations that have been carried out concerning energy levels and magnetic anisotropy have been performed using the crystal structure determined at room temperature, or, at lowest, at 100 K. However, spectroscopic or magnetic anisotropy experiments have been carried out at much lower temperatures. This has lead to a general question in molecular magnetism: can this thermal evolution of the structure critically affect the crystal field splitting and the magnetic anisotropy?

Thus, in this part of the thesis, we are using Dy(^{t}Bu-acac)$_3$bpy as a model system to perform, for the first time, an analysis of the molecular structure evolution effect at different temperatures.[377] In this process we are evaluating the consequences of thermal structural changes over the electronic and magnetic structure. This also permitted us to know the accuracy of the REC model to interpret powder and single-crystal magnetic information in a low-symmetry heteroleptic complex. First-principles calculations were also performed and thus will be included in the description. In both approaches the atomic coordinates from single crystal X-ray crystallography at 20, 100 and 300 K were employed as inputs.

Temperature effects upon the energy levels, CFPs and ground state wave functions are going to be therefore elucidated at the end of this chapter.

10.2 Dy β-diketonate SIMs

Dy(^{t}Bu-acac)$_3$bpy was prepared as an amorphous powder and purified by recrystallisation by the group of Prof. Song Gao. The X-ray diffraction data was measured in a first stage at 100 and 300 K on MoK$_\alpha$ radiation (λ = 0.71073 Å) with a graphite monochromator. A few months later, the 20 K data were collected on synchrotron with liquid-helium for cooling. The molecule crystallises in triclinic P_{-1} space group in the temperature range 20-300 K. The molecular structure as well as the unit cell changes slightly upon the temperature variation. However one has to test the effects of such slight distortions over the experimental properties measured at different temperatures. Concerning the coordination environment, the crystal structures show that the trivalent dysprosium is coordinated by six oxygen atoms from β-diketonate ligands, and two nitrogen atoms from bipyridine (Figure 10.1).

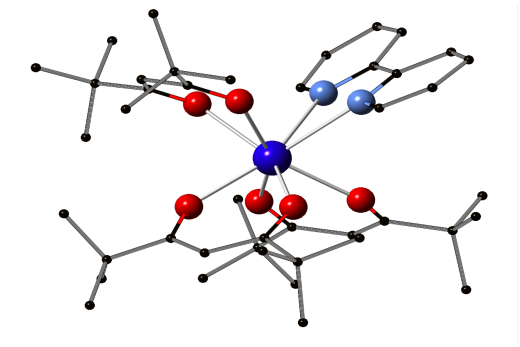

Figure 10.1: Molecular structure of Dy(^{t}Bu-acac)$_3$bpy, measured at 100 K. Hydrogen atoms are omitted for clarity.

Like many reported dysprosium β-diketonate systems, the molecular structure can be viewed as forming a 'paddle-wheel' shape, where the conjugated plane of each ligand forms the wheel. The anti-side wheels are nearly in the same plane. The two planes from the four ligands are approximately perpendicular to each other. The π-π stacking is found between bipyridine ligands of adjacent molecules at a separation of 3.3644 Å at 20 K. The two molecules in the unit cell are related by an inversion centre, meaning that the magnetic principal axes of these molecules are necessarily parallel to each other.

In 2014, Dr. Shang-Da Jiang proceeded with the determination of the magnetic principal axes of this low-symmetry complex mounting a single crystal of 3.07 mg with its (001) face on an L-shaped Cu/Be support, rather than a Teflon cube. This enabled the crystal to perform a rotation near the horizontal spin axis. Such a rotation was made around three orthogonal axes of the support in the temperature range of 1.8 to 15 K. The availability of data concerning single-crystal magnetic susceptibility, the low-symmetry of the system and the resolved crystal structures at three different temperatures allowed the REC model to be tested in the interpretation of the observables of this heteroleptic complex. The predictions given by CASSCF calculations were also benchmarked with the magnetic data. The structural thermal effects that may affect these properties at low temperatures were also investigated by both *ab initio* and *semi-empirical* methods. Such calculations were conducted on the molecular structures determined at the three temperatures.

With respect to the REC calculations, we used the SIMPRE computational package. Powder magnetic susceptibility data (2-300 K) and single-crystal easy axis susceptibility (2-15 K) were simultaneously fitted giving the same weight to each of them. Considering the different

temperature ranges, the crystal structure determined at 100 K was used for powder data, whereas the one resolved at 20 K was used for single crystal. The radial displacement (D_r) and effective charge (Z_i) parameters for the bipyridine ligand were taken from a previous work (D_r = 1.25 Å and Z_i = 0.133).[93] This simplified the problem with the number of free parameters. Thus, only two REC parameters were scanned, namely D_r and Z_i of the oxygen atoms from the β-diketonate ligand. The minimum relative error was achieved when the values of the parameters were that of D_r = 0.57 Å and Z_i = 0.677.

In order to have a better understanding of this molecule, our calculations were complemented with post Hartree-Fock calculations implemented in MOLCAS 7.8.[164,173] CASSCF calculations have been successfully applied to model the magnetic anisotropy of dysprosium single-ion magnets. In the present case, those calculations were undertaken by Dr. Bing-Wu Wang on the single molecule fragments from the single crystal structures at 20, 100 and 300 K. The corresponding outputs generated the possibility of discussing the results from both approaches with the experimental values.

From the experimental point of view, the temperature dependence of the magnetic susceptibility of Dy(^{t}Bu-acac)$_3$bpy (powder) was measured between 2 and 300 K, showing a typical paramagnetic behaviour. Magnetisation at 2 K under an applied field between 0 and 5 T was also included in this set of static magnetic measurements. In Figure 10.2 one can observe the experimental data together with the different theoretical results. The experimental χT product gradually decreases upon cooling due to depopulation of the electronic fine structure and the antiferromagnetic dipolar interaction.

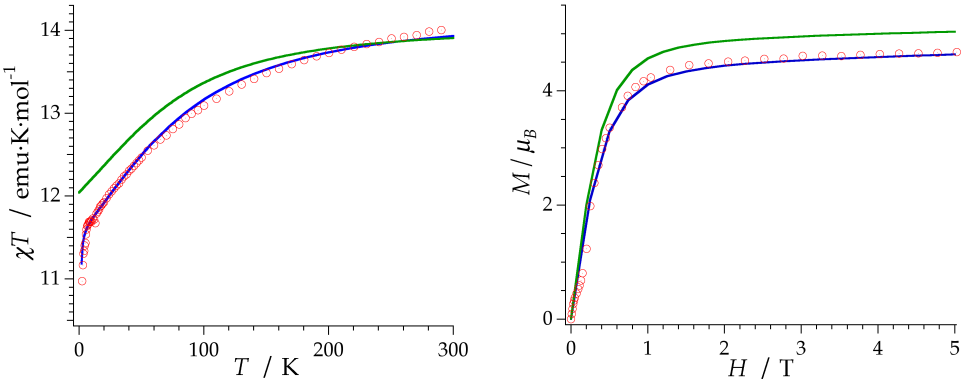

Figure 10.2: (left) Experimental (red circles) and theoretical (lines) χT product between 2 and 300 K at H=1 kOe; (right) Magnetisation measured at 2K and theoretical predictions; CASSCF (green) and REC model (blue).

Regarding the single crystal rotation, a sine curve was observed in all the temperature range with a periodicity of 180° (Figure 10.3(b)), but the sine curves below 3 K were not found to be symmetric in all the three rotations. In the study of the anisotropy of Cp*ErCOT (Chapter 9), it has been shown that the π periodicity can break down when slow magnetic relaxation exists.[367] Therefore this deviation from the central symmetric behaviour could be attributed to the hysteresis effect when the system is suffering a non-equilibrium state of the magnetisation. This occurs during the rotation below the blocking temperature and it could be verified from the splitting temperature of 3 K in the zero-field cooled and field cooled magnetisation measurement taken under 1000 Oe. This is exactly the magnitude of the field that was employed in the single crystal rotation.

The direction of the easy axis is plotted in Figure 10.3(a). It was determined to be nearly in the plane of two β-diketonate ligands which are in the anti-side. Indeed, the predicted magnetic easy axes by both

theoretical approaches were found to be close to the experimental result at 4 K (with deviations of 5.9° and 12.3° for the CASSCF and the REC model, respectively). The calculated angular dependence of magnetic susceptibility at 15 K (Figure 10.3(b), dashed lines) agrees well with the rotation around the *x* axis, both in phase and magnitude. In contrast, obvious deviations can be found for the calculated susceptibilities in the *y* and *z* rotations.

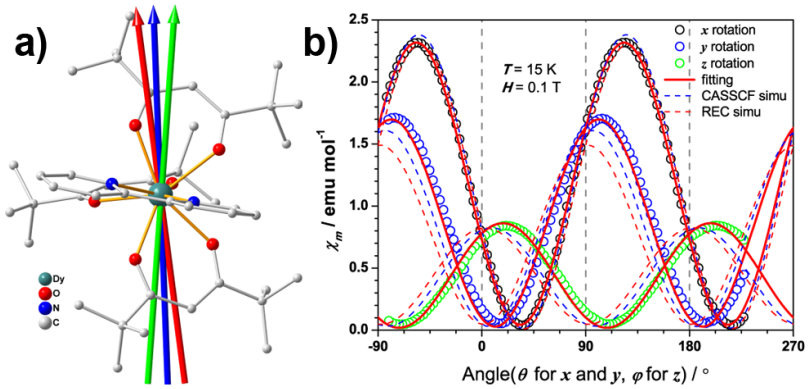

Figure 10.3: (a) View of the molecular structure of Dy(^{t}Bu-acac)$_3$bpy. The red, blue and green arrows indicate the magnetic easy axis directions determined from experiment, CASSCF calculation and the REC model, respectively. (b) Experimental (open circles) and simulated (curves) angular dependence of the magnetic susceptibility at 15 K. Solid and dash curves represent the simulation from the best fitting of the experiment and the two theoretical results. This figure has been adapted by Dr. S.-D. Jiang in Ref. 377.

The thermal variation of χT along the principal axes is plotted in Figure 10.4. Along the easy axis a constant value of 34 emu· K· mol^{-1} is observed, above 3 K, whereas along the other two directions the χT values are less than 0.5 emu· mol^{-1} K.

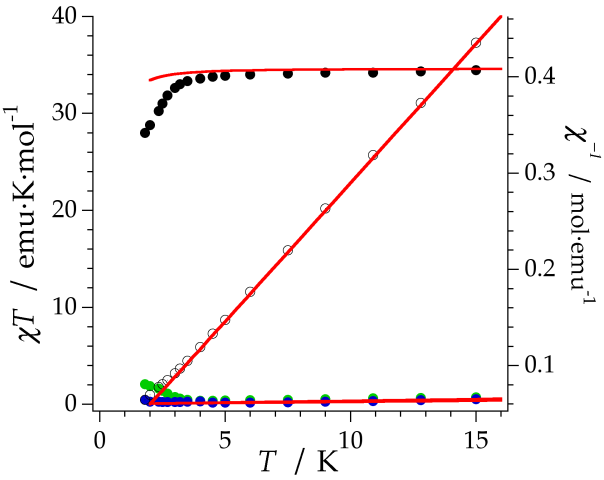

Figure 10.4: Experimental (circles) temperature-dependence of the single-crystal χT value along the principal axes (black: easy; medium: green; hard: blue). Red solid lines represent the REC fit. χ^{-1} along the easy axis: open circles.

The theoretical results presented in this chapter deserve a few comments. Based on the 20 K structure, as shown in Figure 10.2, the CASSCF simulation shows a more pronounced deviation compared with the experimental data in the χT product below 200 K. The information provided by the REC model (using two parameters) is able to reproduce the magnetic susceptibility from both single crystal and powder sample in the whole temperature range. The model has been able to predict accurately the field-dependence magnetisation of the compound (Figure 10.2 (right)). In the latter case, the ground state wave function is found to be composed by 86% $|\pm 15/2\rangle$ and 13% $|\pm 11/2\rangle$, with an effective spin 1/2 having a $g_{//}$ value of 19.11, very close to the value of 19.06 determined by the single crystal magnetisation measurement (linear fit in Figure 10.4). In contrast, CASSCF calculations result in a near-Ising limit with $g_{//}$ of 19.65.

Additionally, the REC model was able to reproduce the single crystal magnetic susceptibility data for the easy, medium and hard axes between 2 and 15 K.

Dynamic magnetisation of the magnetically pure and 5% diluted sample in the absence of an external field showed the presence of a frequency-dependent maximum in the out-of-phase signals (χ''), as can be observed in Figure 10.5. For the undiluted sample, quantum tunnelling of magnetisation was found at low temperatures. This was largely supressed by dilution. The relaxation energy barrier at higher temperature range was fitted to be 181 K in the pure analogue. To get rid of dipolar interactions, we illustrated the single ion behaviour on the diluted sample. In absence of spectroscopic information, it is not wise to sistematically assume that the relaxation happens via an Orbach process. Therefore the *ac* susceptibility data of the diluted sample was independently fitted to either Orbach or Raman relaxation processes. The fitting of the relaxation time upon temperature shows that Raman process is unlikely since the Raman exponent of 12.7 is too large for Kramers systems with isolated doublets. On the contrary, the data were very well reproduced by the Arrhenius fit indicating an Orbach process. Since the quantum tunnelling of magnetisation process is also efficiently suppressed, it therefore makes sense to compare the theoretical energy gap with the experimental effective barrier U_{eff} = 189 K (131 cm^{-1}).

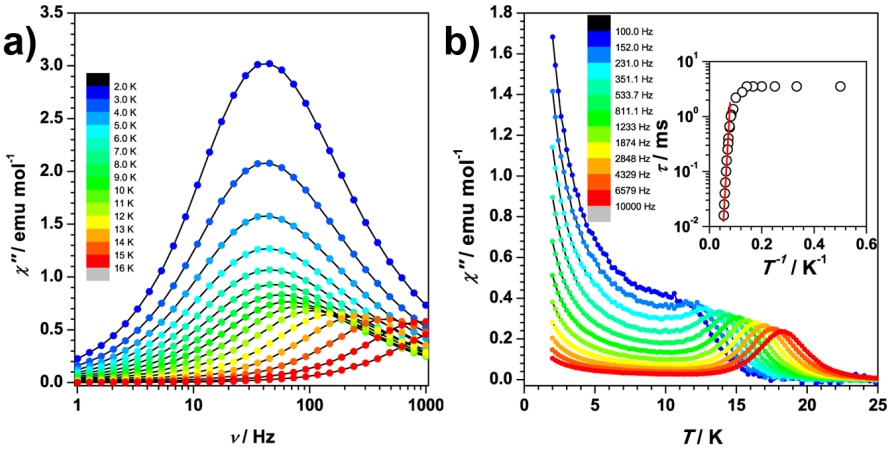

Figure 10.5: Out of phase dynamic susceptibility of magnetically pure sample at zero field as function of frequency (a) and temperature (b). Inset of (b): the relaxation time with respect to the inverse of temperature. The red line is the fitting to Arrhenius law.

We now move on to evaluate the thermal effects on structural distortions and the consequences that they can have on electronic structures. Both theoretical approaches showed that the contribution to the ground Kramers doublet wave function changes quantifiably with temperature. In particular, there is a downward trend in the relative weight of $M_J = \pm 15/2$ contribution upon warming.

At this point, it is necessary to note that the present change of the quantum and magnetic properties is due to structural deformation that alters even the ground-state wave function and not just because of the thermal population of excited wave functions. Regarding the effect of the thermal distortion on the energy levels, both theories predicted a slight decrease of the ligand-field splitting upon warming (Figure 10.6). It is interesting to realise that at the same temperature CASSCF and REC model provided basically the same energy gap: 169 and 165 cm^{-1} at 20 K for REC

and CASSCF, respectively; more shockingly, both methods predicted a gap of 162 cm^{-1} at 100 K and a gap of 156 cm^{-1} at 300 K.

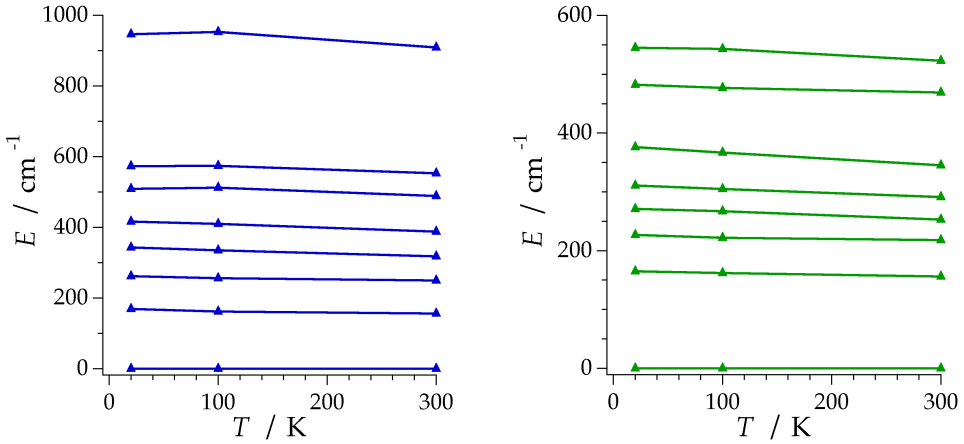

Figure 10.6: Calculated lower lying Kramers doublets using the crystallographic structures measured at 20 K, 100 K and 300 K; (left) REC model, (right) CASSCF.

Thus, both models produce very similar results in terms of the energy splitting between the ground and first excited doublet within the $^6H_{15/2}$ multiplet. Nevertheless, they do present important differences in the prediction of the higher energy levels of the ground multiplet (Figure 10.6). Therefore, further experiments will be needed to verify the theory. In particular, in this case we are not able to perform single crystal magnetisation measurements at higher temperatures due to the largely reduced signal upon warming and the relative large background. The use of techniques as cantilever torque magnetometry proposed by the group of Prof. Roberta Sessoli would be an interesting perspective to extend this research, owing to its high sensitivity at higher temperatures.[150]

These results paint a picture where the most prominent feature is that, at least in the present β-diketonate system, the thermal effects below 100 K on the magnetic properties are negligible. On one hand, the easy axis determined at 4 K makes an angle of 12.3°, 13.8° and 15.3° with the REC model based on the structure at 20, 100 and 300 K, respectively, while these angles for the CASSCF calculations are 5.9°, 6.2° and 7.9°. Both techniques demonstrate that the theoretically calculated magnetic axis does not seem to be sensitive to structural deformations owing to thermal effects. On the other hand, the main contribution to the ground state and the energy gap between ground and first excited state stay within a 2% range. These results illustrate that the electronic and magnetic structures change upon the thermal evolution of the molecular structure within the experimental error.

It is interesting to compare the tiny thermal effect quantified and reported in this thesis with the rather large scaling parameters that appear commonly in the literature and that are at least in part attributed to thermal effects. For example, CASSCF calculations in this system revealed a 2% deviation in the energy of the first excited level between 20 and 100 K, while scale factors of up to 60% have been used to match low-temperature spectroscopy and state-of-the-art *ab initio* calculations[176,177] using a crystal structure determined at 100 K.[152] One can expect that these deviations are not due to thermal perturbations. They should be attributed to intrinsic methodological limitations of current *ab initio* methods, such as the necessarily limited size of the employed basis sets or unaccounted dynamical correlation.

We were therefore able to conclude that in the absence of a critical phase transition, one can safely use the crystal structure information determined at liquid-nitrogen temperature in the magnetic anisotropy

research. The thermal effect of the molecular structure on the electronic structure does exist but it is negligible in practice.

Finally, the obtained REC parameters for the ^{t}Bu-acac ligand (D_r = 0.57 Å; Z_i = 0.677) were used to perform a quick estimation of the energy level scheme and the temperature-dependence magnetic susceptibility of a set of Dy^{3+} and Er^{3+} β-diketonate related systems. Thus, the magnetic and spectroscopic properties of $Dy(acac)_3(phen)$,[71] $Dy(acac)_3(dpq)$,[349] $Dy(acac)_3(dppz)$, $Er(h)_3(bipy)$ and $Er(h)_3(bath)$,[356] where h = 2,4-hexanedione and bath = bathophenanthroline, were predicted using the REC model. Of course, in all these five cases, the donor atoms of the theoretically threated ligands are not exactly equivalent to the ones parameterised. We have to understand these results as an approximation. However, the calculated wave functions are compatible with the SMM behaviour observed experimentally in each analogue. The main contributions to the ground state wave function are that of $M_J = \pm 15/2$ in the easy axis (see Table 10.1), especially dominant in the three studied Dy^{3+} derivatives. In the same table, one can observe that the values of the first excited state calculated by CASSCF (supporting information of *Nature Comm.*, **4**, 2551 (2013))[378] are comparable to the ones reported in this dissertation, as is the easy axis direction.

Table 10.1: First excited state of the ground multiplet calculated by CASSCF and the REC model in the present work of five related β-diketonate complexes. % M_J contribution to the ground doublet calculated by the REC model.

	CASSCF (cm^{-1})	**REC (cm^{-1})**	**Amplitude of $\|M_J>$ contributing to ground doublets (REC)**
$Dy(acac)_3(phen)$	142	151	80% $\|\pm15/2> + 17\%\ \|\pm11/2>$
$Dy(acac)_3(dpq)$	133	150	78% $\|\pm15/2> + 17\%\ \|\pm11/2>$
$Dy(acac)_3(dppz)$	160	180	81% $\|\pm15/2> + 17\%\ \|\pm11/2>$
$Er(h)_3(bpy)$	-	46	58% $\|\pm15/2> + 7\%\ \|\pm13/2>$ +18% $\|\pm9/2> + 11\%\ \|\pm7/2>$
$Er(h)_3(bath)$	-	57	75% $\|\pm15/2> + 8\%\ \|\pm7/2>$

The predicted temperature-dependent magnetic susceptibility shows a good agreement with experimental data in the five complexes (Figure 10.7). Note that temperature-independent paramagnetism and a correction factor F to correct possible deviations between the reported and real weight of the sample measured was added. It is worth mentioning that the predicted results are pretty impressive, because we are assuming the same parameterisation of the ligands of these related systems and it is obvious that they are not identical chemically to the ones investigated here. Nevertheless, this strategy permits a rapid estimation of the magnetic properties in order to choose which metal would be more adequate to be surrounded by a concrete crystal field leading to SMM behaviour.

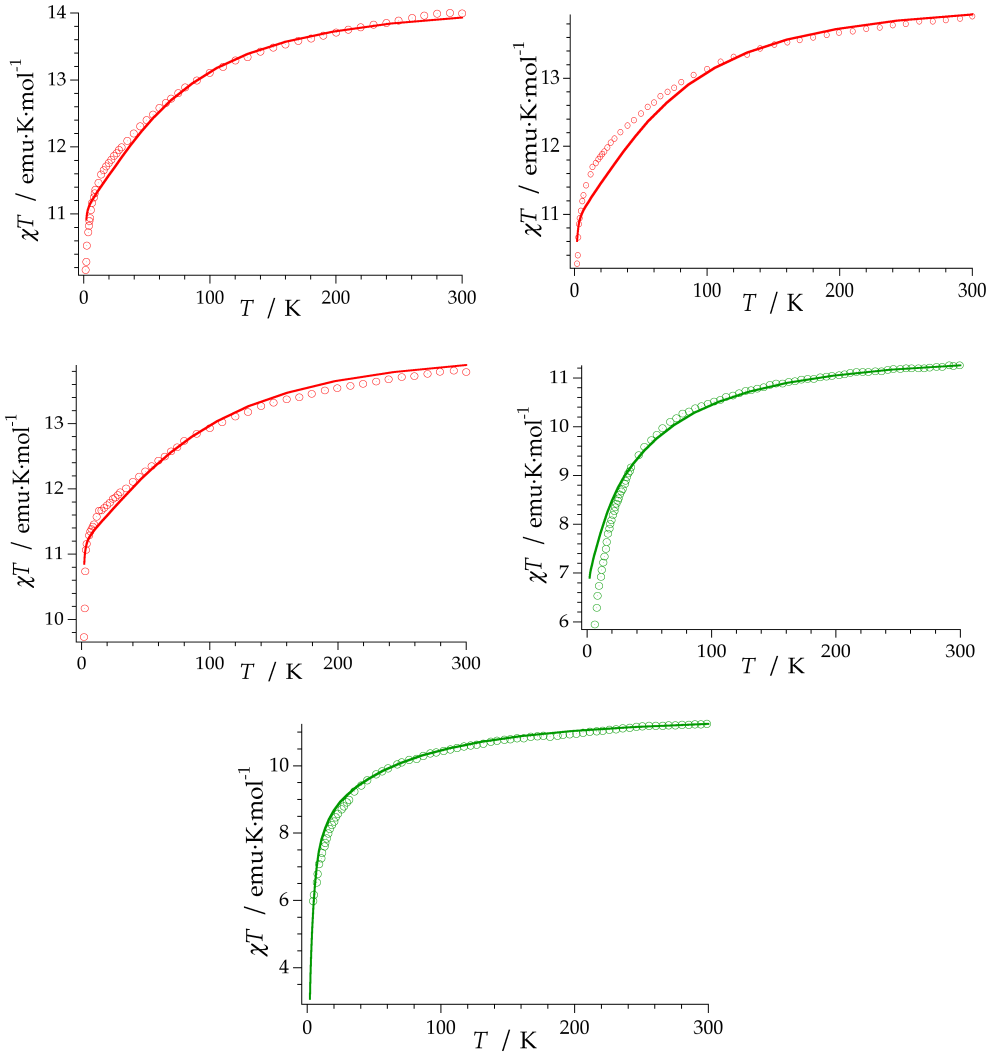

Figure 10.7: Experimental (open circles) and theoretical prediction using the REC model (lines) of the χT product of $Dy(acac)_3(phen)$, $Dy(acac)_3(dpq)$, $Dy(acac)_3(dppz)$, $Er(h)_3(bipy)$ and $Er(h)_3(bath)$.

10.3 Conclusions

This chapter, based on a combination of detailed experimental characterisations and two independent theoretical approaches, allows us to extract a few key insights. The most important one is that, for the first time, we have quantified the influence of the thermal evolution of the molecular structure in the electronic structure and magnetic anisotropy, and found it to be almost negligible, at least in the studied case of Dy^{3+} / β-diketonate, which possesses rather common features. In the absence of expected phase transitions, one can therefore trustingly employ the crystal structure determined at liquid-nitrogen temperature to discuss the magnetic anisotropy properties at liquid-helium temperature.

Regarding the energy level scheme, this also means that one can exclude these small structural variations as source of the rather large scale factors community employed in the CASSCF calculations for CF splitting. This is our main second conclusion. The deviations of the *ab initio* calculation from the experiment should probably be attributed either to a misuse of the technique, e.g. the triple-zeta basis set that is commonly used being insufficient or to fundamental limitations regarding dynamical correlations, rather than to thermal effects in the structure. The studied complex does not have any extraordinary or even unusual chemical features, and this suggests that the conclusions we extract are of general utility. Nevertheless, it is worth noting that the extension of the present study in combination with (a) spectroscopic as well as torque experiments in other systems and (b) to intermediate temperatures is necessary before one can categorically discard non-negligible effects of thermal structural evolution on magnetic anisotropy as a general rule.

Finally, the REC model has been successfully applied here with a combination of both powder and single crystal magnetisation data to reveal the magnetic anisotropy. One of its remarkable advantages compared to CASSCF approach is its high efficiency. With the available molecular structure and magnetic data, one can, on a personal computer, rapidly interpret the important information associated with magnetic anisotropy, including the CFPs, CF splitting, wave function components, magnetic principal axes orientation and the magnetic susceptibility tensor at various temperatures.

11 Single-ion magnets as spin qubits

11.1 Introduction

As described in the introduction of this thesis, a qubit (quantum bit) is a two-level quantum-mechanical system, which represents a unit of quantum information in quantum computing. When considering a molecular spin qubit, the two states can be, for example, the 'up' and 'down' states of the spin in a molecular nanomagnet. Lanthanoid coordination complexes are promising candidates as building blocks for spin qubits and a wide variety of them have been studied so far.[76,77,225–227]

The methods presented in this dissertation were not designed to deal with molecular spin qubits. The work presented so far is focused in the rational design and modelling of the properties of f-element SIMs. However, it is obvious that the description of energy levels and wave functions provided by the program through the REC model can help to understand the use of these systems as spin qubits, since their quantum behaviour is determined by these energies and wave functions.[122] The current version of SIMPRE offers a good starting point to implement new functionalities towards this research direction. In this context, the package

is nowadays under development by Dr. Salvador Cardona-Serra and Luis Escalera-Moreno. New versions of the SIMPRE package will include estimates of decoherence created by different decoherence sources, starting by the nuclear spin bath in SIMPRE 1.2.

In the latest chapter of this dissertation, we will provide several recommendations for the rational design of spin qubits based in lanthanide coordination complexes. This will include a recent example based in the Ho derivative of the family of polyoxopalladates presented in section 6.3.[222] This system has been treated with an extension of the SIMPRE program. A set of some basic ideas concerning the rational design of uranium-based spin qubits will also be reported. Finally, as an example, we will describe some of the features of the polyoxometalate-based single-ion magnet GdW_{30}, in which it was possible to increase the number of coherent rotations by a factor of 10 by matching the Rabi frequency with the frequency of the proton.[221]

11.2 Rational design of spin qubits

The main interest of the molecular approach for the design of spin qubits is that molecules can be chemically engineered to tailor their properties and to endow them with new functionalities.[17] In this regard, chemists can offer a very relevant contribution through the molecular engineering. Some special considerations need to be taken into account when designing an f-element coordination complex for its use as a spin qubit instead of as just a SIM. Such considerations mainly depend on its (i) nuclear spin, (ii) tunnelling splitting, and (iii) environment.

11.2.1 Lanthanides

The first issue for the optimisation of spin qubits, including those with lanthanide compounds, is the isotopic purity of the atom carrying the spin, which in this case means the rare earth. For getting a maximum quantum coherence, isotopic purity is a requeriment, being desirable at the very least. Since the nuclear spin couples with the electron spin, affecting the number, energy and properties of the available eigenstates, a sample with a natural distribution of isotopes contains a random mixture of quantum systems. In that sense, Ho, Tb, Tm and Pr are especially adequate since they only have one stable isotope each. Note that a nuclear spin accessible through contact hyperfine interaction has proven to be a very valuable resource. It can provide access to a larger number of well-defined states,[379] with the added advantage of nuclear spins being more resilient than electron spins towards decoherence. Nuclear spins play also a relevant role in the determination of the parity of the system, i.e. if the ion is Kramers or non-Kramers. Elements with an even atomic number like Dy, Er, Yb, Nd, have half-integer J and some of their isotopes are I=0. Therefore they are Kramers ions. In those cases, even if extradiagonal CFPs will potentially mix the components of the ground state doublet, they will not create a quantum tunnelling splitting. This simplifies the situation and thus can be favourable for some particular studies, but in general is less interesting, as explained below.

The tunnelling splitting (Δ) in the ground state is critical for the manipulation of the quantum state. Large tunnelling splittings can be advantageous both for an easier spin manipulation and for diminishing decoherence.[209] In that sense mononuclear lanthanoid-based qubits/SIMs (with splittings up to Δ= 0.1-1 cm^{-1}) are vastly superior to cluster-type

transition-metal-based SMMs (with usual splittings in the range of $\Delta=10^{-8}$-10^{-4} cm^{-1}). A large tunnelling splitting results from a high-order extradiagonal parameter that mixes $+M_J$ with $-M_J$ in the ground state, either directly or by means of an intermediate M_J. In turn, large extra-diagonal parameters can often be related to molecular high symmetry axes. Hence, for designing molecules with large tunnelling splittings we will need to have a ground M_J doublet that can be mixed by an extra-diagonal term allowed by the symmetry of the molecule.

Let us give two examples based on POM chemistry. The first concerns the series $[Ln(W_5O_{18})_2]^{9-}$ with D_{4d} symmetry, which were deeply analysed in the sixth chapter. In this case the small distortion from an ideal D_{4d} symmetry allows the appearance of non-diagonal terms B_{44} and B_{64}. This facilitates the mixing of a ground state doublet containing $M_J = \pm4$, which is exactly what happens for the Ho derivative. This compound has a tunnelling splitting of $\Delta = 0.3$ cm^{-1}.[313] Recent extensive structural, magnetic and spectroscopic characterisations have raised the possibility of observing coherent spin dynamics in this analogue. The second example involves the Preyssler polyoxometalate anion $[LnW_{30}O_{110}]^{12-}$.[63] This anion shows an atypical geometry with a C_5 axis in such a way that a very high B_{65} non-diagonal parameter can be estimated. Therefore, when the ground state doublet contains a large contribution of $M_J = \pm5$, a very strong mixing through $M_J = 0$ is possible. This situation may occur for the Tb derivative, which, according to our calculations, should lead to a tunnelling splitting $\Delta \sim 0.1$ cm^{-1}.

Last but not least, one needs to consider the interactions that take place beyond the first coordination sphere. The more relevant ones for our purposes are the interaction with other spins (electronic or nuclear) and

electron-phonon coupling. In fact, a recent work shows that decoherence in a model SMM can be tracked down to precisely these three sources: magnons, nuclear spins and phonons.[39,380]

Unwanted interaction with neighbouring spin qubits –in the form of magnons– is a common source of decoherence. In lanthanoids this problem can be easily addressed by diamagnetic dilution. Of course, under certain conditions spin-spin coupling can also be used as a resource instead of just as a problem. This has been exploited to implement an intramolecular Controlled-NOT quantum gate.[226]

Nuclear spins are best kept away from the spin qubit. When the nuclear spin belongs to the lanthanoid its coupling to its electronic spin is strong, and it does not introduce any decoherence. In contrast, the surrounding atoms can introduce a large decoherence. In this context, the most critical region concerns the atoms that are directly coordinated to the lanthanoid ion. Some of them are nuclear spin-free (oxygen or chalcogenides), and thus they are much preferable than those having nuclear spins (nitrogen or halogens). Carbon would be a good option, but in the vast majority of the cases it is bonded to hydrogen, which has the highest gyromagnetic ratio of all elements. In fact, when ^{1}H is present in the sample, deuteration is often the most effective way to minimise decoherence.

Finally, we also need to understand and estimate the state-dependent electron-phonon coupling. Phonons can cause leakage to excited states within the same molecule and they can communicate qubits at long distances even in absence of dipolar coupling. The solution for this is to design qubits that are almost transparent to phonons. This means qubits in which the phonon interactions do not affect the energy differences within the qubit nor the response to experimental stimuli. Of course, this can only

be achieved after a deep magneto-structural analysis. A general recipe would be to have a very rigid coordination sphere for the qubit, while the crystalline environment in which the qubit is embedded is much softer. Molecular-based materials naturally satisfy this requirement.

As a practical example, we are going to describe the performance of $HoPd_{12}$ as a qubit. In particular, this case has been studied by a recently developed extension of SIMPRE. This extension calculates the hyperfine coupling to the nuclear spin bath and estimates decoherence time from this source.[381] Despite the fact that this approximation neglects other decoherence sources and, therefore, it only provides an upper bound for the decoherence time, it is a useful tool to provide a starting point towards an inexpensive theoretical quantification of decoherence for molecular spin qubits based on lanthanoids. Eventually, this will permit to advance beyond the stage of a qualitative characterisation.

Compared to complexes with organic ligands, decoherence due to the coupling to the nuclear spin bath is unusually weak in POMs. This is an expected result in view of the low abundance of protons in the vicinity of the lanthanoid ion. The calculations carried out in this particular example have served to perform an analysis of the adequacy as molecular spin qubits of cubic or near-cubic systems such as $HoPd_{12}$ (Figure 11.1). The most extraordinary feature in such highly symmetric systems is the abundance of degenerate or near-degenerate levels at low energies (see Figure 6.21). The ground state is a doublet and the first excited state is a triplet located at only 2 cm^{-1}. So, there are five electron spin energy levels within the range of conventional pulsed EPR.[222]

We considered the possibility of distorting the cubic site by introducing a moderate axial compression of up to 1% ($\Delta z/z$, where the field is also applied as H_z). Of course, this physical effect can also be

achieved, albeit less systematically, in a chemical way. This procedure will use ligands that generate a nearly cubic environment. In the Ho case, it has been estimated how different degrees of symmetry breaking (in our case, different axial compression ratios from 0 to 1%) and different applied fields (up to 1 T) alter decoherence times, τ_n. For that, 80,000 calculations considering 200 compression factors and 400 applied magnetic fields have been done. This is one of the greatest advantages of this kind of inexpensive calculations: they offer the possibility to perform a high number of outputs in a short time. The crossings of three levels create a "phase diagram" with three different zones (Figure 11.1) which are distinguished by the character of the wave function of the first excited state.

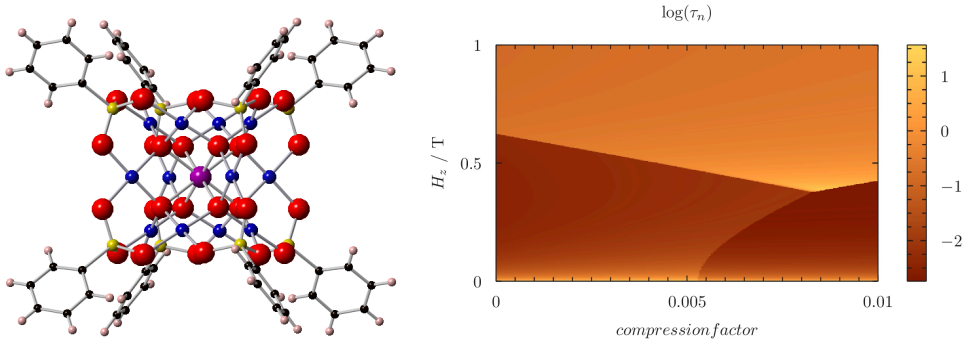

Figure 11.1: (left) Molecular structure of $HoPd_{12}$; (right) variation of the decoherence time in logarithmic scale, $\log(\tau_n)$, considering the coupling to the nuclear spin bath. Vertical axis: applied magnetic field, in Tesla. Horizontal axis: axial compression factor ($\Delta z/z$) of the equilibrium distance.

The different phases also have fairly different decoherence times. They range from tens or hundreds of milliseconds up to 10 seconds. For clarity, the logarithm of τ_n has been represented. These estimates need to be taken with caution. It is known that relatively long decoherence times can

be obtained in cases such as the $(PPh_4)_2[Cu(mnt)_2]$ complex,[82] or HoW_{10} (Coronado, E. & Hill, S. *Submitted*), where like in the present case nuclear spins are absent from the vicinity of the metal. Even in these complexes, actual experimental decoherence times are considerably shorter than the present nuclear-spin-only estimates: 68 μs $(PPh_4)_2[Cu(mnt)_2]$ and 8 μs (HoW_{10}).

The most significant finding is that in a fairly ample region (at fields between 0.4 and 0.5 T and at compressions from 0.5% to 1%) decoherence times are at least two orders of magnitude above those calculated for lower fields or lower compressions. In this region the expectation value $\langle J_z \rangle$ for the first excited state is almost identical to that of the ground state. For example, for a compression of 0.85% and an applied field of 0.39 T the wave functions of the ground and first excited states are mainly composed by, respectively, the following M_J components: $|\Psi_0\rangle = 20\%|-8\rangle + 70\%|-4\rangle + 7.5\%|+4\rangle + 2\%|+8\rangle$; $|\Psi_1\rangle = 32\%|-7\rangle + 62\%|-3\rangle + 4\%|+5\rangle$ and they result in expectation values $\langle J_{z0} \rangle = -3.93$ and $\langle J_{z1} \rangle = -3.86$. In this particular case, another favourable circumstance is the fact that the transitions between $|\Psi_0\rangle$ and $|\Psi_1\rangle$ are allowed by EPR, as the two states are dominated by terms that differ in $\Delta M_J = 1$. As the two states of the qubit $|\Psi_0\rangle$ and $|\Psi_1\rangle$ generate magnetic fields that are also almost identical, the nuclear spins around them, while affected magnetically by the presence of the Ho ion, will not be able to detect the state of the qubit. The key point is that, while the ground state is only slightly and continuously affected by a moderate change in the distortion or the magnetic field, the level crossings means that the first excited level has a completely different character at each of the three zones in the "phase diagram". The triple crossing region,

keeping constant either the compression (left) or the magnetic field (right), is depicted in Figure 11.2.

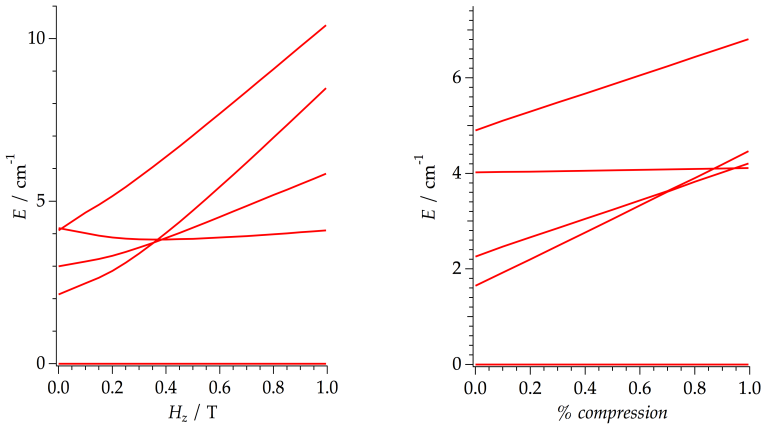

Figure 11.2: Evolution of the five lowest energy levels of $HoPd_{12}$ versus (left) magnetic field between 0 and 1 T at an axial compression of 0.8 % and (right) % of axial compression between 0 and 1% at a magnetic field of 0.41 T.

This extremely unusual situation can provide an alternative strategy to the usual approach based on the use of magnetic molecules having a "large tunnelling splitting". For non-Kramers ions, large tunnelling splittings mean an intense mixing of pseudo-classical "up" and "down" states. As a result, magnetic interactions are minimised, and both decoherence caused by the spin bath and decoherence caused by magnons are quenched. Unfortunately, at the same time large tunnelling splittings increase decoherence caused by phonons.[39]

As transition energy has to be matched eventually by a microwave pulse in an EPR experiment, exceedingly large tunnelling splittings may be impractical in some cases. By using the condition $\langle J_{z0} \rangle \approx \langle J_{z1} \rangle$, as in the present case, decoupling from magnetic interactions can be achieved without these detrimental side effects. Note that both achieve the same

goal: when the nuclear spins are not coupled to the qubit state, they effectively disappear and cannot introduce any decoherence. Moreover, the same argument is valid for decoherence caused by neighbouring qubits: if the state of the qubit affects its $\langle J_z \rangle$ expectation value only marginally, decoherence caused by magnons vanishes. Thus, to operate the system, a third energy level would need to be used each time that the algorithm temporally requires a restoration of this interaction.

Note, however, that this extraordinary performance may come at a cost. Since the situation analysed above is close to two level crossings, there are two energy levels in the immediate vicinity. That means that small inaccuracies in the EPR pulses would result in transitions that would take the system out of the qubit space. One should also take into account that different decoherence sources are essentially additive, so that reducing the spin-spin interactions below certain level just means that most decoherence comes from interaction with phonons. Fortunately, POMs are also ideal systems in that regard, because of their rigidity.

11.2.2 Uranium

Regarding the design of uranium complexes for quantum computing applications, the main difference between U^{4+} and U^{3+} lies with the possibility of using U^{4+} complexes as spin qubits. In fact, this ion can provide examples with a large tunnelling splitting for the ground state. As happens with lanthanoids, uranium complexes with easy-axis ground states $M_J = \pm 4$ or $M_J = \pm 3$, with a fourth-range or with a sixth-range mixing, respectively, will be strongly mixed and therefore will present sizeable tunnelling splittings. But because of the much larger ligand-field of actinoids compared with lanthanoids due to the larger size of the 5f

orbitals, this mixing, and the corresponding tunnelling splitting, will be also much larger than for lanthanoids in favourable cases. These can be translated into uncoupling from magnons and from the nuclear spin bath; thus, into very long decoherence times.

11.3 Coherent manipulation of GdW_{30}

Since molecular spins are quantum objects and not just classical binary memories, the greatest challenge is precisely the manipulation of this single spin during a sufficiently long time. In the terms of quantum computing, this means the preservation of quantum coherence, i.e. all the information of the wave function, during the application of many quantum gate operations.[380] This physics is not necessarily captured by measuring the T_1 and T_2 relaxation times, since this is done in ideal conditions, with pulse sequences that do not reflect actual quantum operations. Since the pulse sequences are typically rich in waiting time, the determined values typically do not depend on the microwave power. A step forward in this direction is to measure the number of Rabi oscillations, a minimal quantum operation that is sensitive to realistic experimental parameters.[193]

In a recent study of the molecular magnet $[V^{IV}_{15}As^{III}_{6}O_{42}(H_2O)]^{6-}$ (V_{15}), the damping time τ_R was found to depend strongly on the microwave power.[213] Indeed, two effects were characterised: (i) a linear dependence of the Rabi decay rate $1/\tau_R$ and the Rabi frequency Ω_R (or, equivalently, the magnetic component of the microwave field) and (ii) a large increase in the decay rate near or below the Larmor frequency of the proton. Effect (i) is a well-known mechanism associated with the dispersion of the Landé g factors of the magnetic molecules and with intercluster dipolar interactions,

but (ii) constituted a new phenomenon related with dissipative electron-nuclear cross-relaxation.

In this section we extend this kind of study to the POM $[GdW_{30}P_5O_{110}]^{12-}$ (in short, GdW_{30}).[220] In this POM structure the lanthanoid cation can occupy two equivalent coordination sites, which show a very unusual fivefold geometry formed by five phosphate oxygens ($d_{Ln\text{-}Op} \approx 2.7$ Å) and five bridging oxygens between two wolfram atoms ($d_{Ln\text{-}OW} \approx 2.9$ Å). The result is a pentagonal antiprism coordination site as can be seen in Figure 11.3.

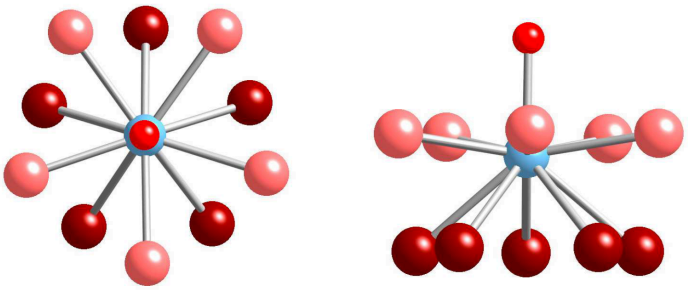

Figure 11.3: Schematic structure of the $[GdW_{30}P_5O_{110}]^{12-}$ anion showing the coordination of the lanthanoid ion in a fivefold environment. The apical water molecule can be seen in the right panel.

The lanthanoid cation is not placed at the centre of this antiprism but closer to the plane formed by the phosphate oxygens. A water molecule placed in an axial position close to the other coordination site completes the coordination sphere ($d_{Ln\text{-}O} \approx 2.2$ Å). The coordination number of the lanthanoid cation is eleven (monocapped pentagonal antiprism). GdW_{30} was prepared and magnetically characterised in 2012 by some members of the group, exhibiting slow relaxation of the magnetisation.[220] The present study was made on polycristalline powder of $K_{12}[YW_{30}P_5O_{110}H_2O]\cdot nH_2O$ doped with 1% and 0.1% of Gd^{3+}. This is a standard procedure that

weakens Gd-Gd interactions, resulting in longer decoherence times and an easier observation of Rabi oscillations. The new experimental results have allowed to find a new effect in this nanomagnet, characterised by a great enhancement in the coherence.[221]

Echo-induced EPR experiments were performed in this analogue by Dr. Helena Prima-García. The measurements were carried out in the region around 350 mT due to the broad maximum observed around this value. The microwave power was varied and the Rabi frequency (Ω_R) and its decay (τ_R) were evaluated. This led to the observation of an abnormally high number (more than 80) of low-amplitude oscillations after the usual fast decay near 15 MHz (Figure 11.4). At the working field B_0 = 349.6 mT, the Larmor frequency of the proton is ν_H = 14.89 MHz, but the hyperfine coupling of the Gd^{3+} ground state $^8S_{7/2}$ is also in this range.

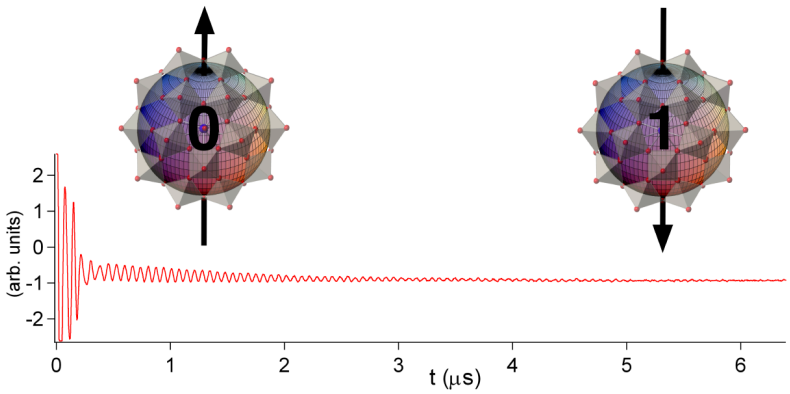

Figure 11.4: Measured $<M_z(t)>$ showing the result of nutation experiments on GdW_{30} at microwave powers that are near values where Rabi frequency coincides with the Larmor frequency of the proton.

For a better understanding of the variation of the observed frequency, it is useful to assign the electronic transitions. The energy level scheme, as a

function of the magnitude and orientation of B_0, (Figure 11.5) was calculated using crystal field parameters determined in a previous work,[220] and introduced in the SIMPRE code. At B_0 = 349.6 mT and for a microcrystalline powder sample the main calculated contributions are transitions with a character that is mainly either ±7/2 ↔ ±5/2 or ±5/2 ↔ ±3/2 (marked with arrows in Figure 11.5 (right)).

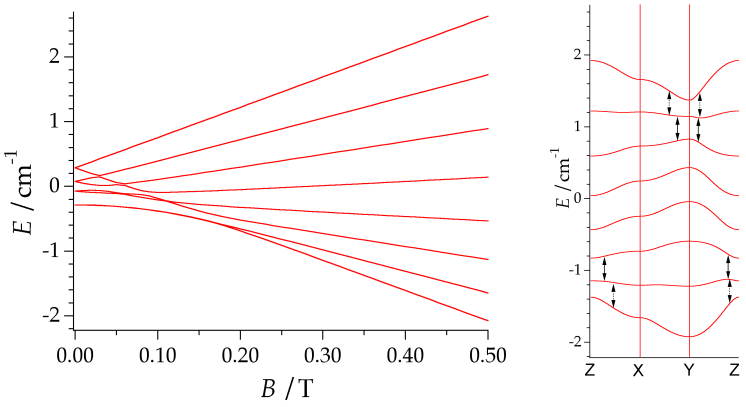

Figure 11.5: Calculated Zeeman splitting of GdW_{30}, sweeping the magnitude of Bz parallel to the molecular symmetry axis (left) and the orientation of |B| = 349.6 mT (right).

Those transitions that take place between ±5/2 and ±3/2 would be ideally expected to bear Rabi transitions 31% larger in frequency than the ones that occur between ±7/2 and ±5/2. In practice, due to the different composition of their wave functions, it is more likely that four different frequencies appear within this window. According to the same type of calculations and due to the different transitions involved, a slightly larger frequency range would be expected for 300 mT and a reduced range would be expected for 400 mT, but the average Rabi frequency should not change.

The Rabi frequencies should be proportional to B_1. In contrast, the observed frequency of long-term oscillations is directly proportional to B_0, like the Larmor frequency of the proton. In fact, apparently a match between the Rabi oscillations and the frequency of the proton, i.e. the Hartmann-Hahn condition,[382] is necessary for observing this phenomenon.

11.4 Conclusions

For the rational design of molecular spin qubits we have to exert control over two levels: the crystal field geometric effect and the interaction with further electron spins, nuclear spins and phonons. The interaction with the environment has already been commented above.

Let us now comment the effect of the crystal field around the lanthanoid. Two are the minimal electronic features required for having a spin qubit: (i) a controlled mixing of the wave functions in a well-defined level subset, and (ii) a sufficient isolation of this subset from the rest of the spectrum. These two requirements are the same than those needed for the design of SIMs. Hence, many SIMs will also be useful as spin qubits. Additionally, lanthanoid complexes can present a large tunnelling splitting in the ground state, Δ, which can minimise decoherence coming from the magnetic noise (dipolar + hyperfine). In this sense, the tunnelling splitting in lanthanoid SIMs can be much higher thant that exhibited by cluster-type SMMs (by a factor larger than 10^9). Hence, this favourable effect for minimising decoherence is expected to be much more pronounced in the case of mononuclear lanthanide complexes. Taking into account this last effect, the three necessary conditions that favour the design of a qubit will be: (i) to use non-Kramers ion (for example, Tb or Ho), (ii) to choose a

geometry for this lanthanoid allowing for a large extra-diagonal CFP, and (iii) to have a ground state doublet ± M_J such that $2M_J$ is a multiple of the order of this extradiagonal operator, q. As the q-value coincides, in general, with the order of the main symmetry axis of the molecule, an easy way to satisfy the third requirement is that of finding a molecular geometry having a q-order axis equal to $2M_J$. Two examples that illustrate this point are provided by the polyoxowolframates $[Ho(W_5O_{18})_2]^{9-}$ (C_{4v}, $M_J = \pm 4$, $\Delta \approx 0.3$ cm^{-1}) and $[TbW_{30}O_{110}]^{12-}$ (C_{5v}, $M_J = \pm 5$, $\Delta \approx 1$ cm^{-1}); both of which have been experimentally found to show unusually long decoherence times.

Secondly, we have studied the possibilities that an octahedral molecule can offer when lifting the strict cubic symmetry and/or when applying an external magnetic field. While we simulated the distortion of the cube by introducing a physical compression, the same effect could be achieved chemically, by crystalline pressure or asymmetric substitution. We used a recently developed method to inexpensively estimate decoherence times from the coupling of the electronic spin with the nuclear spins, which is included in the SIMPRE 1.2 program. In the non-Kramers Ho^{3+} complex we found that, for moderate axial compression and in presence of small magnetic fields, it was possible to reach a regime where decoherence caused by the nuclear spin bath is quenched. This is achieved in the ground doublet when the two qubit states have virtually identical spin expectation values. In this regime the qubit states are invisible to the spin bath, and vice versa. This strategy is a generalisation of the well-known approach based on the presence of large tunnelling splittings. The strategy is quite general and can be applied to systems with a high degeneracy of levels near the ground state. Although a complete estimation of decoherence time would require taking into account all the possible

sources of decoherence, this result should stimulate chemical and physical work on the design and study of nearly-cubic lanthanide complexes.

Finally, we have presented the features that make the POM SIM $[GdW_{30}P_5O_{110}]^{12-}$ of special interest as a spin qubit candidate. These features allow us to do sophisticated EPR manipulations in the context of molecular spintronics and/or quantum algorithms. We have found that in the optimal working conditions the long-term oscillation frequency is governed by the static magnetic field B_0 instead of the microwave magnetic field B_1. This suggests a mechanism of coherence transfer between the electron and nuclear spin at the Hartmann-Hahn condition, which results in a high number of coherent rotations. This behaviour, which to the best of our knowledge has not been described for other SIMs, might be related to the unusual proximity of the apical water to the lanthanide in this polyoxometalate (see Figure 11.3). To actually implement a useful algorithm it is necessary to implement a certain number of quantum operations within the coherence time. In this case, it has been observed that it is possible to perform at least 80 such operations. This is ten times higher than the usual range for molecular spin qubits reported in the literature and thus shows the promising of exploiting this phenomenon in related systems.

Resumen

Resumen

Los imanes monomoleculares o moléculas imán, por sus siglas en inglés SMMs, han suscitado una gran atención en los últimos años debido a sus extraordinarias propiedades físicas. Los cristales de este tipo de moléculas se caracterizan por presentar relajación lenta de la magnetización a baja temperatura, así como curvas de histeresis magnética. Estas moléculas se encuentran entre las entidades con comportamiento magnético más complejas, mostrando fenómenos cuánticos tales como efecto túnel en la magnetización, coherencia cuántica o interferencia cuántica. Por esto, se han postulado como candidatos prometedores para el diseño de bits cuánticos (qubits) de espín en computación cuántica. La primera generación de estos imanes monomoleculares estaba basada en complejos polinucleares formados por clusters magnéticos metálicos con estados fundamentales de alto espín, siendo el más conocido el complejo formado por doce núcleos de manganeso, cuya fórmula es $[Mn_{12}O_{12}(CH_3COO)_{16}(H_2O)_4]$. La posibilidad de sintetizar SMMs usando un solo centro magnético (ion lantánido) fue demostrada por Ishikawa en 2003, a partir de complejos ftalocianinato-lantánido ($LnPc_2$). Éstos presentan una estructura de dos pisos donde dos ligandos planos π conjugados (dianión de ftalocianina), girados 45º respecto al otro, encapsulan el centro metálico de la tierra rara, generando una simetría de campo de ligando D_{4d} alrededor del lantánido. Por otro lado, en 2008 en nuestro grupo se caracterizó la segunda familia de SIMs de lantánido a partir de polioxometalatos. Las diferencias en el comportamiento magnético de ambas familias se pudieron relacionar con pequeñas

diferencias en las estructuras cristalográficas. Dicho estudio abrió las puertas al diseño racional de estos sistemas teniendo en cuenta las diferencias en anisotropía magnética, que está condicionada por la geometría molecular.

La primera parte de este trabajo está centrada en el desarrollo del marco teórico y computacional que se ha utilizado a lo largo de toda la tesis. Cuando se empezó esta investigación, tan solo unos pocos ejemplos de SIMs se habían publicado, por lo que era de imperativa necesidad proporcionar a la comunidad de magnetismo molecular un programa que ayudase a racionalizar qué condiciones debía satisfacer una molécula para exhibir relajación lenta de la magnetización. En este contexto, se desarrolló la principal herramienta de esta tesis, el programa SIMPRE (Single-Ion Magnet PREdiction), que se ha presentado y descrito en el Capítulo 2. En dicho capítulo se ha explicado a manera de tutorial la organización del mismo y se ha puesto como ejemplo un sistema sencillo (un cubo ideal) para ilustrar su uso. El programa está basado en un modelo electrostático de cargas puntuales a partir del cuál se pueden calcular las propiedades espectroscópicas y magnéticas. Esta herramienta es clave para predecir las propiedades estáticas a partir de una estructura molecular determinada, lo cual nos va a permitir guiar la síntesis de nuevos sistemas. En el Capítulo 3 nos enfrentamos por primera vez al gran reto del diseño racional de SIMs. Por supuesto en aquel momento no se podía ofrecer una descripción realista de las propiedades espectroscópicas y magnéticas de sistemas reales, debido a las limitaciones inherentes del PCEM. No obstante, sí que pudimos diferenciar entre la influencia que tiene el lantánido y la del entorno de coordinación a partir de estudios en sistemas ideales. En este contexto, se evaluaron a modo de ejemplo las consecuencias de un entorno puramente axial y otro puramente ecuatorial en sistemas basados en Dy^{3+} y

Er^{3+}, plasmando de una forma más cuantitativa el análisis realizado por Long *et al*. prácticamente en paralelo. Posteriormente, el modelo de cargas puntuales se aplicó a las geometrías más típicas de lantánidos y se estudió la variación de parámetros de campo cristalino al pasar de una geometría ideal a otra, así como la variación de los niveles de energía, lo cual está íntimamente relacionado con las propiedades magnéticas. A continuación se tuvo una primera toma de contacto con medidas de fotoluminiscencia en hexacloroelpasolitas, lo cuál permitió completar los cimientos de esta tesis a partir del desarrollo de dos nuevos modelos electrostáticos que mejoran notablemente el potencial del PCEM, manteniendo su simplicidad. Estos modelos son el modelo de carga efectiva radial (REC) y el modelo de carga efectiva del par solitario (LPEC). La capacidad predictiva de ambos modelos se basa en la posibilidad de asociar dos parámetros para cada tipo de ligando. En el modelo LPEC se introduce un parámetro extra que representa la dirección del par solitario en sistemas con ligandos rígidos, en los que la densidad electrónica del par solitario no apunta directamente al lantánido. La obtención, por medio de ajustes fenomenológicos, y el posterior almacenamiento de estos parámetros en una librería general de ligandos nos va a permitir utilizarlos para predecir el comportamiento de sistemas en el futuro.

En la segunda parte de esta tesis se han aplicado dichos modelos electrostáticos de carga efectiva a diferentes compuestos coordinados por un mismo tipo de átomo dador. En primer lugar, se realizó un estudio sistemático de cuatro familias isoestructurales que se encuentran coordinadas por halógenos (Capítulo 5). Para completar esta tarea se utilizaron datos espectroscópicos de alta calidad, que nos permitieron estimar los parámetros REC para cada átomo dador (flúor o cloro) en función del número de coordinación. Un estudio más profundo de los

resultados obtenidos permitió relacionar dichos parámetros con conceptos químicos como la electronegatividad de Pauling y el número de coordinación a través de una expresión sencilla. Esta ecuación nos va a proporcionar un buen punto de partida para análisis fenomenológicos más sofisticados en los que se tenga en cuenta un conjunto de medidas espectroscópicas y termodinámicas. Posteriormente, nos adentramos en el Capítulo 6, que es el más extenso de esta tesis. El capítulo está enfocado a complejos coordinados por átomos de oxígeno. Un tipo de sistemas de este tipo particularmente interesantes son los polioxometalatos. A este respecto, se ha descrito el estudio de cinco series (LnW_{10}, LnW_{22}, $LnMo_{16}$, $LnMo_{10}$ y $LnPd_{12}$) de POMs octacoordinados que presentan un interés en magnetismo molecular y computación cuántica. Por otro lado, se predijeron los niveles de energía producidos por el desdoblamiento de campo cristalino y las propiedades magnéticas de una familia de oxidiacetato coordinada por nueve átomos de oxígeno (LnODA). La aproximación a esta familia permitió predecir el comportamiento como SMM en los derivados de disprosio y erbio, proponiendo su síntesis experimental y su caracterización magnética. La recolección de estos nuevos datos, junto a los espectros de fotoluminiscencia medidos en la década de los años 90 en estos sistemas, nos proporcionó una oportunidad ideal para testear las capacidades del modelo REC y compararlo a cálculos más sofisticados basados en primeros principios (CASSCF y CASPT2). Como se ha visto, en el caso de DyODA y ErODA el modelo REC ofreció mejores resultados que los calculados por *ab initio*. Por otro lado, el modelo se utilizó para interpretar las propiedades de dos hidróxidos de disprosio organizados en capas, donde se identificaron los diferentes procesos de relajación a partir de los diferentes resultados para cada centro individual. Además, el modelo jugó un papel clave en el diseño racional del primer ejemplo de un

metal-organic framework (MOF) con nodos que se comportan como SMM usando SIMs lantánidos. La estructura fue analizada previamente con el programa, lo que sirvió para predecir dicho comportamiento antes de entrar en el laboratorio. Tras los oxígenos, el siguiente paso natural fue el explorar el siguiente átomo dador en términos de relevancia práctica: el nitrógeno. En el capítulo 7, el modelo LPEC se utiliza por primera vez en la tesis para describir las propiedades magnéticas y espectroscópicas de la primera familia de SIMs, cuyos ligandos son ftalocianinato, en los que la densidad de electrones no está apuntando directamente al lantánido. Asimismo, dos complejos de coordinación con ligandos derivados de pirazol fueron analizados en términos del modelo de REC. Dichos estudios completaron la trilogía presentada en esta parte de la tesis, demostrando el gran potencial de estos modelos semiempíricos, especialmente cuando se tratan sistemas con enlaces iónicos, pero también ofreciendo resultados prometedores en sistemas en los que la covalencia juega un papel importante.

La parte final del trabajo se centra en los retos actuales que tienen las herramientas desarrolladas durante la tesis. En el Capítulo 8 se han analizado las capacidades tanto del programa, como del modelo REC, para hacer frente a la comprensión de los imanes monomoleculares de uranio, que son la siguiente frontera en nanomagnetismo. Las limitaciones que tiene SIMPRE al no contar con estados excitados se complementan con el uso del programa CONDON, que usa el Hamiltoniano completo. Un segundo desafío que se ha estudiado es la modelización de la anisotropía magnética molecular (Capítulo 9). Para ello, se predijeron usando el modelo LPEC dos rotaciones perpendiculares realizadas por magnetometría con un único cristal de Cp*ErCOT. Posteriormente, los parámetros obtenidos para los ligandos Cp* y COT se utilizaron para

predecir y comparar los resultados con las medidas experimentales en dos sistemas relacionados. En el Capítulo 10, el modelo REC se utiliza para investigar el tratamiento de complejos heterolépticos coordinados por átomos de oxígeno y nitrógeno. La determinación de la estructura química a diferentes temperaturas nos permitió cuantificar, por primera vez, los efectos que tiene la evolución térmica de la estructura molecular en la estructura electrónica y la anisotropía magnética. Finalmente, el Capítulo 11 ofrece algunas ideas para el diseño racional de bits cuánticos (qubits) moleculares basados en complejos mononucleares de lantánidos y uranio. A través de dos ejemplos ($HoPd_{12}$ y GdW_{30}), en el capítulo también se han descrito las principales características que hacen a los polioxometalatos particularmente interesantes para información cuántica.

References

References

1. Selwood, P. W. *Magnetochemistry*. (Interscience Publishers, New York, 1956).
2. Kahn, O. *Molecular Magnetism*. (VCH Publishers, Inc. (USA), 1993).
3. Gatteschi, D., Kahn, O., Miller, J. S. & Palacio, F. *Magnetic Molecular Materials*. (Springer Science & Business Media, 2012).
4. Coronado, E., Delhaès, P., Gatteschi, D. & Miller, J.S. *Molecular Magnetism: From Molecular Assemblies to the Devices*. (Springer Science & Business Media, 2013).
5. Kahn, O., Pei, Y., Verdaguer, M., Renard, J. P. & Sletten, J. Magnetic ordering of manganese(II) copper(II) bimetallic chains; design of a molecular based ferromagnet. *J. Am. Chem. Soc.* **110,** 782–789 (1988).
6. Willett, R. D., Gatteschi, D. & Kahn, O. Magneto-structural correlations in exchange coupled systems. (1985).
7. Kahn, O., Kröber, J. & Jay, C. Spin Transition Molecular Materials for displays and data recording. *Adv. Mater.* **4,** 718–728 (1992).
8. Kahn, O. Dinuclear Complexes with Predictable Magnetic Properties. *Angew. Chemie Int. Ed.* **24,** 834–850 (1985).
9. MAGMANet, *Olivier Kahn International Award*.
10. Gatteschi, D. & Benelli, C. *Introduction to Molecular Magnetism: From Transition Metals to Lanthanides*. (Wiley-VCH, 2015).
11. Coronado, E. & Dunbar, K. R. Preface for the forum on molecular magnetism: the role of inorganic chemistry. *Inorg. Chem.* **48,** 3293–5 (2009).
12. Winpenny, R. *Single-Molecule Magnets and Related Phenomena*. **122,** (Springer-Verlag, 2006).
13. Magnets, S., Gatteschi, D. & Sessoli, R. Quantum tunneling of magnetization and related phenomena in molecular materials. *Angew. Chemie Int. Ed.* **42,** 268–297 (2003).
14. Wernsdorfer, W., Aliaga-Alcalde, N., Hendrickson, D. N. & Christou, G. Exchange-biased quantum tunnelling in a supramolecular dimer of single-molecule magnets. *Nature* **416,** 406–9 (2002).
15. Hill, S., Edwards, R. S., Aliaga-Alcalde, N. & Christou, G. Quantum coherence in an exchange-coupled dimer of single-molecule magnets. *Science* **302,** 1015–8 (2003).
16. Wernsdorfer, W., Chakov, N. E. & Christou, G. Quantum phase interference and

spin-parity in Mn_{12} single-molecule magnets. *Phys. Rev. Lett.* **95,** 037203 (2005).

17. Layfield, R. & Murugesu, M. *Lanthanides and Actinides in Molecular Magnetism*. (Wiley-VCH, 2015).
18. Lis, T. Preparation, structure, and magnetic properties of a dodecanuclear mixed-valence manganese carboxylate. *Acta Cryst.* **36,** 2042–2046 (1980).
19. Sessoli, R., Gatteschi, D., Caneschi, A. & Novak, M. A. Magnetic bistability in a metal-ion cluster. *Nature* **365,** 141–143 (1993).
20. Sessoli, R., Tsai, H.-L., Schake, A.R., Wang, S., Vincent, J.B., Folting, K., Gatteschi, D. & Christou, G. High-spin molecules: $[Mn_{12}O_{12}(O_2CR)_{16}(H_2O)_4]$. *J. Am. Chem. Soc.* **115,** 1804–1816 (1993).
21. Paulsen, C., Park, J.-G., Barbara, B., Sessoli, R. & Caneschi, A. Studies of hysteresis in Mn12Ac. *J. Magn. Magn. Mater.* **140-144,** 1891–1892 (1995).
22. Friedman, J. R., Sarachik, M. P., Tejada, J., Maciejewski, J. & Ziolo, R. Steps in the hysteresis loops of a high-spin molecule. *J. Appl. Phys.* **79,** 6031 (1996).
23. Friedman, J., Sarachik, M., Tejada, J. & Ziolo, R. Macroscopic measurement of resonant magnetization tunneling in high-spin molecules. *Phys. Rev. Lett.* **76,** 3830–3833 (1996).
24. Thomas, L. *et al.* Macroscopic quantum tunnelling of magnetization in a single crystal of nanomagnets. *Nature* **383,** 145–147 (1996).
25. Wernsdorfer, W. *et al.* Observation of the Distribution of Molecular Spin States by Resonant Quantum Tunneling of the Magnetization. *Phys. Rev. Lett.* **82,** 3903–3906 (1999).
26. Friedman, J., Sarachik, M., Tejada, J. & Ziolo, R. Macroscopic measurement of resonant magnetization tunneling in high-spin molecules. *Phys. Rev. Lett.* **76,** 3830–3833 (1996).
27. Thomas, L. *et al.* Macroscopic quantum tunnelling of magnetization in a single crystal of nanomagnets. *Nature* **383,** 145–147 (1996).
28. Wernsdorfer, W. *et al.* Observation of the Distribution of Molecular Spin States by Resonant Quantum Tunneling of the Magnetization. *Phys. Rev. Lett.* **82,** 3903–3906 (1999).
29. Aubin, S. M. J. *et al.* Distorted $Mn^{IV}Mn^{III}_3$ Cubane Complexes as Single-Molecule Magnets. *J. Am. Chem. Soc.* **118,** 7746–7754 (1996).
30. Tasiopoulos, A. J., Vinslava, A., Wernsdorfer, W., Abboud, K. & Christou, G. Giant Single-Molecule Magnets: A $\{Mn_{84}\}$ Torus and Its Supramolecular Nanotubes.

Angew. Chemie Int. Ed. **43,** 2117–2121 (2004).

31. Murugesu, M., Habrych, M., Wernsdorfer, W., Abboud, K. A & Christou, G. Single-molecule magnets: a Mn25 complex with a record S = 51/2 spin for a molecular species. *J. Am. Chem. Soc.* **126,** 4766–7 (2004).
32. Murugesu, M. *et al.* Large Mn_{25} single-molecule magnet with spin S = 51/2: magnetic and high-frequency electron paramagnetic resonance spectroscopic characterization of a giant spin state. *Inorg. Chem.* **47,** 9459–70 (2008).
33. Milios, C. J. *et al.* A record anisotropy barrier for a single-molecule magnet. *J. Am. Chem. Soc.* **129,** 2754–2755 (2007).
34. Waldmann, O. A criterion for the anisotropy barrier in single-molecule magnets. *Inorg. Chem.* **46,** 10035–7 (2007).
35. Delfs, C. *et al.* Magnetic-Properties of an Octanuclear Iron(Iii) Cation. *Inorg. Chem.* **32,** 3099–3103 (1993).
36. Barra, A.-L., Debrunner, P., Gatteschi, D., Schulz, C. E. & Sessoli, R. Superparamagnetic-like behavior in an octanuclear iron cluster. *Europhys. Lett.* **35,** 133–138 (1996).
37. Wernsdorfer, W. *et al.* Effects of nuclear spins on the quantum relaxation of the magnetization for the molecular nanomagnet Fe-8. *Phys. Rev. Lett.* **84,** 2965–2968 (2000).
38. Wernsdorfer, W., Sessoli, R., Caneschi, A., Gatteschi, D. & Cornia, A. Nonadiabatic Landau-Zener tunneling in Fe-8 molecular nanomagnets. *Europhys. Lett.* **50,** 552–558 (2000).
39. Takahashi, S. *et al.* Decoherence in crystals of quantum molecular magnets. *Nature* **476,** 76–79 (2011).
40. Yoo, J. *et al.* Single-molecule magnets: A new class of tetranuclear manganese magnets. *Inorg. Chem.* **39,** 3615–3623 (2000).
41. Yamaguchi, A. *et al.* The relaxation times in tetranuclear manganese complex with S=8. *Phys. B-Condensed Matter* **284,** 1225–1226 (2000).
42. Compain, J.-D. *et al.* Iron Polyoxometalate Single-Molecule Magnets. *Angew. Chemie* **121,** 3123–3127 (2009).
43. Ritchie, C. *et al.* Polyoxometalate-Mediated Self-Assembly of Single-Molecule Magnets: $\{[XW_9O_{34}]_2[Mn^{III}_4Mn^{II}_2O_4(H_2O)_4]\}^{12-}$. *Angew. Chemie Int. Ed.* **120,** 5691–5694 (2008).
44. Lin, P.-H. *et al.* A polynuclear lanthanide single-molecule magnet with a record

anisotropic barrier. *Angew. Chem. Int. Ed.* **48,** 9489–92 (2009).

45. Guo, Y.-N. *et al.* Two-step relaxation in a linear tetranuclear dysprosium(III) aggregate showing single-molecule magnet behavior. *J. Am. Chem. Soc.* **132,** 8538–9 (2010).
46. Rinehart, D., Fang, M., Evans, W. J. & Long, R. A N_2^{3-} Radical-Bridged Terbium Complex Exhibiting Magnetic Hysteresis at 14 K. *J. Am. Chem. Soc.* **133,** 14236–14239 (2011).
47. Hewitt, I. J. *et al.* Coupling Dy_3 Triangles Enhances Their Slow Magnetic Relaxation. *Angew. Chemie Int. Ed.* **122,** 6496–6500 (2010).
48. Chibotaru, L. F., Ungur, L. & Soncini, A. The Origin of Nonmagnetic Kramers Doublets in the Ground State of Dysprosium Triangles: Evidence for a Toroidal Magnetic Moment. *Angew. Chemie* **120,** 4194–4197 (2008).
49. Lin, S. Y. *et al.* Coupling Dy_3 triangles to maximize the toroidal moment. *Angew. Chemie Int. Ed.* **51,** 12767–12771 (2012).
50. Woodruff, D. N., Winpenny, R. E. P. & Layfield, R. A. Lanthanide single-molecule magnets. *Chem. Rev.* **113,** 5110–48 (2013).
51. Ishikawa, N., Sugita, M., Ishikawa, T., Koshihara, S. Y. & Kaizu, Y. Lanthanide double-decker complexes functioning as magnets at the single-molecular level. *J. Am. Chem. Soc.* **125,** 8694–8695 (2003).
52. Sorace, L., Benelli, C. & Gatteschi, D. Lanthanides in molecular magnetism: old tools in a new field. *Chem. Soc. Rev.* **40,** 3092–3104 (2011).
53. Sessoli, R. & Powell, A. K. Strategies towards single molecule magnets based on lanthanide ions. *Coord. Chem. Rev.* **253,** 2328–2341 (2009).
54. Campbell, V. E. *et al.* Structural and electronic dependence of the single-molecule-magnet behavior of dysprosium(III) complexes. *Inorg. Chem.* **53,** 2598–605 (2014).
55. Ishikawa, N. *et al.* Determination of ligand-field parameters and f-electronic structures of double-decker bis(phthalocyaninato)lanthanide complexes. *Inorg. Chem.* **42,** 2440–2446 (2003).
56. Takamatsu, S., Ishikawa, T., Koshihara, S. & Ishikawa, N. Significant increase of the barrier energy for magnetization reversal of a single-4f-ionic single-molecule magnet by a longitudinal contraction of the coordination space. *Inorg. Chem.* **46,** 7250–2 (2007).
57. Ganivet, C. R. *et al.* Influence of Peripheral Substitution on the Magnetic Behavior of Single-Ion Magnets Based on Homo- and Heteroleptic Tb^{III} Bis(phthalocyaninate).

Chem. - A Eur. J. **19,** 1457–1465 (2013).

58. Clemente-Juan, J. M., Coronado, E. & Gaita-Ariño, A. Magnetic polyoxometalates: from molecular magnetism to molecular spintronics and quantum computing. *Chem. Soc. Rev.* **41,** 7464 (2012).
59. Aldamen, M. A, Clemente-Juan, J. M., Coronado, E., Martí-Gastaldo, C. & Gaita-Ariño, A. Mononuclear lanthanide single-molecule magnets based on polyoxometalates. *J. Am. Chem. Soc.* **130,** 8874–5 (2008).
60. Shiozaki, R. *et al.* Spectroscopic investigation of a series of sodium lanthanide decatungstates, $Na_7H_2Ln(III)(W_5O_{18})_2{\cdot}nH_2O$ (Ln: La–Yb): the contribution of $4f^n$ electrons to bonding interaction among Ln(III) and polyoxotungstates. *J. Alloys Compd.* **234,** 193–198 (1996).
61. Rinehart, J. D. & Long, J. R. Exploiting single-ion anisotropy in the design of f-element single-molecule magnets. *Chem. Sci.* **2,** 2078 (2011).
62. AlDamen, M. A. *et al.* Mononuclear lanthanide single molecule magnets based on the polyoxometalates $[Ln(W_5O_{18})_2]^{9-}$ and $[Ln(\beta_2\text{-}SiW_{11}O_{39})_2]^{13-}$ (LnIII) Tb, Dy, Ho, Er, Tm, and Yb). *Inorg. Chem.* **48,** 3467–3479 (2009).
63. Cardona-Serra, S. *et al.* Lanthanoid single-ion magnets based on polyoxometalates with a 5-fold symmetry: the series $[LnP_5W_{30}O_{110}]^{12-}$ (Ln^{3+} = Tb, Dy, Ho, Er, Tm, and Yb). *J. Am. Chem. Soc.* **134,** 14982–90 (2012).
64. Creaser, I., Heckel, M. C., Neitz, R. J. & Pope, M. T. Rigid nonlabile polyoxometalate cryptates $[ZP_5W_{30}O_{110}]^{(15-n)-}$ that exhibit unprecedented selectivity for certain lanthanide and other multivalent cations. *Inorg. Chem.* **32,** 1573–1578 (1993).
65. Martínez-Pérez, M. J. *et al.* Gd-based single-ion magnets with tunable magnetic anisotropy: Molecular design of spin qubits. *Phys. Rev. Lett.* **108,** (2012).
66. Feltham, H. L. C. & Brooker, S. Review of purely 4*f* and mixed-metal n*d*-4*f* single-molecule magnets containing only one lanthanide ion. *Coord. Chem. Rev.* **276,** 1–33 (2014).
67. Zhang, P., Guo, Y.-N. & Tang, J. Recent advances in dysprosium-based single molecule magnets: Structural overview and synthetic strategies. *Coord. Chem. Rev.* **257,** 1728–1763 (2013).
68. Jiang, S.-D., Wang, B. W., Sun, H. L., Wang, Z. M. & Gao, S. An organometallic single-ion magnet. *J. Am. Chem. Soc.* **133,** 4730–4733 (2011).
69. Jiang, S.-D. *et al.* Series of lanthanide organometallic single-ion magnets. *Inorg. Chem.* **51,** 3079–3087 (2012).

70. Jiang, S.-D., Wang, B.-W., Su, G., Wang, Z.-M. & Gao, S. A Mononuclear Dysprosium Complex Featuring Single-Molecule-Magnet Behavior. *Angew. Chemie Int. Ed.* **122,** 7610–7613 (2010).
71. Chen, G.-J. *et al.* Coordination-perturbed single-molecule magnet behaviour of mononuclear dysprosium complexes. *Dalton Trans.* **40,** 5579–83 (2011).
72. Car, P.-E. *et al.* Giant field dependence of the low temperature relaxation of the magnetization in a dysprosium(III)-DOTA complex. *Chem. Commun.* **47,** 3751–3 (2011).
73. Cucinotta, G. *et al.* Magnetic anisotropy in a dysprosium/DOTA single-molecule magnet: beyond simple magneto-structural correlations. *Angew. Chem. Int. Ed.* **51,** 1606–10 (2012).
74. Boulon, M.-E. *et al.* Magnetic Anisotropy and Spin-Parity Effect Along the Series of Lanthanide Complexes with DOTA. *Angew. Chemie Int. Ed.* **125,** 368–372 (2013).
75. Chilton, N. F., Collison, D., McInnes, E. J. L., Winpenny, R. E. P. & Soncini, A. An electrostatic model for the determination of magnetic anisotropy in dysprosium complexes. *Nat. Commun.* **4,** 2551 (2013).
76. Giraud, R., Wernsdorfer, W., Tkachuk, A. M., Mailly, D. & Barbara, B. Nuclear Spin Driven Quantum Relaxation in $LiY_{0.998}Ho_{0.002}F_4$. *Phys. Rev. Lett.* **87,** 057203 (2001).
77. Bertaina, S. *et al.* Rare-earth solid-state qubits. *Nat. Nanotechnol.* **2,** 39–42 (2007).
78. Gómez-Coca, S. *et al.* Origin of slow magnetic relaxation in Kramers ions with non-uniaxial anisotropy. *Nat. Commun.* **5,** 4300 (2014).
79. Harman, W. H. *et al.* Slow magnetic relaxation in a family of trigonal pyramidal iron(II) pyrrolide complexes. *J. Am. Chem. Soc.* **132,** 18115–18126 (2010).
80. Zadrozny, J. M. *et al.* Magnetic blocking in a linear iron(I) complex. *Nat. Chem.* **5,** 577–81 (2013).
81. Zadrozny, J. M. & Long, J. R. Slow magnetic relaxation at zero field in the tetrahedral complex $[Co(SPh)_4]^{2-}$. *J. Am. Chem. Soc.* **133,** 20732–4 (2011).
82. Bader, K. *et al.* Room temperature quantum coherence in a potential molecular qubit. *Nat. Commun.* **5,** 5304 (2014).
83. Meihaus, K. R. & Long, J. R. Actinide-based single-molecule magnets. *Dalton Trans.* **44,** 2517–28 (2015).
84. Moro, F., Mills, D. P., Liddle, S. T. & van Slageren, J. The inherent single-molecule magnet character of trivalent uranium. *Angew. Chem. Int. Ed.* **52,** 3430–3 (2013).
85. Rinehart, J. D. & Long, J. R. Slow magnetic relaxation in a trigonal prismatic

uranium(III) complex. *J. Am. Chem. Soc.* **131,** 12558–9 (2009).

86. Maria, L., Campello, M. P., Domingos, Â., Santos, I. & Andersen, R. Synthesis and structure of uranium(III) complexes with dihydrobis(pyrazolyl)borates. *J. Chem. Soc. Dalt. Trans.* 2015–2020 (1999).
87. Rinehart, J. D., Meihaus, K. R. & Long, J. R. Observation of a secondary slow relaxation process for the field-induced single-molecule magnet $U(H_2BPz_2)_3$. *J. Am. Chem. Soc.* **132,** 7572–3 (2010).
88. Rinehart, J. D. & Long, J. R. Slow magnetic relaxation in homoleptic trispyrazolylborate complexes of neodymium(III) and uranium(III). *Dalton Trans.* **41,** 13572–4 (2012).
89. Antunes, M. A. *et al.*: A cationic uranium(III) complex with single-molecule-magnet behavior. *Inorg. Chem.* **50,** 9915–9917 (2011).
90. Coutinho, J. T. *et al.* Single-ion magnet behaviour in $[U(Tp^{Me2})_2I]$. *Dalton Trans.* **41,** 13568–71 (2012).
91. Sun, Y., McDonald, R., Takats, J., Day, V. W. & Eberspacher, T. A. Synthesis and Structure of Bis[hydrotris(3,5-dimethylpyrazolyl)borato]iodouranium(III), $U[HB(3,5\text{-}Me_2pz)_3]_2I$: Unprecedented Side-On Interaction Involving a Hydrotris(pyrazolyl)borate Ligand. *Inorg. Chem.* **33,** 4433–4434 (1994).
92. Coutinho, J. T., Antunes, M. A., Pereira, L. C. J., Marçalo, J. & Almeida, M. Zero-field slow magnetic relaxation in a uranium(III) complex with a radical ligand. *Chem. Commun.* **50,** 10262–4 (2014).
93. Baldoví, J. J., Cardona-Serra, S., Clemente-Juan, J. M., Coronado, E. & Gaita-Ariño, A. Modeling the properties of uranium-based single ion magnets. *Chem. Sci.* **4,** 938 (2013).
94. King, D. M. *et al.* Single-molecule magnetism in a single-ion triamidoamine uranium(V) terminal mono-oxo complex. *Angew. Chemie Int. Ed.* **52,** 4921–4924 (2013).
95. Magnani, N. *et al.* Magnetic Memory Effect in a Transuranic Mononuclear Complex. *Angew. Chemie Int. Ed.* **50,** 1696–1698 (2011).
96. Magnani, N. *et al.* Superexchange coupling and slow magnetic relaxation in a transuranium polymetallic complex. *Phys. Rev. Lett.* **104,** 1–4 (2010).
97. Mills, D. P. *et al.* A delocalized arene-bridged diuranium single-molecule magnet. *Nat. Chem.* **3,** 454–460 (2011).
98. Ouahab, L. *Multifunctional Molecular Materials* (CRC Press Book, 2013).

99. Gaspar, A. B., Ksenofontov, V., Seredyuk, M. & Gütlich, P. Multifunctionality in spin crossover materials. *Coord. Chem. Rev.* **249,** 2661–2676 (2005).

100. Real, J. A., Gaspar, A. B., Niel, V. & Muñoz, M. C. Communication between iron(II) building blocks in cooperative spin transition phenomena. *Coord. Chem. Rev.* **236,** 121–141 (2003).

101. Sato, O., Iyoda, T., Fujishima, a. & Hashimoto, K. Photoinduced Magnetization of a Cobalt-Iron Cyanide. *Science.* **272,** 704–705 (1996).

102. Coronado, E. *et al.* Pressure-induced magnetic switching and linkage isomerism in $K_{0.4}Fe_4[Cr(CN)_6]_{2.8}\cdot 16H_2O$: X-ray absorption and magnetic circular dichroism studies. *J. Am. Chem. Soc.* **130,** 15519–32 (2008).

103. Rikken, G. L. J. A. & Raupach, E. Observation of magneto-chiral dichroism. *J. Am. Chem. Soc.* **390,** 493–494 (1997).

104. Coronado, E., Gómez-García, C. J., Nuez, A., Romero, F. M. & Waerenborgh, J. C. Synthesis, Chirality, and Magnetic Properties of Bimetallic Cyanide-Bridged Two-Dimensional Ferromagnets. *Chem. Mater.* **18,** 2670–2681 (2006).

105. Kibayashi, S., Takahashi, Y., Seki, S. & Tokura, Y. Magnetochiral dichroism resonant with electromagnons in a helimagnet. *Nat. Commun.* **5,** 4583 (2014).

106. Coronado, E., Galán-Mascarós, J. R., Gómez-García, C. J. & Laukhin, V. Coexistence of ferromagnetism and metallic conductivity in a molecule-based layered compound. *Nature* **408,** 447–9 (2000).

107. Minguet, M. *et al.* An Enantiopure Molecular Ferromagnet. *Angew. Chemie Int. Ed.* **41,** 586–589 (2002).

108. Coronado, E. & Day, P. Magnetic molecular conductors. *Chem. Rev.* **104,** 5419–48 (2004).

109. Coronado, E. *et al.* Hybrid magnetic/superconducting materials obtained by insertion of a single-molecule magnet into TaS_2 layers. *Adv. Mater.* **23,** 5021–6 (2011).

110. Coronado, E. *et al.* Hybrid magnetic superconductors formed by TaS_2 layers and spin crossover complexes. *Inorg. Chem.* **52,** 8451–60 (2013).

111. Guillamón, I. *et al.* Enhancement of long-range correlations in a 2D vortex lattice by an incommensurate 1D disorder potential. *Nat. Phys.* **10,** 851–856 (2014).

112. Suderow, H., Guillamón, I., Rodrigo, J. G. & Vieira, S. Imaging superconducting vortex cores and lattices with a scanning tunneling microscope. *Supercond. Sci. Technol.* **27,** 063001 (2014).

113. Heinrich, B. W., Braun, L., Pascual, J. I. & Franke, K. J. Protection of excited spin

states by a superconducting energy gap. *Nat. Phys.* **9,** 765–768 (2013).

114. Wolf, S. A. *et al.* Spintronics: a spin-based electronics vision for the future. *Science* **294,** 1488–95 (2001).
115. Mannini, M. *et al.* Magnetic memory of a single-molecule quantum magnet wired to a gold surface. *Nat. Mater.* **8,** 194–7 (2009).
116. Ladd, T. D. *et al.* Quantum computers. *Nature* **464,** 45–53 (2010).
117. Rocha, J., Carlos, L. D., Paz, F. A. A. & Ananias, D. Luminescent multifunctional lanthanides-based metal-organic frameworks. *Chem. Soc. Rev.* **40,** 926–40 (2011).
118. Clemente-León, M., Coronado, E., Martí-Gastaldo, C. & Romero, F. M. Multifunctionality in hybrid magnetic materials based on bimetallic oxalate complexes. *Chem. Soc. Rev.* **40,** 473–97 (2011).
119. Tobin, G. *et al.* Towards multifunctional lanthanide-based metal-organic frameworks. *Chem. Commun.* **51,** 13313–6 (2015).
120. Baldoví, J. J. *et al.* A SIM-MOF: Three-dimensional organisation of single-ion magnets with anion-exchange capabilities. *Chem. - A Eur. J.* **20,** 10695–10702 (2014).
121. Görller-Walrand, C. & Binnemans, K. Chapter 155 Rationalization of crystal-field parametrization. *Handb. Phys. Chem. Rare Earths* **23,** 121–283 (1996).
122. Baldoví, J. J. *et al.* Rational design of single-ion magnets and spin qubits based on mononuclear lanthanoid complexes. *Inorg. Chem.* **51,** 12565–12574 (2012).
123. Maurice, R. *et al.* Universal Theoretical Approach to Extract Anisotropic Spin Hamiltonians. *J. Chem. Theory Comput.* **5,** 2977–84 (2009).
124. Moreira, I. de P. R. *et al.* Derivation of spin Hamiltonians from the exact Hamiltonian: Application to systems with two unpaired electrons per magnetic site. *Phys. Rev. B* **66,** 134430 (2002).
125. Borrás-Almenar, J. J., Clemente-Juan, J. M., Coronado, E. & Tsukerblat, B. S. High-Nuclearity Magnetic Clusters: Generalized Spin Hamiltonian and Its Use for the Calculation of the Energy Levels, Bulk Magnetic Properties, and Inelastic Neutron Scattering Spectra. *Inorg. Chem.* **38,** 6081–6088 (1999).
126. Borrás-Almenar, J. J., Clemente-Juan, J. M., Coronado, E. & Tsukerblat, B. S. MAGPACK1 A package to calculate the energy levels, bulk magnetic properties, and inelastic neutron scattering spectra of high nuclearity spin clusters. *J. Comput. Chem.* **22,** 985–991 (2001).
127. Gatteschi, D. & Sessoli, R. Quantum tunneling of magnetization and related phenomena in molecular materials. *Angew. Chem. Int. Ed.* **42,** 268–97 (2003).

128. Feng, P. L. *et al.* Origin of magnetization tunneling in single-molecule magnets as determined by single-crystal high-frequency EPR. *Inorganica Chim. Acta* **361,** 3465–3480 (2008).

129. Pederson, M. R., Bernstein, N. & Kortus, J. Fourth-order magnetic anisotropy and tunnel splittings in Mn_{12} from spin-orbit-vibron interactions. *Phys. Rev. Lett.* **89,** 097202 (2002).

130. Bünzli, J.-C. G. Benefiting from the unique properties of lanthanide ions. *Acc. Chem. Res.* **39,** 53–61 (2006).

131. Newman, D. J. Theory of lanthanide crystal fields. *Adv. Phys.* **20,** 197–256 (1971).

132. Morrison, C. A. & Leavitt, R. P. *Handbook on the Physics and Chemistry of Rare Earths Volume 5. Handbook on the Physics and Chemistry of Rare Earths* **5,** (Elsevier, 1982).

133. Schoene, K. A., Quagliano, J. R. & Richardson, F. S. Optical absorption and circular dichroism spectra, transition line strengths, and crystal-field analysis of the erbium(3+) 4f11 electronic energy-level structure in trigonal $Na_3[Er(C_4H_4O_5)_3]\cdot 2NaClO_4\cdot 6H_2O$. *Inorg. Chem.* **30,** 3803–3812 (1991).

134. Duan, C.-K. & Tanner, P. A. What use are crystal field parameters? A chemist's viewpoint. *J. Phys. Chem. A* **114,** 6055–62 (2010).

135. Bethe, H. A. Splitting of Terms in Crystals. *Ann Phys.* **3,** 133–206 (1929).

136. Stevens, K. W. H. Matrix Elements and Operator Equivalents Connected with the Magnetic Properties of Rare Earth Ions. *Proc. Phys. Soc. A* **65,** 209–215 (1952).

137. Wybourne, B. G. *Spectroscopic Properties of Rare Earths*. (Interscience Publishers, 1965).

138. Rudowicz, C. & Chung, C. Y. The generalization of the extended Stevens operators to higher ranks and spins, and a systematic review of the tables of the tensor operators and their matrix elements. *J. Phys. Condens. Matter* **16,** 5825–5847 (2004).

139. Ryabov, I. D. On the generation of operator equivalents and the calculation of their matrix elements. *J. Magn. Reson.* **140,** 141–5 (1999).

140. Rudowicz, C. On standardization and algebraic symmetry of the ligand field Hamiltonian for rare earth ions at monoclinic symmetry sites. *J. Chem. Phys.* **84,** 5045 (1986).

141. Rudowicz, C. & Karbowiak, M. Disentangling intricate web of interrelated notions at the interface between the physical (crystal field) Hamiltonians and the effective (spin) Hamiltonians. *Coord. Chem. Rev.* **287,** 28–63 (2015).

142. Abragam, A. & Bleaney, B. in *Electron Paramagnetic Resonance of Transition Ions* 4, 42,

133–163, 398–406, 417–430,541– 547, 583–599 (1970).

143. Wybourne, B. G. & Smentek, L. *Optical Spectroscopy of Lanthanides: Magnetic and Hyperfine Interactions*. (CRC Press, 2007).

144. Mironov, V. S., Galyametdinov, Y. G., Ceulemans, A., Görller-Walrand, C. & Binnemans, K. Room-temperature magnetic anisotropy of lanthanide complexes: A model study for various coordination polyhedra. *J. Chem. Phys.* **116,** 4673 (2002).

145. Rudowicz, C. Transformation relations for the conventional O_k^q and normalised $O'_k{}^q$ Stevens operator equivalents with k=1 to 6 and $-k \leqslant q \leqslant k$. *J. Phys. C Solid State Phys.* **18,** 1415–1430 (1985).

146. Rudowicz, C. & Misra, S. K. Spin-Hamiltonian formalisms in electron magnetic resonance (EMR) and related spectroscopies. *Appl. Spectrosc. Rev.* **36,** 11–63 (2001).

147. Rudowicz, C., Chua, M. & Reid, M. F. On the standardization of crystal-field parameters and the multiple correlated fitting technique: Applications to rare-earth compounds. *Phys. B Condens. Matter* **291,** 327–338 (2000).

148. Rudowicz, C. & Qin, J. Can the low symmetry crystal (ligand) field parameters be considered compatible and reliable? *J. Lumin.* **110,** 39–64 (2004).

149. Luzon, J. & Sessoli, R. Lanthanides in molecular magnetism: so fascinating, so challenging. *Dalton Trans.* **41,** 13556–67 (2012).

150. Perfetti, M. *et al.* Angular-resolved magnetometry beyond triclinic crystals part II: torque magnetometry of Cp*ErCOT single-molecule magnets. *Chem.–Eur. J.* **20,** 14051–6 (2014).

151. Speldrich, M., Schilder, H., Lueken, H. & Kögerler, P. A Computational Framework for Magnetic Polyoxometalates and Molecular Spin Structures: CONDON 2.0. *Isr. J. Chem.* **51,** 215–227 (2011).

152. van Leusen, J., Speldrich, M., Schilder, H. & Kögerler, P. Comprehensive insight into molecular magnetism via CONDON: Full vs. effective models. *Coord. Chem. Rev.* **289-290,** 137–148 (2015).

153. Judd, B. R. *Operator Techniques in Atomic Spectroscopy*. (Princeton Legacy Library, 2014).

154. Reu, O. S., Palii, A. V, Ostrovsky, S. M., Tregenna-Piggott, P. L. W. & Klokishner, S. I. A model of magnetic and relaxation properties of the mononuclear $[Pc_2Tb]^-TBA^+$ complex. *Inorg. Chem.* **51,** 10955–65 (2012).

155. *3rd International Conference on Nanotechnologies and Biomedical Engineering*. **55,** (Springer Singapore, 2016).

156. Malta, O. L. A simple overlap model in lanthanide crystal-field theory. *Chem. Phys. Lett.* **87,** 27–29 (1982).

157. Malta, O. L. Theoretical crystal-field parameters for the YOCl:Eu3+ system. A simple overlap model. *Chem. Phys. Lett.* **88,** 353–356 (1982).

158. Porcher, P., Couto Dos Santos, M. & Malta, O. Relationship between phenomenological crystal field parameters and the crystal structure: The simple overlap model. *Phys. Chem. Chem. Phys.* **1,** 397–405 (1999).

159. Urland, W. On the ligand-field potential for *f* electrons in the angular overlap model. *Chem. Phys.* **14,** 393–401 (1976).

160. Maynau, D., Evangelisti, S., Guihéry, N., Calzado, C. J. & Malrieu, J.-P. Direct generation of local orbitals for multireference treatment and subsequent uses for the calculation of the correlation energy. *J. Chem. Phys.* **116,** 10060 (2002).

161. Roos, B. O., Taylor, P. R. & Siegbahn, P. E. M. A complete active space SCF method (CASSCF) using a density matrix formulated super-CI approach. *Chem. Phys.* **48,** 157–173 (1980).

162. Siegbahn, P. E. M., Heiberg, A., Roos, B. O. & Levy, B. A Comparison of the Super-Cl and the Newton-Raphson Scheme in the Complete Active Space SCF Method. *Phys. Scr.* **21,** 323–327 (1980).

163. Siegbahn, P. E. M. The complete active space SCF (CASSCF) method in a Newton–Raphson formulation with application to the HNO molecule. *J. Chem. Phys.* **74,** 2384 (1981).

164. Aquilante, F. *et al.* MOLCAS 7: The Next Generation. *J. Comput. Chem.* **31,** 224–247 (2010).

165. M. J. Frisch, G. *et al. Gaussian 09, Revision A. 1; Gaussian. Inc.: Wallingford, CT* 2009–2009 (2009).

166. Neese, F. The ORCA program system. *Wiley Interdiscip. Rev. Comput. Mol. Sci.* **2,** 73 (2012).

167. Werner, H.-J., Knowles, P. J., Knizia, G., Manby, F. R. & Schütz, M. Molpro: a general-purpose quantum chemistry program package. *Wiley Interdiscip. Rev. Comput. Mol. Sci.* **2,** 242–253 (2012).

168. Malmqvist, P. A., Rendell, A. & Roos, B. O. The restricted active space self-consistent-field method, implemented with a split graph unitary group approach. *J. Phys. Chem.* **94,** 5477–5482 (1990).

169. Andersson, K., Malmqvist, P.-A. & Roos, B. O. Second-order perturbation theory

with a complete active space self-consistent field reference function. *J. Chem. Phys.* **96,** 1218 (1992).

170. Malmqvist, P. Å., Roos, B. O. & Schimmelpfennig, B. The restricted active space (RAS) state interaction approach with spin-orbit coupling. *Chem. Phys. Lett.* **357,** 230–240 (2002).
171. Reiher, M. Relativistic Douglas-Kroll-Hess theory. *Wiley Interdiscip. Rev. Comput. Mol. Sci.* **2,** 139–149 (2012).
172. Malrieu, J. P., Caballol, R., Calzado, C. J., de Graaf, C. & Guihéry, N. Magnetic interactions in molecules and highly correlated materials: physical content, analytical derivation, and rigorous extraction of magnetic Hamiltonians. *Chem. Rev.* **114,** 429–92 (2014).
173. Chibotaru, L. F. & Ungur, L. Ab initio calculation of anisotropic magnetic properties of complexes. I. Unique definition of pseudospin Hamiltonians and their derivation. *J. Chem. Phys.* **137,** 064112 (2012).
174. Paulovic, J., Cimpoesu, F., Ferbinteanu, M. & Hirao, K. Mechanism of ferromagnetic coupling in copper(II)-gadolinium(III) complexes. *J. Am. Chem. Soc.* **126,** 3321–31 (2004).
175. Pedersen, K. S. *et al.* Modifying the properties of 4f single-ion magnets by peripheral ligand functionalisation. *Chem. Sci.* **5,** 1650 (2014).
176. Marx, R. *et al.* Spectroscopic determination of crystal field splittings in lanthanide double deckers. *Chem. Sci.* **5,** 3287 (2014).
177. Moreno Pineda, E. *et al.* Direct measurement of dysprosium(III)···dysprosium(III) interactions in a single-molecule magnet. *Nat. Commun.* **5,** 5243 (2014).
178. Mulak, J. & Gajek, Z. *The Effective Crystal Field Potential*. *The Effective Crystal Field Potential* (Elsevier Science, 2000).
179. Cunha, T. da & Jung, J. Magnetic Poles Determinations and Robustness of Memory Effect upon Solubilization in a Dy^{III}-Based Single Ion Magnet. *J. Am. Chem. Soc.* **135,** 16332–5 (2013).
180. Peng, J.-B. *et al.* High-nuclearity 3d-4f clusters as enhanced magnetic coolers and molecular magnets. *J. Am. Chem. Soc.* **134,** 3314–7 (2012).
181. Sanvito, S. Molecular spintronics. *Chem. Soc. Rev.* **40,** 3336–55 (2011).
182. Crommie, M. F. Physics. Manipulating magnetism in a single molecule. *Science* **309,** 1501–2 (2005).
183. Leuenberger, M. N. & Loss, D. Quantum computing in molecular magnets. *Nature*

410, 789–793 (2001).

184. Nielsen, M.A. & Chuang, I. L. *Quantum Computation and Quantum Information* (Cambridge University Press, 2011).
185. DiVincenzo, D. P. Quantum Computation. *Science.* **270,** 255–261 (1995).
186. Stamp, P. C. E. & Gaita-Ariño, A. Spin-Based Quantum Computers made by Chemistry: Hows and Whys. *J. Mater. Chem.* **19,** 1718–1730 (2008).
187. Pérez-Delgado, C. A. & Kok, P. Quantum computers: Definition and implementations. *Phys. Rev. A* **83,** 012303 (2011).
188. Stamp, P. C. E. Quantum information: stopping the rot. *Nature* **453,** 167–8 (2008).
189. Cirac, J. & Zoller, P. Quantum Computations with Cold Trapped Ions. *Physical Review Letters* **74,** 4091–4094 (1995).
190. Kielpinski, D., Monroe, C. & Wineland, D. J. Architecture for a large-scale ion-trap quantum computer. *Nature* **417,** 709–711 (2002).
191. Friedenauer, A., Schmitz, H., Glueckert, J. T., Porras, D. & Schaetz, T. Simulating a quantum magnet with trapped ions. *Nat. Phys.* **4,** 757–761 (2008).
192. Monroe, C. & Kim, J. Scaling the ion trap quantum processor. *Science* **339,** 1164–9 (2013).
193. Brune, M. *et al.* Quantum Rabi nutation in vacuum and coherent fields: a direct test of field quantization in a cavity. *Summ. Pap. Present. Quantum Electron. Laser Sci. Conf.* 2–5 (1996).
194. Knill, E., Laflamme, R. & Milburn, G. J. A scheme for efficient quantum computation with linear optics. *Nature* **409,** 46–52 (2001).
195. Loss, D. & DiVincenzo, D. P. Quantum Computation with Quantum Dots. *Phys. Rev. A* **57,** 12 (1998).
196. Awschalom, D. D., Bassett, L. C., Dzurak, A. S., Hu, E. L. & Petta, J. R. Quantum spintronics: engineering and manipulating atom-like spins in semiconductors. *Science (80-.).* **339,** 1174–9 (2013).
197. Nakamura, Y., Pashkin, Y. A. & Tsai, J. S. Coherent control of macroscopic quantum states in a single-Cooper-pair box. *Nature* **398,** 786 (1999).
198. Clarke, J. & Wilhelm, F. K. Superconducting quantum bits. *Nature* **453,** 1031–42 (2008).
199. Devoret, M. H. & Schoelkopf, R. J. Superconducting circuits for quantum information: an outlook. *Science* **339,** 1169–74 (2013).
200. Bernien, H. *et al.* Heralded entanglement between solid-state qubits separated by

three metres. *Nature* **497,** 86–90 (2013).

201. Dolde, F. *et al.* Room-temperature entanglement between single defect spins in diamond. *Nat. Phys.* **9,** 139–143 (2013).
202. Jelezko, F. & Wrachtrup, J. Single defect centres in diamond: A review. *Phys. status solidi* **203,** 3207–3225 (2006).
203. Affronte, M. *et al.* Single molecule magnets for quantum computation. *J. Phys. D. Appl. Phys.* **40,** 2999–3004 (2007).
204. Troiani, F. & Affronte, M. Molecular spins for quantum information technologies. *Chem. Soc. Rev.* **40,** 3119–3129 (2011).
205. Ardavan, A. & Blundell, S. J. Storing quantum information in chemically engineered nanoscale magnets. *J. Mater. Chem.* **19,** 1754 (2009).
206. Gaita-Ariño, A. DECRESIM A Chemical Approach to Molecular Spin Qubits: Decoherence and Organisation of Rare Earth Single Ion Magnets.
207. Campbell, V. E. *et al.* Subcomponent self-assembly of rare-earth single-molecule magnets. *Inorg. Chem.* **52,** 5194–200 (2013).
208. Jenkins, M. *et al.* Coupling single-molecule magnets to quantum circuits. *New J. Phys.* **15,** 095007 (2013).
209. Palii, A., Tsukerblat, B., Clemente-Juan, J. M., Gaita-Ariño, A. & Coronado, E. Manipulation of the spin in single molecule magnets via Landau-Zener transitions. *Phys. Rev. B* **84,** 184426 (2011).
210. Bertaina, S. *et al.* Quantum oscillations in a molecular magnet. *Nature* **453,** 203–6 (2008).
211. Tejada, J., Chudnovsky, E. M., Barco, E. del, Hernandez, J. M. & Spiller, T. P. Magnetic qubits as hardware for quantum computers. *Nanotechnology* **12,** 181–186 (2001).
212. Lehmann, J., Gaita-Ariño, A., Coronado, E. & Loss, D. Quantum computing with molecular spin systems. *J. Mater. Chem.* **19,** 1672–1677 (2009).
213. Shim, J. H. *et al.* Decoherence window and electron-nuclear cross relaxation in the molecular magnet V_{15}. *Phys. Rev. Lett.* **109,** 050401 (2012).
214. Warner, M. *et al.* Potential for spin-based information processing in a thin-film molecular semiconductor. *Nature* **503,** 504–8 (2013).
215. Zadrozny, J. M., Niklas, J., Poluektov, O. G. & Freedman, D. E. Millisecond Coherence Time in a Tunable Molecular Electronic Spin Qubit. *ACS Cent. Sci.* **1,** 488-492 (2015).

216. Wesenberg, J.H., Ph.D. Thesis: Quantum Information Processing in Rare-Earth-Ion Doped Crystals (2004).

217. Bertaina, S., Shim, J. H., Gambarelli, S., Malkin, B. Z. & Barbara, B. Spin-orbit qubits of rare-earth-metal ions in axially symmetric crystal fields. *Phys. Rev. Lett.* **103,** 226402 (2009).

218. Luis, F. *et al.* Spin-lattice relaxation via quantum tunneling in an Er^{3+}-polyoxometalate molecular magnet. *Phys. Rev. B* **82,** 060403 (2010).

219. Clemente-Juan, J. M., Coronado, E. & Gaita-Ariño, A. Magnetic polyoxometalates: from molecular magnetism to molecular spintronics and quantum computing. *Chemical Society Reviews* **41,** 7464 (2012).

220. Martínez-Pérez, M. J. *et al.* Gd-based single-ion magnets with tunable magnetic anisotropy: Molecular design of spin qubits. *Phys. Rev. Lett.* **108,** 1–5 (2012).

221. Baldoví, J. J. *et al.* Coherent manipulation of spin qubits based on polyoxometalates: the case of the single ion magnet $[GdW_{30}P_5O_{110}]^{14-}$. *Chem. Commun.* **49,** 8922–4 (2013).

222. Baldoví, J. J. *et al.* Molecular spin qubits based on lanthanide ions encapsulated in cubic polyoxopalladates: design criteria to enhance quantum coherence. *Inorg. Chem. Front.* **2,** 893–897 (2015).

223. Timco, G. a *et al.* Engineering the coupling between molecular spin qubits by coordination chemistry. *Nat. Nanotechnol.* **4,** 173–178 (2009).

224. Candini, A. *et al.* Entanglement in supramolecular spin systems of two weakly coupled antiferromagnetic rings (purple-Cr_7Ni). *Phys. Rev. Lett.* **104,** 1–4 (2010).

225. Aromí, G., Aguilà, D., Gamez, P., Luis, F. & Roubeau, O. Design of magnetic coordination complexes for quantum computing. *Chem. Soc. Rev.* **41,** 537 (2012).

226. Luis, F. *et al.* Molecular prototypes for spin-based CNOT and SWAP quantum gates. *Phys. Rev. Lett.* **107,** 1–5 (2011).

227. Aguilà, D. *et al.* Heterodimetallic [LnLn'] Lanthanide Complexes: Toward a Chemical Design of Two-Qubit Molecular Spin Quantum Gates. *J. Am. Chem. Soc.* **136,** 14215–14222 (2014).

228. Baibich, M. N., Broto, J. M., Fert, A. & Van Dau, F. N. Giant magnetoresistance of (001) Fe/(001) Cr magnetic superlattices. *Phys. Rev. Lett.* **61,** 2472–2475 (1988).

229. Binasch, G., Grünberg, P., Saurenbach, F. & Zinn, W. Enhanced magnetoresistance in layered magnetic structures with antiferromagnetic interlayer exchange. *Phys. Rev. B* **39,** 4828–4830 (1989).

230. Akerman, J. Toward a Universal Memory. *Science.* **308,** 508–510 (2005).

231. Prejbeanu, I. L. *et al.* Thermally assisted MRAM. *J. Phys. Condens. Matter* **19,** 165218 (2007).

232. Georges, B. *et al.* Coupling efficiency for phase locking of a spin transfer nano-oscillator to a microwave current. *Phys. Rev. Lett.* **101,** 4–7 (2008).

233. Petta, J. R. *et al.* Coherent manipulation of coupled electron spins in semiconductor quantum dots. *Science.* **309,** 2180 (2005).

234. Rocha, A. R. *et al.* Towards molecular spintronics. *Nat. Mater.* **4,** 335–9 (2005).

235. Sanvito, S. & Rocha, A. R. Molecular-Spintronics: the art of driving spin through molecules. *J. Comput. Theor. Nano.* **3**, 874-9 (2006).

236. Coronado, E. *et al*. Molecular spintronics and quantum computing. *J. Mater. Chem.* **19,** 1670 (2009).

237. Suaud, N., Gaita-Ariño, A., Clemente-Juan, J. M. & Coronado, E. Electron delocalization and electrostatic repulsion at the origin of the strong spin coupling in mixed-valence keggin polyoxometalates: ab initio calculations of the one- and two-electron processes. *Chem.–Eur. J.* **10,** 4041–53 (2004).

238. Borrás-Almenar, J. J. *et al.* MVPACK: A package to calculate energy levels and magnetic properties of high nuclearity mixed valence clusters. *J. Comput. Chem.* **31,** 1321–1332 (2010).

239. Maestre, J. M., Poblet, J. M., Bo, C., Casañ-Pastor, N. & Gomez-Romero, P. Electronic Structure of the Highly Reduced Polyoxoanion $[PMo_{12}O_{40}(VO)_2]^{5-}$: A DFT Study. *Inorg. Chem.* **37,** 3444–3446 (1998).

240. Lehmann, J., Gaita-Arino, A., Coronado, E. & Loss, D. Spin qubits with electrically gated polyoxometalate molecules. *Nat. Nanotechnol.* **2,** 312–317 (2007).

241. Cardona-Serra, S. *et al.* Modelling electric field control of the spin state in the mixed-valence polyoxometalate $[GeV_{14}O_{40}]^{8-}$. *Chem. Commun.* **49,** 9621–3 (2013).

242. Cardona-Serra, S. *et al.* Electrically switchable magnetic molecules: inducing a magnetic coupling by means of an external electric field in a mixed-valence polyoxovanadate cluster. *Chem.–Eur. J.* **21,** 763–9 (2015).

243. Suaud, N., Masaro, Y., Coronado, E., Clemente-Juan, J. M. & Guihéry, N. Origin of the Paramagnetic Properties of the Mixed-Valence Polyoxometalate $[GeV_{14}O_{40}]^{8-}$ Reduced by Two Electrons: Wave Function Theory and Model Hamiltonian Calculations. *Eur. J. Inorg. Chem.* **2009,** 5109–5114 (2009).

244. Secheresse, F. *Polyoxometalate Chemistry: Some Recent Trends*. (World Scientific, 2013).

245. Bogani, L. & Wernsdorfer, W. Molecular spintronics using single-molecule magnets.

Nat. Mater. **7,** 179–186 (2008).

246. Heersche, H. *et al.* Electron Transport through Single Mn_{12} Molecular Magnets. *Phys. Rev. Lett.* **96,** 206801 (2006).
247. Park, J. *et al.* Coulomb blockade and the Kondo effect in single-atom transistors. *Nature* **417,** 722–5 (2002).
248. Liang, W., Shores, M. P., Bockrath, M., Long, J. R. & Park, H. Kondo resonance in a single-molecule transistor. *Nature* **417,** 725–9 (2002).
249. Urdampilleta, M., Klyatskaya, S., Cleuziou, J.-P., Ruben, M. & Wernsdorfer, W. Supramolecular spin valves. *Nat. Mater.* **10,** 502–6 (2011).
250. Ganzhorn, M., Klyatskaya, S., Ruben, M. & Wernsdorfer, W. Strong spin-phonon coupling between a single-molecule magnet and a carbon nanotube nanoelectromechanical system. *Nat. Nanotechnol.* **8,** 165–9 (2013).
251. Candini, A., Klyatskaya, S., Ruben, M., Wernsdorfer, W. & Affronte, M. Graphene spintronic devices with molecular nanomagnets. *Nano Lett.* **11,** 2634–9 (2011).
252. Thiele, S. *et al.* Electrical readout of individual nuclear spin trajectories in a single-molecule magnet spin transistor. *Phys. Rev. Lett.* **111,** 037203 (2013).
253. Malavolti, L. *et al.* Erratic magnetic hysteresis of TbPc2 molecular nanomagnets. *J. Mater. Chem. C* **1,** 2935–2942 (2013).
254. Urdampilleta, M. *et al.* Molecular quantum spintronics: supramolecular spin valves based on single-molecule magnets and carbon nanotubes. *Int. J. Mol. Sci.* **12,** 6656–67 (2011).
255. Kyatskaya, S. *et al.* Anchoring of rare-earth-based single-molecule magnets on single-walled carbon nanotubes. *J. Am. Chem. Soc.* **131,** 15143–15151 (2009).
256. Giménez-López, M. del C. *et al.* Encapsulation of single-molecule magnets in carbon nanotubes. *Nat. Commun.* **2,** 407 (2011).
257. Giusti, A. *et al.* Magnetic Bistability of Individual Single-Molecule Magnets Grafted on Single-Wall Carbon Nanotubes. *Angew. Chemie Int. Ed.* **121,** 5049–5052 (2009).
258. Fahrendorf, S. *et al.* Accessing 4f-states in single-molecule spintronics. *Nat. Commun.* **4,** 2425 (2013).
259. Bogani, L. A perspective on slow-relaxing molecular magnets built from rare-earths and nitronyl-nitroxide building blocks. *J. Appl. Phys.* **109,** 07B115 (2011).
260. Bernot, K. *et al.* Magnetic anisotropy of dysprosium(III) in a low-symmetry environment: a theoretical and experimental investigation. *J. Am. Chem. Soc.* **131,** 5573–9 (2009).

261. Peng, Y.-H. *et al.* Syntheses, structures, and magnetic properties of heterobimetallic clusters with tricyanometalate and pi-conjugated ligands containing 1,3-dithiol-2-ylidene. *Inorg. Chem.* **49,** 1905–12 (2010).

262. Wang, X., Bao, X., Xu, P. & Li, L. From Discrete Molecule to One-Dimension Chain: Two New Nitronyl Nitroxide-Lanthanide Complexes Exhibiting Slow Magnetic Relaxation. *Eur. J. Inorg. Chem.* **2011,** 3586–3591 (2011).

263. Wang, X.-L. *et al.* Slow magnetic relaxation in lanthanide complexes with chelating imino nitroxide radicals. *Inorg. Chem. Commun.* **14,** 1728–1731 (2011).

264. Coronado, E. *et al.* Single-molecule magnetic behavior in a neutral terbium(III) complex of a picolinate-based nitronyl nitroxide free radical. *Inorg. Chem.* **50,** 7370–2 (2011).

265. Mannini, M. *et al.* Magnetic behaviour of $TbPc_2$ single-molecule magnets chemically grafted on silicon surface. *Nat. Commun.* **5,** 4582 (2014).

266. Faucher, M. & Garcia, D. Electrostatic crystal-field contributions in rare-earth compounds with consistent multipolar effects. I. Contribution to *k*-even parameters. *Phys. Rev. B* **26,** 5451–5468 (1982).

267. Baldoví, J. J. *et al.* SIMPRE: A software package to calculate crystal field parameters, energy levels, and magnetic properties on mononuclear lanthanoid complexes based on charge distributions. *J. Comput. Chem.* **34,** 1961–1967 (2013).

268. Baldoví, J. J., Clemente-Juan, J. M., Coronado, E., Gaita-Ariño, A. & Palii, A. An updated version of the computational package SIMPRE that uses the standard conventions for Stevens crystal field parameters. *J. Comput. Chem.* **35,** 1930–4 (2014).

269. Jörgensen, C. K., Pappalardo, R. & Schmidtke, H.-H. Do the "Ligand Field" Parameters in Lanthanides Represent Weak Covalent Bonding? *J. Chem. Phys.* **39,** 1422 (1963).

270. Russell, H. N. & Saunders, F. A. New Regularities in the Spectra of the Alkaline Earths. *Astrophys. J.* **61,** 38 (1925).

271. Edvardsson, S. & Klintenberg, M. Role of the electrostatic model in calculating rare-earth crystal-field parameters. *J. Alloys Compd.* **275,** 230–233 (1998).

272. Gajek, Z. On standardization of low symmetry crystal fields. *J. Phys. Chem. Solids* **82,** 21–27 (2015).

273. Hutchings, M. Point-charge calculations of energy levels of magnetic ions in crystalline electric fields. *Solid State Phys.* **16,** 227–273 (1964).

274. Karbowiak, M. & Rudowicz, C. Software package SIMPRE-Revisited. *J. Comput.*

Chem. **35,** 1935–41 (2014).

275. Baldoví, J. J., Clemente-Juan, J. M. & Gaita-Ariño, A. SIMPRE: Installation and User Manual. arXiv:1407.6576v1 (2014).
276. Boča, R. *Theoretical Foundations of Molecular Magnetism*. (Elsevier Science, 1999).
277. Weisstein, E. W. Euler Angles. *MathWorld – A Wolfram Web Resource*. http://mathworld.wolfram.com/EulerAngles.html.
278. Planitz, M. LAPACK Users Guide. *Math. Gaz.* **79,** 210 (1995).
279. Hund, F. Atomtheoretische Deutung des Magnetismus der seltenen. Erden. *Zeitschrift für Phys.* **33,** 855–859 (1925).
280. Laporte, O. Zur Interpretation des Paramagnetismus der Eisengruppe. *Zeitschrift für Phys.* **47,** 761–769 (1928).
281. Van Vleck, J. H. On σ-Type Doubling and Electron Spin in the Spectra of Diatomic Molecules. *Phys. Rev.* **33,** 467–506 (1929).
282. Van Vleck, J. H. & Frank, A. The Effect of Second Order Zeeman Terms on Magnetic Susceptibilities in the Rare Earth and Iron Groups. *Phys. Rev.* **34,** 1494–1496 (1929).
283. Kittel, C. Introduction to Solid State Physics, 8th Edition (Wiley, 2004).
284. Faulkner, S., Pope, S. J. A. & Burton-Pye, B. P. Lanthanide Complexes for Luminescence Imaging Applications. *Appl. Spectrosc. Rev.* **40**, 1-31 (2007).
285. Bradley, D. C., Ghotra, J. S. & Hart, F. A. Low co-ordination numbers in lanthanide and actinide compounds. Part I. The preparation and characterization of tris{bis(trimethylsilyl)-amido}lanthanides. *J. Chem. Soc. Dalt. Trans.* 1021 (1973).
286. Meihaus, K. R. & Long, J. R. Magnetic blocking at 10 K and a dipolar-mediated avalanche in salts of the bis(η^8-cyclooctatetraenide) complex $[Er(COT)_2]^-$. *J. Am. Chem. Soc.* **135,** 17952–7 (2013).
287. Barsukova, M. *et al.* Polyoxopalladates Encapsulating Yttrium and Lanthanide Ions, $[(XPd_{12}^{II})Pd^{III}(AsPh)_8O_{32}]^{5-}$ (X = Y, Pr, Nd, Sm, Eu, Gd, Tb, Dy, Ho, Er, Tm, Yb, Lu). *Chem. Eur. J.* **16,** 9076–9085 (2010).
288. Álvarez, S. *et al.* Shape maps and polyhedral interconversion paths in transition metal chemistry. *Coord. Chem. Rev.* **249,** 1693–1708 (2005).
289. Enrique, B. G. Optical Spectrum and Magnetic Properties of Er^{3+} in CaWO4. *J. Chem. Phys.* **55,** 2538 (1971).
290. Rajnak, K. & Wybourne, B. G. Configuration Interaction in Crystal Field Theory. *J. Chem. Phys.* **41,** 565 (1964).

291. Ellis, M. M. Crystal Field in Rare-Earth Trichlorides. I. Overlap and Exchange Effects in $PrCl_3$. *J. Chem. Phys.* **47,** 1986 (1967).
292. Newman, D. J. & Ng, B. *Crystal Field Handbook*. (Cambridge University Press, 2007).
293. Newman, D. J. & Ng, B. The superposition model of crystal fields. *Reports Prog. Phys.* **52,** 699–762 (1999).
294. Baldoví, J. J., Borrás-Almenar, J. J., Clemente-Juan, J. M., Coronado, E. & Gaita-Ariño, A. Modeling the properties of lanthanoid single-ion magnets using an effective point-charge approach. *Dalton Transactions* **41,** 13705 (2012).
295. Jiang, S.-D. & Qin, S.-X. Prediction of the quantized axis of rare-earth ions: the electrostatic model with displaced point charges. *Inorg. Chem. Front.* **2,** 613–619 (2015).
296. Baldoví, J. J., Gaita-Ariño, A. & Coronado, E. Modeling the magnetic properties of lanthanide complexes: relationship of the REC parameters with Pauling electronegativity and coordination number. *Dalton Trans.* **44,** 12535–8 (2015).
297. Cotton, S. A. Establishing coordination numbers for the lanthanides in simple complexes. *Comptes Rendus Chim.* **8,** 129–145 (2005).
298. Jayasankar, C. K., Richardson, F. S. & Reid, M. F. Phenomenological spin-correlated crystal-field analyses of energy levels in Ln^{3+}:$LaCl_3$ systems. *J. Less Common Met.* **148,** 289–296 (1989).
299. Jayasankar, C. K., Reid, M. F. & Richardson, F. S. Comparative Crystal-Field Analyses of $4f^N$ Energy Levels in $LiYF_4$:Ln^{3+} Systems. *Phys. status solidi* **155,** 559–569 (1989).
300. Liu, G., Carnall, W., Jones, R. P., Cone, R. & Huang, J. Electronic energy level structure of Tb^{3+} in $LiYF_4$. *J. Alloys Compd.* **207-208,** 69–73 (1994).
301. Tanner, P. A., Ravi Kanth Kumar, V. V., Jayasankar, C. K. & Reid, M. F. Analysis of spectral data and comparative energy level parametrizations for Ln^{3+} in cubic elpasolite crystals. *J. Alloys Compd.* **215,** 349–370 (1994).
302. Tanner, P. A., Faucher, M. D. & Zhou, X. Electronic spectra and crystal field analysis of energy levels of Ho^{3+} in HoF_6^{3-}. *J. Phys. Chem. A* **115,** 2557–67 (2011).
303. Zhou, X., Tanner, P. A. & Faucher, M. D. Electronic Spectra and Crystal Field Analysis of Er^{3+} in Cs_2NaErF_6. *J. Phys. Chem. C* **111,** 683–687 (2007).
304. Tanner, P. A. & Faucher, M. D. Electronic spectra and crystal field analysis of. *Chem. Phys. Lett.* **445,** 183–187 (2007).
305. Jayasankar, C. K., Richardson, F. S., Reid, M. F., Porcher, P. & Caro, P. Spin-

correlated crystal-field interactions in NdF_3, Nd^{3+}:LaF_3, and Nd^{3+}:$LiYF_4$. *Inorganica Chim. Acta* **139,** 287–290 (1987).

306. Richardson, F. S., Reid, M. F., Dallara, J. J. & Smith, R. D. Energy levels of lanthanide ions in the cubic $Cs_2NaLnCl_6$ and Cs_2NaYCl_6:Ln^{3+} (doped) systems. *J. Chem. Phys.* **83,** 3813 (1985).
307. Zolnierek, Z. Crystal field parameters in a modified point charge model. *J. Phys. Chem. Solids* **45,** 523–528 (1984).
308. Tanner, P. A. & Ning, L. Electronegativity, charge transfer, crystal field strength, and the point charge model revisited. *J. Phys. Chem. A* **117,** 1503–7 (2013).
309. Evans, C. H. *Biochemistry of the Lanthanides*. **11,** (Springer Science & Business Media, 2013).
310. Baldoví, J. J. *et al.* Construction of a general library for the rational design of nanomagnets and spin qubits based on mononuclear f-block complexes. The polyoxometalate case. *Inorg. Chem.* **53,** 9976–80 (2014).
311. Monteiro, B. *et al.* Magnetic properties of the layered lanthanide hydroxide series $Y_xDy_{8-x}OH_{20}Cl_4{\cdot}6H_2O$: from single ion magnets to 2D and 3D interaction effects. *Inorg. Chem.* **54,** 1949–57 (2015).
312. AlDamen, M. A. *et al.* Mononuclear Lanthanide Single Molecule Magnets Based on the Polyoxometalates $Ln(W_5O_{18})_2^{9-}$ and $Ln(\beta_2\text{-}SiW_{11}O_{39})_2^{13-}$ (Ln(III) = Tb, Dy, Ho, Er, Tm, and Yb). *Inorg. Chem.* **48,** 3467–3479 (2009).
313. Ghosh, S. *et al.* Multi-frequency EPR studies of a mononuclear holmium single-molecule magnet based on the polyoxometalate $[Ho^{III}(W_5O_{18})_2]^{9-}$. *Dalton Transactions* **41,** 13697 (2012).
314. Ozeki, T. & Yamase, T. Effect of lanthanide contraction on the structures of the decatungstolanthanoate anions in $K_3Na_4H_2[LnW_{10}O_{36}]{\cdot}nH_2O$ (Ln = Pr, Nd, Sm, Gd, Tb, Dy) crystals. *Acta Crystallogr. Sect. B Struct. Sci.* **50,** 128–134 (1994).
315. Kitamura, A., Ozeki, T. & Yagasaki, A. β-Octamolybdate as a Building Block. Synthesis and Structural Characterization of Rare Earth−Molybdate Adducts. *Inorg. Chem.* **36,** 4275–4279 (1997).
316. Lehmann, J., Gaita-Ariño, A., Coronado, E. & Loss, D. Spin qubits with electrically gated polyoxometalate molecules. *Nat. Nanotechnol.* **2,** 312–7 (2007).
317. Qi, W. & Wu, L. Polyoxometalate/polymer hybrid materials: fabrication and properties. *Polym. Int.* **58,** 1217–1225 (2009).
318. Dolbecq, A., Dumas, E., Mayer, C. R. & Mialane, P. Hybrid organic-inorganic

polyoxometalate compounds: from structural diversity to applications. *Chem. Rev.* **110,** 6009–48 (2010).

319. Bustos, C. *et al.* Aryldiazenido derivatives: A new entry to the functionalization of Keggin polyoxometalates. *Inorganica Chim. Acta* **363,** 4262–4268 (2010).
320. Hopkins, T. A., Metcalf, D. H. & Richardson, F. S. Electronic State Structure and Optical Properties of $Tb(oda)_3^{3-}$ Complexes in Trigonal $Na_3[Tb(oda)_3]\cdot 2NaClO_4\cdot 6H_2O$ Crystals. *Inorg. Chem.* **37,** 1401–1412 (1998).
321. Metcalf, D. H., Hopkins, T. A. & Richardson, F. S. Electronic spectra, optical activity, and crystal-field energy-level structure of Dy^{3+} in trigonal $Na_3[Dy(oda)_3]\cdot 2NaClO_4\cdot 6H_2O$ crystals. *Inorg. Chem.* **34,** 4868–4878 (1995).
322. Moran, D. M., De Piante, A. & Richardson, F. S. Optical-absorption spectra, crystal-field energy levels, and transition line strengths of holmium in trigonal $Na_3[Ho(oda)_3]\cdot 2NaClO_4\cdot 6H_2O$. *Phys. Rev. B* **42,** 3317–3330 (1990).
323. Moran, D. M. & Richardson, F. S. Parametric analysis of f - f transition intensities in trigonal $Na_3[Ho(oda)_3]\cdot 2NaClO_4\cdot 6H_2O$. *Phys. Rev. B* **42,** 3331–3344 (1990).
324. Lennartson, A. & Håkansson, M. Total spontaneous resolution of nine-coordinate complexes. *Cryst. Eng. Comm.* **11,** 1979 (2009).
325. Fronczek, F. R., Banerjee, A. K., Watkins, S. F. & Schwartz, R. W. Absolute configuration and circular dichroism of the lanthanide complex: trisodiumtris(oxydiacetato)europate(III) bis(sodium tetrafluoroborate) hexahydrate. *Inorg. Chem.* **20,** 2745–2746 (1981).
326. Geng, F. *et al.* Structural study of a series of layered rare-earth hydroxide sulfates. *Inorg. Chem.* **50,** 6667–72 (2011).
327. Wang, Q. & O'Hare, D. Recent advances in the synthesis and application of layered double hydroxide (LDH) nanosheets. *Chem. Rev.* **112,** 4124–55 (2012).
328. Coronado, E. & Mínguez Espallargas, G. Dynamic magnetic MOFs. *Chem. Soc. Rev.* **42,** 1525–39 (2013).
329. Abellán, G. *et al.* Photo-switching in a hybrid material made of magnetic layered double hydroxides intercalated with azobenzene molecules. *Adv. Mater.* **26,** 4156–62 (2014).
330. Geng, F. *et al.* General synthesis and structural evolution of a layered family of Ln8(OH)20Cl4 x nH2O (Ln = Nd, Sm, Eu, Gd, Tb, Dy, Ho, Er, Tm, and Y). *J. Am. Chem. Soc.* **130,** 16344–50 (2008).
331. Geng, F., Ma, R. & Sasaki, T. Anion-exchangeable layered materials based on rare-

earth phosphors: unique combination of rare-earth host and exchangeable anions. *Acc. Chem. Res.* **43,** 1177–85 (2010).

332. Hasegawa, Y. *et al.* Enhanced Luminescence and Photomagnetic Properties of Surface-Modified EuO Nanocrystals. *Angew. Chemie Int. Ed.* **41,** 2073 (2002).
333. Xiang, Y. *et al.* Synthesis of Highly Luminescent and Anion-Exchangeable Cerium-Doped Layered Yttrium Hydroxides for Sensing and Photofunctional Applications. *Adv. Funct. Mater.* **21,** 4388–4396 (2011).
334. Yoon, Y. *et al.* Surface Modification of Exfoliated Layered Gadolinium Hydroxide for the Development of Multimodal Contrast Agents for MRI and Fluorescence Imaging. *Adv. Funct. Mater.* **19,** 3375–3380 (2009).
335. Lechevallier, S. *et al.* Gadolinium−Europium Carbonate Particles: Controlled Precipitation for Luminescent Biolabeling. *Chem. Mater.* **22,** 6153–6161 (2010).
336. Yoon, Y., Byeon, S.-H. & Lee, I. S. Unexplored thermal transformation behavior of two-dimensionally bound gadolinium hydroxide layers: fabrication of oriented crystalline films of gadolinium oxychloride nanosheets suitable for the multicolor luminescence with color tunability. *Adv. Mater.* **22,** 3272–6 (2010).
337. Lee, B.-I., Lee, E. & Byeon, S.-H. Assembly of Layered Rare-Earth Hydroxide Nanosheets and SiO2 Nanoparticles to Fabricate Multifunctional Transparent Films Capable of Combinatorial Color Generation. *Adv. Funct. Mater.* **22,** 3562–3569 (2012).
338. Wang, L. *et al.* Tunable compositions and luminescent performances on members of the layered rare-earth hydroxides $(Y_{1-x}Ln_x)_2(OH)_5NO_3{\cdot}nH_2O$ (Ln = Tb, Eu). *Dalton Trans.* **40,** 11781–7 (2011).
339. Monteiro, B. *et al.* A 2D Layered Lanthanide Hydroxide Showing Slow Relaxation of Magnetization - $Dy_8(OH)_{20}Cl_4{\cdot}6H_2O$. *Eur. J. Inorg. Chem.* **2013,** 5059–5063 (2013).
340. Hill, R. J. *et al.* Unprecedented bilayer topologies in 5- and 6-connected framework polymers. *Chem. Commun.* 1792–3 (2004).
341. Long, D.-L., Blake, A. J., Champness, N. R., Wilson, C. & Schröder, M. Unprecedented Seven- and Eight-Connected Lanthanide Coordination Networks. *Angew. Chemie Int. Ed.* **113,** 2509–2513 (2001).
342. Long, D.-L. *et al.* Non-natural eight-connected solid-state materials: a new coordination chemistry. *Angew. Chem. Int. Ed.* **43,** 1851–4 (2004).
343. James, S. L. Metal-organic frameworks. *Chem. Soc. Rev.* **32,** 276–288 (2003).
344. Long, J. R. & Yaghi, O. M. The pervasive chemistry of metal-organic frameworks. *Chem. Soc. Rev.* **38,** 1213–4 (2009).

345. Ishikawa, N., Sugita, M. & Wernsdorfer, W. Nuclear spin driven quantum tunneling of magnetization in a new lanthanide single-molecule magnet: bis(phthalocyaninato)holmium anion. *J. Am. Chem. Soc.* **127,** 3650–1 (2005).

346. Poneti, G. *et al.* A rational approach to the modulation of the dynamics of the magnetisation in a dysprosium-nitronyl-nitroxide radical complex. *Chem. Commun.* 1807–9 (2007).

347. Ruiz, J. *et al.* Field and dilution effects on the slow relaxation of a luminescent DyO_9 low-symmetry single-ion magnet. *Chem. Commun.* **48,** 7916–8 (2012).

348. Sun, C.-Y. *et al.* Highly stable crystalline catalysts based on a microporous metal-organic framework and polyoxometalates. *J. Am. Chem. Soc.* **131,** 1883–8 (2009).

349. Ishikawa, N., Otsuka, S. & Kaizu, Y. The effect of the f-f interaction on the dynamic magnetism of a coupled $4f^8$ system in a dinuclear terbium complex with phthalocyanines. *Angew. Chem. Int. Ed.* **44,** 731–3 (2005).

350. Ishikawa, N., Mizuno, Y., Takamatsu, S., Ishikawa, T. & Koshihara, S. Effects of chemically induced contraction of a coordination polyhedron on the dynamical magnetism of bis(phthalocyaninato)disprosium, a single-4f-ionic single-molecule magnet with a Kramers ground state. *Inorg. Chem.* **47,** 10217–9 (2008).

351. Gomez-Segura, J. *et al.* 2-D Self-Assembly of the Bis(Phthalocyaninato) Terbium(Iii) Single-Molecule Magnet Studied by Scanning Tunnelling Microscopy. *Chem. Commun.* 2866–2868 (2006).

352. Robb, M. A., Haines, W. J. & Csizmadia, I. G. Theoretical definition of the size of electron pairs and its stereochemical implications. *J. Am. Chem. Soc.* **95,** 42–48 (1973).

353. Meihaus, K. R., Rinehart, J. D. & Long, J. R. Dilution-induced slow magnetic relaxation and anomalous hysteresis in trigonal prismatic dysprosium(III) and uranium(III) complexes. *Inorg. Chem.* **50,** 8484–9 (2011).

354. Baldoví, J. J., Clemente-Juan, J. M., Coronado, E. & Gaita-Ariño, A. Two pyrazolylborate dysprosium(III) and neodymium(III) single ion magnets modeled by a Radial Effective Charge approach. *Polyhedron* **66,** 39–42 (2013).

355. Reddmann, H., Apostolidis, C., Walter, O. & Amberger, H.-D. Zur Elektronenstruktur hochsymmetrischer Verbindungen der f-Elemente. 40. Parametrische Analyse des Kristallfeld-Aufspaltungsmusters von Tris(hydrotris(1-pyrazolyl)borato)neodym(III). *Zeitschrift für Anorg. und Allg. Chemie* **632,** 1405–1408 (2006).

356. Rinehart, J. D., Harris, T. D., Kozimor, S. A., Bartlett, B. M. & Long, J. R. Magnetic

exchange coupling in actinide-containing molecules. *Inorg. Chem.* **48,** 3382–95 (2009).

357. Morss, L.R., Edelstein, N. & Fuger, J. *The Chemistry of the Actinide and Transactinide Elements (3rd ed., Volumes 1-5)*. (Springer, 2007).
358. Lukens, W. W. & Walter, M. D. Quantifying exchange coupling in f-ion pairs using the diamagnetic substitution method. *Inorg. Chem.* **49,** 4458–65 (2010).
359. Freeman, A. J. & Darby, J. B. J. Actinides: electronic structure and related properties. Volume II. (Academic Press, 1974).
360. Grunzweig-Genossar, J., Kuznietz, M. & Friedman, F. Magnetic Properties of Uranium Compounds with Elements of the V A and VI A Groups. I. Compounds of UX Type. *Phys. Rev.* **173,** 562–573 (1968).
361. Moore, K. T. & van der Laan, G. Nature of the 5f states in actinide metals. *Rev. Mod. Phys.* **81,** 235–298 (2009).
362. Antunes, M. A. *et al.* A Mononuclear Uranium(IV) Single-Molecule Magnet with an Azobenzene Radical Ligand. *Chem.–Eur. J.* **21,** 17817–26 (2015).
363. Monteiro, B. *et al.* Triamidotriazacyclononane complexes of group 3 metals. Synthesis and crystal structures. *Inorg. Chem.* **42,** 4223–31 (2003).
364. Apostolidis, C. *et al.* Zur Elektronenstruktur hochsymmetrischer Verbindungen der f-Elemente (44). Erstmalige parametrische Analyse des Absorptionsspektrums einer Molekülverbindung des trivalenten Urans: Tris[hydrotris(1-pyrazolyl)borato]uran(III). *Zeitschrift für Anorg. und Allg. Chemie* **636,** 201–208 (2010).
365. Karbowiak, M. & Rudowicz, C. Properties of uranium- and lanthanide-based single-ion magnets modelled by the complete and restricted Hamiltonian approach. *Polyhedron* **93,** 91–98 (2015).
366. Murugesu, M. Magnetic anisotropy: The orientation is in the details. *Nat. Chem.* **4,** 347–348 (2012).
367. Boulon, M.-E. *et al.* Angular-resolved magnetometry beyond triclinic crystals: out-of-equilibrium studies of Cp*ErCOT single-molecule magnet. *Chemistry* **19,** 13726–31 (2013).
368. Layfield, R. A. Organometallic Single-Molecule Magnets. *Organometallics* **33,** 1084–1099 (2014).
369. Amberger, H.-D., Schultze, H. & Edelstein, N. M. The electronic structure of organometallic complexes of the f elements—XVI. Absorption spectrum and parameterization of the crystal field splitting pattern of the cyclohexylisocyanide adduct derived from tris (η^5-cyclopentadienyl)-neodymium(III). *Spectrochim. Acta*

Part A Mol. Spectrosc. **42,** 657–667 (1986).

370. Unrecht, B. *et al.* The electronic structure of organometallic complexes of the f elements XLI. *J. Alloys Compd.* **250,** 383–386 (1997).
371. Chen, G.-J. *et al.* Enhancing anisotropy barriers of dysprosium(III) single-ion magnets. *Chemistry* **18,** 2484–7 (2012).
372. Wang, Z.-G. *et al.* Single-ion magnet behavior of a new mononuclear dysprosium complex. *Inorg. Chem. Commun.* **27,** 127–130 (2013).
373. Bi, Y. *et al.* Capping ligand perturbed slow magnetic relaxation in dysprosium single-ion magnets. *Chem.–Eur. J.* **17,** 12476–81 (2011).
374. Wang, Y., Li, X.-L., Wang, T.-W., Song, Y. & You, X.-Z. Slow relaxation processes and single-ion magnetic behaviors in dysprosium-containing complexes. *Inorg. Chem.* **49,** 969–76 (2010).
375. Fatila, E. M., Hetherington, E. E., Jennings, M., Lough, A. J. & Preuss, K. E. Syntheses and crystal structures of anhydrous Ln(hfac)3(monoglyme). Ln = La, Ce, Pr, Sm, Eu, Gd, Tb, Dy, Er, Tm. *Dalton Trans.* **41,** 1352–62 (2012).
376. Aravena, D. & Ruiz, E. Shedding light on the single-molecule magnet behavior of mononuclear Dy(III) complexes. *Inorg. Chem.* **52,** 13770–8 (2013).
377. Qian, K. *et al.* Does the thermal evolution of molecular structures critically affect the magnetic anisotropy? *Chem. Sci.* **6,** 4587–4593 (2015).
378. Chilton, N. F., Collison, D., McInnes, E. J. L., Winpenny, R. E. P. & Soncini, A. An electrostatic model for the determination of magnetic anisotropy in dysprosium complexes. *Nat. Commun.* **4,** 2551 (2013).
379. Fuchs, G. D., Burkard, G., Klimov, P. V. & Awschalom, D. D. A quantum memory intrinsic to single nitrogen–vacancy centres in diamond. *Nat. Phys.* **7,** 789–793 (2011).
380. Stamp, P. C. E. Environmental decoherence versus intrinsic decoherence. *Philos. Trans. A. Math. Phys. Eng. Sci.* **370,** 4429–53 (2012).
381. Rosaleny, L. E. & Gaita-Ariño, A. Theoretical evaluation of lanthanide binding tags as biomolecular handles for the organization of single ion magnets and spin qubits. *Inorg. Chem. Front.* (2016). doi:10.1039/C5QI00127G
382. Hartmann, S. R. & Hahn, E. L. Nuclear Double Resonance in the Rotating Frame. *Phys. Rev.* **128,** 2042–2053 (1962).

A la memoria de mis abuelos

Amparo A. Milla Milla
04/07/1930 – 07/01/2016

José Baldoví Gallego
31/10/1925 – 09/01/2016